Bergische Universität Wuppertal
Fachbereich C - Mathematik und Naturwissenschaften
Physik - Gittereichtheorie

Inaugural-Dissertation zur Erlangung des Dr.rer.nat.

Precision Physics from the Lattice
Calculation of the Hadron Spectrum, Quark Masses
and Kaon Bag Parameter

Autor:	Thorsten Kurth
Datum:	August 2, 2011
Preprint-ID:	WUB/11-09
Doktorvater:	Prof. Zoltán Fodor

Contents

1. Introduction

Many interesting processes of the strong interaction are not accessible by perturbation theory because they occur at energy scales around $\Lambda_{QCD} \approx 200\,\mathrm{MeV}$. Thus, a different approach has to be taken and the most prominent and important method today is the *lattice discretization of QCD* or *lattice QCD* in short. When it was invented by Kenneth Wilson in 1974, its application was limited to analytical calculations in the strong coupling limit since computer technology and the development of algorithms were still at their very early stages. This has dramatically changed over the past years: today, every smartphone is much more powerful than any supercomputer thirty years ago, and new or improved algorithms further optimized the overall costs per flop. It is especially important to stress the latter point: back in 2001, with the algorithms available at that time, it seemed to be quite unrealistic that lattice calculations will be able to reach the physical pion mass even if petaflop computers were available. Today, in 2011, 'armed' with these petaflop computers and highly efficient algorithms, we were able to reach the physical pion mass in our calculations.

Since a few years, lattice QCD can give serious and precise predictions and provide important insights and answers to fundamental questions. However, it should not be forgotten that lattice computations still require cutting-edge hard- and software, and a lot of effort goes into writing code, tuning simulation parameters, generating configurations and analyzing data. Especially important for successful lattice computations is the careful choice of algorithms and actions. Conceptually more attractive lattice actions often come with large additional CPU costs. We found a good balancing and were able to give answers to important questions.

The logical structure of this thesis can be summarized as follows: the introductory section 2 describes all methods we used in our studies and also gives a brief introduction into lattice and continuum QCD. Beside textbook methods and formulas, this part contains descriptions of methods we applied in order to reach remarkable percent-level precisions in our calculations. One of those methods is the new ratio-difference method (cf. section 2.3.7). The others are the non-perturbative continuum running as well as the trace-subtraction (cf. 2.4.3). Another important ingredient to our calculations is link smearing (cf. section 2.3.3 for details).

The goal of the calculations presented in section 4 was the pre- or post-diction of important physical observables with full control over and minimization of all errors. Before such expensive and elaborate calculations can be started, a suitable lattice action has to be designed. We decided to use two different actions, both involving link smearing and tree-level clover improved Wilson fermions. The difference between the two actions is the type of smearing, denoted by 6 EXP and 2 HEX respectively (see section 2.3.3 for details). It is important to study newly designed lattice actions carefully and especially check whether they have the desired properties. This is done in detail in chapter 3 and summarized in subsection 3.3.

After these important and successful scaling tests, we used our new actions to perform ab initio calculations of important observables. These are discussed in detail in the main chapter 4. We determined the physical spectrum of low-lying hadron masses (4.1), light quark masses

(4.2) and the kaon bag parameter B_K (4.3). The level of theoretical and computational complexity increases with each section: the physical spectrum required the extraction of hadron masses and some additional techniques to treat finite volume effects. The quark mass determination required the additional calculation of non-perturbative renormalization factors from quark bilinears, whereas the renormalization of B_K involved four-fermion operators and the additional subtraction of contributions from chirally enhanced operators.

The different projects of chapter 4 are summarized in 4.1.4 (spectrum), 4.2.5 (quark masses) and 4.3.4 (kaon bag parameter) respectively.

The final chapter 5 contains an overall summary and provides an outlook on how this work can be extended in the future.

As mentioned before, many projects presented here involved large scale computations with testing, parameter tuning, method and program code optimization, data analysis, etc.. The large amount of manpower and CPU time necessary to perform all these tasks, can only be provided by a large collaboration, such as the Budapest-Marseille-Wuppertal collaboration I am part of. This in turn means, that almost every collaboration member is an author of the papers this thesis is based on. Therefore, I briefly summarize the main points I worked on in order to help the reader estimate my contributions to the presented papers:

- *prediction of B_K*: I performed the analysis for the precision prediction of B_K in full QCD. This involved the implementation and computation of four-fermion operator matrix elements as well as renormalization constants. The calculation of B_K is the main part of this thesis.

- *scaling studies*: I performed the scaling studies for the quark masses, B_K, as well as hadron masses. Note that I did not perform the locality and stability tests on my own. They were already finished when I took over the action tests.

- *computing renormalization factors*: I computed the renormalization factors used in the corresponding projects.

- *renormalization*: I implemented an optimized code for the non-perturbative renormalization of fermion bilinears and four-fermion operators and added it to the recent existing and frequently used codes.

- *data analysis*: I measured meson and baryon correlation functions and PCAC masses using the same code. I added the gluonic definition of the topological charge to the existing codes. Using these measurements, I computed masses and autocorrelation times for different observables.

- *configuration generation*: I generated some of the gauge configurations for all our projects, using available high-performance code for different machines, such as the Blue-Gene P and Juropa at FZ Jülich, IDRIS at Paris and some local clusters at the Bergische Universität Wuppertal.

Some of the results were already published in scientific journals or the corresponding publication is in preparation. Thus, this thesis is based on [Durr et al., 2009, 2011b, 2010, 2011a] and [Dürr et al., 2008] along with its corresponding "Supporting Online Material" (SOM).

2. Theoretical Overview

In the first two sections of this chapter (2.1 and 2.2), I will give a brief overview over the *standard model of particle physics* (*SM* in short) and the mathematical framework of *Quantum Field Theory* (*QFT*) behind it. It is not intended to be comprehensive here since more detailed information can be found in today's textbooks [e.g. such as Peskin and Schroeder, 1995; Weinberg, 1995, 1996] which usually fill several hundreds of pages.

This chapter is meant to be as comprehensive as needed to understand the difficulties of calculations within the QFT framework for making predictions in QCD as well as the methods which help to overcome those. One of these difficulties is, that many strong interaction processes occur at momentum regions which cannot be accessed by standard perturbation theory (cf. section 2.2). The most powerful and straightforward method to overcome this difficulty is lattice QCD, which we also used in our studies.

In part 2.3 of this introduction, I will sketch the basic ideas of lattice QCD, give definitions of the actions and discuss the algorithms we have used in our calculations. I am also going to discuss the method of link smearing (or filtering) to tame UV fluctuations as it plays an important role in our calculations. I will close this overview with a brief discussion on data analysis and the assessment of statistical and systematic errors.

2.1. The standard model

The *standard model of particle physics* is a theory describing the strong- and electroweak interaction between twelve different fermions (spin $S = 1/2$). These particles can be categorized into two groups called *leptons* (greek: light) and *quarks*.

The lepton-group consists of six particles with electromagnetic charge $C = \{0, -1\}$ (see below). Three of them are electron-types ($C = -1$), the other three are the so-called neutrinos ($C = 0$). The charged leptons are massive, whereas the neutrinos have zero masses[1]. Additionally, it is possible to define three families (or generations), each consisting of a charged lepton and a corresponding neutrino, within which the masses of the family members increase from left to right (cf. Table 2.1).

The second group, quarks, also consists of three families within which the same mass hierarchy applies as in the case of the leptonic families. Hence the u, d quarks are the lightest ones and masses increase from left to right (cf. Table 2.1). The quarks carry fractional charges of $C = \{+2/3, -1/3\}$ respectively and, in addition, a color charge allowing them to interact strongly (see below).

In nature, free quark states are not observed (except for the top-quark, which decays before it can form a hadronic state) but only color singlets (see section 2.2). This phenomenon is commonly referred to as *confinement* or *infrared slavery* and it leads to the fact that it is not

---

[1]For recent developments and reviews related to neutrino masses and mixing, see [Nakamura et al., 2010].

possible to separate quarks on macroscopic distances. Hence, low energy quarks form bound states which are called *hadrons*.
Every particle has its corresponding *anti-particle*, carrying the opposite charge and helicity. Due to CPT invariance, the masses of particles and anti-particles are the same.

The interactions (or *forces*) of the standard model are the strong and electroweak interaction, where each one is mediated by particles called *gauge-bosons*. The electroweak interaction is a unification of the gauge group SU(2) with the abelian U(1) introduced by Glashow, Weinberg and Salam (GWS). At energy scales of present day experiments, the SU(2) × U(1) symmetry is broken spontaneously by the Higgs mechanism, generating the massive $W^{\pm}, Z$ gauge-bosons and a massless photon [cf. Peskin and Schroeder, 1995, p. 690ff for details]. Due to the different macroscopic behaviour of these gauge-bosons, I formally split the electroweak interaction into the electromagnetic and weak force. Thus we can summarize:[2]

- *electromagnetic (EM) force*: electromagnetically charged particles interact by exchanging massless *photons*.

- *weak interaction*: this force is mediated by the massive vector bosons $Z, W^{\pm}$. It violates parity maximally and CP to a certain extent. It is responsible for radioactive β-decays.

- *strong interaction*: the gauge particle is the massless *gluon*. This force is responsible for heavy particle formation and also for the nuclear force.

For the sake of completeness, we list an additional force, which is not part of the standard model:

- *gravity*: its gauge-boson is assumed to be the massless, spin-2 *graviton*. Since the gravitational charge is unsigned, gravity is the most relevant force on cosmic scales. The reason for not including gravity in the standard model is, that naive quantization of gravitation (i.e. the Einstein-Hilbert action) leads to a perturbatively non-renormalizable theory ['t Hooft and Veltman, 1974].[3]

$l\,(C=-1)$	electron e	muon μ	tau τ
	$m_e \approx 0.511$	$m_\mu \approx 105.7$	$m_\tau \approx 1776.8$
$\nu\,(C=0)$	e-neutrino ν_e	μ-neutrino ν_μ	τ-neutrino ν_τ
	$m_{\nu_e} < 2 \cdot 10^{-6}$	$m_{\nu_\mu} < 0.19$	$m_{\nu_\tau} < 18.2$
$u-$type $(C=+2/3)$	up u	charm c	top t
	$m_u \approx 1.7 - 3.3$	$m_c \approx 1270$	$m_t \approx 172 \cdot 10^3$
$d-$type $(C=-1/3)$	down d	strange s	bottom b
	$m_d \approx 4.1 - 5.8$	$m_s \approx 101$	$m_b \approx 4.2 \cdot 10^3$

Table 2.1.: Standard model fundamental fermions, all masses are in MeV [taken from Nakamura et al., 2010]. All particles are accompanied by anti-particles which carry the opposite charge and helicity.

---

[2] I omit the yet unidentified scalar Higgs boson of the electroweak theory.

[3] This is due to the fact that there is no *asymptotically free theory* or *Gaussian fixed-point*. Beside other theories of quantum gravity, there are some ideas which relax this requirement to an *asymptotically safe* scenario [Niedermaier and Reuter, 2006], where the theory is not free in the UV.

The strong force is responsible for the existence of nuclear particles; it binds two up- and one down-quarks together to form a proton, as well as two down- and one up-quark to form a neutron. These particles are very heavy compared to their constituents: gluons are massless and up- and down-quarks have a very small mass, compared to the nucleon mass of around 1 GeV [Nakamura et al., 2010]. As a result of our studies [Dürr et al., 2008], we show that it is the binding energy which makes up the majority of that mass.

Beside the well-known nucleons, several other elementary particles exist which also consist of three quarks. These usually include up-, down-, strange-, charm-quarks and sometimes bottom-quarks. Top-quarks decay too fast to form a bound state. These kind of particles are called *baryons* which acquire integer charge and fractional spin.

Another possibility to form color singlets is to tie a quark and an anti-quark together. The resulting particles are then called *mesons* with integer charges and spin.

Except for the nucleons, all these particles are unstable and decay very fast in different channels.[4] This is why all our atomic nuclei only consist of two types of hadrons, the neutron and the proton, and not more.

Residual strong force effects between nucleons, effectively modeled by (multi-)meson exchanges, may be responsible for binding them into heavy nuclei. Although this question is still open and not yet fully answered, there is some evidence that this assumption is true [cf. e.g. Ishii et al., 2007].

Thus, studying the strong force and predicting (or post-dicting) physical quantities is important to understand how our world works at the smallest length scales. It is an important result if a QCD calculation can reproduce the experimental results, because then we know that QCD suffices to explain strong physics at the considered energy scales. However, it is even more interesting if one can find observables where the experiment and QCD calculations disagree. In that case, there is a possibility that the experimental measurements are influenced by physical effects which are not yet included in the theoretical framework. They are commonly referred to as *beyond the standard model* (BSM) effects.

2.2. Quantum field theoretical formulation of QCD and renormalization

This section is a brief synthesis of selected topics from standard textbooks [Peskin and Schroeder, 1995; DeTar and DeGrand, 2006; Cheng and Li, 2004], including many well known calculations and formulas. For a more detailed explanation of the topics discussed here, please follow these references and the references therein.

The theory of strong interaction has developed over several decades since the discovery of the strong force in experiments with atomic nuclei. In the 1950's and 1960's, several experiments and theoretical considerations improved our understanding of the strong force. The modern form of QCD was formulated in the 1970's as an SU(3) gauge theory of interacting quarks and gluons as fundamental particles [Gross and Wilczek, 1973; Weinberg, 1973; Fritzsch et al., 1973]. It became soon, along with its companion gauge theories, a part of the standard model.

---

[4]The free neutron decays into a proton, an electron and anti-electron-neutrino. However, bound inside a nucleus, the neutron is usually stable.

Up to now, QCD could not be falsified in experiment and thus seems to be a correct description of the strong interaction at energy scales which could be reached in these experiments.

In a modern field theory, all interactions and fundamental particles are encoded in a mathematical term known as *Lagrange density*. For QCD, it is given by

$$\mathcal{L} = -\frac{1}{2} \operatorname{Tr} \left[F_{\mu\nu} F^{\mu\nu}(x) \right] + \sum_{i=1}^{N_f} \bar{\psi}_i(x)(i\slashed{D} - m_i)\psi_i(x), \tag{2.1}$$

where ψ_i is a quark field of flavour i with mass m_i and $F_{\mu\nu} = \partial_\mu A_\nu - \partial_\nu A_\mu - ig[A_\mu, A_\nu]$ is the field-strength tensor of QCD. The last term in this sum gives rise to gluonic self-couplings, which are absent on *leading order* (LO) in abelian gauge theories. The gauge fields A_μ are elements of the Lie-algebra of SU(3), i.e. $A_\mu \in \mathfrak{su}(3)$. Being color octets, they transform according to the adjoint representations of SU(3). Thus they can be written as

$$A_\mu = \sum_{a=1}^{8} A_\mu^a \lambda^a, \tag{2.2}$$

where the λ^a are the generators of SU(3). These can be represented by the Gell-Mann matrices which are normalized via $\operatorname{Tr}[\lambda^a \lambda^b] = \delta_{ab}/2$.
The sum in the second term of the Lagrangian in (2.1) runs over all possible quark flavours i with masses m_i. The quark fields ψ_i are color triplets and therefore transform according to the fundamental representation of SU(3) in color space. Due to the fact that quarks are fermions, the ψ fields are spin-1/2 variables and therefore transform as spinors in Dirac space. The covariant derivative

$$\slashed{D} = \gamma^\mu \left(\partial_\mu - ig A_\mu \right) \tag{2.3}$$

finally couples the quarks to the gluons and makes the kinetic quark term gauge invariant. It is easy to show that a local transformation

$$\psi \to (1 + i\alpha)\psi \tag{2.4}$$

$$A_\mu^a \to A_\mu^a + f^{abc}\alpha^b A_\mu^c + \partial_\mu \alpha^a / g, \tag{2.5}$$

with $\alpha \equiv \alpha(x) = \alpha^a(x) \lambda^a$ and the, fully anti-symmetric, structure constants of QCD f^{abc}, leaves the Lagrangian in (2.1) invariant.
In a quantum field theory, the number of allowed terms in the Lagrangian is highly restricted if renormalizability is enforced (cf. 2.2.4). Nevertheless, note that we could have written down a term of the type

$$\mathcal{L}_\theta \propto \theta \operatorname{Tr} \left[F_{\mu\nu} \tilde{F}^{\mu\nu} \right], \tag{2.6}$$

where $\tilde{F}_{\mu\nu} = \varepsilon_{\mu\nu\alpha\beta} F^{\alpha\beta}/2$ is the dual field-strength tensor and θ the *vacuum angle*. This term is gauge invariant, a Lorentz scalar and a dimension 4 operator. Depending on the value of θ, it can break CP invariance of the strong force. However, experiment suggests that θ is extremely small. The reasons for this are still unknown and referred to as *strong CP problem*. I will revisit this issue in section 2.3.2.

2.2.1. Chiral symmetry

It is important to consider continuous global symmetries, which give rise to conserved currents
and therefore, in case of a quantum theory, to certain quantum numbers.
It is easy to verify that the Lagrangian (2.1) is invariant under charge conjugation and parity.
In case of zero quark masses (the so-called *chiral limit*), the classical theory exhibits a chiral
$U(N_f)_L \times U(N_f)_R$ symmetry in flavour space. To illustrate this, let us think of ψ as a super-
vector, collecting all quark flavours into one large single vector. We can then define its left-
and right-handed parts via

$$\psi^L = \frac{1 - \gamma_5}{2}\psi; \quad \psi^R = \frac{1 + \gamma_5}{2}\psi. \tag{2.7}$$

Now we can rewrite the fermionic part of (2.1) as follows:

$$\bar{\psi}\,i\slashed{D}\,\psi = \bar{\psi}^L\,i\slashed{D}\,\psi^L + \bar{\psi}^R\,i\slashed{D}\,\psi^R, \tag{2.8}$$

where the sum of (2.1) is incorporated within the scalar products. Hence, we can rotate the
left- and right-handed party independently in flavour space. The chiral theory is a bad ap-
proximation if all six quark flavours are considered, since the charm-, bottom- and top-quark
masses are large. However, the masses of the light up-, down- and strange-quark are small.
Therefore, it is suitable to split the quark-flavour super-vector into a light and heavy part,
considering only the light part in the following.
If we assume that the light quarks are massless, the classical Lagrangian possesses a $U(3)_L \times$
$U(3)_R$ symmetry on the light flavour sector. However, the $U(1)_A$ symmetry is broken by quan-
tum effects, resulting in the *Adler-Bell-Jackiw anomaly* [Adler, 1969; Adler and Bardeen,
1969; Bardeen, 1969; Bell and Jackiw, 1969]. Thus, the remaining symmetry group after
quantization is $SU(3)_L \times SU(3)_R \times U(1)_V$, where $U(1)_V$ induces baryon number conservation.
This allows for classifying hadrons into mesons and baryons [cf. Scherer, 2003, p. 74].
The $SU(3)_L \times SU(3)_R \times U(1)_V$ symmetry is also present in the chiral QCD Hamiltonian,
naively leading to an organization of hadrons into approximately degenerate particle mul-
tiplets according to the dimensionalities of the irreducible representations of this group [cf.
Scherer, 2003, p. 74]. Thus, in the chiral limit, the low-energy spectrum of baryons would
contain an additional degenerate baryon octet with negative parity [cf. Scherer, 2003, p. 74f].
In nature, the light quarks are not exactly massless but their small masses can be treated as a
perturbation. In that sense, an approximately degenerate negative-parity copy of the baryon
octet is not observed, indicating that $SU(3)_L \times SU(3)_R$ is spontaneously broken to $SU(3)_V$.
Thus, the remaining light-flavour-symmetry-group of QCD is $SU(3)_V \times U(1)_V$.
In the chiral limit, the spontaneous breakdown of $SU(3)_A$ generates $3^2 - 1 = 8$ massless par-
ticles, the *Goldstone bosons*. In case of small but non-vanishing quark masses, these particles
become massive and are referred to as *pseudo Goldstone bosons*. Candidates for these parti-
cles are the three pions, four kaons and the eta.
Explicit chiral symmetry breaking induced by small quark masses can be treated systemati-
cally within *chiral perturbation theory* (χPT) [Gasser and Leutwyler, 1985], an effective field
theory framework. Using this, it is possible to derive relations between quark masses and
pseudo Goldstone boson masses or decay constants. Chiral perturbation theory has become
a useful tool in lattice QCD so that I am going to discuss it briefly in section 2.2.5.

2.2.2. Quantum theory of QCD

In the preceding part, we discussed the classical Lagrangian of QCD and its symmetries. In the following section, we will use the path integration method to quantize QCD and discuss the implications.

The method of path integration was originally developed by Feynman [Feynman, 1948; Feynman and Hibbs, 1965] based on earlier work by Dirac [1933] for applications in classical quantum mechanics. Over time, the method has been generalized to quantum field theories. Today, path integration methods play an important role when considering statistical systems.

Path integral

It is well known that the partition function of a quantum system with fields $\phi_k(\tau, \mathbf{x})$ at Minkowskian coordinates $(\tau, \mathbf{x}) \in M^4$ can be written as[5]

$$Z = \int \mathrm{D}\phi \, e^{iS[\phi]}, \tag{2.9}$$

where S is the classical action of the system and

$$\mathrm{D}\phi = \prod_{k,\tau,\mathbf{x}} \mathrm{d}\phi(\mathbf{x}, \tau) \tag{2.10}$$

the integration measure. The degrees of freedom can be either bosonic or fermionic and are treated differently as discussed below. Expression (2.9) is numerically of limited use because of the oscillatory integrand. This can be resolved by rotating the system to Euclidian time t, i.e. setting $\tau = it$:

$$Z = \int \mathrm{D}\phi \, e^{-S_E[\phi]}, \tag{2.11}$$

where S_E denotes the Euclidian rotated action of S. In the following, we will always use the Euclidian action and therefore drop the index E.

The procedure of rotating the theory to imaginary times is also called *Wick rotation* [e.g. Gattringer and Lang, 2010, p. 7]. It ensures that the integrand in (2.11) is real and thus can be treated as a weight factor (see section 2.3 for details). Note that the Wick rotation rotates the Minkowski metric of M^4 to the Euclidian metric of $\mathbb{R}^4$. For convenience, also the Dirac matrices are redefined, i.e. $\gamma_k^E = -i\gamma_k$ and $\gamma_4^E = \gamma_0$. This changes the Dirac operator from $i\not{D} - m$ to $\not{D}_E + m$. Again, I drop the subscript E for the rest of this work.

In order to compute n-point Greens functions from (2.11), we introduce the scalar 'source' field $J(\mathbf{x})$:

$$
\begin{aligned}
G^{(n)}(\mathbf{x}_1, \mathbf{x}_2, \dots, \mathbf{x}_n) &= \langle \phi(\mathbf{x}_1)\phi(\mathbf{x}_2)\cdots\phi(\mathbf{x}_n)\rangle \\
&= \frac{1}{Z}\frac{\delta}{\delta J(\mathbf{x}_1)}\frac{\delta}{\delta J(\mathbf{x}_2)}\cdots\frac{\delta}{\delta J(\mathbf{x}_n)}\int \mathrm{D}\phi \, e^{-S[\phi]+\int \mathrm{d}^4 y \, J(\mathbf{y})\phi(\mathbf{y})}\bigg|_{J=0}
\end{aligned} \tag{2.12}
$$

The path integral formulation of quantum field theory is advantageous for numerical simulations. Arbitrary Greens functions can be computed by performing operator averages over

---

[5]see [cf. Weinberg, 1995, p. 378ff] for a detailed derivation

background field configurations.

We mentioned that the degrees of freedom $\phi_k(\tau, \mathbf{x})$ can be either bosonic or fermionic. A bosonic Gaussian path integral can be evaluated analytically. Consider

$$I_B(M, \chi^\dagger, \chi) = \int \mathrm{D}\phi^\dagger \mathrm{D}\phi \, e^{\phi^\dagger M \phi + \phi^\dagger \chi + \chi^\dagger \phi}, \tag{2.13}$$

with $\mathrm{D}\phi^\dagger \mathrm{D}\phi = (\prod_k \mathrm{d}\phi_k^\dagger \, \mathrm{d}\phi_k)$ and bosonic degrees of freedom $\phi, \phi^\dagger$.[6] The exponent can be rewritten by completing the square

$$\phi^\dagger M \phi + \phi^\dagger \chi + \chi^\dagger \phi = \left(\phi^\dagger + \chi^\dagger M^{-1}\right) M \left(\phi + M^{-1}\chi\right) - \chi^\dagger M^{-1}\chi \tag{2.14}$$

and applying the substitution

$$\phi' = \phi + M^{-1}\chi; \quad \phi'^\dagger = \phi^\dagger + \chi^\dagger M^{-1}. \tag{2.15}$$

This yields

$$I_B(M, \chi^\dagger, \chi) = e^{-\chi^\dagger M^{-1}\chi} \int \mathrm{D}\phi'^\dagger \mathrm{D}\phi' e^{\phi'^\dagger M \phi'}. \tag{2.16}$$

Assume M can be diagonalized by the matrix O, so that $O^\dagger M O$ is diagonal with eigenvalues λ_i. Using the substitution

$$\phi' = Ox; \quad \phi'^\dagger = x^\dagger O^\dagger, \tag{2.17}$$

we find

$$\int \mathrm{D}\phi'^\dagger \mathrm{D}\phi' e^{\phi'^\dagger M \phi'} = \prod_i \int \mathrm{d}x_i^\dagger \mathrm{d}x_i \, e^{-|x_i|^2 \lambda_i} \propto \prod_i \frac{1}{\lambda_i} = \det(M^{-1}). \tag{2.18}$$

Hence

$$I_B(M, \chi^\dagger, \chi) \propto \det(M^{-1}) \, e^{-\chi^\dagger M^{-1}\chi}. \tag{2.19}$$

Thus, the result is proportional to the inverse determinant of M.

Consider now the fermionic action $S[\bar{\psi}, \psi] = \bar{\psi} M \psi$ with bilinearform M and the corresponding path integral:

$$I_F(M, \bar{\theta}, \theta) = \int \mathrm{D}\psi \mathrm{D}\bar{\psi} \exp(\bar{\psi} M \psi + \bar{\theta}\psi + \bar{\psi}\theta). \tag{2.20}$$

As in (2.14), we can complete the square in the exponent to obtain the expression

$$I_F(M, \bar{\theta}, \theta) = e^{-\bar{\theta} M^{-1}\theta} \int \mathrm{D}\psi' \mathrm{D}\bar{\psi}' \, e^{\bar{\psi}' M \psi'}. \tag{2.21}$$

Again, we diagonalize M to obtain the eigenvalues λ_i and the corresponding left- and right-eigenvectors $\bar{\xi}_i, \xi_i$. The exponential can thus be expanded in powers of $\bar{\xi}_i \xi_i$, where only the term containing each pair $\bar{\xi}_i \xi_i$ exactly once survives the integration. This yields for the

---

[6]In literature one often finds that $\mathrm{D}\phi^\dagger \mathrm{D}\phi = (\prod_k \mathrm{d}\mathrm{Re}\phi_k \, \mathrm{d}\mathrm{Im}\phi_k)$ which is essentially the same

remaining integral:

$$\int \mathrm{D}\psi' \mathrm{D}\bar{\psi}' \, e^{\bar{\psi}' M \psi'} = \int \left(\prod_k \mathrm{d}\xi_k \, \mathrm{d}\bar{\xi}_k \right) \left(\prod_i \bar{\xi}_i \xi_i \lambda_i \right), \tag{2.22}$$

Now we can reorder this expression as follows:

$$\int \left(\prod_k \mathrm{d}\xi_k \, \mathrm{d}\bar{\xi}_k \right) \left(\prod_i \bar{\xi}_i \xi_i \lambda_i \right) = \int \left(\prod_k \mathrm{d}\xi_k \, \mathrm{d}\bar{\xi}_k \, \lambda_k \, \bar{\xi}_k \xi_k \right). \tag{2.23}$$

Note that pairs such as $\bar{\xi}_i \xi_i$ are bosonic variables which commute with bosonic variable of the kind $\mathrm{d}\xi_i \, \mathrm{d}\bar{\xi}_i$. Hence we obtain

$$\int \left(\prod_k \mathrm{d}\xi_k \, \mathrm{d}\bar{\xi}_k \, \lambda_k \, \bar{\xi}_k \xi_k \right) = \prod_k \lambda_k = \det(M). \tag{2.24}$$

The full result for I_F then is

$$I_F(M, \bar{\theta}, \theta) = \det(M) \, e^{-\bar{\theta} M^{-1} \theta}. \tag{2.25}$$

In this case, the result is proportional the the determinant of M. Since the fermionic part of the QCD path integral is usually of the form (2.20) with $M = \slashed{D} + m$ being the Dirac operator, the fermionic degrees of freedom can be integrated out analytically. However, since $\det M$ is a global quantity, it is numerically impossible to compute it exactly. This problem is circumvented by combining the expressions (2.19) and (2.25), allowing to transform fermionic degrees of freedom into bosonic degrees of freedom (cf. 2.3 for details).

Haar measure

The bosonic degrees of freedom in QCD are represented by the SU(3) matrices U. Therefore the partition function for the Yang-Mills theory (QCD without fermions) is given by

$$Z = \int \mathrm{D}U \, e^{-S_G[U]}, \tag{2.26}$$

where the integral over U at each space-time point extends over the gauge-group SU(3).[7] Not only the action itself, but also the path integral should be invariant under gauge transformations $U \to U'$. This requires that $\mathrm{D}U = \mathrm{D}U'$. Due to the definition of the path integral measure (2.10) and the locality of the gauge transformation, this requirement reduces to $\mathrm{d}U = \mathrm{d}U'$. Hence, the measure $\mathrm{d}U$ has to be left and right invariant under SU(3) transformations. Such kind of measure is known as the *Haar measure* in mathematical literature. It satisfies the already mentioned invariance conditions

$$\mathrm{d}U = \mathrm{d}(U \, V) = \mathrm{d}(V \, U), \quad \forall V \in \mathrm{SU}(3), \tag{2.27}$$

---

[7]In lattice QCD, the gauge degrees of freedom are represented by $U \in \mathrm{SU}(3)$ instead of $A \in \mathfrak{su}(3)$ (cf. section 2.3).

and is normalized, so that

$$\int \mathrm{d}U = 1. \tag{2.28}$$

It is important to note that the measure is separately invariant under left and right transformations and not only under the transformation $U \to GUG^\dagger$. As we will see in section 2.3.1, the endpoints of the gauge links transform differently via $U_\mu(x) \to G(x)U_\mu(x)G^\dagger(x + \hat{\mu})$.

2.2.3. Topology

We are interested in the quasi-classical (finite action) solutions to the field equations of Yang-Mills theory in Euclidian space. The derivation is based on [Cheng and Li, 2004, p. 479ff] and [Coleman, 1988, p. 282ff] and carried out for SU(2), but the result can easily be generalized to SU(N). Consider the gauge fields

$$A_\mu = \frac{\tau^a}{2} A_\mu^a, \quad F_{\mu\nu} = \frac{\tau^a}{2} F_{\mu\nu}^a, \quad \forall \, a = 1, 2, 3, \tag{2.29}$$

with the rescaling

$$A_\mu \to A_\mu/g. \tag{2.30}$$

This simplifies the following calculations since the explicit dependence on the coupling g drops out. This transformation changes the Lagrangian to

$$\mathcal{L} = \frac{1}{2g^2} \, \mathrm{Tr} \left(F_{\mu\nu} F^{\mu\nu} \right) \tag{2.31}$$

as well as the field strength tensor to

$$F_{\mu\nu} = \partial_\mu A_\nu - \partial_\nu A_\mu + [A_\mu, A_\nu]. \tag{2.32}$$

Under an arbitrary gauge transformation $G \in$ SU(N), the A_μ-fields transform via

$$A'_\mu = G \, A_\mu G^\dagger + G \, \partial_\mu G^\dagger. \tag{2.33}$$

We require the quasi-classical solution to vanish at the boundaries, i.e.

$$\oint_{\partial \mathbb{R}^4} \mathrm{d}f \, \mathrm{Tr} \left(F_{\mu\nu} F^{\mu\nu} \right) = 0, \tag{2.34}$$

what amounts to

$$F_{\mu\nu}(\mathbf{x}) \overset{|\mathbf{x}| \to \infty}{\longrightarrow} 0. \tag{2.35}$$

The assumption that A_μ itself has to vanish at the boundary is too restrictive. It is sufficient to assume, that

$$\exists G \curvearrowright A_\mu(\mathbf{x}) \overset{|\mathbf{x}| \to \infty}{\longrightarrow} G \, \partial_\mu G^\dagger, \tag{2.36}$$

which is a gauge transformation of $A_\mu = 0$ at the boundaries. The points at infinity can be identified with points on the three sphere S^3, thus

$$G : \mathbf{x} \mapsto G(\mathbf{x}) \tag{2.37}$$

is a mapping from $S^3 \to \mathrm{SU}(2)$. It is easy to prove that this mapping is not gauge invariant: consider $H \in \mathrm{SU}(2)$ and

$$A_\mu \to H A_\mu H^\dagger + H \partial_\mu H^\dagger, \tag{2.38}$$

which implies that G transforms as $G \to HG$. One can argue that all gauge transformations HG of G are in the same homotopy class [cf. Coleman, 1988, p. 284f]. Therefore, all mappings G and thus, using (2.36), all quasi-classical solutions A_μ can be classified by their corresponding homotopy class.

These homotopy classes differ by their *winding numbers* (or *Pontryagin indices*), which can be calculated as follows: consider the current [Cheng and Li, 2004, p. 480]

$$K_\mu = 4\varepsilon_{\mu\nu\lambda\rho} \, \mathrm{Tr} \left(A_\nu \, \partial_\lambda A_\rho + \frac{2}{3} A_\nu \, A_\lambda \, A_\rho \right), \tag{2.39}$$

with the property

$$\partial_\mu K_\mu = 2 \, \mathrm{Tr} \left(F_{\mu\nu} \tilde{F}^{\nu\mu} \right). \tag{2.40}$$

With the help of Gauss' theorem, we can write

$$\int \mathrm{d}^4 x \, \mathrm{Tr} \left(F_{\mu\nu} \tilde{F}^{\nu\mu} \right) = \frac{1}{2} \int \mathrm{d}^4 x \, \partial_\mu K_\mu = \frac{1}{2} \oint_{\partial\mathbb{R}^4} \mathrm{d}f_\mu K_\mu. \tag{2.41}$$

At the boundary, the gauge fields A_μ are given by (2.36), so we find

$$K_\mu = \frac{4}{3} \varepsilon_{\mu\nu\lambda\rho} \, \mathrm{Tr} \left((G \, \partial_\nu G^\dagger)(G \, \partial_\lambda G^\dagger)(G \, \partial_\rho G^\dagger) \right). \tag{2.42}$$

Inserting this expression into (2.41) and using a general theorem about the winding number, we obtain:

$$\nu = \frac{1}{16\pi^2} \int \mathrm{d}^4 x \, \mathrm{Tr} \left(F_{\mu\nu} \tilde{F}^{\mu\nu} \right). \tag{2.43}$$

Expression (2.43) holds also for the general case of SU(N). When referring to ν, we will generally speak of *topological charge* in order to emphasize its importance in physics. The topological charge is associated with quasi-particles called *instantons*.

One might ask of what relevance quasi-classical solutions to the Yang-Mills equations are in a quantum field theoretical setup. The important point is, that the term

$$\Delta\mathcal{L} \sim \frac{\theta}{16\pi^2} \, \mathrm{Tr} \left(F_{\mu\nu} \tilde{F}^{\mu\nu} \right) \tag{2.44}$$

is 'evoked' by quantum effects through the axial anomaly: $\mathrm{U}(1)_A$ is a symmetry of the action for vanishing quark masses but not a symmetry of the corresponding path integral due to non-trivial transformation properties of the measure.[8] This gives rise to an effective CP odd term such as (2.44) in the QCD Lagrangian, where θ is strength of strong CP violation. It is

---

[8]This issue is discussed in detail in [Weinberg, 1996, p. 362ff].

easy to show that the QCD partition function (2.26) decomposes into a series of path integrals
over a fixed topological sector [Leutwyler and Smilga, 1992]:

$$Z(\theta) = \sum_{\nu=-\infty}^{\infty} e^{i\theta\nu} Z_\nu = \sum_{\nu=-\infty}^{\infty} e^{i\theta\nu} \int [\mathrm{D}U]_\nu \, e^{-S_G[U]}. \tag{2.45}$$

Thus, the QCD vacuum is a superposition of denumerably infinite topological sectors between
which tunneling occurs.

It is worth to note that the topological charge is directly related to the zero modes of the
Dirac operators by the *Atiyah-Singer index theorem* [Weinberg, 1996, p. 368ff]:

$$\nu = n_- - n_+, \tag{2.46}$$

where n_- and n_+ are the numbers of left- and right-handed zero modes respectively.

The strong CP problem

In experiment, strong CP violation can be measured by probing the electric dipole moment of
the neutron [Cheng and Li, 2004; Ramsey, 1978; Altarev et al., 1981]. Electroweak diagrams
for neutron scattering at an infinitely heavy source cancel at LO, NLO and NNLO. The
next possible larger contribution can come through the anomaly term of QCD. Hence, an
experimental bounds on the neutron electric dipole moment establishes a bound on θ which
is found to be extremely small [$\theta < 10^{-10}$, Baker et al., 2006]. The fundamental question
is, why this value for θ is so small. The simplest solution to the strong CP problem is a
massless quark: consider $Z(\theta)$ of equation (2.45) with dynamical quarks included [Leutwyler
and Smilga, 1992]:

$$Z(\theta) = \sum_{\nu=-\infty}^{\infty} e^{i\theta\nu} Z_\nu = \sum_{\nu=-\infty}^{\infty} e^{i\theta\nu} \int [\mathrm{D}U]_\nu \, e^{-S_G[U]} \det(\slashed{D}[U] + \tilde{M}), \tag{2.47}$$

where

$$\tilde{M} = \frac{1}{2}(1 - \gamma_5)M + \frac{1}{2}(1 + \gamma_5)M^\dagger \tag{2.48}$$

is a general complex quark mass matrix. The nonzero eigenvalues of $\slashed{D}[U]$ come in pairs
$(\lambda_n, -\lambda_n)$ and the index theorem tells us that there are at least $|\nu|$ left- or right-handed zero
modes for each ν. For $\nu > 0$, we can write for the fermion determinant in (2.47)[9]

$$\det(\slashed{D} + \tilde{M}) = (\det M)^\nu \prod_{\lambda_n > 0} \det(\lambda_n^2 + MM^\dagger). \tag{2.49}$$

This means that the partition function Z only depends on θ and the quark matrix M through
the product $M \exp(i\theta/N_f)$. Hence, a change in the phase of the quark mass matrix is equiv-
alent to a change in θ. Furthermore, if one of the quarks becomes massless, we find

$$(e^{i\theta} \det M)^\nu = \delta_{\nu 0}, \tag{2.50}$$

---

[9]For $\nu<0$, one should replace $(\det M)^\nu$ by $(\det M^\dagger)^{-\nu}$ [Leutwyler and Smilga, 1992].

i.e. Z becomes independent of θ and the strong CP problem would be solved. This problem can also be viewed as the appearance of a global U(1) symmetry as soon as one quark becomes massless. Using this additional symmetry, the θ phase can be rotated away. The 'natural' candidate for this quark would be the light up-quark. However, our result for the asymmetry parameter $(m_d - m_u)/(m_d + m_u)$ deviates from one by about 22 standard deviations and thus strongly disfavors the $m_u = 0$ solution to the strong CP problem (cf. 4.2.3).

2.2.4. Renormalization

When doing perturbative calculations in quantum field theories beyond tree-level, diverging momentum integrals may be encountered. The regularization of these integrals introduces some kind of arbitrariness since one has the freedom to add additional non-divergent terms besides the necessary removal of the divergencies. The specific choice of these terms is called *renormalization scheme*, and all renormalized quantities will be stated in a corresponding scheme. Different schemes differ by a finite renormalization called *conversion factor*.
We will now have a closer look on that from a different perspective which helps to understand the origin of divergent integrals and renormalization in quantum field theories.
Since the measurement of some specific renormalized quantities is the main part of this thesis, it is worth to be more detailed here than in the other introductory parts.

Wilson's picture of renormalization

This method was originally derived by Wilson and uses the path integral formalism discussed before. With some abbreviations, I follow the argumentation and derivations from [Peskin and Schroeder, 1995, p. 393ff], where all necessary calculations have been worked out for a scalar field in ϕ^4 theory. The conclusions basically hold for any renormalizable theory with an UV fixed point, e.g. any non-abelian gauge theory ['tHooft and Veltman, 1972] such as QCD. Of course, the calculations are much more involved when non-abelian gauge groups are used. A further review on this approach to renormalization is given by Wilson and Kogut [1974].

The idea is to consider the quantum theory as a statistical system, analogously to e.g. popular statistical models for magnets.[10] The Lagrangians of these models usually incorporate only nearest neighbor couplings, i.e. they are defined at a large ultraviolet cutoff Λ. Thus, the interaction range (or correlation length) ξ is of the order of this cutoff. In case of magnets, the cutoff is equal to the distance between neighboring atoms inside the solid state body. For some relevant models we know that we can tune the theory to a critical temperature, where the correlation length diverges. In that case, the interaction range becomes much larger than the atomic spacing.
Compared to a solid state body, the cutoff of a quantum field theory with an UV fixed point is artificial, since it incorporates a energy scale at which we expect new physics to occur. At that scale, the typical mass of the system is $m \sim \Lambda$, but we are interested in energy scales $m \ll \Lambda$. The relation $m \sim \xi^{-1}$ implies that we have to tune the Lagrangian bare parameters close to the critical point where $\xi \to \infty$.

---

[10]A well-known example for such a model is the Ising model.

We illustrate this by discussing the Euclidian scalar ϕ^4 theory as an example. Consider
the Lagrangian

$$\mathcal{L}[\phi] = \frac{1}{2}\left(\partial_\mu\phi\right)^2 + \frac{m}{2}\phi^2 + \frac{\lambda}{4!}\phi^4, \tag{2.51}$$

and the corresponding partition function with a finite cutoff Λ in d dimensions:

$$Z = \int [\mathrm{D}\phi]_\Lambda \exp\left(-\int \mathrm{d}^d x \mathcal{L}[\phi]\right), \tag{2.52}$$

where $[\mathrm{D}\phi]_\Lambda$ means that the integration extends only over fields at momenta $|k| < \Lambda$. Now,
choose $b < 1$ and divide the ϕ fields into two different groups. Let $\phi(k)$ be the Fourier modes
of $\phi(x)$ and define[11]

$$\hat{\phi}(k) = \left\{ \begin{array}{cc} \phi(k) & \forall\, b\Lambda \le |k| < \Lambda \\ 0 & \text{otherwise} \end{array} \right. , \quad \tilde{\phi}(k) = \left\{ \begin{array}{cc} \phi(k) & \forall\, |k| \le b\Lambda \\ 0 & \text{otherwise} \end{array} \right. . \tag{2.53}$$

Now we have to replace ϕ in the Lagrangian by $\tilde{\phi} + \hat{\phi}$ and rewrite (2.52):

$$
\begin{aligned}
Z &= \int \mathrm{D}\tilde{\phi} \int \mathrm{D}\hat{\phi} \exp\left(-\int \mathrm{d}^d x \left[\frac{1}{2}\left(\partial_\mu\tilde{\phi} + \partial_\mu\hat{\phi}\right)^2 + \frac{m}{2}(\tilde{\phi} + \hat{\phi})^2 + \frac{\lambda}{4!}(\tilde{\phi} + \hat{\phi})^4\right]\right) \\
&= \int [\mathrm{D}\phi]_{b\Lambda}\, e^{-\int \mathrm{d}^d x\, \mathcal{L}[\phi]} \int \mathrm{D}\hat{\phi} \exp\left(-\int \mathrm{d}^d x \left[-\frac{1}{2}(\partial_\mu\hat{\phi})^2 + \frac{m}{2}\hat{\phi}^2 \right.\right. \\
&\qquad \left.\left. +\lambda\left(\frac{1}{6}\phi^3\hat{\phi} + \frac{1}{4}\phi^2\hat{\phi}^2 + \frac{1}{6}\phi\hat{\phi}^3 + \frac{1}{4!}\hat{\phi}^4\right)\right]\right) \tag{2.54} \\
&\equiv \int [\mathrm{D}\phi]_{b\Lambda}\, e^{-\int \mathrm{d}^d x\, \mathcal{L}_{\mathrm{eff}}[\phi]}, \tag{2.55}
\end{aligned}
$$

where all quadratic terms of the form $\phi\hat{\phi}$ vanish due to orthogonality in Fourier space. We also
renamed $\tilde{\phi}$ to ϕ for the sake of clarity. Using diagrammatic expansions or Wick contractions,
the integration over the high momentum modes $\hat{\phi}$ can be carried out. Consider for example

$$-\int \mathrm{d}^d x \frac{\lambda}{4}\phi^2 \overbrace{\hat{\phi}\hat{\phi}} = -\frac{1}{2}\int \frac{\mathrm{d}^d k}{(2\pi)^d}\mu\phi(k_1)\phi(-k_1), \tag{2.56}$$

where

$$\mu = \frac{\lambda}{2} \int\limits_{b\Lambda \le |k| < \Lambda} \frac{\mathrm{d}^d k}{(2\pi)^d}\frac{1}{k^2} = \frac{\lambda}{(4\pi)^d \Gamma\left(\frac{d}{2}\right)}\frac{1 - b^{d-2}}{d-2}\Lambda^{d-2}. \tag{2.57}$$

This means that we can include the contributions from the integration over the high momen-
tum shells $b\Lambda \le |k| < \Lambda$ by redefining the mass m. The same can be shown for the coupling
λ. Thus, running down a theory defined at a large ultraviolet scale to energy scales reachable
at present day experiments by integrating out the high energy degrees of freedom, is the same
as modifying the parameters in the Lagrangian accordingly.

---

[11]Lattice QCD literature discussing renormalization usually focuses on the coordinate space aspect of this trans-
formation: since the momentum cutoff Λ is reduced to $b\Lambda$, the 'granularity' of space-time is increased by a
factor b^{-1}. This is often referred to as *coarse graining* or *blocking transformation*, but the reasoning is basically
the same.

In order to allow for a better comparison of (2.52) and (2.55) we can rewrite this transformation by rescaling the momenta $k' = k/b$ and distances $x' = xb$. To see what happens to other operators under this transformation, consider the most general theory of scalar fields:

$$
\int \mathrm{d}^d x\, \mathcal{L}_{\text{eff}}[\phi] = \int \mathrm{d}^d x \left[\frac{1}{2}(1 + \Delta Z)(\partial_\mu \phi)^2 + \frac{1}{2}(m^2 + \Delta m^2)\phi^2 \right.
$$
$$
\left. + \frac{1}{4!}(\lambda + \Delta \lambda)\phi^4 + (C + \Delta C)(\partial_\mu \phi)^4 + (D + \Delta D)\phi^6 + \ldots \right]. \quad (2.58)
$$

After rescaling we find

$$
\int \mathrm{d}^d x\, \mathcal{L}_{\text{eff}}[\phi] = \int \mathrm{d}^d x'\, b^{-d} \left[\frac{1}{2}(1 + \Delta Z)b^2(\partial'_\mu \phi)^2 + \frac{1}{2}(m^2 + \Delta m^2)\phi^2 \right.
$$
$$
\left. + \frac{1}{4!}(\lambda + \Delta \lambda)\phi^4 + (C + \Delta C)\, b^4(\partial'_\mu \phi)^4 + (D + \Delta D)\phi^6 + \ldots \right]. (2.59)
$$

Defining rescaled fields via $\phi' = \sqrt{b^{2-d}(1 + \Delta Z)}\phi$, we obtain:

$$
\int \mathrm{d}^d x\, \mathcal{L}_{\text{eff}}[\phi] = \int \mathrm{d}^d x' \left[\frac{1}{2}(\partial'_\mu \phi')^2 + \frac{1}{2}m'^2 \phi'^2 \right.
$$
$$
\left. + \frac{1}{4!}\lambda' \phi'^4 + C'(\partial'_\mu \phi')^4 + D' \phi'^6 + \ldots \right], \quad (2.60)
$$

where

$$
m'^2 = (m^2 + \Delta m^2)(1 + \Delta Z)^{-1}b^{-2}, \quad (2.61)
$$
$$
\lambda' = (\lambda + \Delta \lambda)(1 + \Delta Z)^{-2}b^{d-4}, \quad (2.62)
$$
$$
C' = (C + \Delta C)(1 + \Delta Z)^{-2}b^d, \quad (2.63)
$$
$$
D' = (D + \Delta D)(1 + \Delta Z)^{-3}b^{2d-6}. \quad (2.64)
$$

If we choose b close to 1, the transformations become continuous. In that case they are often referred to as *renormalization group transformations (RGT)*, although they do not form a group in the strict mathematical sense.[12] Hence, we can consider any arbitrary starting point of parameters and think of a renormalization group flow induced by the transformation. In ϕ^4-theory, there is a trivial fixed point with respect to these transformations, namely the free-field fixed point ($m = \lambda = C = D = \ldots = 0$). In the vicinity of this point, the shifts Δm, $\Delta \lambda$, etc. are negligible and we have the simple transformation law:

$$
m'^2 = m^2 b^{-2}, \quad \lambda' = \lambda b^{d-4}, \quad C' = C b^d, \quad D' = D b^{2d-6}, \quad \ldots \quad (2.65)
$$

The terms with positive order in b will die out in the $b \to 0$ limit and are therefore called *irrelevant operators* (e.g. C, D). The associated irrelevant directions span the *critical surface* which contains the fixed point, since all renormalization group transformations on that surface converge to that point.[13] On the other hand, terms with negative orders in b will

---

[12]The RGT is usually not invertible.

[13]In theories where no UV fixed point exists, the renormalization group transformations may meander randomly or approaching some limit cycle. In theory with more than one fixed-point, the associated basins of attraction define the universality classes of the theory [cf. Gupta, 1997, p. 68ff].

explode under renormalization group transformations and are therefore called *relevant operators* (e.g. mass m). They pull the parameters away from the critical surface along the relevant directions. The terms of order b^0 are called *marginal* operators (e.g. coupling λ in four dimensions), and in order to decide whether they grow or shrink, we would have to include higher order corrections. Typically, the renormalization factors for these operators run logarithmically such as the QCD coupling α_s.

In the vicinity of the critical surface, any arbitrarily complicated Lagrangian degenerates under RGT into a Lagrangian with a finite number of renormalizable couplings.

The bottom line is: the bare couplings of any UV theory, defined in the vicinity of the fixed point, have to be renormalized in order to describe physics at lower energy scales. The renormalization is attributed to the procedure of analytically integrating out contributions from the high-momentum components of the fields and compensating these effects in a redefinition of the couplings.

Running coupling of QCD

The coupling constant α_s of QCD is a Lagrangian parameter and hence has to be renormalized. Using the Callan-Symanzik equations, one can calculate the running coupling of QCD to arbitrary loop order. At one loop order, the running can be stated in a closed formula

$$\alpha_s(\mu^2) = \frac{\alpha_s(\mu_0^2)}{1 + (b_0\alpha_s(\mu_0^2)/4\pi)\ln(\mu^2/\mu_0^2)}, \tag{2.66}$$

where μ_0^2 is the reference scale. Note that $b_0 = 11 - 2/3N_f > 0$ in real world physics. This means that the coupling goes to zero for $\mu^2 \to \infty$. This behaviour is commonly referred to as *asymptotic freedom*. We can recast equation (2.66) into a different form

$$\alpha_s(\mu^2) = \frac{4\pi}{b_0 \ln\left(\mu^2/\Lambda_{\text{QCD}}^2\right)}, \tag{2.67}$$

where we defined

$$\alpha_s(\mu_0^2)\frac{b_0}{4\pi}\ln\left(\frac{\mu_0^2}{\Lambda_{\text{QCD}}^2}\right) = 1. \tag{2.68}$$

Therefore, perturbation theory breaks down at a scale of Λ_{QCD}. From measurements one can deduce $\Lambda_{\text{QCD}} \approx 200\,\text{MeV}$, hence the convergence of the perturbative series can be trusted down to several GeV, where $\alpha_s(\mu^2) \lesssim 0.4$. Below this scale, strong physics is described by highly non-perturbative processes such as hadron formation, rendering the separation of a single quark from a color-neutral set of quarks impossible. This phenomenon is often referred to as *infrared slavery* or *confinement*. This mechanism is still not fully understood and its theoretical explanation is considered to be a 'holy grail of quantum chromodynamics'.

The bottom-line is that QCD dynamically generates a characteristic energy scale through quantum effects, inducing the anomalous breaking of scale invariance.

2.2.5. Chiral perturbation theory

As discussed in section 2.2.1, the $SU(3)_L \times SU(3)_R$ flavour symmetry of the chiral QCD La-
grangian is spontaneously broken to $SU(3)_V$.[14] This gives rise to eight massless Goldstone
bosons. For non-vanishing but small quark masses, these particles become massive and are
then referred to as pseudo Goldstone bosons. They can be identified with the physical pions,
kaons and the eta.

It is possible to systematically derive an effective field theory (EFT), describing the low energy
regime of QCD. This theory is called *chiral perturbation theory* and was first introduced by
Gasser and Leutwyler [1985]. The low energy effective Lagrangian has to respect all symme-
tries of the underling theory, e.g. $SU(3)_L \times SU(3)_R \times U(1)_V$ in the chiral limit. Additionally,
the preserved symmetries after the chiral symmetry breaking have to be manifest. One can
show that the fields within this framework cannot be expressed by a linear representation,
but a so-called *non-linear realization*. This means that the Lagrangian contains the fields

$$U = \exp\left(i\frac{\phi(x)}{F_0}\right), \tag{2.69}$$

where

$$\phi(x) = \sum_{a=1}^{8} \lambda_a \phi_a(x) \equiv \begin{pmatrix} \pi^0 + \frac{1}{\sqrt{3}}\eta & \sqrt{2}\pi^+ & \sqrt{2}K^+ \\ \sqrt{2}\pi^- & -\pi^0 + \frac{1}{\sqrt{3}}\eta & \sqrt{2}K^0 \\ \sqrt{2}K^- & \sqrt{2}\bar{K}^0 & -\frac{2}{\sqrt{3}}\eta \end{pmatrix}. \tag{2.70}$$

In this framework, a chiral transformation becomes a local 'gauge' transformation, i.e. $U \rightarrow RUL^\dagger$, with $R, L \in SU(3)$. All terms containing combinations of U fields which are invariant
under a chiral transformation are allowed in the Lagrangian. Following Weinberg's recipe for
defining effective field theories [cf. Weinberg, 1996, p. 163ff], which states that one has to
incorporate all possible terms respecting the symmetries of the underlying theory into the
Lagrangian, one ends up with infinitely many terms and the theory is non-renormalizable.
Perturbative calculations in effective theories rely on Weinbergs *power counting scheme* [Wein-
berg, 1980], allowing to perform an asymptotic expansion in powers of the momentum p. As
χPT is a low energy effective theory, one can hope that contributions from higher momentum
Lagrangians become less important. For example, the fundamental Lagrangian of $\mathcal{O}(p^2)$ is
given by

$$\mathcal{L}_2 = \frac{F_0^2}{4} \text{Tr}[\partial_\mu U \partial^\mu U^\dagger],$$

where F_0 is a parameter which depends on the dynamics of the underlying theory of QCD.[15]
In order to obtain a perturbative series depending on the observable pion fields ϕ_a, the U-fields
have to be expanded up to the desired power in p. Furthermore, higher order Lagrangian
terms L_{2n} have to be included and expanded to the equivalent order in ϕ_a. The Lagrangian
parameters from these terms renormalize loop diagrams from Lagrangians of lower order.
Thus, the theory has to be 'renormalized order by order', i.e. by introducing additional
counterterms at each order. In practice, it is often not suitable to go beyond one loop level
because the number of Lagrangian parameters rapidly grows with the momentum order p^{2n}.

---

[14]The charge operator Q_A^a for the axial charge does not annihilate the ground state [cf. Scherer, 2003].

[15]This means that F_0 cannot be predicted by chiral perturbation theory itself and has to be determined using
different methods, e.g. by performing lattice calculations.

Furthermore, the chiral expansion is an asymptotic expansion and its range of validity is still unclear.[16]

Nevertheless, chiral perturbation theory is a good tool for lattice physicists because it can describe how specific QCD observables depend on the quark masses (cf. [Sharpe, 1992, 2006] for the quenched and full theory respectively). These masses can be incorporated by introducing *spurion fields* χ, transforming exactly as the U-fields under chiral rotations. Thereby, chiral invariant expressions can be built up from the U and χ fields (and additional left- and right-handed currents l_μ, r_μ). To lowest order we find:

$$\mathcal{L}_2 = \frac{F_0^2}{4} \operatorname{Tr}[D_\mu U \, (D^\mu U)^\dagger] + \frac{F_0^2}{4} \operatorname{Tr}[\chi U^\dagger + U \chi^\dagger], \tag{2.71}$$

with $D_\mu A = \partial_\mu A - r_\mu A + i A l_\mu$ and setting $\chi = 2B_0 \operatorname{diag}(m_u, m_d, m_s)$ in the end of the calculation. Now it is possible to compute the quark mass dependence of observables such as decay constants or meson masses. Most results on this can be found in the literature so that we will state the corresponding formulas along with the references wherever we use them.

It is important to remark that continuum chiral perturbation theory can be extended or modified in several ways. For example, the chiral group can be reduced from SU(3) to SU(2). This is motivated by the fact that the average up- and down-quark masses are much smaller than the strange quark mass (cf. e.g. section 4.2). The resulting SU(2) chiral perturbation theory often fits lattice data better than its SU(3) counterpart [cf. e.g. Allton et al., 2008]. Furthermore, it is possible to incorporate discretization effects for example. Although these effects affect the UV behaviour of the theory, they often also break chiral symmetry (such as the Wilson term (2.114)) and therefore modify the chiral behaviour of certain observables. Within this thesis, I will mainly use continuum SU(2) chiral perturbation theory. This is, owing to the quality of our data, completely justified.

Chiral perturbation theory is also very useful when dealing with finite volume corrections (cf. 2.3.5) because it can predict the strength of such effects for different sets of parameters.

2.2.6. Neutral kaon mixing and bag parameter B_K

The neutral kaons K^0 and $\bar{K}^0$ mix through weak interaction processes. But even without the GWS formalism of the standard model, it is easy to understand the mixing of these states through their common $\pi\pi$ decays, i.e. $K^0 \leftrightarrow \pi\pi \leftrightarrow \bar{K}^0$. Phenomenologically, we may write the neutral kaon wavefunction as[17]

$$|\psi(t)\rangle = a(t)|K^0\rangle + b(t)|\bar{K}^0\rangle, \tag{2.72}$$

where $a(t)$ and $b(t)$ are time-dependent complex functions. The time development is then given by the Schroedinger equation

$$i\frac{\mathrm{d}}{\mathrm{d}t}|\psi(t)\rangle = \left(M - \frac{i}{2}\Gamma\right)|\psi(t)\rangle. \tag{2.73}$$

---

[16]The convergence radius is zero by definition, but the momentum range in which the truncated series still gives good approximations can be much larger.

[17]This section follows closely the argumentation of Donoghue et al. [1992, p. 232ff].

The elements of the complex mass matrix on the r.h.s. are given by the transition amplitudes

$$\left[M - \frac{i}{2}\Gamma \right]_{ij} = \frac{1}{2m_K}\langle K_i^0|H_{\text{eff}}|K_j^0\rangle \tag{2.74}$$

$$\approx m_K^{(0)}\delta_{ij} + \frac{\langle K_i^0|H_{\text{int}}|K_j^0\rangle}{2m_K} + \frac{1}{2m_K}\sum_n \frac{\langle K_i^0|H_{\text{int}}|n\rangle\langle n|H_{\text{int}}|K_j^0\rangle}{m_K^{(0)} - E_n + i\epsilon} \tag{2.75}$$

to second order in perturbation theory. Here, $H_{\text{eff}} = m_K^{(0)}\mathbf{1} + H_{\text{int}}$ is the full effective Hamiltonian and H_{int} its interacting part. Using the definition for the principal value

$$\frac{1}{\omega - E_n + i\epsilon} = \text{P}\left(\frac{1}{\omega - E_n}\right) - i\pi\,\delta(E_n - \omega) \tag{2.76}$$

we can write for the matrix elements of Γ

$$\Gamma_{ij} = \frac{1}{2m_K}\sum_n \langle K_i^0|H_{\text{int}}|n\rangle\langle n|H_{\text{int}}|K_j^0\rangle\,2\pi\,\delta(E_n - m_K), \tag{2.77}$$

where the other terms on the r.h.s. of (2.75) contribute to the difference $m_K^{(0)} - m_K$. The matrices M and Γ are Hermitian and the diagonal elements of the mass matrix have to be equal due to CPT invariance. Thus we can write

$$M - \frac{i}{2}\Gamma = \begin{pmatrix} A & p^2 \\ q^2 & A \end{pmatrix},$$

with some complex numbers A, p^2 and q^2. The states K^0 and $\bar{K}^0$ are CP conjugate, i.e.

$$\text{CP}|K^0\rangle = \lambda|\bar{K}^0\rangle \tag{2.78}$$

with $|\lambda|^2 = 1$. We choose $\lambda = -1$ for convenience. In case of CP invariance, we would have $\text{CP}H_{\text{eff}}(\text{CP})^{-1} = H_{\text{eff}}$ and thus

$$\langle K^0|H_{\text{eff}}|\bar{K}^0\rangle = \langle K^0|(\text{CP})^{-1}\,\text{CP}H_{\text{eff}}(\text{CP})^{-1}\,\text{CP}|\bar{K}^0\rangle = \langle \bar{K}^0|H_{\text{eff}}|K^0\rangle. \tag{2.79}$$

This would imply $p = q$ and, combined with the hermiticity of M and Γ, that $p, q \in \mathbb{R}$. If CP invariance is violated, we have $p \neq q$ an hence the mass matrix eigenstates

$$\left| K_S^L \right\rangle = \frac{1}{\sqrt{|p|^2 + |q|^2}}\left[p|K^0\rangle \pm q|\bar{K}^0\rangle \right], \tag{2.80}$$

with eigenvalues $E_{L/S} = A \pm qp$, cannot be CP eigenstates. The ratio p/q is given by

$$\frac{p}{q} = \sqrt{\frac{M_{12} - \frac{i}{2}\Gamma_{12}}{M_{12}^* - \frac{i}{2}\Gamma_{12}^*}}, \tag{2.81}$$

with $M_{21} = M_{12}^*$ and $\Gamma_{21} = \Gamma_{12}^*$ due to hermiticity, as well as

$$M_{12} - \frac{i}{2}\Gamma_{12} = \langle K^0|H_{\text{eff}}|\bar{K}^0\rangle. \tag{2.82}$$

The eigenvalue difference evaluates to

$$
\begin{aligned}
2qp &= (m_L - m_S) - \frac{i}{2}(\Gamma_L - \Gamma_S) = 2\sqrt{\left(M_{12} - \frac{i}{2}\Gamma_{12}\right)\left(M_{12}^* - \frac{i}{2}\Gamma_{12}^*\right)} \\
&\approx 2\,\mathrm{Re}M_{12} - i\mathrm{Re}\Gamma_{12},
\end{aligned}
\tag{2.83}
$$

where the approximation is only valid for small CP violation, i.e. $\mathrm{Im}M_{12}/\mathrm{Re}M_{12} \ll 1$ and $\mathrm{Im}\Gamma_{12}/\mathrm{Re}\Gamma_{12} \ll 1$. The subscripts L and S in (2.80) stand for 'long' and 'short' and refer to the respective lifetimes of the corresponding states.

To understand this, consider the CP conserving limit $p = q$: in that case, K_S and K_L become CP-even and CP-odd respectively. Their decay states would also have to obey CP invariance and hence K_S can decay into 2π whereas K_L has to decay into 3π. Since the phase space for the former decay exceeds the one for the latter, $K_L \to 3\pi$ is considerably suppressed with respect to $K_S \to 2\pi$. In a non CP invariant world, K_S and K_L can be expanded in terms of CP eigenstates:

$$
\left|K_{\substack{L\\S}}\right\rangle = \frac{1}{\sqrt{1+|\bar{\epsilon}|^2}}\left(|K_{\mp}^0\rangle + \bar{\epsilon}|K_{\pm}^0\rangle\right), \quad \frac{p}{q} = \frac{1+\bar{\epsilon}}{1-\bar{\epsilon}},
\tag{2.84}
$$

with $|K_{\pm}^0\rangle = (|K^0\rangle \pm |\bar{K}^0\rangle)/\sqrt{2}$. Note that $\bar{\epsilon}$ can be expanded in terms of real and imaginary parts of the $K^0 - \bar{K}^0$ transition matrix element:

$$
\bar{\epsilon} = \frac{p-q}{p+q} \approx \frac{i}{2}\frac{\mathrm{Im}M_{12} - i\mathrm{Im}\Gamma_{12}/2}{\mathrm{Re}M_{12} - i\mathrm{Re}\Gamma_{12}/2} \approx \frac{1}{2}\frac{M_{12} - M_{21} - \frac{i}{2}(\Gamma_{12} - \Gamma_{21})}{m_L - m_S - \frac{i}{2}(\Gamma_L - \Gamma_S)}.
\tag{2.85}
$$

The time development of an initially prepared K^0 or $\bar{K}^0$ state is experimentally measurable. Using the results from above, it can be written as

$$
|K^0(t)\rangle = g_+(t)|K^0\rangle + \frac{q}{p}g_-(t)|\bar{K}^0\rangle,
\tag{2.86}
$$

$$
|\bar{K}^0(t)\rangle = \frac{p}{q}g_-(t)|K^0\rangle + g_+(t)|\bar{K}^0\rangle,
\tag{2.87}
$$

$$
g_\pm(t) = \frac{1}{2}e^{-it(m_L - i\Gamma_L/2)}\left(1 \pm e^{it(\Delta m + i\Delta\Gamma/2)}\right).
\tag{2.88}
$$

The differences $\Delta\Gamma = \Gamma_S - \Gamma_L$ and $\Delta m = m_L - m_S$ are both positive quantities by definition.

CP violation in the standard model framework

The standard model supports CP violation by the *Cabibbo-Kobayashi-Maskawa (CKM) matrix*. This matrix quantifies the probability of quark flavour changing under W-boson mediation. Because there are three quark generations, the CKM matrix is a 3×3 complex matrix:

$$
V_{CKM} = \begin{pmatrix} V_{ud} & V_{us} & V_{ub} \\ V_{cd} & V_{cs} & V_{cb} \\ V_{td} & V_{ts} & V_{tb} \end{pmatrix}.
$$

In the standard model formalism, the CKM matrix appears in the Lagrangian after rotating the quark fields from electroweak eigenstates to mass matrix eigenstates.[18]. Due to that, the CKM matrix has to be unitary in the standard model.

A unitary 3×3 matrix can be described by nine real parameters, where three of them are angles (rotation in three dimensions) and six are phases (in the diagonal and upper or lower triangular part). Five of these phases can be removed by rephasing the quark fields and thus have no physical significance. However, a sixth, overall phase remains and this is where CP violation enters the standard model. Note that a 2×2 unitary matrix only has three phases for four quark fields. This means that they can be completely removed and thus there is no CP violation via the CKM mechanism in a world with only two quark generations.[19]

Applying the unitarity conditions

$$V_{CKM}^\dagger V_{CKM} = V_{CKM} V_{CKM}^\dagger = \mathbf{1} \tag{2.89}$$

allows for rewriting the CKM matrix into the *Wolfenstein parametrization* [Nakamura et al., 2010], which is often used in phenomenological applications. Consider:[20]

$$V_{ud} = 1 - \frac{1}{2}\lambda^2 - \frac{1}{8}\lambda^4 + \mathcal{O}(\lambda^6),$$

$$V_{us} = \lambda + \mathcal{O}(\lambda^7),$$

$$V_{ub} = A\lambda^3(\rho - i\eta),$$

$$V_{cd} = -\lambda + \frac{1}{2}A^2\lambda^5\big[1 - 2(\rho + i\eta)\big] + \mathcal{O}(\lambda^7),$$

$$V_{cs} = 1 - \frac{1}{2}\lambda^2 - \frac{1}{8}\lambda^4(1 + 4A^2) + \mathcal{O}(\lambda^6),$$

$$V_{cb} = A\lambda^2 + \mathcal{O}(\lambda^8),$$

$$V_{td} = A\lambda^3(1 - \bar\rho - i\bar\eta) + \mathcal{O}(\lambda^7),$$

$$V_{ts} = -A\lambda^2 + \frac{1}{2}A(1 - 2\rho)\lambda^4 - i\eta A\lambda^4 + \mathcal{O}(\lambda^6),$$

$$V_{tb} = 1 - \frac{1}{2}A^2\lambda^4 + \mathcal{O}(\lambda^6),$$

with expansion parameter $\lambda = |V_{us}| \approx 0.23$ [Nakamura et al., 2010] and

$$\bar\rho \equiv \rho\left(1 - \frac{1}{2}\lambda^2\right), \quad \bar\eta \equiv \eta\left(1 - \frac{1}{2}\lambda^2\right). \tag{2.90}$$

To very good accuracy, one can replace ρ, η in the above relations by $\bar\rho$ and $\bar\eta$ respectively. We will see that this parametrization becomes particularly useful for testing the unitarity of the CKM matrix in experiment. Consider

$$V_{ud}V_{ub}^* + V_{cd}V_{cb}^* + V_{td}V_{tb}^* = 0 \tag{2.91}$$

---

[18]See [Donoghue et al., 1992, p. 60ff] or [Peskin and Schroeder, 1995, p. 719ff]

[19]In fact, before a third generation of quarks was observed in experiment, Kobayashi and Maskawa [1973] considered it as a possibility to introduce CP violation in the standard model.

[20]for a more detailed derivation and discussion read [Buras, 1998]

which is implied by unitarity constraints on V_{CKM}. We can apply the substitution

$$V_{cd}V_{cb}^* \rightarrow -A\lambda^3 \qquad (2.92)$$

to excellent accuracy, as higher order corrections are proportional to λ^7. Note that this quantity is real, as it does not involve η. Analogously we find up to $\mathcal{O}(\lambda^5)$ corrections:

$$\frac{1}{A\lambda^3}V_{ud}V_{ub}^* = \bar{\rho} + i\bar{\eta}, \quad \frac{1}{A\lambda^3}V_{td}V_{tb}^* = 1 - (\bar{\rho} + i\bar{\eta}). \qquad (2.93)$$

Thus (2.91) defines a triangle in the complex plane with corners $(0,0)$, $(0,1)$ and $(\bar{\rho}, \bar{\eta})$ (cf. figure 2.1). Note that any phase rotation applied to (2.91) only rotates the *unitary triangle* in the complex plane, but does not change the angles or side lengths. Thus, two angles and a side length or the area are physical parameters — the so-called *rephasing invariants* — which can be determined in experiment. A very important rephasing invariant is the so-called *Jarlskog invariant J* [Jarlskog, 1985]. It is directly proportional to the imaginary part of the CKM matrix and thus has to appear in all CP violating observables. Though it is defined by taking the imaginary part of a product of four CKM matrix elements, it can be directly computed by calculating the area of a unitary triangle. Consider equation (2.91) which lead to the unitary triangle picture shown in figure 2.1. This time, we do not rescale all the sides by a factor of $1/(A\lambda^3)$ and compute the area:[21]

$$A_\Delta = \frac{1}{2}\begin{vmatrix} A\lambda^3 & A\lambda^3\bar{\rho} \\ 0 & A\lambda^3\bar{\eta} \end{vmatrix} = \frac{1}{2}A^2\lambda^6\bar{\eta} = \frac{J}{2},$$

where all other unitary triangles give the same result.

In experiment, the CKM mechanism can be tested in CP *conserving* decays which are sensitive to $|V_{us}|$, $|V_{ub}|$, $|V_{cb}|$ and $|V_{td}|$ [Buras, 1998]. This is possible because the CKM mechanism closely relates quark mixing and CP violation.

Recent results on standard model CKM physics are collected by the PDG [Nakamura et al., 2010]. For more details on how the fitting to standard model flavour mixing data is performed, see the proceedings of CKMfitter [Hocker et al., 2001, and updates] and UTfit [Ciuchini et al., 2001, and updates].

Application to neutral kaon mixing

Back to kaon mixing, the CKM matrix enters the relevant Feynman diagrams displayed in figure 2.2.[22] The external legs of these diagrams have to be contracted with kaon states, rendering the process non-perturbative. The strong dynamics can be computed on the lattice, whereas this is difficult for the electroweak part. In order to define a low energy effective operator for the latter, a careful analysis of the diagrams in figure 2.2 is necessary to identify the dominant electroweak contributions.

Note that all diagrams are affected by the GIM mechanism [Glashow et al., 1970], so that K^0 and $\bar{K}^0$ would not mix if all up-type quark masses were degenerate. These cancellations

---

[21]The corrections to this quantity are of $\mathcal{O}(\lambda^{10})$ and thus truly negligible.

[22]Analogous to [Donoghue et al., 1992, p. 235], we left out diagrams containing internal Higgs lines [Gaillard and Lee, 1974; Inami and Lim, 1981]. However, the computation of Higgs diagrams can be avoided by computing the diagrams from figure 2.2 in the unitary gauge (see e.g. section D).
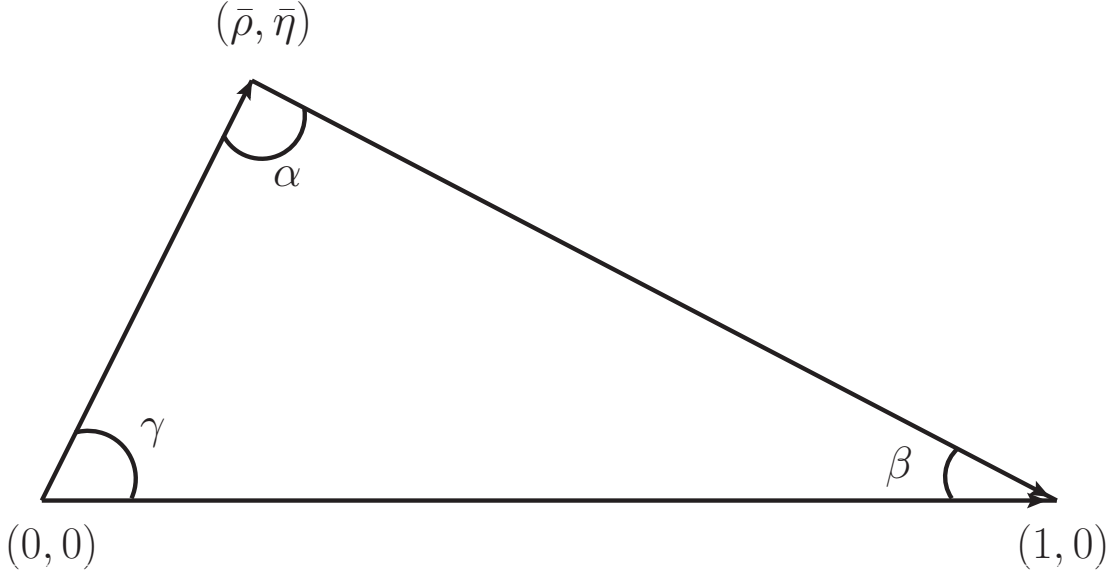
Figure 2.1.: One of six unitary triangles in the Wolfenstein parametrization as defined by unitarity constraints on V_{CKM} in (2.91). In a CP invariant world there is $\bar{\eta} = 0$ and therefore the area would be equal to zero. Together with $|V_{us}|$ and $|V_{cb}|$, suitable for determining λ and A, this picture contains the full information on the CKM matrix.

are logarithmic in diagram (c), suppressing it by factors of m_K^2/m_c^2 with respect to the box contributions (a) and (b) [see Donoghue et al., 1992, p. 236 for details]. Since lattice calculations are slowly reaching a percent level accuracy [Constantinou et al., 2011; Aubin et al., 2010; Aoki et al., 2010; Bae et al., 2010], those contributions will become relevant in future computations. However, in state-of-the-art lattice calculations, such as ours presented in section 4.3, these contributions are neglected.

Diagram (d) has a short distance and long distance part, and thus might give a significant contribution to neutral kaon mixing. However, using experimental data from direct CP violation in $K^0 \to \pi\pi$ decays, it is possible to argue that its contribution to the $K^0 - \bar{K}^0$ mixing amplitude is also small. Consider for example the CP-odd $|K_-^0\rangle$ state: it can directly decay into CP-even $\pi\pi$ states and thus violating CP *directly*. Hence, an initial $|K_L\rangle$ state can decay into two pions either by indirect CP violation, i.e. if the CP-even $|K_+\rangle$ admixture decays, or by direct CP violation, i.e. if the CP-odd $|K_-\rangle$ admixture decays. Thus, we can write the two possible decays schematically as

$$K_L \to K_+ \to \pi\pi, \quad K_L \to K_- \to \pi\pi. \tag{2.94}$$

Since CP violation appears as a complex phase in the Lagrangian, it can only affect physical processes by interference. These two processes above clearly interfere and thus can be used to measure CP violation. This can be done by defining the ratios (see e.g. [Donoghue et al., 1992, p. 238f] or [Nakamura et al., 2010])

$$\eta_{00} = \frac{\langle \pi^0\pi^0|H_{\text{int}}|K_L\rangle}{\langle \pi^0\pi^0|H_{\text{int}}|K_S\rangle} = \epsilon + \epsilon', \quad \eta_{+-} = \frac{\langle \pi^+\pi^-|H_{\text{int}}|K_L\rangle}{\langle \pi^+\pi^-|H_{\text{int}}|K_S\rangle} = \epsilon - 2\epsilon'. \tag{2.95}$$
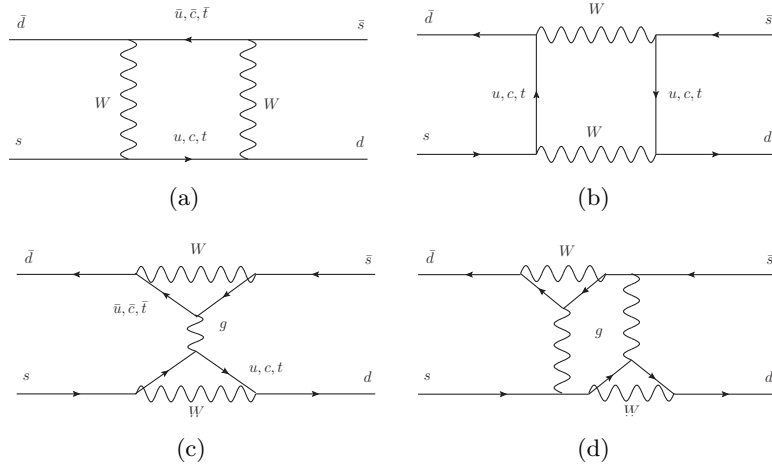
Figure 2.2.: Perturbative leading order diagrams contributing to $K^0-\bar{K}^0$ mixing. The $\Delta S = 2$ box diagrams (a) and (b) dominate over diagrams (c) and (d) containing $\Delta S = 1$ interactions.

The current experimental results for these ratios are obtained by fitting $K \to \pi\pi$ data [Nakamura et al., 2010]:

$$|\eta_{00}| = (2.221 \pm 0.011) \times 10^{-3}, \tag{2.96}$$

$$|\eta_{+-}| = (2.232 \pm 0.011) \times 10^{-3}, \tag{2.97}$$

$$\phi_{00} = \arg(\eta_{00}) = (43.51 \pm 0.05)^\circ, \tag{2.98}$$

$$\phi_{+-} = \arg(\eta_{+-}) = (43.52 \pm 0.05)^\circ, \tag{2.99}$$

where the latter values were obtained by fits assuming CPT invariance. This translates into [Nakamura et al., 2010]

$$|\epsilon| = (2.228 \pm 0.011)| \times 10^{-3}, \quad \mathrm{Re}(\epsilon'/\epsilon) = (1.65 \pm 0.26) \times 10^{-3}. \tag{2.100}$$

The physical interpretation of the parameter ϵ' is the following: in any kaon decay, the final state pions can have either isospin $I = 0$ or $I = 2$ due to Bose symmetry. Because the kaon has isospin $I = 1/2$, these two different possible final states correspond to $\Delta = 1/2$ and $\Delta = 3/2$ transitions. The interference between these two processes is quantified by ϵ', whereas the interference of $K_L \to K_+ \to \pi\pi$ and $K_L \to K_- \to \pi\pi$ is quantified by both, ϵ and ϵ'. However, the second relation in (2.100) tells us that the contribution of ϵ' to the neutral kaon mixing amplitude must be small. To finish the argumentation, note that the major contributions to ϵ' come from penguin diagrams like those displayed in figure 2.3. Finally, diagram 2.2 (d) consists of a combination of such diagrams and hence its contribution to the full kaon mixing amplitude is expected to be small.

  Therefore, we are left with the box diagrams 2.2 (a) and (b). Unfortunately, the real parts of these diagrams receive large long-distance contributions induced by charm quark propagation along the internal quark lines, rendering computations of K_L, K_S mass differences extremely
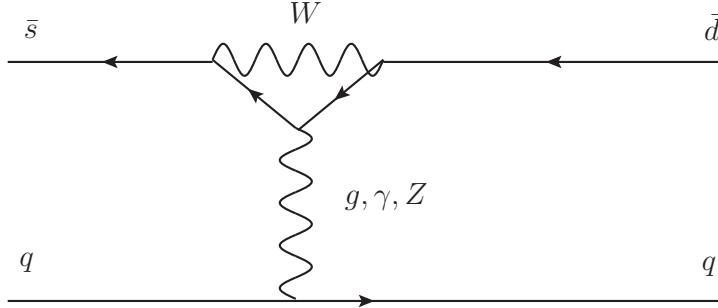
Figure 2.3.: Perturbative leading order contributions to $\Delta S = 1$ decays.

difficult.[23] However, this does not apply to computations of the indirect CP violating parameter ϵ, which is in principle proportional to the imaginary part of these diagrams.[24] It turns out that this part is dominated by momentum scales between m_c and m_t and therefore well suited for lattice computations (see appendix D for diagrammatic details and section 2.3.8 for the lattice setup). Note, that also ϵ is affected by long-distance corrections induced by e.g. active charm quarks. However, recent estimates argue that all long-range corrections to ϵ contribute by around -5% [Buras and Guadagnoli, 2008; Buras et al., 2010] and are thus subdominant.

Therefore we can contract the internal propagator lines of diagrams (a) and (b) onto a point to obtain the low energy effective four-fermion operator $O^{\Delta S=2}$

$$O^{\Delta S=2} = \left(\bar{d}\gamma_\mu (1 - \gamma_5)s \right) \left(\bar{d}\gamma_\mu (1 - \gamma_5)s \right) = (\bar{d}s)_{V-A}(\bar{d}s)_{V-A}. \tag{2.101}$$

The superscript $\Delta S = 2$ denotes that this operator changes the strangeness in the system by an amount of two, since a strange quark is converted into an anti-strange or vice versa. Using this, we define the so-called *kaon bag parameter* B_K via

$$B_K = \frac{\langle K^0 | O^{\Delta S=2} | \bar{K}^0 \rangle}{\frac{8}{3}\langle K^0 | (\bar{d}\gamma_\mu \gamma_5 s) | 0 \rangle \langle 0 | (\bar{d}\gamma^\mu \gamma_5 s) | \bar{K}^0 \rangle} = \frac{\langle K^0 | O^{\Delta S=2} | \bar{K}^0 \rangle}{\frac{8}{3} M_K^2 F_K^2}, \tag{2.102}$$

where the numerator represents the so-called *vacuum saturation approximation VSA*, an obsolete method to estimate CP violation in the neutral kaon system. We still use this ratio in lattice simulations because it cancels some statistical and systematic effects. Note that since $O^{\Delta S=2}$ is an effective operator, it has to be renormalized as discussed in detail in section 2.4.2. It is important to keep in mind that the renormalized B_K can be directly related to the indirect CP violation parameter ϵ.[25]

The bottom line of this whole derivation is that we are able to predict the strength of CP violation visible in the neutral kaon system because perturbative electroweak contributions and hadronic corrections accessible on the lattice factorize (cf. section 2.3.8 for details).

---

[23]See [Christ, 2010] for a recent proposal on how this observable can be computed on the lattice. Also cf. [Sachrajda, 2010] for a summarizing review on new lattice techniques for computing weak matrix elements.

[24]See [Lellouch, 2011, p. 21ff] or appendix D for a detailed discussion.

[25]See [Lellouch, 2011, p. 28f] or appendix D.

2.3. Lattice discretization of QCD

The starting point for the lattice discretization of QCD is the Euclidian partition function

$$Z = \int \mathrm{D}U \, \det(\slashed{D}[U] + m) \, e^{-S_G[U]}. \tag{2.103}$$

Compared to expression (2.47), the sum over nontrivial topological sectors is implied by integrating over all possible gauge degrees of freedom and not only those with a fixed winding number ν.

Solving this path integral or computing corresponding Greens functions analytically is almost impossible. In 1974 however, Kenneth G. Wilson found a way to discretize this path integral [Wilson, 1974].[26] Although it was originally designed for analytical calculations in the strong coupling limit, his *lattice discretization* is well suited for numerical treatment. In the lattice picture, the path integral is approximated by a sum over configurations defined on a four dimensional finite grid of volume V and lattice spacing a. The discretization errors of $\mathcal{O}(a^n)$ can be removed by considering finer and finer lattices and extrapolating $a \to 0$. This limit most probably exists since there is strong evidence that QCD has a UV fixed point. Additionally, Wilson showed that lattice QCD exhibits confinement in the strong coupling limit, induced by the area suppression of Wilson loops [Wilson, 1974]. Confinement is necessary to reproduce the behaviour of continuum QCD and there is strong evidence that quarks on the lattice are also confined outside the strong coupling regime.[27]

The first step in each lattice calculation is to generate an ensemble $\{U_i\}_{i=1}^N$ of field configurations which is distributed according to the weight

$$w[U] = \det(\slashed{D}[U] + m) \, \exp(-S_G[U])/Z. \tag{2.104}$$

Once this ensemble is obtained, operator expectation values can be approximated by simply computing the average

$$\langle O \rangle = \int \mathrm{D}U \, w[U] \, O(U) \approx \frac{1}{N} \sum_{i=1}^N O(U_i). \tag{2.105}$$

The rightmost expression is an approximation in various aspects: first, the ensemble is finite and so the correct distribution $w[U]/Z$ can only be approximated to finite precision. This will lead to statistical errors which have to be treated accordingly. The configurations will be generated within a Markov chain (cf. section 2.3.4), so subsequent configurations within an ensemble will not be entirely decorrelated. One has to include and estimate these autocorrelation effects.

Second, the box size is finite because the integral is carried out on a computer with finite memory. This leads to finite volume effects which can be estimated by studying different volumes.

Finally, the integral is discretized and therefore suffers from discretization effects. As discussed above, these kinds of errors can be accounted for by extrapolating the results to $a \to 0$

---

[26] Jan Smit and Alexander Polyakov also developed lattice gauge theory independently and may be mentioned as co-inventors here, cf. [Wilson, 2005].

[27] Note that we restrict ourselves to zero-temperature QCD.

in the suitable power n of a, depending on the action used in the simulations.
I will discuss the algorithms used to generate our ensembles in section 2.3.4 and the treatment of statistical as well as systematic errors in 2.3.5.

In any numerical computation, all measured observables such as masses, decay constants etc. are dimensionless. Thus, only combinations of the type Xa^k are measured, where k is the mass dimension of X. However, renormalization group theory tells us that the lattice theory has to be tuned to continuum QCD in order to reproduce the correct behaviour in the continuum limit. Ideally, the quark masses are kept fixed to their physical values while performing this limit. To be able to do so, the intrinsic length scale a has to be converted into physical units. Therefore, in order to fix the scale and quark masses in calculations involving N_f degenerate quark flavours, one has to 'sacrifice' $N_f + 1$ physical observables, typically meson or hadron masses (cf. sections 4.1,4.2). Once the scale is determined and the input masses are tuned to their physical values, other observables can be predicted.
A common observable for setting the scale in the quenched theory is r_0 (cf. app. B for details), where the advantages of this *Sommer radius* are listed in the original paper [Sommer, 1994b]. Furthermore, the dependence of r_0/a on the bare coupling β is already precisely known for the plaquette action [cf. Necco and Sommer, 2002].
However, if results obtained in units of r_0 are converted into physical units, a physical value for r_0 has to be assumed. This can be done in several ways (cf. e.g. [Garden et al., 2000; Necco and Sommer, 2002; Aubin et al., 2004a; Khan et al., 2006]), where the obtained physical values for r_0 differ by about 10%. This spread reflects the fact, that the neglected sea-quark contributions usually differ for different processes. The associated systematic uncertainty is commonly referred to as *scale-setting ambiguity* and often the major source of uncertainty in quenched calculations. In modern lattice calculations including dynamical up- down- and strange-quarks, this ambiguity has become subdominant (cf. e.g. [Davies et al., 2004]).

2.3.1. Actions

As discussed in 2.2, the action of QCD decomposes into a bosonic and a fermionic part. In this section, I will describe how the different terms can be discretized and what kind of cutoff effects are expected from our action. The order of the discretization errors has to be considered separately for the gluonic and fermionic action. In case of the fermionic action, chirality is important as well, i.e. in how far the lattice discretization respects chiral symmetry at vanishing quark masses. For some special quantities, improving the dispersion relations of the propagator might prove effective as well.

Gauge action

There are two main ingredients to construct a lattice gauge theory: it has to have the right continuum limit and must be gauge invariant. The most popular gauge actions place the gluonic variables, which are elements of the fundamental representation of SU(3), on the links of the lattice, connecting two neighbouring sites in a gauge invariant way. These links are defined by

$$U_\mu(x) = \exp\left[igaA_\mu(x)\right], \tag{2.106}$$

where $A_\mu(x)$ are the gluon fields we know from continuum QCD and the scalar g is the gauge coupling. These link matrices act as parallel transporters of a color three-vector from lattice site x to $x + \hat{\mu}$. Thus, we can construct parallel transporters along arbitrary paths by multiplying the corresponding links along that path. A gauge transformation $W(x) \in$ SU(3) $\forall\, x$ rotates the links according to

$$U_\mu(x) \to W(x)U_\mu(x)W^\dagger(x + \hat{\mu}). \tag{2.107}$$

Therefore, one class of gauge invariant terms which can be constructed out of the link matrices are closed loops:

$$W_C = \mathrm{tr}\left[P \prod_C U_\mu(x)\right], \tag{2.108}$$

hence path ordered products P of links along a closed contour C. If these contours have a rectangular shape, they are also called *Wilson loops*.[28] The most simple Wilson loop is called the *plaquette*

$$P_{\mu\nu}(x) = \mathrm{Tr}\left[U_\mu(x)U_\nu(x + \hat{\mu})U_\mu^\dagger(x + \hat{\nu})U_\nu^\dagger(x)\right],$$

where we used the relation $U_{-\mu}(x) = U_\mu^\dagger(x - \hat{\mu})$. The action only consisting of a plaquette term is called *Wilson* or *plaquette action*:

$$S_G^{\mathrm{plaq}} = \beta \sum_x \sum_{\mu<\nu} \left(1 - \mathrm{Re}P_{\mu\nu}(x)/3\right), \tag{2.109}$$

with $\beta = 6/g^2$. Using (2.106), it is straightforward to show that expression (2.109) converges to the continuum gauge action of QCD for $a \to 0$. The discretization effects are of $\mathcal{O}(a^2)$.

Note that the discretization of the gauge action is not unique. In principle, arbitrarily many irrelevant operators can be added to (2.109). Doing this in a clever way, these operators will cancel contributions of higher orders in a and thus improving the scaling. The easiest modification to (2.109) is adding gauge invariant terms involving higher order Wilson loops, e.g. traces of 2×1 rectangles $R_{\mu\nu}$:

$$S_G^{\mathrm{Sym}} = \beta \sum_x \sum_{\mu<\nu} \left[c_0\left(1 - \mathrm{Re}P_{\mu\nu}(x)/3\right) + c_1\left(1 - \mathrm{Re}R_{\mu\nu}(x)/3\right)\right], \tag{2.110}$$

which is the so-called *Symanzik improved* or *Lüscher-Weisz gauge action* [Luscher and Weisz, 1985]. The coefficients c_0 and c_1 can be determined using lattice perturbation theory. Their tree-level values are

$$c_1 = -1/12; \quad c_0 = 1 - 8c_1 = 5/3. \tag{2.111}$$

In case of tree-level improvement, the Symanzik action is of order $\mathcal{O}(\alpha_s a^2)$. In order to remove $\mathcal{O}(a^2)$ effects completely, a non-perturbative determination of the c_i would be necessary. Lattice perturbation theory allows at least for computing the coefficients to higher order in α_s, improving the scaling accordingly. However, lattice perturbation theory is often not available for complicated actions such as those involving iterative smearing (cf. section 2.3.3).

---

[28]Closed paths of links extending into three lattice dimensions and thus forming chair-like or parallelogram-like curves are called *non-planar*. If the Wilson loop lies exactly within a plane of the coordinate system, it is called *planar*.

In most cases, nested smearing modifies the quark-gluon-vertex in a non-trivial way, rapidly complicating the Feynman rules [cf. e.g. the appendix of Capitani et al., 2006]. The good news is that smearing itself improves the scaling and thus tree-level improvement is sufficient in many cases (cf. 2.3.3).

Fermions

In contrast to the straightforward gluonic part, discretizing the fermionic action is not as simple. The problem is the impossibility of defining a Dirac operator which is local (cf. section 3.1), doubler-free (see below), posesses the continuum chiral symmetry for massless quarks and reproduces the correct continuum limit [Nielsen and Ninomiya, 1981a,c,b]. One can go into two directions from here: either sacrificing chiral symmetry on the lattice completely in order to obtain 'lightweight' fermion formulations, which are relatively inexpensive and easy to implement. On the other hand, one could redefine the chiral transformation on the lattice, ending up with a Dirac operator satisfying the Ginsparg-Wilson relation [Ginsparg and Wilson, 1982]. This yields fermions which possess an exact chiral symmetry but also leads to computationally very expensive calculations.[29] Since exact chiral symmetry was not a crucial feature in our studies in contrast to performance and CPU time, we took the first approach.

The most simple fermion discretization are the *naive fermions*. They are obtained by the straightforward discretization of the Dirac operator:

$$\bar{\psi}(x)\,(\slashed{D}+m)\psi(x) \to \frac{1}{2a}\left(\bar{\psi}_n\,\gamma_\mu U_\mu(x)\,\psi(x+\hat{\mu}) - \bar{\psi}_n\,\gamma_\mu U_\mu^\dagger(x-\hat{\mu})\,\psi(x-\hat{\mu})\right) + m\bar{\psi}(x)\psi(x). \tag{2.112}$$

The free propagator can easily be calculated [DeTar and DeGrand, 2006, p. 103]:

$$\frac{1}{a}S(p) = \frac{-i\gamma_\mu\,\sin(p_\mu a) + ma}{\sum_\mu \sin^2(p_\mu a) + m^2 a^2}. \tag{2.113}$$

Obviously, this momentum-space Dirac operator has 2^4-1 unwanted zero modes in the first Brillouin zone, corresponding to unphysical degrees of freedom. These are called *doublers* and can be removed by adding a second-derivative-like term

$$W_\mu = -\frac{r}{2a}\bar{\psi}(x)\big[\psi(x+\hat{\mu}) - 2\psi(x) + \psi(x-\hat{\mu})\big] \tag{2.114}$$

to the naive operator, where r is an arbitrary, nonzero constant. The corresponding propagator is given by

$$\frac{1}{a}S(p) = \frac{-i\gamma_\mu\,\sin(p_\mu a) + ma - r\sum_\mu(\cos(p_\mu a) - 1)}{\sum_\mu \sin^2(p_\mu a) + [ma - r\sum_\mu(\cos(p_\mu a) - 1)]^2}. \tag{2.115}$$

Therefore, the doublers acquire a mass proportional to $1/a$ and will be removed in the continuum limit. The price which has to be payed for this un-doubling is explicit chiral symmetry

---

[29]The most important fermion discretizations of that kind are overlap [Narayanan and Neuberger, 1993a, 1994, 1993b, 1995; Neuberger, 1998a,b] and domain-wall fermions [Callan and Harvey, 1985; Frolov and Slavnov, 1993; Kaplan, 1992; Shamir, 1993].

breaking, significantly complicating the computation of observables that are sensitive to chiral symmetry.

In order to apply on-shell improvement to the fermionic action, we add the *Sheikholeslami-Wohlert* (or *clover-*)term to the Wilson operator [Sheikholeslami and Wohlert, 1985]:

$$SW = c_{SW}\bar{\psi}(x)\sigma_{\mu\nu}\,F^{\mu\nu}(x)\psi(x). \tag{2.116}$$

This gives the following fermionic action

$$
\begin{aligned}
S_f \;=\; & \sum_x \bar{\psi}(x)\psi(x) \\
& -\kappa \sum_{x,\mu}\left[\bar{\psi}(x)(r-\gamma_\mu)U_\mu(x)\psi(x+\hat{\mu}) + \bar{\psi}(x)(r+\gamma_\mu)U_\mu^\dagger(x-\hat{\mu})\psi(x-\hat{\mu})\right] \\
& -\frac{r\kappa c_{SW}}{2}\sum_{x,\mu,\nu}\bar{\psi}(x)\sigma_{\mu\nu}F^{\mu\nu}(x)\psi(x).
\end{aligned}
\tag{2.117}
$$

We rescaled the fields via $\psi \to \sqrt{2\kappa}\psi$ using the hopping parameter $\kappa = (ma + 4r)^{-1}/2$. The field strength tensor can be efficiently calculated using the clover-leaf product of links. Consider

$$G_{\mu\nu}(x) =$$
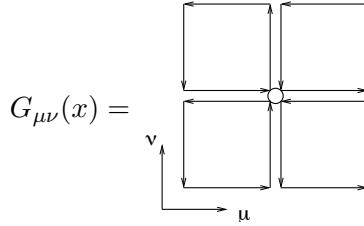
where the circle marks the site x. The field strength tensor is then given by

$$F_{\mu\nu}(x) = \frac{1}{8}\left(G_{\mu\nu}(x) - G_{\mu\nu}^\dagger(x)\right). \tag{2.118}$$

Like c_0, c_1 in the Lüscher-Weisz action, c_{SW} can be in principle computed non-perturbatively. Since we are using link smearing, we found that the tree-level value $c_{SW} = 1$ yielded sufficient improvement.

2.3.2. Topological charge

A definition of the lattice equivalent to the topological charge can be obtained by applying a straightforward discretization to (2.43). Therefore consider [30]

$$q = \frac{1}{16\pi^2}\sum_x F_{\mu\nu}(x)\tilde{F}^{\mu\nu}(x), \tag{2.119}$$

where the field strength tensor is calculated using the clover-leaf average from (2.118). We refer to this definition as *gluonic* or *naive* charge. Note that q is not an integer as its continuum counterpart ν. The reason for this is that the lattice is not a manifold and hence some assumptions in the derivations for the continuum topological charge do not hold. However,

---

[30]I denote the discretized topological charge by q and the continuum charge by ν.

since q and ν are continuum equivalent, the former is close to integer values on sufficiently fine lattices and a suitable binning to the distribution of q-values can be applied.[31]

We apply several smearing steps (e.g. from 10-30 HYP steps, cf. section 3.1.2) before calculating (2.119), driving the charge closer to integer values.

The renormalization factor Z will be determined on a given ensemble $\{U_i\}_{i\in I}$ with charges $\{q_i\}_{i\in I}$ by minimizing

$$\chi^2 = \sum_{i\in I} \left(Z\, q_i - \text{round}(Z\, q_i)\right)^2, \tag{2.120}$$

where the round operation casts the argument to the nearest integer [Dürr et al., 2007]. Using this, we define the renormalized charge via

$$q_{\text{ren}} = \text{round}(Z\, q). \tag{2.121}$$

This charge is integer by definition and equals ν in the continuum limit.[32] Since the topological charge is a global quantity, autocorrelation effects are large. The corresponding autocorrelation times are assumed to be a good measure for estimating the ergodicity of the algorithm at a given set of parameters. We therefore monitor the topological charge in all our runs, especially at large β where the topological sector tunneling rate may significantly decrease (cf. 3.1.2).

2.3.3. Smearing

Observables measured on plain configurations are often contaminated by short distance fluctuations. It is possible to improve the signal by using *smearing* (or *filtering*) methods. The basic procedure, common to most smearing recipes, is the averaging of the *thin* link matrices $U_\mu(x)$ over their surrounding neighbours. The idea behind this is that the direct, single-link gauge connection is not the only possibility to connect two neighbouring lattice sites in a gauge covariant way. It is possible to choose other, extended paths around the lattice connecting these two sites, which are less sensitive to ultraviolet fluctuations. The most basic smearing recipes are based on (weighted) averages of the thin link with the next simplest gauge connections, i.e. the surrounding staples. Replacing the single link gauge connection in the fermion operator[33] with a smeared (*fat*) link amounts to adding an irrelevant operator to the action. This operator vanishes in the continuum limit, as long as the smearing prescription, i.e. the smearing method, smearing parameters and iteration level, remains constant in the continuum limit. This can easily be understood by noting that the physical extend of the smearing decreases with a and reduces to a point in the continuum limit. At finite lattice spacing however, the coupling of the physical observables to the unphysical UV modes is suppressed and hence the scaling is improved. Note that smearing does not change the structure of the Dirac operator (2.117). The only modification is replacing the thin links by their smeared counterparts.

---

[31]What 'sufficiently fine' means in this context is highly dependent on the specific choice of the action.

[32]It has been checked that within the Symanzik scaling regime [Symanzik, 1983a,b], fermionic and gluonic definitions of the topological charge give the same continuum limit [Alles et al., 1998; Cundy et al., 2002; Del Debbio and Pica, 2004].

[33]including the clover term

Over the last decade, smeared clover-link fermions have been well established [DeGrand et al., 1998; Bernard and DeGrand, 2000; Stephenson et al., 2001; Bernard et al., 2001b; Zanotti et al., 2002; Capitani et al., 2006]. It was found that all improvement coefficients appearing in the unsmeared fermion action such as c_{SW} are driven closer to their tree-level values and the normality of the Dirac operator is improved [Hoffmann et al., 2007; Horsley et al., 2008; Durr et al., 2009]. Another important effect of link smearing is the reduction of the inherent additive mass renormalization of Wilson-type fermions [Capitani et al., 2006]. This can easily be understood by noting that the unphysical doubler modes, located in the corners of the first Brioullin zone, couple to the physical $p = 0$ mode by exchanging hard gluons. Suppressing this coupling reduces the influence of doubler modes on the physical spectrum and thus reduces the size of the additive quark mass renormalization. Furthermore, smeared link fermion actions are not (or much less) affected by some pathologies thin link actions may show at large cutoffs (cf. [Della Morte et al., 2005a; Aoki et al., 2005] and section 3.1). The most important feature of smeared actions is that the spectrum of the Dirac operator is stabilized and hence small eigenvalue fluctuations are suppressed [DeGrand et al., 1999; Stephenson et al., 2001]. This allows to perform lattice calculations at or even below physical pion masses (cf. section 4.2 and Durr et al., 2011b, 2010), which is significantly more difficult without link smearing.

Note that recent works were able to find a relation between successive infinitesimal EXP smearing steps and renormalization group flows [Narayanan and Neuberger, 2006; Luscher, 2010a,b,c]. Literature offers smearing recipes for different purposes [cf. Albanese et al., 1987; Hasenfratz and Knechtli, 2001; Morningstar and Peardon, 2004; Capitani et al., 2006; Hasenfratz et al., 2007; Durr, 2009; Schaefer et al., 2007; Hoffmann et al., 2007; Moran and Leinweber, 2008] but I only present those which have been used in our studies. All these recipes are gauge covariant and hence no gauge fixing is needed.

APE and HYP blocking

The APE smearing [Albanese et al., 1987] is the oldest smearing recipe. The original link U_μ is replaced by the average of the surrounding staples:

$$V_\mu(x) = \mathrm{P}_{\mathrm{SU(3)}} \left[(1 - \alpha) U_\mu(x) + \frac{\alpha}{6} \sum_{\pm\nu\neq\mu} U_\nu(x) U_\mu(x + \hat{\nu}) U_\nu^\dagger(x + \hat{\mu}) \right] \qquad (2.122)$$

where $P_{\mathrm{SU(3)}}$ is a projection to SU(3).[34] It is possible to apply several iterative smearing steps in order to improve the smearing effect.

The HYP blocking [Hasenfratz and Knechtli, 2001] is a slight modification of the APE idea. One can think of it as applying three successive APE smearing steps, where the staples involved in formula (2.122) are chosen in such a way, that the dependence of the fat link V_μ

---

[34]Note that except for the SU(2)-case, a linear combination of SU(N) matrices is not necessarily proportional to an element of SU(N).

on its surrounding gauge fields U_ν is restricted to the hypercube. The formula is given by

$$V_{\mu:\rho\nu}^{(1)}(x) = P_{SU(3)} \left[(1-\alpha_3)U_\mu(x) + \frac{\alpha_3}{2} \sum_{\pm\eta\neq\rho,\nu,\mu} U_\eta(x)U_\mu(x+\hat{\eta})U_\eta^\dagger(x+\hat{\mu}) \right]$$

$$V_{\mu:\nu}^{(2)}(x) = P_{SU(3)} \left[(1-\alpha_2)U_\mu(x) + \frac{\alpha_2}{4} \sum_{\pm\rho\neq\nu,\mu} V_{\rho:\nu\mu}^{(1)}(x)V_{\mu:\rho\nu}^{(1)}(x+\hat{\rho})V_{\rho:\nu\mu}^{(1)\,\dagger}(x+\hat{\mu}) \right]$$

$$V_\mu(x) = P_{SU(3)} \left[(1-\alpha_1)U_\mu(x) + \frac{\alpha_1}{6} \sum_{\pm\nu\neq\mu} V_{\nu:\mu}^{(2)}(x)V_{\mu:\nu}^{(2)}(x+\hat{\nu})V_{\nu:\mu}^{(2)\,\dagger}(x+\hat{\mu}) \right].\quad(2.123)$$

For a better understanding, the pictorial description of this procedure is given in figure 2.4. In principle, a single HYP blocking is equivalent to 3 APE smearing steps if suitable smearing parameters are chosen.[35]

(a)   (b)
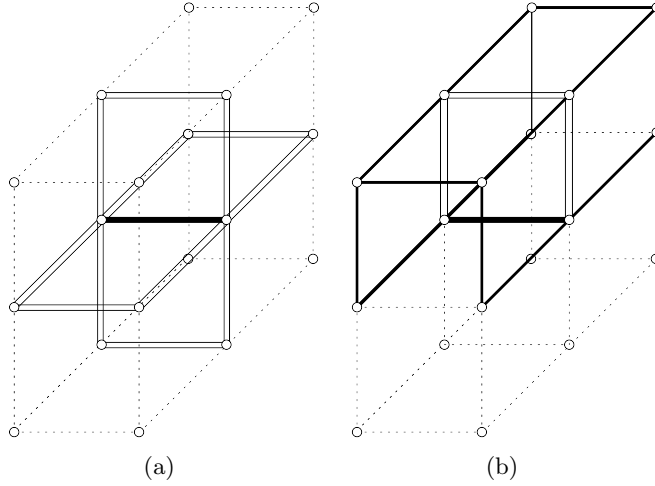
Figure 2.4.: HYP blocking procedure in three dimensions. The fat link in the middle of the cube is the staple average of the surrounding links (a). These links again consist of staple averages of their surrounding links (b), only including staples belonging to the same hypercube as the initial link [cf. Hasenfratz and Knechtli, 2001].

Analytic EXP- and HEX-blocking

The disadvantage of the above discussed smearing recipes is the SU(3) projection step. This operation is usually not analytic, i.e. one cannot compute the derivative of the smearing operation. However, the smearing has to be analytic in order to use it within a molecular dynamics trajectory (cf. 2.3.4). Nevertheless, both recipes described above can be easily

---

[35]It is generally not fully equivalent since three APE steps also touch links outside the hypercube. However, an equivalent improvement of certain observables can be found (cf. section 3.2).

made analytic by choosing a proper projection method.[36] In this work, we use the so called EXP (or *stout*) links, which are defined by

$$
\begin{aligned}
\Gamma_\mu(x) &= \sum_{\pm\nu\neq\mu} U_\mu(x)U_\mu(x+\hat{\nu})U_\nu^\dagger(x+\hat{\mu}) \\
V_\mu(x) &= \exp\left(\rho\,\mathrm{P_{TA}}\left\{\Gamma_\mu U_\mu^\dagger(x)\right\}\right)U_\mu(x),
\end{aligned}
\tag{2.124}
$$

where $\mathrm{P_{TA}}$ projects any 3×3 matrix Ω to its traceless anti-Hermitian part:

$$
\mathrm{P_{TA}}\{\Omega\} = \frac{1}{2}\left[\Omega - \Omega^\dagger\right] - \frac{1}{6}\,\mathrm{Tr}\left[\Omega - \Omega^\dagger\right].
\tag{2.125}
$$

It is straightforward to prove that this smearing is analytic for any iteration level (cf. section E.2).

The HEX smearing is equivalent to the HYP blocking, where all APE links have to be replaced by stout smeared links [Capitani et al., 2006]. In straight analogy to the HYP blocking, one has the freedom to choose three smearing parameters $(\alpha_1, \alpha_2, \alpha_3)$ to determine the smearing strength of a single iteration level:

$$
\begin{aligned}
\Gamma^{(1)}_{\mu:\nu\rho}(x) &= \sum_{\pm\sigma\neq(\mu,\nu,\rho)} U_\sigma(x)U_\mu(x+\hat{\sigma})U_\sigma^\dagger(x+\hat{\mu}) \\
V^{(1)}_{\mu:\nu\rho}(x) &= \exp\left(\frac{\alpha_3}{2}\,\mathrm{P_{TA}}\left\{\Gamma^{(1)}_{\mu:\nu\rho}(x)U_\mu^\dagger(x)\right\}\right)U_\mu(x) \\
\Gamma^{(2)}_{\mu:\nu}(x) &= \sum_{\pm\sigma\neq(\mu,\nu)} V^{(1)}_{\sigma:\mu\nu}(x)V^{(1)}_{\mu:\nu\sigma}(x+\hat{\sigma})V^{(1)\,\dagger}_{\sigma:\mu\nu}(x+\hat{\mu}) \\
V^{(2)}_{\mu:\nu}(x) &= \exp\left(\frac{\alpha_2}{4}\,\mathrm{P_{TA}}\left\{\Gamma^{(2)}_{\mu,\nu}(x)U_\mu^\dagger(x)\right\}\right)U_\mu(x) \\
\Gamma^{(3)}_{\mu}(x) &= \sum_{\pm\nu\neq\mu} V^{(2)}_{\nu:\mu}(x)V^{(2)}_{\mu:\nu}(x+\hat{\nu})V^{(2)\,\dagger}_{\nu:\mu}(x+\hat{\mu}) \\
V_\mu(x) &= \exp\left(\frac{\alpha_1}{6}\,\mathrm{P_{TA}}\left\{\Gamma^{(3)}_{\mu}(x)U_\mu^\dagger(x)\right\}\right)U_\mu(x).
\end{aligned}
\tag{2.126}
$$

This smearing recipe was used in our studies as well and is compared to EXP smearing in section 3.2.

I finish this section with a general remark on smearing. One argument against smearing is that excessive use of smearing destroys gauge field locality of the action and badly influences the short-distance behaviour of certain observables. This argument is especially true, if the smearing level or parameters are adjusted with respect to the lattice cutoff a. For example, if the smearing extent is held constant in physical units by tuning the number of smearing steps accordingly, this information will propagate into the continuum. In our calculations, we use a constant number of 6 steps EXP and 2 steps HEX smearing with constant and moderate smearing parameters. The information content of an individual link propagates within a single smearing step by following a diffusion law [cf. Capitani et al., 2006], hence even slower than the mathematically worst case (factor $\simeq \sqrt{2}$ for each iteration or HYP-level). I will

---

[36]The derivatives of the simple staple averages in (2.122) or (2.123) can be computed by considering the fat link as a sum of paths and take the derivative by 'following these paths'. However, this methods becomes inapplicable if iterative smearing is used [DeTar and DeGrand, 2006, p. 211ff].

discuss the locality of our actions in section 3.1.

2.3.4. Algorithms

In addition to the lattice discretization of the action, the choice of adequate algorithms is of great importance as well. In case of quenched calculations, i.e. calculations in which the functional determinant of the Dirac operator is set to one[37], Monte-Carlo based algorithms such as overrelaxation and pseudo heatbath are the methods of choice (see below).
Today, quenched QCD is mainly used as an inexpensive testbed for new methods, because calculations in full QCD are now feasible.[38] Besides the growth in computational power, this is partly attributed to the tremendous progress which has been made in improving algorithms. These algorithms are mostly molecular dynamics based, such as the (R)HMC (see below).
Note, that due to the accumulation of rounding errors, the updated gauge field links may deviate from unitarity after a certain number of updates. Therefore, reunitarization steps have to be applied regularly, independent of the used update algorithm [Gattringer and Lang, 2010, p. 82].

Before discussing more optimized methods, it is useful to understand the most basic importance-sampling method called *Metropolis algorithm*. Because of its generality, it can be applied to many statistical systems or being combined with more specialized algorithms.

Monte-Carlo integration and Metropolis criterion

Let us recall the statistical interpretation of quantum field theory: we want to obtain an ensemble $\{U_i\}_{i \in I}$ which is distributed according to the Boltzmann weight

$$\rho[U] = \frac{e^{-S[U]}}{Z}. \tag{2.127}$$

This can be achieved by producing a Markov chain of configurations U_i by means of Monte-Carlo integration. Every new configuration U_{n+1} is computed from an existing one U_n by applying a suitable, algorithm dependent transformation to U_n. This yields a candidate configuration U' which is set equal to U_{n+1} (and thus being *accepted*) with a probability of

$$P[U_n \to U'] = \min\left\{1, \frac{\rho[U']}{\rho[U_n]}\right\}. \tag{2.128}$$

The update is *rejected* and U_{n+1} set equal to U_n with the inverse probability. This condition is referred to as *Metropolis criterion*.
The algorithm satisfies *detailed balance*, i.e. for any two configurations U, U' the equation

$$\rho[U]\, P[U \to U'] = \rho[U']\, P[U' \to U] \tag{2.129}$$

---

[37] This is equivalent to neglecting diagrams containing internal quark lines in perturbative calculations.

[38] However, the quenched approximation is still very important in some special fields of lattice gauge theory. A good example for this are *large N_c theories*, where diagrams containing quark loop become strongly suppressed when increasing N_c. Thus, the quenched diagrams will give the major contributions to all observables in that limit.

holds. Along with ergodicity and aperiodicity, detailed balance is a *sufficient* condition to guarantee that the algorithm converges towards the equilibrium distribution (2.127) [cf. Creutz et al., 1983]. Aperiodicity means, that $P[U \to U] \neq 0 \, \forall \, U$, whereas ergodicity states that the algorithm can reach any possible field configuration within a finite number of steps. If even $P[U' \to U] > 0$ is satisfied for any pair U, U', the algorithm can reach every configuration in a single step. This feature is called *strong ergodicity*. The question whether an update algorithm is ergodic or not is difficult to answer. For example, local update algorithms may have problems in sampling global properties of the equilibrium distribution correctly.

Algorithms used in the quenched approximation

The first more specialized algorithm to be discussed is the Monte-Carlo based *pseudo heat bath* algorithm. It chooses the transition probability equal to the weight of the final configuration, irrespective of the initial one. Therefore, it demands that[39]

$$P[U \to U'] = \rho[U'],$$

which obviously satisfies detailed balance. Due to the large configuration space, one cannot implement this requirement fully numerically. Instead, we can visit the lattice site by site and update only single links U_x. Let us denote all links which are kept fixed in a single update by $\breve{U}_x$. The canonical weight is then given by

$$\rho[U] = \rho[U_x|\breve{U}_x] \, \breve{\rho}[\breve{U}_x], \tag{2.130}$$

where $\breve{\rho}[\breve{U}_x]$ is the weight of U by ignoring the link U_x. Hence, the transition probability factorizes into

$$P[U \to U'] = P_x[U_x \to U'_x|\breve{U}_x] \, \delta(\breve{U}_x - \breve{U}'_x), \tag{2.131}$$

where $P_x[U_x \to U'_x|\breve{U}_x]$ is the transition probability of going from U_x to U'_x under the condition that the other links $\breve{U}_x$ are kept fixed. The heat bath requires

$$P_x[U_x \to U'_x|\breve{U}_x] = \rho[U'_x|\breve{U}_x]. \tag{2.132}$$

The probability density function can be written as

$$\mathrm{d}E_{\breve{U}_x}[U_x] = \rho[U_x|\breve{U}_x] \, \mathrm{d}U_x. \tag{2.133}$$

As a total derivative, the measure $\mathrm{d}E_{\breve{U}_x}$ is translationally invariant and we can obtain a new link U'_x by integrating $\mathrm{d}E_{\breve{U}_x}$ with respect to U_x, shifting the result by a random number $r \in [0; 1[$ and applying an inversion:

$$U'_x = E_{\breve{U}_x}^{-1}\left(E_{\breve{U}_x}(a) + r[E_{\breve{U}_x}(b) - E_{\breve{U}_x}(a)]\right). \tag{2.134}$$

Here $[a; b]$ is the interval of all allowed links. Of course, the inverse of the density function is hard to compute and it is more suitable to work with an approximation ρ_0 of ρ and $E_{0,\breve{U}_x}$ of

---

[39]This section is based on [Montvay and Münster, 1994, p. 396ff], following closely the argumentation of [cf. Kurth, 2007, p. 45ff].

$E_{\breve{U}_x}$ and combining the update with an accept-reject step:

$$r' \leq \frac{\rho[U'_x|\breve{U}_x]}{\rho_0[U'_x|\breve{U}_x]} \min_{U_x \in [a;b]} \left(\frac{\rho_0[U_x|\breve{U}_x]}{\rho[U_x|\breve{U}_x]} \right) \leq 1. \tag{2.135}$$

For the gauge group SU(2), these approximations can be found rather easily. It is well known that each $U \in$ SU(2) can be represented by a quaternionic unit vector $a = (a_0, \mathbf{a})$ via

$$U = a_0 + \imath \sum_{k=1}^{3} a_k \, \sigma_k. \tag{2.136}$$

This means that linear combinations of SU(2) group elements, such as the staple sum S_x belonging to U_x can be directly reprojected into SU(2) by simple normalization. This allows us to define an element of SU(2) by setting

$$U_0 = \sqrt{\det S_x}\, S_x^{-1} = \alpha S_x^{-1}. \tag{2.137}$$

Recall that we demanded the transition probability to be equal to the weight of the phase space, i.e.

$$\rho[U_x|\breve{U}_x]\,\mathrm{d}U_x \propto \exp\left(\frac{\beta}{2} \mathrm{Re}\,\mathrm{Tr}[U_x S_x] \right), \tag{2.138}$$

where S_x solely depends on some links of $\breve{U}_x$. Using relation (2.137) yields

$$U_x S_x = \alpha U_x U_0^{-1} = \alpha U_{0,x} = \alpha \left(a_0 + i \sum_{k=1}^{3} \sigma_k a_k \right). \tag{2.139}$$

Since $U_0^{-1} \in$ SU(2), the Haar measure is invariant under the transformation $U_x \to U_x U_0^{-1} = U_{0,x}$. Thus, we obtain

$$\int_{\mathrm{SU}(2)} \mathrm{d}U_x \, \rho[U_x|\breve{U}_x] = \int_{\mathrm{SU}(2)} \mathrm{d}U_{0,x} \, \rho[U_{0,x}|\breve{U}_{0,x}]. \tag{2.140}$$

Using the quaternionic representation of the SU(2) Haar measure, we end up with the probability density of the parameters of a single link

$$p(a_1, a_2, a_3)\mathrm{d}^3 a = \mathrm{d}a_0 \sqrt{1 - a_0^2}\, e^{\beta \alpha a_0} \mathrm{d}^2\Omega, \tag{2.141}$$

where $a_0 = \sqrt{1 - (a_1^2 + a_2^2 + a_3^2)}$ and $\mathrm{d}^2\Omega$ is the solid angle with respect to the three-vector $\mathbf{a}$. Although a generalization of that algorithm to $N_c > 2$ is difficult, it is possible to apply the SU(2) heatbath successive to all diagonal SU(2) subgroups of the SU(N_c) link. This method is called *pseudo heat bath*. Detailed balance is also fulfilled for this derived algorithm which goes back to Cabibbo and Marinari [1982].

The second important gauge-update algorithm is the *overrelaxation method*. The idea is to find a rotation U_0 which, when applied to the original link via $U'_x = U_0 U_x^\dagger U_0$, maximizes

$$\mathrm{Re}\,\mathrm{Tr}(U'_x U_x), \tag{2.142}$$

while preserving the action at the same time. This guarantees that the update will always be accepted. However, such an update is not ergodic since it generates the microcanonical ensemble instead of the canonical one. Nevertheless, in combination with a heat bath algorithm, overrelaxation speeds up the decorrelation of subsequent configurations in the Markov chain [Petronzio and Vicari, 1990].

We found it to be most efficient to combine four overrelaxation steps with one pseudo heat bath step. We used this setup for generating our quenched configurations for the scaling test of the quenched strange quark mass (cf. 3.2.2) and quenched B_K (cf. 3.2.3).

Hybrid-Monte-Carlo

Performing simulations with dynamical fermions is much more involved compared to the pure gauge case. In Yang-Mills theory, the action is ultra-local and thus changes in the action can be also computed locally. In case of fermion fields, this is not true. The fermion functional determinant introduces a global quantity. Recall that

$$Z = \int \mathrm{D}U \int \mathrm{D}\overline{\psi} \int \mathrm{D}\psi \, e^{-S_G[U] - \overline{\psi}\,(\slashed{D}[U]+m)\psi} = \int \mathrm{D}U \, \det(\slashed{D}[U] + m) \, e^{-S_G[U]}. \qquad (2.143)$$

We rewrite expression (2.143) using the identity $\det(M) = \exp(\mathrm{Tr}[\ln M])$, obtaining

$$Z = \int \mathrm{D}U \, e^{-S_G[U] - S_F[U]}, \qquad (2.144)$$

where $S_F[U] = -\mathrm{Tr}[\ln(\slashed{D}[U] + m)]$. This expression is at least as difficult to compute numerically as the determinant before and we only use it for notational means. The idea behind many fermionic algorithms is to exploit the path integral identities between bosonic and fermionic variables (cf. formulae (2.19) and (2.25)). Assuming non-vanishing eigenvalues, we have $\det(D) = 1/\det(D^{-1})$.[40] For even numbers of degenerate flavours we can rewrite the fermionic path integral via[41]

$$\int \left(\prod_{i=1}^{n} \mathrm{D}\psi_i \mathrm{D}\bar{\psi}_i \, \mathrm{D}\xi_i \mathrm{D}\bar{\xi}_i \right) e^{-\sum_{i=1}^{n}\left(\bar{\psi}_i D_i \psi_i + \bar{\xi}_i D_i \xi_i\right)} = \prod_{i=1}^{n} \det(D_i^2) \qquad (2.145)$$

$$= \prod_{i=1}^{n} \det(D_i D_i^{\dagger}) \qquad (2.146)$$

$$\propto \int \left(\prod_{i=1}^{n} \mathrm{D}\phi_i^{\dagger} \mathrm{D}\phi_i \right) e^{- \sum_{i=1}^{n} \phi_i^{\dagger} (D_i D_i^{\dagger})^{-1} \phi_i}. \qquad (2.147)$$

We concentrate on two degenerate flavours ($n = 1$), but the calculations can be easily extended to arbitrary n.

The configurations we want to obtain should be distributed by $\exp(-S[U])/Z$, where $S[U] =$

---

[40] For brevity, I denote $\slashed{D} + m$ by D.

[41] I follow the argumentation from Gattringer and Lang [2010, p. 190ff] and also use a similar notation. However, I leave out the description of the MD algorithm in flat space [cf. Gattringer and Lang, 2010, p. 191ff] for brevity and start by discussing the SU(3) algorithm invented by [Duane et al., 1987].

$S_G[U] - \phi^\dagger(DD^\dagger)^{-1}\phi$. The updates of ϕ can be performed by generating a complex random vector χ which is distributed by $\exp(-\chi^\dagger\chi)$ and then setting $\phi = D\chi$.

A molecular dynamics method is then applied for updating to the gauge fields U, where the ϕ are treated as external constant fields. In order to ensure reversibility even when using relatively large MD timesteps $\Delta\tau$, a Metropolis accept-reject step at the end of each trajectory has to be applied.

In detail, the update is computed as follows: first, express all link variables $U_\mu(x)$ using the Lie-algebra generators λ_i and eight real numbers $\omega_\mu^i(x)$:

$$U_\mu(x) = \exp\left(i\sum_{i=1}^8 \omega_\mu^i(x)\lambda_i\right) = \exp(iQ_\mu(x)). \tag{2.148}$$

To each coordinate variable Q_μ belongs a momentum variable

$$P_\mu(x) = \exp\left(i\sum_{i=1}^8 P_\mu^i(x)\lambda_i\right), \tag{2.149}$$

where $P_\mu^i(x) \in \mathbb{R}$, $\forall i, \mu, x$. The variables Q_μ, P_μ are conjugate[42] and allow for sampling the micro-canonical ensemble using an MD algorithm. The micro-canonical Hamiltonian involves the expression

$$\frac{1}{2}\sum_{x,\mu,i}\left(P_\mu^i(x)\right)^2 = \sum_{x,\mu}\text{Tr}[P_\mu(x)^2]. \tag{2.150}$$

For performing the molecular dynamics evolution, we have to compute the derivative of the action with respect to the Q_μ. I am going to discuss this for a thin-link action where no smearing is applied.[43]

Derivatives live in the tangent space of the corresponding manifold. In case of SU(3), this is the Lie algebra $\mathfrak{su}(3)$ and thus can be expressed using the corresponding basis vectors. The action is a function of the links U. Therefore, we define the Lie-derivative of an arbitrary, lie-differentiable function f to be

$$\delta_{U_i}f(U) = \frac{\partial f(U)}{\partial\omega^i} = \partial_\omega f\left(e^{i\omega\lambda_i}U\right)\Big|_{\omega=0} = \lim_{\omega\to 0}\frac{f\left(e^{i\omega\lambda_i}U\right) - f(U)}{\omega}. \tag{2.151}$$

Using this, we can define the derivative of f with respect to some group element U via

$$\frac{\delta f}{\delta U} = \sum_i \lambda_i\,\delta_{U_i}f(U) \tag{2.152}$$

Thus, the MD force is given by the Lie algebra element

$$F[U,\phi] = \frac{\delta}{\delta U}\left(S_G[U] + \phi^\dagger(DD^\dagger)^{-1}\phi\right). \tag{2.153}$$

Computing the numerical derivative of the gauge action is straightforward when rewriting it as a trace of products of U and the corresponding staples. The function is linear in U and

---

[42]More precisely, ω_μ^i and P_μ^i form a set of conjugate variables.
[43]For a detailed discussion of the smeared action, please read the appendix E.2

the derivative can be easily computed (remember that the staple is independent of U). The fermionic part of the force can be rewritten via (cf. appendix E.1)

$$
\begin{aligned}
\partial_i \big(\phi^\dagger (DD^\dagger)^{-1} \phi \big) &= -\phi^\dagger (DD^\dagger)^{-1} \big(\partial_i DD^\dagger \big) (DD^\dagger)^{-1} \phi \\
&= -\big((DD^\dagger)^{-1} \phi \big)^\dagger \Big((\partial_i D) D^\dagger + D(\partial_i D^\dagger) \Big) \big((DD^\dagger)^{-1} \phi \big).
\end{aligned}
\tag{2.154}
$$

It is obvious, that the most expensive parts of the update are the inversions of $DD^\dagger$ and the computation of the derivative of D. Therefore, the performance of the algorithm mainly depends on the speed of the algorithm used for the inversions. We use a mixed precision [Durr et al., 2009] conjugate gradient [CG, cf. Press et al., 2007, p. 87f] solver which is well balanced concerning memory consumption and convergence rate. Using a CG solver is possible because $DD^\dagger$ is a Hermitian matrix.

In order to obtain detailed balance it is necessary to use an integrator which provides *reversibility of the trajectory* as well as *preservation of the integration measure* $DU\,DP$ (or *area conservation*) inside the MD evolution. The well known leapfrog algorithm [Press et al., 2007, p. 1038ff] satisfies both [cf. Gattringer and Lang, 2010, p. 192f].

The full algorithm can be summarized as follows ($n\,\Delta\tau = 1$):

1. Compute the pseudofermion field $\phi = D\chi$, where χ is distributed by $\exp(-\chi^\dagger \chi)$.

2. Compute eight real numbers P^i for each link U_0 in order to obtain P_0, where the P^i have to be distributed by $\exp(-\operatorname{Tr}(P_0^2))$.

3. Calculate the starting value for the leapfrog algorithm using an initial half-step:

$$
P_{1/2} = P_0 - \frac{\Delta\tau}{2}\, F[U,\phi]\big|_{U=U_0}.
\tag{2.155}
$$

4. Apply $n-1$ full intermediate steps for $k = 1, \ldots, n-1$:

$$
U_k = \exp\big(i\Delta\tau P_{k-1/2}\big) U_{k-1}; \quad P_{k+1/2} = P_{k-1/2} - \Delta\tau\; F[U,\phi]\big|_{U=U_k}.
\tag{2.156}
$$

5. Finish with a half-step:

$$
U_n = \exp\big(i\Delta\tau P_{n-1/2}\big) U_{n-1}; \quad P_n = P_{n-1/2} - \frac{\Delta\tau}{2}\, F[U,\phi]\big|_{U=U_n}.
\tag{2.157}
$$

6. Close the trajectory by applying the Metropolis criterion (2.128). The action is given by integrating over the full microcanonical Hamiltonian, i.e.

$$
S[U,P,\phi] = \operatorname{Tr}(P^2) + S_G[U] + \phi^\dagger (DD^\dagger)^{-1}\phi.
\tag{2.158}
$$

Due to the Metropolis step at the end, this algorithm is exact. Formally it corrects for $\mathcal{O}(\Delta\tau^2)$ discretization errors in MD time and in principle allows for using larger time steps. Of course, increasing the step size has to be done carefully since this results in a reduced acceptance rate and therefore in larger autocorrelation times. It is good to tune the algorithm to obtain at least 80% acceptance. In our work we tried to obtain a sustained acceptance rate $> 90\%$.

Rational HMC

The HMC cannot treat odd numbers of fermions. The reason is that the Dirac operator enters quadratically via $DD^\dagger$, which guarantees the convergence of the pseudofermionic path integral. Using D^{-1} alone therefore causes trouble.

If $\det D > 0$,[44] the solution to this is using the operator $(DD^\dagger)^{-1/2}$ within the standard HMC, where the inverse square root has to be approximated by a suitable functional form. In our case we use a rational ansatz of the form[45]

$$M^{-\frac{1}{2}} \approx \alpha_0 + \sum_{i=1}^{d} \frac{\alpha_i}{\beta_i - M}, \tag{2.159}$$

with the *zolotarev coefficients* α_i, β_i and the order d chosen appropriately. The algorithm is named after this kind of approximation, viz. *rational HMC* (RHMC) [Clark et al., 2003; Clark and Kennedy, 2007]. The approximation may be rather crude, since the Metropolis step at the end of each (R)HMC trajectory also corrects for truncation errors in (2.159). In order to guarantee a good acceptance rate by preserving a good performance, one has to tune the expansion order d: increasing d improves the approximation and thus the acceptance rate, but involves more expensive inversions of the Dirac operator. A multishift solver [Frommer et al., 1995] serves well here. Analogous to the HMC, the RHMC is an exact algorithm.

Mass preconditioning - Hasenbusch Trick

This method goes back to Martin Hasenbusch [Hasenbusch, 2001]. The fermion determinant is split up via

$$\det M = \det(M_n) \left(\prod_{k=2}^{n} \det(M_k^{-1} M_{k-1}) \right) \det(M_1^{-1} M), \tag{2.160}$$

where a stochastic estimator is used for all of the factors. The advantage is, that one can use the M_k^{-1} matrices as preconditioners. We chose Dirac operators with different masses as preconditioners for the different insertions in our calculations. This isolates the heavily fluctuating UV part of the force so that it can be treated separately (see below).

Multiple timescale integration

Inside the force of the MD evolution (2.153), different terms usually contribute by different orders of magnitude when using a fixed step size $\Delta\tau$. This means that after a full MD step, some terms contribute less to the total fermion force than others. Hence, they can be integrated on a much larger timescale $\Delta\tau_l$ while preserving the overall discretization error $\mathcal{O}(\Delta\tau^2)$. This can be achieved by a so-called *Sexton-Weingarten integration scheme* [Sexton and Weingarten, 1992]. Within the MD part of the HMC, the step size for integration of each individual part of the force is chosen individually to achieve an equal contribution of each term to the total force. While this does not reduce the acceptance rate, it does reduce

---

[44] Which is satisfied if D is γ_5-Hermitian, as it is the case for the Wilson Dirac operator.

[45] One can also choose a Padé ansatz such as $M^{-\frac{1}{2}} \approx c_0 \prod_{i=1}^{d} \frac{\alpha_i - M}{\beta_i - M}$.

the computational costs. Combining the mass preconditioning with the Sexton-Weingarten integration scheme leads to a very efficient algorithm: the less expensive UV part of the force can be integrated on much smaller timescales, whereas the demanding IR part of the force can be integrated using a relatively large step size [Ali Khan et al., 2003; Urbach et al., 2006a]. For instance, the heavy quark flavours can be integrated on much smaller timescales than the expensive light quark flavours.

Omelyan integrator

The omelyan integrator applies a slight modification to the leapfrog algorithm within the MD: before and after the leapfrog step, a small momentum update (reduced by $\lambda \approx 0.193$) is added and shortens the original leapfrog momentum update by a factor of $1 - 2\lambda$. This scheme increases the computational costs by a factor of $\simeq 2$ but in turn improves the MD energy conservation by about one order of magnitude. This allows for chosing a larger step size $\Delta\tau$ which leads to an overall performance benefit of around 50% [Takaishi and de Forcrand, 2006].

All these algorithmic improvements shifted the "Berlin-Wall" of computational costs [Jansen et al., 2006; Urbach et al., 2006b] to smaller pion masses (cf. e.g. [Jung, 2009]).

2.3.5. Error treatment

Monte-Carlo techniques used for generating gauge-configurations are statistical techniques. The QCD path integral is approximated by a sum over a finite number of configurations obtained by importance sampling. The uncertainty attributed to neglecting the configurations 'missed' by the sampling algorithm can be expressed by assigning a statistical error to all lattice results. Thus, it can be reduced by increasing the number of configurations in an ensemble. In the limit of large statistics, this error is expected to decrease with $1/\sqrt{N}$, where N is the size of the sample.[46]

A second source of uncertainty is related to the specifics of the action, the methods used in the final analysis, etc.. Some examples are the use of quark masses much larger than the physical ones or the use of a fermion discretization which is not chirally symmetric for vanishing quark masses. The former setup involves an extrapolation to the physical point, introducing a systematic uncertainty attributed to the choice of the extrapolation formula. The latter setup complicates the computation of observables sensitive to chiral symmetry and thus introduces a systematic uncertainty attributed to the method used for correcting for these effects. The error associated to these kind of uncertainties is called *systematic error* and can bias the final results. Therefore, it is important but often difficult to estimate it in a reliable way. In this section, I will present a method on how this error can be estimated.[47] This method also allows for giving error budgets, i.e. for disentangling the different contributions to the systematic error. This helps identifying the dominant sources of uncertainty and thus deciding how future calculations can be improved.

Finite volume effects can be viewed as a special kind of systematic uncertainties and literature

---

[46]The sections related to the assessment of statistical errors is based on [Gattringer and Lang, 2010, p. 97].

[47]This method was already used and its description is published in the SOM for [Dürr et al., 2008] and [Durr et al., 2010].

offers methods allowing to correct for them [cf. Luscher, 1986a,b, 1991a,b; Colangelo et al., 2005]. I will briefly discuss these techniques in the end of this section, following closely the argumentation from our SOM for [Dürr et al., 2008].

Thermalization and autocorrelation

Gauge configurations belonging to the same Markov chain (cf. section 2.3.4) are generally not statistically independent. Thus, expectation values of observables evaluated on different subsets of these configurations are correlated. These correlations are referred to as *autocorrelations* and they strongly depend on the update algorithm and specific observable. It is easy to understand, that global quantities such as the topological charge have a larger autocorrelation than local observables such as the plaquette. It is possible to measure the autocorrelation for any observable $\mathcal{O}$, as long as the expectation value of this observable can be measured on a single configuration.[48] Consider the *autocorrelation function*

$$C_{\mathcal{O}}(t) = \langle (\mathcal{O}_i - \langle \mathcal{O}_i \rangle)(\mathcal{O}_{i+t} - \langle \mathcal{O}_{i+t} \rangle) \rangle = \langle \mathcal{O}_i \mathcal{O}_{i+t} \rangle - \langle \mathcal{O}_i \rangle \langle \mathcal{O}_{i+t} \rangle, \qquad (2.161)$$

where the time difference t is in Monte-Carlo time. The *normalized autocorrelation function* $\Gamma_{\mathcal{O}}$ exhibits exponential behaviour for large time separations t:

$$\Gamma_{\mathcal{O}}(t) = \frac{C_{\mathcal{O}}(t)}{C_{\mathcal{O}}(0)} \sim \exp\left(-\frac{t}{\tau_{\mathcal{O}}}\right), \qquad (2.162)$$

where the decay constant $\tau_{\mathcal{O}}$ is the *exponential autocorrelation time of observable $\mathcal{O}$* [Gattringer and Lang, 2010, p. 94]. Autocorrelation leads to systematic errors of order $\exp(-t/\tau_{\mathcal{O}})$. Since the exponential autocorrelation time is difficult to measure, it is recommended to use the *integrated autocorrelation time*:

$$\tau_{\mathcal{O},\text{int}} = \frac{1}{2} + \sum_{t=1}^{N} \Gamma_{\mathcal{O}}(|t|) \approx \int_{0}^{\infty} \mathrm{d}t \, e^{-t/\tau} = \tau. \qquad (2.163)$$

For large t the statistics will be very limited and the errors on the autocorrelation function (2.162) very large. Thus, the sum in expression (2.163) should be truncated at the first t-value, where $\Gamma_{\mathcal{O}}(|t+1|)$ is compatible with zero within errors. This gives a fair estimate of the real autocorrelation time $\tau_{\mathcal{O}}$. Comparing integrated autocorrelation times for different lattice sizes and pion masses gives a hint on the strength of the inherent *critical slowing down*. The integrated autocorrelation time usually behaves as

$$\tau_{\mathcal{O},\text{int}} \sim \xi_{\mathcal{O}}^z, \qquad (2.164)$$

where the *dynamical critical exponent z* depends on the update algorithm. Near critical points we have $\xi_{\mathcal{O}} \approx L$ on finite lattices ($\xi_{\mathcal{O}} \to \infty$ in the continuum) and therefore in the worst case

$$\tau_{\mathcal{O},\text{int}} \sim L^z, \qquad (2.165)$$

---

[48]It is difficult to define a reasonable autocorrelation function for e.g. hadron masses, since the correlation functions from which hadron masses are extracted have to be averaged over (a subset of) an ensemble.

where the numerical costs grow accordingly.

Thermalization is also related to autocorrelation. When starting from a random configuration, it takes several $N \cdot \tau$ sweeps or trajectories to thermalize the system, i.e. bring it into thermal equilibrium. Of course, all non-thermalized configurations should be thrown away and we carefully watch for possible remaining thermalization effects in our configurations. This is also to be done for the autocorrelation effects of the most critical observables such as the topological charge.

In our computations, autocorrelation time is calculated using a more sophisticated setup described by Wolff [2004], where we basically used the MATLAB code supplied by the author. The best method to deal with these autocorrelations is to take every $\tau \cdot n$th configuration with $n \sim 3 - 5$. Unfortunately, this is not always feasible in present day simulations. Even if it were, some minor autocorrelation effects would still remain. A possible solution to this is data binning, but it requires large statistics and calculating reliable errors is very difficult. The (moving block) bootstrap method I am going to describe now is well suited for calculating trustable errors on datasets with small autocorrelation effects.

Statistical error treatment: Bootstrap analysis

The *bootstrap procedure* [Press et al., 2007, p. 809f] is a simple and computationally cheap Monte-Carlo data sampling method [Press et al., 2007, p. 807ff], where no assumptions about the underlying process or the nature of the measurement errors have to be made. Assume having a dataset D_0 consisting of N *independent and identically distributed (iid)* data points. We generate M synthetic data sets $\{D_k\}_{k=1}^{M}$ by drawing N random data points *with replacement* from the original sample D_0. Hence, each generated data sample contains $\approx 37\%$ *duplicated* original points [cf. Press et al., 2007, p. 810]. For any observable of interest $\mathcal{O}$ we can calculate the means $\bar{\mathcal{O}}_k$ on each of these samples via

$$\bar{\mathcal{O}}_k = \frac{1}{N} \sum_{i=1}^{N} \mathcal{O}_{ki}, \; \forall \mathcal{O}_{ki} \in D_k. \tag{2.166}$$

The *(biased) bootstrap estimate $\tilde{\mathcal{O}}$ and error* $\sigma_{\mathcal{O}}$ is then given by

$$\tilde{\mathcal{O}} \equiv \frac{1}{M} \sum_{k=1}^{M} \bar{\mathcal{O}}_k; \quad \sigma_{\mathcal{O}}^2 \equiv \frac{1}{M} \sum_{k=1}^{M} \left(\bar{\mathcal{O}}_k - \tilde{\mathcal{O}}\right)^2. \tag{2.167}$$

As the final result one should quote $\bar{\mathcal{O}}_0 \pm \sigma_{\mathcal{O}}$.[49] The major drawback of the standard bootstrap method is the iid assumption. Due to non-vanishing autocorrelation effects, this requirement is violated. Methods allowing to relax this assumption are currently under research. In our work, we use the *moving block bootstrap technique* [Mignani and Rosa, 1995]. The basic idea is to draw overlapping blocks of subsequent measurements instead of a single measurement at a time. A multiple of the integrated autocorrelation time serves well as an estimate for the optimal block length l. For $l = 1$, the standard bootstrap technique is recovered. A major

---

[49] Please note that [Gattringer and Lang, 2010, p. 97] contains an error in the paragraph following formula (4.71). According to their notation, the expectation value computed from the full sample $\hat{\theta}$ should be used for the central value, since the mean of the bootstrap means $\tilde{\theta}$ is biased.

advantage of bootstrapping over data blocking methods is that it is possible to obtain reliable errors for functions of expectations values. The function has to be applied to the bootstrap sample means $\mathcal{O}_k$ before calculating the bootstrap error according to (2.167).

Systematic error treatment

For ab initio computations of physical quantities it is extremely important to carry out an unbiased data analysis. Any preference based on prejudices and estimates and not on facts related to the choice of fitting intervals, fitting functions, scale setting, etc. should be avoided. Our method is basically an extended version of the frequentist method [Nakamura et al., 2010], following the philosophy, that any potential source of systematic error has to be taken into account as long as it is not proven to be sub-dominant and therefore can be neglected. Translated into a cooking recipe, this means: we repeat the whole data analysis, from the very beginning to the very end, using e.g. different fit ranges for correlators, different mass cuts, different functional forms for the fits, etc.. Hence we consider many possible methods for analyzing the data, where every single one is completely reasonable and may be used as the 'main method' in standard approaches. Thus, we obtain several 'final' values for the observable a_i which can be weighted by using their quality of fit $q_i = 1 - \Gamma(n_i/2, \chi_i^2/2)$.[50] All a_i form a (usually non-Gaussian) distribution and we can calculate the final value $\bar{a}$ by computing the median and the systematic error $\sigma_{a,\text{syst}}$ by calculating the central 68% probability. There is no ambiguity related to data binning which is necessary to obtain the probability density function (PDF), since both quantities can be computed from the unambiguous cumulative distribution function (CDF).

Note that this method allows for computing error budgets: assume that we want to estimate the influence of the variation of method b (which might be the choice of fit ranges for example) on the final result. We assume further that we have n reasonable replacements for method b (e.g. n different fit ranges). Thus we can perform n analyses, keeping the method b fixed but different for each of those and varying over all other uncertainties. We obtain n averaged values $\bar{a}_b$ and compute the central 68% of those in order to estimate the influence of the variation of method b on the final result.

Note that the assumption of 'only using reasonable methods in the data analysis' is mathematically not solid and relies on the intuition of the person performing the analysis. In many cases it is clear which methods should be included in the analysis and which should not. However, there are borderline cases where this is not entirely clear. In our studies, this applies to the assumption for the scaling behavior of the action, i.e. whether it is dominated by $\mathcal{O}(\alpha_s a)$ or $\mathcal{O}(a^2)$ effects. However, including both possibilities is a conservative choice which may at worst lead to an overestimation of the systematic error.[51]

A common difficulty is to combine the statistical and systematic errors. Since the systematic error is usually non-Gaussian, it is, strictly speaking, not allowed to add these two in quadrature. Hence, we quote both errors separately and only add them in quadrature for illustration purposes.

---

[50]Here, Γ is the incomplete gamma function and n_i the number of degrees of freedom.
[51]Note, that we are not including terms proportional to $\alpha_s a$ and a^2 in the same fit. Our data are not precise enough and do not cover a sufficiently broad range in a allowing the fit to discriminate between these terms.

Finite volume corrections

The finite volume effects are a source of systematic errors which in principle cannot be avoided completely in lattice QCD. Nevertheless, they can be made arbitrarily small by using sufficiently large lattices. If this is computationally not feasible or possible, they can at least be estimated and subtracted.

In principle there are two different types of finite volume corrections. The first type results from virtual pion exchanges between different copies of the periodic system and it tends to shift the energy levels of single particle states to higher values. The second type is only relevant to resonant states, in regions of parameter space where they would decay in infinite volume.

The frameworks for treating finite volume corrections have been established by Luscher [1986a,b]; Colangelo et al. [2005] for stable and by Luscher [1991a,b] for unstable states. They allow treating finite volume corrections in a self-consistent manner, i.e. in a way in which only the results of the lattice computation and the axioms of quantum field theory are used.

The first type of finite volume effects are most transparent in case of non-singlet meson masses at 1-loop level χPT.[52] Let us consider the pion mass M_π: up to higher orders in M_π, its relative shift from finite to infinite volume is given by

$$R_\pi(L) = \frac{M_\pi(L)}{M_\pi} - 1 = \text{const.} \cdot M_\pi^2 \, \tilde{g}_1(M_\pi \, L), \tag{2.168}$$

where $\tilde{g}_1$ has a well behaved expansion in terms of a Bessel function of the second kind

$$\tilde{g}_1(x) = \frac{24 \, K_1(x)}{x} + \frac{48 \, K_1(\sqrt{2}x)}{\sqrt{2}x} + \dots. \tag{2.169}$$

The Bessel function K_1 can be expanded for large x via

$$K_1(x) = \left(\frac{\pi}{x}\right)^{1/2} e^{-x} \left(1 + \frac{3}{8x} + \dots\right), \tag{2.170}$$

which implies that finite volume corrections are exponentially suppressed at large L [Luscher, 1986a].[53] In principle, the analytic results from these references along with (2.168) can be used to correct lattice data for finite volume effects. This can either be done by fitting dedicated finite volume data to these formulas or using the predictions for the corresponding coefficients from χPT.[54] We will see in section 3.2.4 that finite volume effects on our quantities of interest are tiny. However, we still correct for them.

The second type of finite volume corrections has to be treated differently. Consider the hypothetical case in which we have a resonant state which does not couple to its scattering state as it would do in infinite volume. In a finite box with size L, the spectrum in the center

---

[52]Higher orders have been worked out in [Colangelo et al., 2005].

[53]Analytic results for finite volume corrections of the nucleon are given in [Ali Khan et al., 2004; Colangelo et al., 2006, 2010a].

[54]A good check for testing the chiral behaviour of the action is to compare both approaches.

of mass frame consists of two particle states with energy

$$E = \sqrt{M_1^2 + \mathbf{k}^2} + \sqrt{M_2^2 + \mathbf{k}^2}, \tag{2.171}$$

where $\mathbf{k} = \mathbf{n}2\pi/L$, $\forall \mathbf{n} \in \mathbb{Z}^3$ and M_1, M_2 are the masses of the lighter particles (with applied finite volume corrections as described in the last paragraph). Let us denote the mass of the resonant state by M_X (again with corrections of type I). When increasing L or lowering the quark masses[55], the energy of the scattering state E can become smaller than M_X. In the presence of interactions, the resonant and its scattering state mix. Hence in continuum theory, the spectral density of the scattering state will show a peak in its multi-particle-continuum region. The position of the peak can be interpreted as the mass M_X of the resonant state and the width is proportional to its decay constant Γ_X. Inside a finite volume however, the spectrum is discrete and non-degenerate. This leads to an avoided level crossing phenomenon of the scattering and resonant state (cf. figure 2.5). The resulting volume dependent mass shifts can distort the chiral extrapolation of hadron masses to the physical point.

Literature [Luscher, 1986a,b, 1991a,b] provides a conceptually satisfactory basis and good mathematical tools to deal with resonances in lattice QCD: each measured energy corresponds to a momentum $k = |\mathbf{k}|$ through a complicated non-linear equation. We will discuss the ρ-resonance as an example: this particle decays almost exclusively into two pions π with a total energy

$$W = 2\sqrt{k^2 + M_\pi^2} \tag{2.172}$$

in the center of mass frame. The $\pi\pi$ scattering phase $\delta_{11}(k)$ in the isospin $I = 1$ and angular momentum $J = 1$ channel passes through $\pi/2$ at the resonance energy. This corresponds to a pion momentum of

$$k = k_\rho = \sqrt{M_\rho^2/4 - M_\pi^2}. \tag{2.173}$$

The effective range formula

$$\frac{k^3}{W} \cot \delta_{11}(k) = a + bk^2 \tag{2.174}$$

yields

$$a = -bk_\rho^2 = \frac{4k_\rho^5}{M_\rho^2 \, \Gamma_\rho}, \tag{2.175}$$

where Γ_ρ is the decay width of the ρ.[56] The bottom line is that the energy levels are still given by (2.172) but with k being the solution of the non-linear equation

$$n\pi - \delta_{11}(k) = \phi\left(\frac{kL}{2\pi}\right), \tag{2.176}$$

with $0 < k < \sqrt{3}M_\pi$, $n \in \mathbb{N}$ and ϕ being a known kinematical function which was evaluated numerically for our analysis [cf. Luscher, 1991b, for details].

Therefore, the spectrum of resonant states is determined by M_X, the masses of the scattering states M_1, M_2 and the coupling g_X which is related to the width of the resonance.

---

[55]The masses of light hadrons depend stronger on the masses of their constituents compared to heavier hadrons.
[56]The decay width can also be parametrized by an effective coupling g between the ρ and $\pi\pi$ states. This coupling can then be measured directly on the lattice and hence additional experimental input can be avoided.

(a) Free theory

(b) Interacting theory
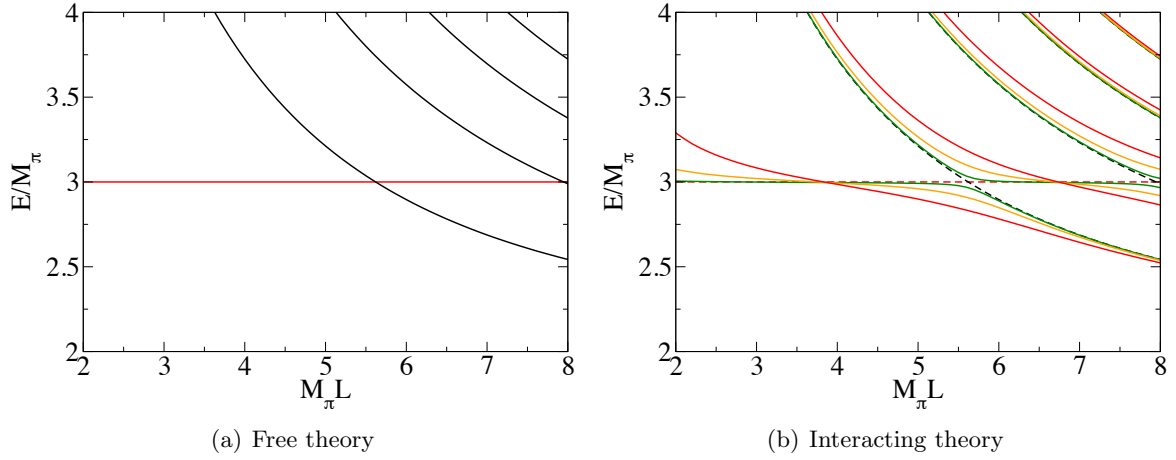
Figure 2.5.: Energy levels for the resonant M_X and $\pi\pi$ scattering state W in non-interacting (a) and interacting (b) theory in dependence of $M_\pi L$. In the left panel, the M_X state has energy $E/M_\pi = 3$ (red line) and the discrete energies of the $\pi\pi$ scattering states are represented by different hyperbolic black curves. On the right side, we observe a clear distortion of the energy spectrum when interaction is switched on. The different colors denote the spectrum for different choices of coupling g [taken from Frison et al., 2010, with the permission for reprint from the authors].

Besides hadron masses and decay constants, also B_K defined in (2.102) is affected by finite volume corrections. However, since this quantity is a ratio of matrix elements with similar chiral structure, cancellations in the chiral expansions render the finite volume corrections to this ratio small [cf. Becirevic and Villadoro, 2004]. Furthermore, SU(3) flavour symmetry relations lead to cancellations in χPT diagrams for large pion masses. Therefore, an additional suppression of finite volume corrections to B_K is observed in that energy region. In section 4.3, we show that our expected finite volume corrections to B_K are even smaller than that to M_π and thus well under control. However, we use the formulas from [Becirevic and Villadoro, 2004] to correct for the small remaining effects.

2.3.6. Spectroscopy

One of the most important tasks in lattice gauge theory is to measure the masses of hadrons, mainly of pions and kaons. Even if these quantities are not of interest in themselves, they can be used as input quantities (cf. 2.3).
In order to extract energy levels in lattice QCD, we have to define interpolating operators O which have non-vanishing overlap with the state $|h\rangle$ we are interested in, i.e. $O|h\rangle \neq 0$.[57] In the following, we are going to discuss only operators which are local in coordinate space. For mesons, these operators may be written as

$$O_{\text{meson}}(\mathbf{x}, t) = \bar{q}^{(1)}(\mathbf{x}, t)\Gamma\, q^{(2)}(\mathbf{x}, t), \tag{2.177}$$

---

[57]This section is based on [Gattringer and Lang, 2010, p. 123ff] and [DeTar and DeGrand, 2006, p. 215ff].

where Γ is a projection operator, projecting to proper spin and parity of the desired meson (i.e. $\Gamma = \gamma_5$ for obtaining a pion-interpolating-operator). Baryons are colour singlets consisting of three valence quarks. The corresponding local interpolating-operators can be written as

$$O_{\text{baryon}}(\mathbf{x}, t) = \epsilon_{abc}\, q_a^{(1)}(\mathbf{x}, t)\big(q_b^{(2)\,T}(\mathbf{x}, t)\, F\, \Gamma q_c^{(3)}(\mathbf{x}, t)\big), \qquad (2.178)$$

where again Γ projects to the correct spin and parity and F can be a charge conjugation or something similar, which makes use of isospin symmetries of octet or decuplet.[58] For hadrons, it is possible to construct composed operators which are linear combinations of expressions (2.177) or (2.178) with different quark contents and projectors Γ, F. The masses of hadronic states $|h\rangle$, having the same quantum numbers as O and satisfying $O|h\rangle \neq 0$, can then be obtained by calculating correlators

$$C(t) = \frac{1}{V} \sum_{\mathbf{x}, \mathbf{y}} \left\langle O(\mathbf{x}, t)\, O^\dagger(\mathbf{y}, 0) \right\rangle = \sum_k \frac{\langle 0|O|k\rangle\langle k|O^\dagger|0\rangle}{2(E_k - E_0)}\, e^{-t\,(E_k - E_0)} = \sum_k \frac{|\langle 0|O|k\rangle|^2}{2m_k}\, e^{-t\,m_k},$$
$$(2.179)$$

where we inserted a spectral sum of eigenstates $|k\rangle$ with energy-eigenvalues E_k. Since the sum over all positions $\mathbf{x}, \mathbf{y}$ projects the hadron onto zero-momentum, we can consider the energy difference $E_k - E_0$ to be the mass m_k of state $|k\rangle$ in lattice units. If O is local, the vacuum overlap $|\langle 0|O|k\rangle|$ is related to the corresponding decay constant of $|k\rangle$.
If $|h\rangle$ is the lowest energy state, we have $m_1 = m_h$. Due to $m_k > m_l, \forall k > l$, all excited states die out faster in time than the ground state because of the stronger exponential suppression. Therefore, the time extent of the correlator has to be sufficiently large in order to be able to compute m_h with insignificant excited states contributions.[59] This yields

$$C(t) \xrightarrow{t \to \infty} \frac{|\langle 0|O|h\rangle|^2}{2m_h} e^{-m_h t}. \qquad (2.180)$$

On a periodic lattice, the correlator receives contributions coming from the opposite boundary in t direction. This gives rise to contributions proportional to

$$\tilde{C}(t) \xrightarrow{(T-t) \to \infty} \epsilon\, \frac{|\langle 0|O^\dagger|\tilde{h}\rangle|^2}{2m_{\tilde{h}}} e^{-m_{\tilde{h}}(T-t)}, \qquad (2.181)$$

where $\epsilon = \pm 1$, depending on the number of quark fields in the interpolating operator and whether anti-periodic boundary conditions in time direction are established. The state $|\tilde{h}\rangle$ is equal to $|h\rangle$ if the lowest lying states of O and $O^\dagger$ are the same. In this work we used operators satisfying $|\langle 0|O|h\rangle|^2 = |\langle 0|O^\dagger|\tilde{h}\rangle|^2$ and $|h\rangle = |\tilde{h}\rangle$, which simplifies the sum $C + \tilde{C}$. Further corrections arise from states whose propagators are 'wraping' around the lattice several times. For the ground state, these contributions can be resummed yielding a factor of $(1 - \exp(-m_h T))^{-1}$, where T is the time extent of the lattice. Since we are only interested in m_h and this factor is usually very close to one, we absorb it into the fitted vacuum overlap $|\langle 0|O|h\rangle|^2$.

---

[58] The operators from (2.178) cannot be chosen such that they exclusively couple to spin-3/2 states [Leinweber et al., 1992]. In order to eliminate the spin-1/2 contributions, an additional projection has to be applied. However, Leinweber et al. [1992] see no indications for these contributions being large.

[59] Extracting excited states is rather difficult and beyond the scope of this work.

Therefore, the functional form of our hadron correlators is given by

$$
C(t) + \tilde{C}(t) \sim \begin{cases} \cosh(m_h\,(t - T/2)) & \text{for } \epsilon = +1 \\ \sinh(m_h\,(t - T/2)) & \text{for } \epsilon = -1 \end{cases}, \tag{2.182}
$$

for $t \to T/2$ and $T/2 \gg 0$ and ϵ from (2.181).

In order to obtain m_h, we fit our correlators to the suitable form of (2.182) after investigating the effective mass plateau defined by [cf. e.g. Gattringer and Lang, 2010, p.145]

$$
m_{\text{eff}}(t + 1/2) = \ln \frac{C(t)}{C(t+1)}. \tag{2.183}
$$

This is necessary for adjusting the fit window in order to ensure that excited states contributions are subdominant.

In practice, the hadronic correlators can be obtained by computing traces of *quark propagators*. Consider for example the meson-correlator:

$$
\frac{1}{V} \sum_{\mathbf{x},\mathbf{y}} \left\langle \mathcal{O}^\dagger(\mathbf{x},t)\mathcal{O}(\mathbf{y},0) \right\rangle
$$

$$
= \frac{1}{V} \sum_{\mathbf{x},\mathbf{y}} \left\langle \left(\bar{q}^{(1)}\Gamma q^{(2)}\right)^\dagger(\mathbf{x},t)\left(\bar{q}^{(1)}\Gamma q^{(2)}\right)(\mathbf{y},0) \right\rangle
$$

$$
= \pm \frac{1}{V} \sum_{\mathbf{x},\mathbf{y}} \left\langle \bar{q}^{(2)}(\mathbf{x},t)\Gamma^\dagger q^{(1)}(\mathbf{x},t)\bar{q}^{(1)}(\mathbf{y},0)\Gamma q^{(2)}(\mathbf{y},0) \right\rangle
$$

$$
= \pm \left\langle \text{Tr}\left[S^{(2)}(0,t)\,\Gamma^\dagger\,S^{(1)}(t,0)\Gamma\right] - \delta_{(1)(2)}\,\text{Tr}\left[S(t,t)\,\Gamma^\dagger\right]\text{Tr}\left[S(0,0)\Gamma\right] \right\rangle, \tag{2.184}
$$

where the $\pm$ depends on the result of the permutation of γ_4 with $\Gamma^\dagger$ and the (computationally demanding) disconnected contribution is present only if the quark fields $q^{(1)}$ and $q^{(2)}$ are of the same flavour. The quantity $S^{(i)}(t_1, t_0)$ is the quark propagator, describing the propagation of quark i from time-slice t_0 to t_1, where the momentum-zero projection by averaging over all spatial positions $\mathbf{y}, \mathbf{x}$ at these time-slices is implied. The same calculation can be carried out for baryonic correlation functions, but, due to the larger quark content, the contractions are more complicated.

In order to efficiently compute the sum over $\mathbf{y}$ in (2.179), extended sources can be used. A common example are U(1) random wall sources which are discussed in appendix E.3. However, if energy levels of hadrons are extracted, it is more efficient to use appropriately smeared sources and sinks which have a better overlap with the desired state. For extracting masses, we found that Gaussian smeared quark fields serve well. These are defined by

$$
\psi(\mathbf{x}) = \theta\big(\xi - |\mathbf{x} - \mathbf{x}_0|\big)\,\delta(t - t_0)\,\frac{e^{-r\,|\mathbf{x} - \mathbf{x}_0|}}{N}, \tag{2.185}
$$

with a hard cutoff ξ, radius $r > 0$, normalization N and position $x_0 = (t_0, \mathbf{x}_0)$. Extended sinks can be obtained by convoluting the sink shape function $\bar{\psi}$ into $D^{-1}\psi$, accelerated by using fast-fourier-transformations [Hauswirth, 2002, p. 50f]. Note that the Gaussian source is not gauge covariant, hence gauge fixing is required before the inversion is performed. We use the Coulomb gauge (cf. app. C) for calculating spectral observables.

PCAC mass

Consider the isovector axial current A_μ^a and the pseudoscalar density P^a

$$A_\mu^a(x) = \frac{1}{2}\bar{\psi}(x)\,\gamma_\mu\gamma_5\tau^a\,\psi(x), \tag{2.186}$$

$$P^a(x) = \frac{1}{2}\bar{\psi}(x)\,\gamma_5\tau^a\,\psi(x), \tag{2.187}$$

with $\tau^0 = \mathbf{1}_{2\times 2}$ and $\tau^k = \sigma^k$, $\forall\, k = 1, 2, 3$. The τ-matrices act as rotations in 2-flavour space and we consider degenerate up- and down-quark masses, i.e. $m_u = m_d = m$. Also consider the axial rotation with

$$\delta\psi = \gamma_5\frac{\tau^a}{2}\psi, \quad \delta\bar{\psi} = -\bar{\psi}\gamma_5\frac{\tau^a}{2}. \tag{2.188}$$

The Ward identity for arbitrary (multi-)local operators $O(y)$ under this transformation can be obtained by computing

$$\delta\langle O(y)\rangle = \langle\delta O(y)\rangle - \langle O(y)\,\delta S\rangle = 0, \tag{2.189}$$

where δS is the variation of the action. For $\delta O(y) = 0$ and in the continuum limit, expression (2.189) reads:[60]

$$\langle(\partial_\mu A_\mu^a(x))\,O(y)\rangle = 2\,m\,\langle P^a(x)\,O(y)\rangle. \tag{2.190}$$

In a chiral theory where $m = 0$, the isovector axial current is conserved and therefore is referred to as *partially conserved axial current (PCAC)*. After multiplying the suitable renormalization constants and considering non-vanishing lattice spacing a, expression (2.190) reads

$$\langle(\hat{\partial}_\mu A_\mu^{a\,(\text{ren})}(x)\,O^{(\text{ren})}(y)\rangle = 2\,m^{(\text{ren})}\,\langle P^{a\,(\text{ren})}(x)\,O^{(\text{ren})}(y)\rangle + \text{contact terms} + \mathcal{O}(a^k), \tag{2.191}$$

where the scaling exponent k depends on the level of improvement of A_μ^a, P^a. The renormalized unimproved operators are expected to have $\mathcal{O}(a)$ discretization effects. The improved operators defined by

$$A_\mu^{a\,(\text{ren})}(x) = Z_A(1 + b_A\,ma)\left(A_\mu^a(x) + c_A\,a\,\hat{\partial}_\mu P^a(x)\right) \tag{2.192}$$

$$P^{a\,(\text{ren})}(x) = Z_p(1 + b_P\,ma)\,P^a(x), \tag{2.193}$$

with appropriately chosen improvement coefficients b_A, b_P, c_A, are expected to scale as $\mathcal{O}(a^2)$. Using the tree level values $c_A = 0, b_A = b_P = 1$ yields formally $\mathcal{O}(\alpha_s a)$ scaling, where α_s is the strong coupling.

The *renormalized PCAC or Axial Ward identity (AWI) mass* can be defined by [cf. Gattringer and Lang, 2010, p. 220]

$$m_{\text{AWI}}^{(\text{ren})} = \frac{Z_A}{Z_P}\frac{\left\langle\left(\hat{\partial}_\mu A_\mu^a(x) + c_A\,a\,\hat{\partial}^\mu\hat{\partial}_\mu P^a(x)\right)P^a(x)\right\rangle}{2\,\langle P^a(x)\,P^a(x)\rangle} = \frac{Z_A}{Z_P}m^{\text{PCAC}}. \tag{2.194}$$

---

[60]Equation (2.190) holds up to contact terms. For derivation of this Ward identity, cf. [Gattringer and Lang, 2010, p.270ff] or [Kurth, 2007, p. 91f]. A more detailed discussion of this WI including off-shell terms and lattice irrelevant operators can be found in [Bochicchio et al., 1985].

Due to Goldstone's theorem, the AWI mass vanishes for $M_\pi^2 = 0$ and thus does not suffer from possible additive renormalization such as the VWI mass (see below). As a byproduct, we obtained the renormalization factor for the AWI quark mass:

$$Z_{m^{\mathrm{AWI}}} = \frac{Z_A}{Z_P}. \tag{2.195}$$

VWI mass

There is a second definition of quark masses on the lattice, more closely related to the Lagrangian bare parameters: the so-called *vector-Ward-identity (VWI) quark mass*. Consider the local vector current operator

$$V_\mu^a(x) = \frac{1}{2}\bar{\psi}(x)\,\gamma_\mu\tau^a\,\psi(x). \tag{2.196}$$

On the lattice using Wilson-type fermions, this current is not conserved. However, it can be modified to a point-split conserved vector current

$$V_\mu^{a,C}(x) = \frac{1}{4}\left[\bar{\psi}(x)\,(\gamma_\mu - r)\,U_\mu(x)\,\psi(x+\hat{\mu})\right. \tag{2.197}$$

$$\left. +\bar{\psi}(x+\hat{\mu})\,(\gamma_\mu + r)\,U_\mu^\dagger(x)\,\psi(x) + (x \to x - \hat{\mu})\right] \tag{2.198}$$

$$\equiv \bar{\psi}(x)\,\gamma_\mu\,\psi(x) - \frac{ra}{2}\bar{\psi}(x)\left(\overleftarrow{D}_\mu - \overrightarrow{D}_\mu\right)\psi(x), \tag{2.199}$$

where D_μ is the Wilson Dirac operator and conservation implies that $Z_{VC} = 1$. The Ward identity for this current reads

$$\langle\partial^\mu V_\mu^{C,a}(x)\,O(y)\rangle = \langle\bar{\psi}(x)[\bar{M},\tau^a]\psi(x)\,O(y)\rangle + \text{contact terms} + \mathcal{O}(a), \tag{2.200}$$

where $\bar{M}$ is the subtracted quark mass matrix. The subtraction term $m^{(\mathrm{crit})}$, commonly referred to as *additive mass renormalization*, can be obtained by fitting m^{PCAC} linearly in the bare quark mass $m^{(\mathrm{bare})}$. Since the former vanishes in the chiral limit and is not affected by additive renormalization, the x-axis intersection of the fit determines $m^{(\mathrm{crit})}$.

Multiplying both sides of (2.200) with the suitable renormalization factors, we obtain the multiplicative VWI-mass renormalization constant

$$Z_{m^{\mathrm{VWI}}} = \frac{1}{Z_S}. \tag{2.201}$$

Here, Z_S is the scalar density renormalization factor, necessary to renormalize terms proportional to $\langle\bar{\psi}\psi\rangle$. I have to point out, that the derivation of this result did not include non-vanishing singlet diagrams appearing in the mass renormalization due to the Wilson and clover terms.[61]

---

[61]For a brief discussion of this issue see 2.3.7.

2.3.7. The ratio-difference-method

We introduced this method in our quark mass determinations [Durr et al., 2011b, 2010] and this section will closely follow these publications.

For Wilson-type fermions there are two options for obtaining the renormalized quark mass. One possibility is to start with the Lagrangian parameter $am^{(\mathrm{bare})}$ and apply both additive and multiplicative renormalization to build the quark mass[62]

$$m^{\mathrm{VWI}} = \frac{1}{Z_S} \left[1 - \frac{1}{2} b_S \, am^W + \mathcal{O}(a^2) \right] m^W, \qquad (2.202)$$

where $m^W = m^{(\mathrm{bare})} - m^{(\mathrm{crit})}$, $Z_S = Z_S(\mu^2)$ is the scalar density renormalization constant, b_S the on shell improvement constant and $m^{(\mathrm{crit})}$ the critical mass. The label VWI stands for 'Vector Ward Identity', albeit this specific WI only restricts differences of quark masses. In the following, we use m^{VWI} only in such differences and the dependence on $m^{(\mathrm{crit})}$ only persists in an $\mathcal{O}(a)$ suppressed term. A second method to obtain the renormalized quark mass is to use the PCAC relation (2.194) together with additional on-shell improvement terms:

$$m^{\mathrm{AWI}} = \frac{Z_A}{Z_P} \frac{1 + b_A \, am^W + \mathcal{O}(a^2)}{1 + b_P \, am^W + \mathcal{O}(a^2)} \, m^{\mathrm{PCAC}}, \qquad (2.203)$$

with improvement coefficients b_P, b_A. If one is content with $\mathcal{O}(a)$ scaling, all these factors can be set to zero. In our studies we use the tree level parameters $b_S = b_P = b_A = 1$ and $c_A = 0$ in (2.194). In any case, the difference of m^{AWI} and m^{VWI} vanishes in the continuum, so it does not matter which quark mass definition is used. Please note that both choices do have specific advantages and disadvantages: the AWI mass avoids additive renormalization but the multiplicative renormalization factor involves the pseudoscalar density renormalization constant Z_P. In a RI scheme involving exceptional momenta, this quantity is affected by pion pole contributions [Martinelli et al., 1995] and therefore hard to determine. In case of the VWI mass, only Z_S is needed, which is not affected by this effect. On the other hand, m^{VWI} has to be renormalized additively which usually enhances the errors of this quantity.[63]

For simplifying the following derivations, assume that all improvement coefficients are set to zero. The more general case will be discussed later.

In this setup, it is natural to use m^W in quark mass *differences* whereas m^{PCAC} should be used in quark mass *ratios*. This means that we use $d = am_s^W - am_{ud}^W = am_s^{(\mathrm{bare})} - am_{ud}^{(\mathrm{bare})}$ and $r = m_s^{\mathrm{PCAC}}/m_{ud}^{\mathrm{PCAC}}$. The renormalized quark masses can be then obtained by computing

$$am_{ud}^{(\mathrm{ren})} = \frac{1}{Z_S} \frac{d}{r-1}, \quad am_s^{(\mathrm{ren})} = \frac{1}{Z_S} \frac{rd}{r-1}. \qquad (2.204)$$

In the following, we are going to refer to this strategy as *ratio-difference-method*. Applying tree-level improvement to (2.203) (i.e. $c_A = 0$, $b_P = b_A = 1$) does not change this reasoning and thus we are safe to do so. Tree-level improvement of am^W makes things a little bit more complicated, since setting $b_S = 1$ in (2.202) introduces quadratic terms in am^W so that $am_s^W - am_{ud}^W$ does not coincide with $am_s^{(\mathrm{bare})} - am_{ud}^{(\mathrm{bare})}$ anymore. Additionally, note that in a full dynamical theory, the improvement pattern itself is slightly more complicated because

---

[62]in order to avoid a cumbersome notation, I drop the superscript (ren) in the following derivations
[63]Remember that the bare quark mass is known exactly because it is a parameter of the calculation.

of the presence of quark-line disconnected diagrams [Gockeler et al., 2006; Bhattacharya et al., 2006; Rakow, 2005]. We will see that our ratio-different-method steers around both complications and that the quark masses can be computed via (2.204), where the quantities r, d are slightly more complicated (see below).

The ratio-difference-method in full QCD

We apply the findings of [Bhattacharya et al., 2006] to our method, adopting their notation, except that we will not denote renormalized quantities by a hat ^. Instead, we will write out the renormalization factors explicitly, so that it is easier to see which renormalization constants are involved. Equations (2.202) and (2.203) now read

$$m_j^{\text{VWI}} = \frac{1}{Z_S} m_j^W \left[1 - \frac{1}{2} b_S \, am_j^W - \bar{b}_S \, a \, \text{Tr}(M) + \mathcal{O}(a^2) \right] + \ldots \qquad (2.205)$$

$$m_j^{\text{AWI}} = \frac{Z_A}{Z_P} m_j^{\text{PCAC}} \left[1 + (b_A - b_P)am_j^W + (\bar{b}_A - \bar{b}_P) \, a \, \text{Tr}(M) + \mathcal{O}(a^2) \right], \qquad (2.206)$$

where M is the flavour diagonal quark mass matrix and the dots in (2.205) denote terms of higher orders in $\text{Tr}(M)^k$ and $\text{Tr}(M^k)$. Furthermore, Z_X are the flavour *non-singlet* renormalization constants and $b_X = 1 + \mathcal{O}(\alpha_s)$, $\bar{b}_X = \mathcal{O}(\alpha_s^2)$, $c_A = \mathcal{O}(\alpha_s)$ denote N_f-dependent improvement coefficients. The quantities $\bar{b}_X$ correct for the appearance of non-vanishing flavour singlet diagrams and hence start off at two-loop order (the external quark line is connected to a quark loop containing the operator insertion by two gluon lines, cf. figure 2.6). Finally, $m_j^W = m_j^{(\text{bare})} - m^{(\text{crit})}$, where $m^{(\text{crit})}$ is the N_f=3 critical mass (i.e. in the *unitary direction*).

   When comparing the simplified expressions (2.202) and (2.203) to (2.205) and (2.206), note the additional term proportional to $\text{Tr}(M) = \sum_f m_f^W$. It renders the renormalized m_j being dependent on all other quark masses m_k. Evidently, this term comes from quark loops in the functional determinant and a perturbative expansion shows that the related improvement coefficients $\bar{b}_X$ start out at $\mathcal{O}(\alpha_s^2)$. This means that they enter through two-loop effects, i.e. a gluon-loop which attaches quark-loop to the external quark (cf. figure 2.6). Taking the differences of two VWI masses and the ratio of two AWI masses yields

$$m_j^{\text{VWI}} - m_k^{\text{VWI}} = \frac{1}{Z_S}(m_j^W - m_k^W) \left[1 - \frac{1}{2} b_S \, a(m_j^W + m_k^W) - \bar{b}_S \, a \, \text{Tr}(M) + \mathcal{O}(a^2) \right], \quad (2.207)$$

$$\frac{m_j^{\text{AWI}}}{m_k^{\text{AWI}}} = \frac{m_j^{\text{PCAC}}}{m_k^{\text{PCAC}}} \left[1 - \frac{1}{2} \, b_S \, a(m_j^W - m_k^W) - \bar{b}_S \, a \, \text{Tr}(M) + \mathcal{O}(a^2) \right]. \qquad (2.208)$$

Considering the N_f=2+1 flavour case, with d and r as defined before, gives

$$am_s^{\text{VWI}} - am_{ud}^{\text{VWI}} = \frac{d}{Z_S} \left[1 - \frac{1}{2} b_S \, a(m_s^W + m_{ud}^W) - \bar{b}_S \, a(m_S^W + 2m_{ud}^W) + \mathcal{O}(a^2) \right], \quad (2.209)$$

$$\frac{am_s^{\text{AWI}}}{am_{ud}^{\text{AWI}}} = r \left[1 + (b_A - b_P)a(m_s^W - m_{ud}^W) + \mathcal{O}(a^2) \right]. \qquad (2.210)$$

(a) non-singlet and singlet contribution   (b) singlet contribution only
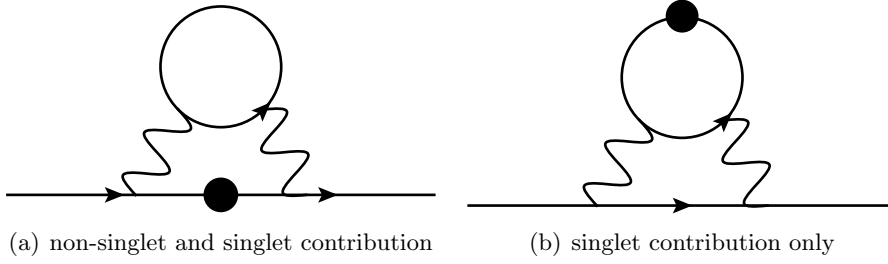
Figure 2.6.: Diagrams giving rise to two-loop contributions to the mass renormalization for non-singlet and singlet parts (a) and singlet part only (b). The scalar insertion is denoted by the black dot. The latter diagramm contains 5 gamma matrices (2 from vertices and 3 from quark propagators) and is therefore zero in the continuum and chiral limit. However, this is not the case for Wilson or clover fermions.

We can further write

$$am_s^W + am_{ud}^W = (am_s^W - am_{ud}^W)\frac{m_s^W/m_{ud}^W + 1}{m_s^W/m_{ud}^W - 1} \simeq d\frac{r+1}{r-1}, \tag{2.211}$$

$$am_s^W + 2am_{ud}^W = (am_s^W - am_{ud}^W)\frac{m_s^W/m_{ud}^W + 2}{m_s^W/m_{ud}^W - 1} \simeq d\frac{r+2}{r-1}, \tag{2.212}$$

where the last equality is only valid up to $\mathcal{O}(a^2)$. Accordingly, we can express the differences of the VWI and ratios of AWI masses through d and r as

$$am_s^{\text{VWI}} - am_{ud}^{\text{VWI}} = \frac{1}{Z_S}d^{\text{imp}}, \quad \frac{m_s^{\text{AWI}}}{m_{ud}^{\text{AWI}}} = r^{\text{imp}}, \tag{2.213}$$

where

$$d^{\text{imp}} = d\left[1 - \frac{1}{2}b_S\,d\frac{r+1}{r-1} - \bar{b}_S\,d\frac{r+2}{r-1} + \mathcal{O}(a^2)\right], \tag{2.214}$$

$$r^{\text{imp}} = r\left[1 + (b_A - b_P)d + \mathcal{O}(a^2)\right]. \tag{2.215}$$

Note that when tree-level improvement is used, all sub-leading terms in the brackets vanish except for the one proportional to b_S. Thus, using d^{imp} and r^{imp} instead of d and r in (2.204) allows us to compute the renormalized quark masses m_s and m_{ud} using only the differences d and ratios r, avoiding the use of the pseudoscalar renormalization constant Z_P and critical mass $m^{(\text{crit})}$.

2.3.8. Matrix elements of four-fermion operators on the lattice

In section 2.2.6, I discussed how standard model CP violation in the neutral kaon system is related to the kaon bag parameter B_K defined in formula (2.102). In this section I show how

B_K can be computed on the lattice: consider the 3-point function[64]

$$C_3(\tau, t_1, t_0) = \left(\frac{a}{L}\right)^3 \sum_{\mathbf{x}_1, \mathbf{x}_0, \mathbf{x}} \langle (\bar{s}\gamma_5 d)(t_1, \mathbf{x}_1)\, O^{\Delta S=2}(\tau, \mathbf{x})\, (\bar{s}\gamma_5 d)(t_0, \mathbf{x}_0) \rangle, \qquad (2.216)$$

where the sums over $\mathbf{x}_1, \mathbf{x}_2$ project the external kaon states onto zero momenta and the sum over $\mathbf{x}$ is a volume average for increasing statistics. We will discuss below, how these sums are performed efficiently in practice.

Since the operator $(\bar{s}\gamma_5 d)(t)$ is a pion interpolating function, expression (2.216) has the following interpretation: for sufficiently large separations of τ, t_1 and t_0, an anti-kaon is created at $t = t_0$, converted into a kaon by $O^{\Delta S=2}$ at $t = \tau$ and annihilated at $t = t_1$. In this limit, the overlap of $(\bar{s}\gamma_5 d)(t)$ with the kaon ground state is maximal and thus

$$C_3(\tau, t_1, t_0) \xrightarrow{t_0 \ll \tau \ll t_1} \langle 0|\bar{s}\gamma_5 d(t_1)|K^0\rangle \langle \bar{K}^0|\bar{s}\gamma_5 d(t_0)|0\rangle \left(\frac{a}{L}\right)^3 \sum_{\mathbf{x}} \langle K^0|O^{\Delta S=2}(\tau, \mathbf{x})|\bar{K}^0\rangle$$

$$= \frac{e^{-M_K(t_1-t_0)}}{4M_K^2} \langle 0|\bar{s}\gamma_5 d(0)|K^0\rangle \langle \bar{K}^0|\bar{s}\gamma_5 d(0)|0\rangle \left(\frac{a}{L}\right)^3 \sum_{\mathbf{x}} \langle K^0|O^{\Delta S=2}(0, \mathbf{x})|\bar{K}^0\rangle.$$
$$(2.217)$$

Note that the r.h.s. is τ-independent since $M_{K^0} = M_{\bar{K}^0} \equiv M_K$. This expression is proportional to the desired matrix element $\langle K^0|O^{\Delta S=2}(0)|\bar{K}^0\rangle$, but still contains additional factors. These can in principle be computed on the lattice by studying kaon-kaon correlation functions. However, since the vacuum overlaps $\langle \bar{K}^0|\bar{s}\gamma_5 d(0)|0\rangle$ and $\langle 0|\bar{s}\gamma_5 d(0)|K^0\rangle$ are multiplied by an exponential, it is very difficult to extract it reliably. Additionally, a correct normalization of all quantities involved is necessary. This explains why we use the ratio defined in equation (2.102) for extracting B_K. In that ratio, many statistical and systematic effects cancel. Consider the correlation function

$$C_{2\,\mu}(\tau, t) = \left(\frac{a}{L}\right)^3 \sum_{\mathbf{x}_1, \mathbf{x}} \langle (\bar{s}\gamma_5 d)(t, \mathbf{x}_1)(\bar{d}\gamma_\mu \gamma_5 s)(\tau, \mathbf{x}) \rangle. \qquad (2.218)$$

For large separations $t - \tau$ we can insert intermediate kaon states and obtain

$$C_{2\,\mu}(\tau, t) \rightarrow \frac{e^{-M_K(t-\tau)}}{2M_K} \langle 0|\bar{s}\gamma_5 d(0)|K^0\rangle \left(\frac{a}{L}\right)^3 \sum_{\mathbf{x}} \langle K^0|\bar{d}\gamma_\mu \gamma_5 s(0, \mathbf{x})|0\rangle \qquad (2.219)$$

Analogously, we define

$$\bar{C}_{2\,\mu}(\tau, t) = \left(\frac{a}{L}\right)^3 \sum_{\mathbf{x}_1, \mathbf{x}} \langle (\bar{d}\gamma_\mu \gamma_5 s)(\tau, \mathbf{x})(\bar{s}\gamma_5 d)(t, \mathbf{x}_1) \rangle, \qquad (2.220)$$

which yields

$$\bar{C}_{2\,\mu}(\tau, t) \rightarrow \frac{e^{-M_K(\tau-t)}}{2M_K} \left(\frac{a}{L}\right)^3 \langle \bar{K}^0|\bar{s}\gamma_5 d(0)|0\rangle \sum_{\mathbf{x}} \langle 0|\bar{d}\gamma_\mu \gamma_5 s(0, \mathbf{x})|\bar{K}^0\rangle. \qquad (2.221)$$

---

[64]See e.g. [Lellouch, 2011, p. 32ff] for more details.

Combining everything gives

$$\frac{C_3(\tau, t_1, t_0)}{C_{2\mu}(\tau, t_1)\bar{C}_2^\mu(\tau, t_0)} \to \left(\frac{L}{a}\right)^3 \frac{\sum_{\mathbf{x}}\langle K^0|O^{\Delta S=2}(0, \mathbf{x})|\bar{K}^0\rangle}{\sum_{\mathbf{x}_1}\langle K^0|\bar{d}\gamma_\mu\gamma_5 s(0, \mathbf{x}_1)|0\rangle \sum_{\mathbf{x}_2}\langle 0|\bar{d}\gamma^\mu\gamma_5 s(0, \mathbf{x}_2)|\bar{K}^0\rangle} \quad (2.222)$$

$$= B_K(a), \quad (2.223)$$

where the argument a emphasizes that the regularization scheme is the lattice scheme. The matching to a continuum scheme can be achieved by using the Rome-Southampton method as discussed in part 2.4.2. Since we are using chirality breaking Wilson fermions, $O^{\Delta S=2}$ mixes with other dimension six operators. Thus, in order to obtain B_K on the lattice, we have to measure the matrix elements of all five mixing operators O_k (cf. section 2.4.2 for details). Thus, we have to compute[65]

$$\tilde{Q}_k(\tau) = \frac{C_{3\,k}(\tau, T/2, 0)}{C_{2\mu}(\tau, T/2)\bar{C}_2^\mu(\tau, 0)}, \quad (2.224)$$

where

$$C_{3\,k}(\tau, t_1, t_0) = \left(\frac{a}{L}\right)^3 \sum_{\mathbf{x}_1, \mathbf{x}_0, \mathbf{x}} \langle (\bar{s}\gamma_5 d)(t_1, \mathbf{x}_1)\, O_k(\tau, \mathbf{x})\, (\bar{s}\gamma_5 d)(t_0, \mathbf{x}_0)\rangle. \quad (2.225)$$

Note that this ratio is automatically tree-level, on-shell $\mathcal{O}(a)$ improved, since all improvement factors cancel. The r.h.s. of (2.224) can be measured on the lattice by performing the contractions displayed in figure 2.7. The factor of two in the numerator arises from diagrammatic symmetries, and the two addends are called trace-disconnected and trace-connected respectively. As the second addend involves only a single trace, it is suppressed by a factor of $1/N_c$ with respect to the first one in large N_c theory. Because of the same sign of both addends, a partial cancellation is at work which increases the statistical error. The volume averages in (2.224) are obtained by using random wall sources at $t = 0$ and $t = T/2$, i.e. at the kaon insertions (cf. appendix E.3 for details on random wall sources). When using two different random sources per configuration, we end up with four Dirac operator inversions: one for each source and mass m_{ud} and m_s. Increasing the number of random sources by a factor of N^2 would reduce the statistical error by a factor of N. However, since measurements on same configurations are correlated, it is often better to use more configurations instead. Of course, the situation changes on fine expensive lattices with small pion masses. The CPU costs for obtaining a factor of two in statistical accuracy can be much lower when using multiple random sources instead of enlarging the ensemble.

The average over the spatial positions of the O_k insertion is exact. Note the computational difference between the trace-disconnected term in the numerator and the VSA terms in the denominator: for the former, one has to first compute the product of traces at each operator insertion point $\mathbf{x}$ and then perform the average, whereas the volume average is carried out before multiplying the traces for the latter. Of course, the average over the configurations is always implied.

In the limit of large separations, all $\tilde{Q}_k(\tau)$ are independent on τ. Thus, once the $\tilde{Q}_k(\tau)$ are

---

[65]We denote them by $\tilde{Q}_k$ instead of Q_k as it is done in part 2.4.2, because these quantities differ by the denominator given by the VSA of B_K. However, the renormalization pattern does not change, since the same denominator is used for all five $\tilde{Q}_k$.
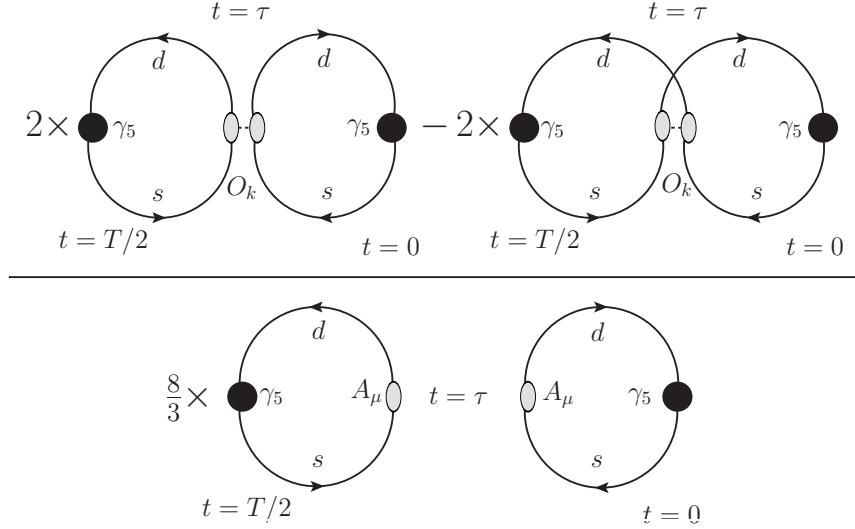
Figure 2.7.: Diagrammatic description of contractions necessary to compute the matrix elements in (2.224). The factor of two in the numerator is a symmetry factor, because there are two possibilities of contracting the external quark lines with the kaon states. The first term in the numerator is the trace-disconnected and the second one the trace-connected part. The relative minus sign arises from different numbers of fermion field anti-commutations. Large N_c theory predicts that the trace-disconnected contribution is enhanced by a factor of N_c with respect to the trace-connected contribution. In practice, both contributions have the same sign so that a partial cancellation is at work.

obtained, a constant fit or average over the region where this function is flat in τ yields the desired matrix elements $\tilde{Q}_k$. Using the measured vector $(\tilde{Q}_1, \tilde{Q}_2, \tilde{Q}_3, \tilde{Q}_4, \tilde{Q}_5)$ together with non-perturbative data obtained in the RI scheme (cf. part 2.4.2), converts the cutoff dependent B_K into a continuum scheme, allowing for comparison with experimental quark flavour mixing data.

2.4. Non-perturbative renormalization

In QCD, observables related to Lagrangian parameters or effective operators usually require renormalization. On the lattice as well as in the continuum, a regulator is applied to the calculations in order to make the results finite, but the way how divergences are subtracted differ. The lattice acts as a regulator since it introduces a momentum cutoff π/a. This means that a renormalized operator is matched to the bare one via

$$\mathcal{O}^{\mathrm{ren}}(1/a) = Z_{\mathcal{O}}^{\mathrm{lat}}(1/a)\,\mathcal{O}^{\mathrm{bare}}. \tag{2.226}$$

In the continuum, the modified-minimal-subtraction-scheme ($\overline{\mathrm{MS}}$-scheme) is used in most perturbative calculations. In that scheme, $1/\epsilon$ poles coming from dimensional regularization

along with the constant $\ln 4\pi + \gamma_E$ are subtracted. This allows for matching the bare operator to the renormalized one via

$$\mathcal{O}^{\text{ren}}(\mu) = Z_{\mathcal{O}}^{\overline{\text{MS}}}(\mu) \, \mathcal{O}^{\text{bare}}. \tag{2.227}$$

For $\mu \sim a^{-1}$, both schemes differ by a multiplicative, finite renormalization, i.e. a *conversion* (or *matching*) factor. This means that matrix elements of this operator can be immediately matched [cf. DeTar and DeGrand, 2006, p. 249]

$$\langle \alpha | \mathcal{O}(\mu) | \beta \rangle = Z_{\mathcal{O}}(\mu, a) \, \langle \alpha | \mathcal{O}(1/a) | \beta \rangle, \tag{2.228}$$

where $Z_{\mathcal{O}}(\mu, a) = Z_{\mathcal{O}}^{\overline{\text{MS}}}(\mu)/Z_{\mathcal{O}}^{\text{lat}}(1/a)$. This *operator matching* decouples the renormalization scale μ from the lattice cutoff π/a. It allows for comparing lattice results in continuum perturbation schemes and helps providing input for phenomenological calculations.

Renormalization constants of lattice operators can either be computed perturbatively or non-perturbatively. The advantage of perturbative calculations is that they do not require large amounts of CPU time. The disadvantage is that they can be very difficult if one uses complicated actions such as our 2 HEX approach. Furthermore, the perturbative series has to be truncated at a finite order and it is mostly difficult to estimate the uncertainties coming from higher order corrections.[66] This problem is solved by the non-perturbative renormalization method, which is computationally demanding on the other hand. Furthermore, a non-perturbative calculation is sensitive to non-perturbative physics, possibly rendering the matching to continuum perturbation theory difficult. A well-known example for this is the pion pole [Martinelli et al., 1995] appearing in the infrared region of the pseudoscalar renormalization constant Z_P, if it is calculated at exceptional momenta[67]. This pole is a non-perturbative Goldstone boson effect, since the pseudoscalar operator $\bar{\psi}\gamma_5\psi$ has a strong overlap with the pion wave function.

In our calculations, we use non-perturbative renormalization in the *RI scheme* together with Ward identity methods for calculating bilinear and four-fermion operator renormalization constants on the lattice.

2.4.1. Three-point function WI method

Ward identities provide an elegant way for computing the vector current renormalization Z_V non-perturbatively up to a high precision.[68] Since Z_V is scheme independent, it can be used to calculate Z_q^{RI} by computing $(Z_q/Z_V)^{\text{RI}} Z_V$, where the ratio $(Z_q/Z_V)^{\text{RI}}$ is obtained from the RI formalism (cf. section 2.4.2). The vector-current WI is related to the global $U(1)_V$ or $U(1)_{f_1} \times \ldots \times U(1)_{f_2}$ symmetries[69]

$$\psi \to e^{i\alpha_\psi}\psi, \quad \bar{\psi} \to \bar{\psi}e^{-i\alpha_\psi}, \tag{2.229}$$

---

[66]In unimproved thin-link lattice perturbation theory, these corrections tend to be rather large. However, this issue is mostly resolved if fat-links or tadpole resummation are used [cf. Capitani, 2003, and references therein].

[67]i.e. momentum transfer $q^2 = 0$

[68]Read [Bakeyev et al., 2004] or follow the the ideas of Martinelli et al. [1991, 1992].

[69]The $U(1)_V$ symmetry is related to baryon number conservation and the $U(1)_{f_1} \times \ldots \times U(1)_{f_2}$ symmetry implies that there are no flavour changing neutral currents in QCD.

which are also satisfied for non-chiral fermion formulations such as the Wilson Dirac operator. By applying Noether's theorem, this global symmetry leads to the conserved current

$$J_\mu^{(\psi)}\left(x + \frac{\hat{\mu}}{2}\right) = \frac{1}{2}\left[\bar{\psi}(x)(\gamma_\mu - 1)U_\mu(x)\psi(x + \hat{\mu}) - \bar{\psi}(x + \hat{\mu})(\gamma_\mu + 1)U_\mu^\dagger(x)\psi(x)\right]. \quad (2.230)$$

Due to the appearance of gauge fields, mediating between quarks on neighbouring sites, this expression is sometimes called *point-split vector current*. The WI related to this current is given by

$$\left\langle \Omega(x)\Delta_\mu J_\mu^{(\psi)}\left(x + \frac{\hat{\mu}}{2}\right)\right\rangle = \left\langle \frac{\delta\Omega(x)}{\delta\psi(x)}\psi(x)\right\rangle + \left\langle \bar{\psi}(x)\frac{\delta\Omega(x)}{\delta\bar{\psi}(x)}\right\rangle, \quad (2.231)$$

where $\Delta_\mu f(x) = (f(x) - f(x - \hat{\mu}))/2$ is the backward derivative and the expectation value is meant to be taken over all gauge configurations U and fermion fields ψ. Obviously, the r.h.s. of (2.231) is equal to zero if $\Omega(x)$ contains neither $\psi(x)$ nor $\bar{\psi}(x)$. This not only true on average, but on every single configuration. Effectively, the r.h.s. counts the quark and anti-quark content of Ω at x. Let us now consider the ratio function

$$\zeta(\tau) = \frac{\langle \bar{P}(T/2)O(\tau)P(0)\rangle}{\langle \bar{P}(T/2)P(0)\rangle}, \quad (2.232)$$

where we choose $\Omega(t) = P(t) = \sum_\mathbf{x} \bar{\psi}(\mathbf{x}, t)\gamma_5\psi(\mathbf{x}, t)$ instead of baryonic operators as in [Bakeyev et al., 2004]. This function has a jump discontinuity at $\tau = T/2$, where the height of the jump is exactly equal to 1 in case of $O(\tau) = J_4(\tau)$. When inserting the non-conserved vector current $V_4(\tau) = \sum_\mathbf{x} \bar{\psi}(\mathbf{x}, \tau)\gamma_4\psi(\mathbf{x}, \tau)$, the height of the jump is proportional to Z_V. More precisely, we can write

$$Z_V(1 + b_V \, am^W) = \frac{1}{|\zeta(t_1) - \zeta(t_2)|} \quad \text{for} \quad 0 < t_1 < T/2 < t_2 < T, \quad (2.233)$$

where $(1 + b_V \, am^W)$ is an on-shell $\mathcal{O}(a)$ tree-level improvement factor.[70]

In order to compute (2.232) on the lattice, the contractions displayed in figure 2.8 have to be carried out. By choosing $\Omega(t) = \langle \bar{P}(t)P(0)\rangle$, the r.h.s. of (2.231) becomes zero and the disconnected contribution from figure 2.8 will only yield an additive normalization. Therefore, it does not contribute to the discontinuity so that we can omit the difficult calculation of the disconnected part and remain with the (numerically inexpensive) connected parts. This computation can be simply done by using point propagators, but it turns out that statistical noise can be efficiently reduced if $U(1)$ random wall sources are used (cf. appendix E.3). These are inserted at $t = 0$ and $t = T/2$, allowing to compute the spatial average at $t = \tau$ exactly.

The major advantage of the non-perturbative WI method for renormalization is the avoidance of calculating Z_q^{RI} directly in the RI scheme as discussed in 2.4.2. The value for Z_V obtained by this method is far more precise compared to the quantity $(Z_V/Z_q)^{\mathrm{RI}}Z_q^{\mathrm{RI}}$ obtained from RI computations (see below). The reason for this is, that while relations in the RI scheme are only valid for propagator averages because of the broken translation invariance of single configuration propagators, the WI Z_V relations are in principle valid on every single

---

[70]The relation (2.233) can be immediately obtained by choosing $\mu = 0$ in (2.231) and integrating over t.
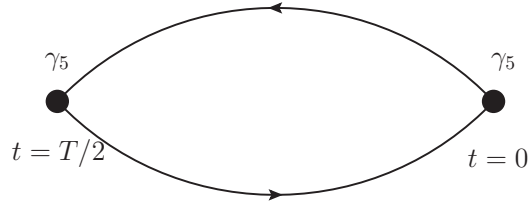
(a) Diagrammatic description of the $\langle \bar{P}(T/2)P(0)\rangle$ correlator.
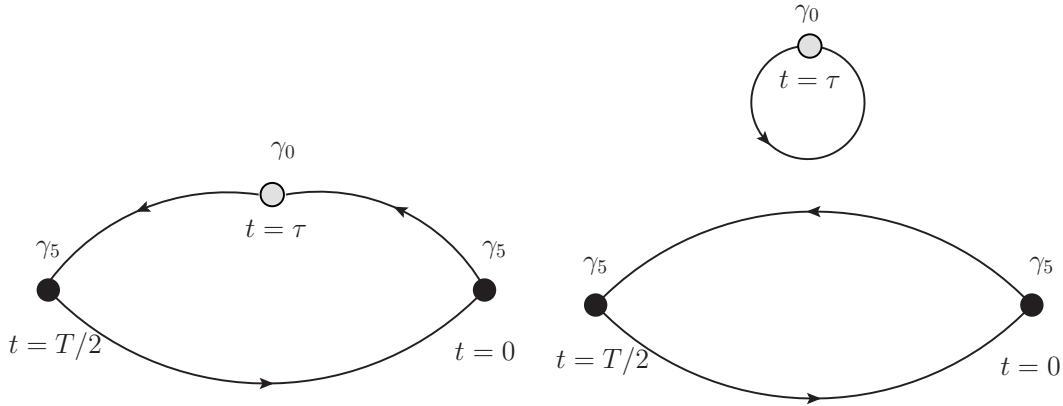
(b) Diagrammatic description of the $\langle \bar{P}(T/2)O(\tau)P(0)\rangle$ correlator, connected and disconnected parts.

Figure 2.8.: Quark-line contractions necessary to compute (2.232).

configuration. This results in a much better noise suppression compared to RI quantities.

2.4.2. Regularization independent scheme

The *regularization independent (RI) scheme* (more precisely called *RI/MOM-scheme*, cf. [Martinelli et al., 1995]) provides a complete framework for calculating renormalization constants non-perturbatively on the lattice and matching them perturbatively to a continuum scheme such as $\overline{\text{MS}}$. Additionally, many perturbative calculations in this scheme have already been carried out so that the lattice data can be immediately matched to the perturbative results for checking their agreement or identifying non-perturbative effects.

In our studies, we need the renormalization factors of two- and four-fermion-operators: the former are needed for quark mass as well as the axial current renormalization, whereas the latter are necessary for renormalizing $O^{\Delta S=2}$ (cf. expression (2.101)).

Renormalization of quark bilinears

The principles of the RI scheme are simple: the quark and gluon amputated Greens functions are computed in a smooth gauge[71], where a large Euclidian momentum p^2 is assigned to all external quark-lines. Consider for example the general bilinear quark operator

$$O_\Gamma(x) = \bar{\psi}(x)\Gamma\psi(x), \tag{2.234}$$

where Γ can be a combination of Dirac matrices or a more complicated structure. Let us denote the off-shell single particle momentum eigenstates by $|p\rangle$. Then, the momentum space matrix elements of O_Γ in the interacting theory can be related to the matrix elements of O_Γ in the free-field theory (i.e. the bare operator) via

$$Z_\Gamma^{\mathrm{RI}}(\mu) \, \langle p|O|p\rangle_{p^2=\mu^2} = \langle p|O|p\rangle_{\mathrm{bare}}, \tag{2.235}$$

or equivalently

$$Z_\Gamma^{\mathrm{RI}}(\mu) \, \frac{1}{12} \, \mathrm{Tr}\left[\langle p|O|p\rangle_{p^2=\mu^2} \, \langle p|O|p\rangle_{\mathrm{bare}}^{-1}\right] = 1. \tag{2.236}$$

Hence, the second factor inside the trace is a projector I will denote by P_Γ. The first factor inside the trace is the amputated Greens function $\Lambda_\Gamma(p)$ modulus the wave function renormalization Z_q^{RI}. This yields[72]

$$\frac{Z_\Gamma^{\mathrm{RI}}(\mu)}{Z_q^{\mathrm{RI}}(\mu)} \, \frac{1}{12} \, \mathrm{Tr}\left[\Lambda_\Gamma(p)\,\mathrm{P}_\Gamma\right]_{p^2=\mu^2} = 1. \tag{2.237}$$

This renormalization condition states that the renormalized vertex function $\Lambda_\Gamma(p)$ at $p^2 = \mu^2$ is set to its tree-level value (cf. figure 2.9).

Computing amputated Greens functions on the lattice is a two-step process: first, one has to
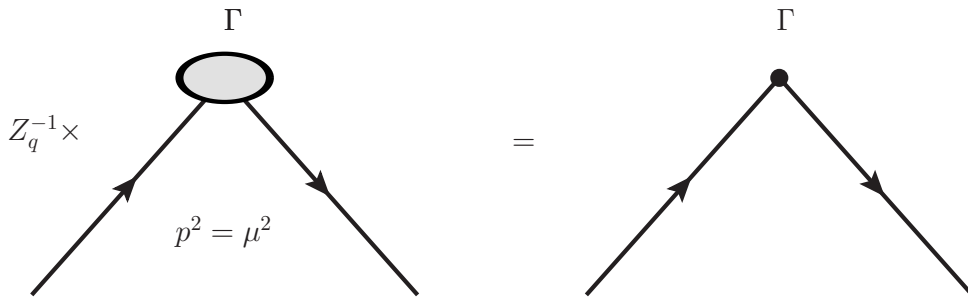
Figure 2.9.: Depiction of the renormalization conditions in formula (2.237).

compute the non-amputated Greens function $G_\Gamma(p)$ and propagators $S(p)$. After performing

---

[71] We use the Landau gauge, cf. appendix C.

[72] The definition of Z_q^{RI} in this text may differ from the wave function renormalization constants in other literature by a simple inversion [cf. e.g. DeTar and DeGrand, 2006, p. 255]. Within this work I stick to the convention of Martinelli et al. [1995].

ensemble averages over each of those, the amputation can be performed, i.e.

$$\Lambda_\Gamma(p) = S^{-1}(p)\, G_\Gamma(p)\, \gamma_5 (S^{-1}(p))^\dagger \gamma_5, \tag{2.238}$$

with

$$S(p) = \frac{1}{N} \sum_{i=1}^{N} S_i(p|0) \tag{2.239}$$

and

$$G_\Gamma(p) = \frac{1}{N} \sum_{i=1}^{N} S_i(p|0)\Gamma\, \gamma_5 S_i^\dagger(p|0)\gamma_5, \tag{2.240}$$

where the sums run over the ensemble. The single-configuration-quark-propagator $S_k(p|0)$ is defined being the Fourier transform of the coordinate space propagator

$$S_k(p|0) = \int \mathrm{d}^4 x\, e^{-ipx}\, S_k(x|0) \tag{2.241}$$

and is not translationally invariant. This is only true for the average (2.239) in the limit of large statistics. Therefore, it is possible to improve translational invariance by using more than one source position x_0 per configuration, i.e.

$$S_k(p) = \frac{1}{N} \sum_{k=1}^{N} \frac{1}{\#X} \sum_{x_0 \in X} \int \mathrm{d}^4 x\, e^{-ip(x-x_0)}\, S_k(x|x_0), \tag{2.242}$$

with $X = \{x_{0,1}, x_{0,2}, \ldots, x_{0,M}\}$ and where formula (2.240) has to be modified accordingly. In addition, it is suitable to improve the non-perturbatively calculated quark propagators by subtracting an $\mathcal{O}(a)$ contact term (cf. section 2.4.3). Mathematically this correction amounts to replacing the unimproved $S_k(x|0)$ by the improved $\bar{S}_k(x|0)$ in (2.242) and (2.240).

It is straightforward to calculate $Z_A/Z_q, Z_P/Z_q, Z_S/Z_q$ as well as Z_V/Z_q and Z_T/Z_q at a given scale μ in the RI scheme.[73] The scale μ should be chosen such that

$$\frac{1}{L} \ll \Lambda_{\mathrm{QCD}} \ll \mu \ll \pi/a, \tag{2.243}$$

which is sometimes referred to as *window condition*. The dispersion relation of many lattice Dirac operators significantly deviates from the linear dispersion relation of the continuum Dirac operator D at large momenta. Therefore, it is better to choose $\mu \leq \pi/(2a)$ and I will refer to this conservative choice for the upper bound on μ as *strict window condition*.[74] the wave function renormalization Z_q^{RI} is also needed. In principle it can be calculated using the RI relation

$$Z_q^{\mathrm{RI}} = \frac{-i}{12}\, \mathrm{Tr} \left[\frac{\partial S^{-1}(p)}{\partial \slashed{p}} \right]. \tag{2.244}$$

However, it is difficult to extract derivatives on the lattice precisely. As a replacement, one can use the so called RI$'$ prescription, which projects the quark propagator against the free-field

---

[73]See appendix A for definitions of the operators S, P, T, V, and A.
[74]This renders the extraction of renormalization factors on coarser lattices difficult. A solution to this problem is provided in section 2.4.3.

one:

$$\frac{1}{Z_q^{\mathrm{RI}'}} = \frac{1}{12} \operatorname{Tr} \left[S(p)\, S_0^{-1}(p) \right]. \tag{2.245}$$

This definition is equivalent to Z_q^{RI} at NLO perturbation theory. In our studies we apply a hybrid approach: we calculate Z_V using the three point function method explained in section 2.4.1 and use it together with the ratio $(Z_V/Z_q)^{\mathrm{RI}}$ in order to calculate Z_q^{RI}.

Note that perturbative calculations are usually done in a massless scheme. In contrast to that, all propagators computed on the lattice have to be infrared regularized by a finite mass. In practice, this means that one has to compute the renormalization constants at different values for the quark mass and then perform a chiral extrapolation to the massless scheme. This can be done in several ways, where some of them are described in 3.2.2, 4.2 and 4.3.

Renormalization of four-fermion operators

In contrast to the bilinear case, the renormalization of four-fermion operators is in general much more involved. The reason for this is, that the considered dimension six operators mix with other dimension six operators under renormalization. The RI renormalization prescription for $\Delta S = 2$ operators has been worked out with care in [Donini et al., 1999]. I give an overview over this work in this section, but omit some of the details.

The idea is to compute physical amplitudes such as

$$A_{\beta \to \alpha} = C_W(\mu)\, Z_O(\mu, a)\, \langle \alpha | O(1/a) | \beta \rangle, \tag{2.246}$$

where C_W is a Wilson coefficient in the corresponding OPE, $\langle \alpha | O(1/a) | \beta \rangle$ the corresponding matrix element of the bare lattice operator O and Z_O its renormalization factor. For example, in case of neutral kaon mixing, we are interested in the matrix element $\langle K_0 | O^{\Delta S=2}(\mu) | \bar{K}_0 \rangle$ (see (2.102) in section 2.2.6). The operator inducing this mixing (cf. 2.3.8) can be expressed in the basis[75]

$$\begin{aligned} &O_{VV}, O_{AA}, O_{SS}, O_{PP}, O_{TT}, \\ &O_{VA}, O_{AV}, O_{SP}, O_{PS}, O_{T\tilde{T}}, \end{aligned} \tag{2.247}$$

where

$$O_{\Gamma^{(1)}\Gamma^{(2)}} = (\bar{\psi}_1 \Gamma^{(1)} \psi_2)(\bar{\psi}_3 \Gamma^{(2)} \psi_4), \tag{2.248}$$

and the ψ_i represent the external fermion lines. The basis (2.247) is not the most optimal choice: it can be simplified by considering discrete symmetries such as Fierz transformation, i.e. interchanging flavour $2 \leftrightarrow 4$, parity transformation, charge conjugation as well as the flavour switching symmetries $1 \leftrightarrow 2, 3 \leftrightarrow 4$ and $1 \leftrightarrow 4, 2 \leftrightarrow 3$. This basis decomposes into subgroups, where no mixing occurs between them. Furthermore, these operators do not mix with lower-dimensional operators since those cannot have a four-flavour content. Using this

---

[75]Note that 'kaon mixing' should not be confused with 'operator mixing'. The first is a physical process and the second a technical subtlety, arising when computing renormalization constants of effective four-fermion operators.

information, we can define two sets of basis operators as described in table 2.2.[76] We use the

Parity even	Parity odd
$O_1^\pm = O_{[VV+AA]}^\pm$	$\mathcal{O}_1^\pm = O_{[VA+AV]}^\pm$
$O_2^\pm = O_{[VV-AA]}^\pm$	$\mathcal{O}_2^\pm = O_{[VA-AV]}^\pm$
$O_3^\pm = O_{[SS-PP]}^\pm$	$\mathcal{O}_3^\pm = -O_{[SP-PS]}^\pm$
$O_4^\pm = O_{[SS+PP]}^\pm$	$\mathcal{O}_4^\pm = O_{[SP+PS]}^\pm$
$O_5^\pm = O_{TT}^\pm$	$\mathcal{O}_5^\pm = O_{T\tilde{T}}^\pm$

Table 2.2.: Decomposed basis of four-fermion operators according to their chiral properties.
The notation $O^\pm$ is explained in (2.249) and (2.250).

notation

$$O_{XY}^\pm = \frac{1}{2}\left[O_{XY} \pm O_{XY}^F\right], \tag{2.249}$$

where O_{XY}^F it obtained from O_{XY} by interchanging the flavours 2 and 4. Furthermore we define

$$O_{[\Gamma^{(1)}\Gamma^{(2)}\pm\Gamma^{(2)}\Gamma^{(1)}]} = O_{\Gamma^{(1)}\Gamma^{(2)}} \pm O_{\Gamma^{(2)}\Gamma^{(1)}}. \tag{2.250}$$

Donini et al. [1999] show that operators containing colour rotations λ^a can be reduced to linear combinations of those defined in table 2.2. Since the two groups do not mix, the renormalization for the matrix elements of these operators is given by

$$Q_i^{\text{ren}\pm} = Z_{ij}^\pm Q_j^\pm, \quad \mathcal{Q}_i^{\text{ren}\pm} = \mathcal{Z}_{ij}^\pm \mathcal{Q}_j^\pm, \tag{2.251}$$

where Q_i and $\mathcal{Q}_i$ are matrix elements of O_i and $\mathcal{O}_i$ respectively, e.g. $Q_i = \langle\alpha|O_i|\beta\rangle$. Using more symmetry arguments, it can be shown that the renormalization matrix $\mathcal{Z}^\pm$ has to be block-diagonal. Thus

$$\begin{pmatrix} \mathcal{Q}_1^{\text{ren}} \\ \mathcal{Q}_2^{\text{ren}} \\ \mathcal{Q}_3^{\text{ren}} \\ \mathcal{Q}_4^{\text{ren}} \\ \mathcal{Q}_5^{\text{ren}} \end{pmatrix}^\pm = \begin{pmatrix} \mathcal{Z}_{11} & 0 & 0 & 0 & 0 \\ 0 & \mathcal{Z}_{22} & \mathcal{Z}_{23} & 0 & 0 \\ 0 & \mathcal{Z}_{32} & \mathcal{Z}_{33} & 0 & 0 \\ 0 & 0 & 0 & \mathcal{Z}_{44} & \mathcal{Z}_{45} \\ 0 & 0 & 0 & \mathcal{Z}_{54} & \mathcal{Z}_{55} \end{pmatrix}^\pm \begin{pmatrix} \mathcal{Q}_1 \\ \mathcal{Q}_2 \\ \mathcal{Q}_3 \\ \mathcal{Q}_4 \\ \mathcal{Q}_5 \end{pmatrix}^\pm. \tag{2.252}$$

Note that the operator mixing of $\mathcal{Q}_2, \mathcal{Q}_3$ as well as $\mathcal{Q}_4, \mathcal{Q}_5$ is physical because there is no symmetry of the QCD action forbidding this.

In case of the parity even (or *conserving*) operators, this is different. The selection rules for operator mixing within this subset are highly dependent on the presence of chiral symmetry. On the lattice, chiral symmetry is explicitly broken for many currently used fermion discretizations. Therefore, one cannot exclude mixing between any of the Q_i. If chiral symmetry is conserved, a mixing pattern analoguous to (2.252) applies. Donini et al. [1999] construct the full mixing pattern of the parity even operator basis by using the hypothetical intermediate *chirally regulated scheme* χ_{RS}, which assumes the use of a chirally symmetric regularization. Despite the hypothetical character of this scheme, it is very useful for lattice calculations since chiral symmetry is restored in the continuum limit. This means, that for (small) finite

---

[76]We denote the basis operators by $O_i, \mathcal{O}_i$ in contrast to $Q_i, \mathcal{Q}_i$ as done by Donini et al. [1999]. By $Q_i, \mathcal{Q}_i$ we denote matrix elements of these operators (see text).

lattice spacings, the mixing attributed to chiral symmetry breaking can be quantified by small contributions Δ_{ik}, vanishing logarithmically in a. Therefore, the full mixing pattern for the parity conserving operators is given by

$$
\begin{pmatrix} Q_1^{\text{ren}} \\ Q_2^{\text{ren}} \\ Q_3^{\text{ren}} \\ Q_4^{\text{ren}} \\ Q_5^{\text{ren}} \end{pmatrix}^{\pm} = \begin{pmatrix} Z_{11} & 0 & 0 & 0 & 0 \\ 0 & Z_{22} & Z_{23} & 0 & 0 \\ 0 & Z_{32} & Z_{33} & 0 & 0 \\ 0 & 0 & 0 & Z_{44} & Z_{45} \\ 0 & 0 & 0 & Z_{54} & Z_{55} \end{pmatrix}^{\pm} \begin{pmatrix} 1 & \Delta_{12} & \Delta_{13} & \Delta_{14} & \Delta_{15} \\ \Delta_{21} & 1 & 0 & \Delta_{24} & \Delta_{25} \\ \Delta_{31} & 0 & 1 & \Delta_{34} & \Delta_{35} \\ \Delta_{41} & \Delta_{42} & \Delta_{43} & 1 & 0 \\ \Delta_{51} & \Delta_{52} & \Delta_{53} & 0 & 1 \end{pmatrix}^{\pm} \begin{pmatrix} Q_1 \\ Q_2 \\ Q_3 \\ Q_4 \\ Q_5 \end{pmatrix}^{\pm} .
$$
(2.253)

The *unmixing matrix* $\mathbf{1} + \Delta^{\pm}$, with

$$
\Delta = \begin{pmatrix} 0 & \Delta_{12} & \Delta_{13} & \Delta_{14} & \Delta_{15} \\ \Delta_{21} & 0 & 0 & \Delta_{24} & \Delta_{25} \\ \Delta_{31} & 0 & 0 & \Delta_{34} & \Delta_{35} \\ \Delta_{41} & \Delta_{42} & \Delta_{43} & 0 & 0 \\ \Delta_{51} & \Delta_{52} & \Delta_{53} & 0 & 0 \end{pmatrix}^{\pm}
$$
(2.254)

can be interpreted as a change of basis from the lattice scheme into χ_{RS} in which the continuum mixing pattern can be applied. The entries of $\Delta^{\pm}$ are small if the fermion discretization used possesses a good chiral symmetry.

I will now explain how to compute the additive and multiplicative renormalization factors on the lattice. The approach is analogous to the bilinear case: we define the connected one-particle-irreducible Green's function via

$$
G_{\Gamma^{(1)}\Gamma^{(2)}}^{\pm}(x_1, x_2, x_3, x_4) = \langle \psi_1(x_1)\,\bar{\psi}_2(x_2) O_{\Gamma^{(1)}\Gamma^{(2)}}^{\pm}(0)\,\psi_3(x_3)\,\bar{\psi}_4(x_4) \rangle,
$$
(2.255)

where

$$
O_{\Gamma^{(1)}\Gamma^{(2)}}^{\pm}(0) = \frac{1}{2}\left[\bar{\psi}_1(0)\Gamma^{(1)}\psi_2(0)\,\bar{\psi}_3(0)\Gamma^{(2)}\psi_4(0) \pm \bar{\psi}_1(0)\Gamma^{(1)}\psi_4(0)\,\bar{\psi}_3(0)\Gamma^{(2)}\psi_2(0) \right].
$$
(2.256)

By contracting all fermion-fields with external sources we can write for the components of $G_{\Gamma^{(1)}\Gamma^{(2)}}^{\pm}$ in momentum space:

$$
\left[G_{\Gamma^{(1)}\Gamma^{(2)}}^{\pm}(p) \right]_{\alpha\beta\gamma\delta}^{ABCD} = \frac{1}{2}\left[\langle \Gamma^{(1)}(p)_{\alpha\beta}^{AB}\Gamma^{(2)}(p)_{\gamma\delta}^{CD} \rangle \mp \langle \Gamma^{(1)}(p)_{\alpha\delta}^{AD}\Gamma^{(2)}(p)_{\gamma\beta}^{CB} \rangle \right],
$$
(2.257)

where

$$
\Gamma^{(k)}(p)_{\alpha\beta}^{AB} = S(p|0)_{\alpha\rho}^{AR}\,\Gamma_{\rho\sigma}^{(k)}\left[\gamma_5 S^{\dagger}(p|0)\gamma_5\right]_{\sigma\beta}^{RB},
$$
(2.258)

and $S_k(p|0)$ as defined in (2.241). Note the sign-flip at the r.h.s. of (2.257), attributed to a net relative fermion anti-commutation.

In principle, the Greens functions of four-fermion operators are tensor products of two quark bilinears, where an additional Fierz transformation applied. The amputation is completely straightforward:

$$
\left[\Lambda_{\Gamma^{(1)}\Gamma^{(2)}}^{\pm}\right]_{\rho\sigma\eta\xi}^{RSTU} = S^{-1}(p)_{\rho\alpha}^{RA}\left[\gamma_5(S^{-1}(p))^{\dagger}\gamma_5\right]_{\beta\sigma}^{BS}\left[G_{\Gamma^{(1)}\Gamma^{(2)}}^{\pm}(p)\right]_{\alpha\beta\gamma\delta}^{ABCD} S^{-1}(p)_{\eta\gamma}^{TC}\left[\gamma_5(S^{-1}(p))^{\dagger}\gamma_5\right]_{\delta\xi}^{DU}.
$$
(2.259)

This high-rank tensor will be projected onto all possible Dirac structures. We define the projector

$$\mathrm{P}_{\Gamma^{(1)}\Gamma^{(2)}} = \mathrm{P}_{\Gamma^{(1)}} \otimes \mathrm{P}_{\Gamma^{(2)}}, \tag{2.260}$$

where its application to (2.259) is defined by

$$\mathrm{Tr}\,\mathrm{P}_{\Gamma^{(1)}\Gamma^{(2)}} \Lambda^{\pm}_{\Gamma^{(1)}\Gamma^{(2)}} = \left[\mathrm{P}_{\Gamma^{(1)}}\right]_{\sigma\rho} \left[\mathrm{P}_{\Gamma^{(2)}}\right]_{\xi\eta} \left[\Lambda^{\pm}_{\Gamma^{(1)}\Gamma^{(2)}}(p)\right]^{RRTT}_{\rho\sigma\eta\xi}. \tag{2.261}$$

The explicit form of the projectors belonging to the operators $O_k, \mathcal{O}_k$ can be worked out by considering the projection of the corresponding tree-level amputated Greens functions.[77] For applying the renormalization conditions, it is convenient to use projectors which fulfill the orthogonality relations

$$\mathrm{Tr}\,\mathrm{P}^{\pm}_i \Lambda^{(0)\pm}_k \;\; = \;\; \delta_{ik}, \tag{2.262}$$

$$\mathrm{Tr}\,\mathcal{P}^{\pm}_i \mathcal{L}^{(0)\pm}_k \;\; = \;\; \delta_{ik}, \tag{2.263}$$

where we denote the tree-level amputated Greens functions for the parity conserving and violating case by $\Lambda^{(0)\pm}_k, \mathcal{L}^{(0)\pm}_k$ respectively. Writing the Greens functions as 1×5 row vectors and the corresponding projectors as 5×1 column vectors, allows for using the matrix notation

$$\mathrm{P}^{\pm} \cdot \Lambda^{(0)\pm} = \mathbf{1}, \quad \mathcal{P}^{\pm} \cdot \mathcal{L}^{(0)\pm} = \mathbf{1}. \tag{2.264}$$

In case of the parity violating operators, the renormalized amputated Greens function is given by the row vector

$$\mathcal{L}^{\mathrm{ren}\pm}(p/\mu) = Z_q^{-2}(\mu a)\,\mathcal{L}^{\pm}(pa)\left(\mathcal{Z}^{\pm}(\mu a)\right)^t. \tag{2.265}$$

We rewrite the amputated Greens function $\mathcal{L}^{\pm}$ as a product of the bare one $\mathcal{L}^{(0)\pm}$ with a matrix $\mathcal{D}^{\pm}$, containing the dynamics of $\mathcal{L}^{\pm}$:

$$\mathcal{L}^{\pm} = \mathcal{L}^{(0)\pm}\,\mathcal{D}^{\pm}. \tag{2.266}$$

Using the relations (2.264) yields

$$\mathcal{D}^{\pm} = \mathcal{P}^{\pm} \cdot \mathcal{L}^{\pm}. \tag{2.267}$$

The matrix $\mathcal{Z}^{\pm}$ is determined by the RI renormalization conditions

$$\mathcal{P}^{\pm} \cdot \mathcal{L}^{\mathrm{ren}\pm}(p/\mu)\big|_{p^2=\mu^2} = \mathbf{1}. \tag{2.268}$$

Using this relation together with expressions (2.265) and (2.267), we obtain after some algebra

$$\mathcal{Z}^{\pm} = Z_q^2\big([\mathcal{D}^{\pm}]^t\big)^{-1}. \tag{2.269}$$

The wave function renormalization Z_q can be obtained the same way as in the bilinear case.

In case of parity conserving operators, the approach for calculating $Z^{\pm}$ has to be slightly modified, because the mixing attributed to chiral symmetry breaking has to be subtracted first. The mixing coefficients $\Delta^{\pm}_{ik}$ are momentum independent, since they can be computed by using the appropriate Ward identities. Hence, they are constant in p and should be sub-

---

[77] I omit this part here and just give the final forms in appendix A.

tracted before $Z^\pm$ can be determined as in the parity violating case. Analogous to (2.265) we can write

$$\Lambda^{\mathrm{ren}\pm}(p/\mu) = Z_q^{-2}(\mu a)\, \Lambda^\pm(pa)\, (\mathbf{1} + \Delta^\pm)^t \left(Z_\chi^\pm(\mu a)\right)^t, \tag{2.270}$$

where Z_χ is the renormalization matrix in the χ_{RS} scheme, hence the first factor at the r.h.s. of (2.253). With

$$\Lambda^\pm = \Lambda^{(0)\pm}\, D^\pm, \tag{2.271}$$

as well as

$$D^\pm = P^\pm \cdot \Lambda^\pm. \tag{2.272}$$

The mixing matrix $\Delta^\pm$ as well as the renormalization constants $Z_\chi^\pm$ can be obtained by applying the renormalization conditions

$$\mathrm{P}^\pm \cdot \Lambda^\pm(p/\mu)\big|_{p^2=\mu^2} = \mathbf{1} \tag{2.273}$$

and by combining them with the previous equations (2.270), (2.271) and (2.272). This yields

$$Z_q^{-2}\, D^\pm\, (\mathbf{1} + \Delta^\pm)^t\, (Z_\chi^\pm)^t = \mathbf{1}, \tag{2.274}$$

or, in index notation,

$$D_{kl}^\pm + \sum_{j=1}^{5} D_{kj}^\pm \Delta_{lj}^\pm = Z_q^2 (Z_\chi^\pm)_{lk}^{-1}. \tag{2.275}$$

Given the structure of $\Delta^\pm$ (2.254), it is possible to determine its elements by solving the linear system of equations

$$D_{kj}^\pm \Delta_{lj}^\pm = -D_{kl}^\pm, \tag{2.276}$$

for all possible k. After applying this unmixing step, the renormalization coefficients can be obtained by computing

$$Z_\chi^\pm = Z_q^2 \left([D^\pm]^t\right)^{-1}, \tag{2.277}$$

which is completely analogous to equation (2.269). Nevertheless, one has to keep in mind that the un-mixing $\mathbf{1} + \Delta^\pm$ has to be applied to the vector of the measured matrix elements $\{Q_1, Q_2, Q_3, Q_4, Q_5\}$ in order to transform this vector into the χ_{RS} scheme so that the renormalization can proceed as in the parity violating case.

For the determination of Q_1 which is related to the kaon bag parameter B_K (see 2.3.8), the extraction of the relevant mixing coefficients Δ_{1k} is a delicate procedure. This is due to the fact that the contributions from $Q_2, \ldots, Q_5$ are chirally enhanced with respect to Q_1 [cf. e.g. Aoki et al., 2006].

2.4.3. Improvement techniques for RI renormalization factors

It is recommended to use improvements for computing renormalization factors in the RI scheme, since discretization errors as well as non-perturbative effects render the matching to perturbation theory difficult. Essential ingredients in our calculations are the trace-subtraction method, which removes an $\mathcal{O}(a)$ contact term, as well as the ratio-extrapolation which helps to circumvent the RI window condition and allows us to obtain non-perturbative continuum running. Especially in case of the four-fermion operator renormalization, the mix-

ing coefficients are dominated by unphysical discretization effects which are removed by using the trace subtraction. The same applies to the quark mass renormalization $1/Z_S$, where the situation there is not so severe. The ratio extrapolation allowed us to have continuum running and significantly improved the matching of the non-perturbative data to continuum perturbation theory. This is especially important for comparing our results to other lattice determinations or for providing input for phenomenological calculations. I give a short overview over these two methods in the following.

Trace-subtraction

Consider the tree-level Wilson propagator (2.115)

$$\frac{1}{a}S(p,m) = \frac{-i\gamma_\mu \sin(p_\mu a) + ma - r\sum_\mu(\cos(p_\mu a) - 1)}{\sum_\mu \sin^2(p_\mu a) + [ma - r\sum_\mu(\cos(p_\mu a) - 1)]^2}. \tag{2.278}$$

We expand the trigonometrical functions up to the appropriate powers and find

$$\frac{1}{a}S(p,m) = \frac{-i(\not{p}a) + ma + r\frac{(pa)^2}{2} + \mathcal{O}(a^3)}{(pa)^2 + \left[(ma) + r\frac{(pa)^2}{2}\right]^2 + \mathcal{O}(a^4)}, \tag{2.279}$$

where we defined

$$(pa)^2 = \sum_\mu (p_\mu a)^2, \quad (\not{p}a) = \sum_\mu \gamma_\mu (p_\mu a). \tag{2.280}$$

Now we remove all irrelevant terms proportional to $(pa)^2$. This can be achieved by adding irrelevant operators to $S(p)$:

$$
\begin{aligned}
(1 + r\,ma)\frac{S}{a} - \frac{r}{2} &= \frac{-i(\not{p}a) + ma + r\frac{(pa)^2}{2} - i\,r(\not{p}a)(ma) + r(ma)^2 + r^2\frac{(pa)^2(ma)}{2} + \mathcal{O}(a^3)}{(pa)^2 + \left[(ma) + r\frac{(pa)^2}{2}\right]^2 + \mathcal{O}(a^4)} \\
&\quad -\frac{r}{2}\frac{\left[(pa)^2 + (ma)^2 + r(ma)(pa)^2\right] + \mathcal{O}(a^3)}{(pa)^2 + \left[(ma) + r\frac{(pa)^2}{2}\right]^2 + \mathcal{O}(a^4)} \\
&= \frac{-i(\not{p}a) + ma - i\,r(\not{p}a)(ma) - \frac{r(ma)^2}{2} + \mathcal{O}(a^3)}{(pa)^2 + \left[(ma) + r\frac{(pa)^2}{2}\right]^2 + \mathcal{O}(a^4)}
\end{aligned}
\tag{2.281}
$$

The denominator can be rewritten as follows:

$$\frac{1}{(pa)^2 + \left[(ma) + r\frac{(pa)^2}{2}\right]^2 + \mathcal{O}(a^4)} = \frac{1}{(pa)^2 + (ma)^2 + r(pa)^2(ma) + \mathcal{O}(a^4)}. \tag{2.282}$$

Since we consider on-shell improvement, we obtain $(pa)^2 = -(ma)^2$ from the classical equations of motion. Therefore

$$\frac{1}{(pa)^2 + (ma)^2 + r(pa)^2(ma) + \mathcal{O}(a^4)} = \frac{1}{(pa)^2 + (m^{\mathrm{I}}a)^2 + \mathcal{O}(a^4)}, \tag{2.283}$$

where we defined the improved mass by

$$m^{\mathrm{I}}a = ma(1 - r\,ma/2). \tag{2.284}$$

This yields for the full expression (2.281):

$$(1 + r\,ma)\frac{S(p, m^{\mathrm{I}})}{a} - \frac{r}{2} = \frac{-i(\not{p}/a) + m^{\mathrm{I}}a - i\,r(\not{p}/a)(m^{\mathrm{I}}a)}{(pa)^2 + (m^{\mathrm{I}}a)^2} + \mathcal{O}(a). \tag{2.285}$$

This result allows us to define an improved propagator via [Heatlie et al., 1991; Martinelli et al., 1991, 1995]

$$S^{\mathrm{I}}(p, m^{\mathrm{I}}) = (1 + r\,am^{\mathrm{I}})S(p, m^{\mathrm{I}}) - \frac{ar}{2}, \tag{2.286}$$

where the discretization effects are of $\mathcal{O}(a^2)$ in the chiral limit. For finite quark mass, the discretization effects are $\mathcal{O}(a)$ and caused by the term proportional to $(\not{p}/a)(ma)$. However, they can be removed by using off-shell improvement, i.e. by applying the substitution

$$(1 + r\,ma)S \to \left(1 + \frac{ar}{4}(-i\not{p} + m)\right) S \left(1 + \frac{ar}{4}(-i\not{p} + m)\right), \tag{2.287}$$

where we recover our on-shell improved results by again using $i\not{p} = -m$. Heatlie et al. [1991] show, that the improvement effectively removes contact terms of $\mathcal{O}(a)$, which are diagonal in spin and colour. Greens functions constructed and amputated from propagators as defined in (2.286) are $\mathcal{O}(a)$ improved.

This improvement can also be achieved by applying a different technique [Capitani et al., 2001; Becirevic et al., 2000; Martinelli et al., 2001; Maillart and Niedermayer, 2008]: we may define our improved propagator as

$$\bar{S}(p, m^{\mathrm{I}}) = S(p, m^{\mathrm{I}}) - \frac{\mathrm{Tr}_D[S(p, m^{\mathrm{I}})]}{4}, \tag{2.288}$$

where the index D denotes that the trace is taken in Dirac space. It is easy to see that on tree-level

$$\bar{S}(p, m^{\mathrm{I}}) = S^{\mathrm{I}}(p, m^{\mathrm{I}}) - \frac{m^{\mathrm{I}}(1 - i\,r\not{p})}{p^2 + (m^{\mathrm{I}})^2} + \mathcal{O}(a^2), \tag{2.289}$$

i.e. the trace subtracted propagator is equal to the improved propagator on $\mathcal{O}(a)$ without the physical mass term and the term proportional to $m^{\mathrm{I}}\not{p}$. The removal of the latter term yields $\mathcal{O}(a)$ improvement even outside the chiral limit but the price to pay is the removal of physical contributions proportional to the mass. However, the RI renormalization scheme is a massless scheme and thus any computed renormalization factors have to be extrapolated into the chiral limit at some point. In practice, renormalization factors computed from trace subtracted propagators agree much better with perturbative expectations than those computed with the standard improvement (2.286).

Ratio-extrapolation

In order to improve the matching of non-perturbative renormalization factors as well as circumventing the strict RI window condition (2.243), we computed the continuum limit of the

ratio [Constantinou et al., 2010; Arthur and Boyle, 2011; Durr et al., 2010]

$$R_X(\mu, \mu', a) = \frac{Z_X(\mu, a)}{Z_X(\mu', a)},$$ (2.290)

where Z_X is the RI renormalization factor[78] of operator X, e.g. $X = S, B_K$, etc.. Note that this limit exists since the numerator and denominator are renormalized by the same counterterms. We denote the continuum limit of this ratio by $R_X(\mu, \mu')$. The scales μ should be chosen such that it fulfills the strict window condition for a sufficiently large set of lattice spacings, so that the continuum extrapolation can be safely performed. If μ is even chosen to be well inside the perturbative region, the non-perturbative data can be safely matched to continuum perturbation theory.
The scale μ' has to be chosen such that it fulfills the strict window condition for all lattice spacings included in the analysis. Thus we obtain $Z_X(\mu, a)$ on all lattices via

$$Z_X(\mu, a) = R_X(\mu, \mu') \times Z_X(\mu', a).$$ (2.291)

Therefore, $R_X(\mu, \mu')$ describes the non-perturbative continuum running of X from μ' to μ.

In section 4.2.2, we will also compute the continuum limit of the ratio

$$R_{S,\text{RI}\rightarrow\text{RI}-m}(\mu, a) = \frac{Z_S^{\text{RI}-m}(\mu, a)}{Z_S^{\text{RI}}(\mu, a)},$$ (2.292)

which converts quark masses from the massive intermediate scheme RI-m to the massless RI scheme at a given scale μ. The existence of this limit is not obvious, so I discuss this issue here. Usually, one would expect that the divergent structure is not necessarily the same and thus spoiling the continuum limit. However, this is at least not true for the quark mass renormalization factor $1/Z_S$. Since quark masses are protected by chiral symmetry, the superficial degree of divergence of all massless quark mass diagrams is at most logarithmically. These divergences arise from loop integrals of the form

$$\int \frac{d^4k}{k^4}.$$ (2.293)

Massive quarks give rise to terms proportional to

$$\int \frac{d^4k}{k^4} \frac{m^\alpha}{k^\alpha},$$ (2.294)

with $\alpha > 0$ and the factor $k^{-\alpha}$ cancels the additional mass dimensions in the numerator. This integral is in fact even less than logarithmically divergent, i.e. it is finite. This means that the massive RI-m and the massless RI scheme differ by a finite renormalization and thus the limit of (2.292) exists.

---

[78]This method also works for different schemes, as long as the counterterms in the numerator and denominator are the same. We define this ratio in the RI scheme so that we can drop the superscript RI in the following.

Removing non-perturbative contributions

The RI Greens functions computed on the lattice carry information on the perturbatively inaccessible hadron spectrum. This means that some of the operators inserted into the Greens functions have an overlap with hadronic states, i.e. pseudoscalar-operator $\bar{q}\gamma_5 q$ with several pseudoscalar meson states. These effects are dominant in the infrared, whereas for large momenta the perturbative and non-perturbative contributions can in principle be disentangled because of their different dependence on the momentum p [Martinelli et al., 1995]. However, on coarse lattices even the largest momenta may be significantly affected by these kind of effects. Typically, the renormalization factors Z_P, Z_A, and those necessary to renormalize four fermion operators like Z_{11}^+ are affected. It is assumed that these effects are mainly attributed to virtual zero-momentum pion exchanges inside the non-perturbatively computed vertex [Aoki et al., 2008; Sturm et al., 2009]. The standard RI prescription (cf. 2.4.2) uses so-called *exceptional* configurations, i.e. configurations with $q = p_1 - p_2 = 0$, where p_1 and p_2 are the momenta of the incoming and outgoing quark. The non-perturbative contributions inside the vertex are proportional to a pion propagator with momentum q, which then badly diverges in the chiral limit if exceptional momenta are used. One possibility to overcome this problem is the use of non-exceptional momenta, i.e. momenta which fulfill $p_1^2 = p_2^2 = (p_1 - p_2)^2 = q^2$ [Sturm et al., 2009]. The resulting scheme is called *symmetric MOM* (or SMOM) scheme and provides an elegant way to significantly suppress these non-perturbative effects. The drawback of this approach is that the number of available momenta fulfilling the symmetric momentum condition is very small. For example, assuming periodic boundary conditions in all directions, a valid pair of momenta would be $p_{\mu\nu}(n)$, $p_{\mu\rho}(n)$, where $\nu \neq \rho$ and

$$p_{\mu\nu}(n) = (e_\mu - e_\nu)\frac{2\pi n}{L}, \qquad (2.295)$$

with e_ν being a unit vector in direction ν and $n \in \{1, \ldots, L-1\}$. Different choices of μ and ν give degenerate momenta and also many possible choices for n when using the bosonic momenta. If some sensible momentum cuts are applied to the data, only $n = L/4$ non-degenerate momenta remain from this construction. This renders the mapping of the functional form of the resulting renormalization factors difficult, which in turn complicates the estimation of cut-off effects. More complicated setups such as the use of twisted boundary conditions [Arthur and Boyle, 2011] in combination with momentum sources [Gockeler et al., 1999] substantially increase the computational costs. Furthermore, this setup induces unitarity violations and finite volume corrections, which are not fully understood yet. Thus we do not use the SMOM scheme in this work.

Our treatment of such terms is data-driven: consider the projected amputated greens function Γ at two different quark masses m_1, m_2. The pion pole together with massive $\mathcal{O}(a)$ corrections suggests a form

$$\Gamma(p^2, m) = A(p^2, m) + \frac{B(p^2)}{p^2 m} + \mathcal{O}(a^2) + \mathcal{O}\left(\frac{1}{p^4}\right) \qquad (2.296)$$

The term $A(p^2, m)$ gives the perturbative value of Γ in the chiral limit and the term proportional to $B(p^2)$ includes the non-perturbative pole contributions. We can fit the different

contributions by either applying a combined fit or computing the difference

$$\Gamma^{\text{sub}}(p^2, m_1, m_2) = \frac{m_1 \Gamma(p^2, m_1) - m_2 \Gamma(p^2, m_2)}{m_1 - m_2} \tag{2.297}$$

as suggested by Giusti and Vladikas [2000]. All discretization and other non-perturbative effects can be fitted out without having to take care of the pion pole term. An analogous treatment can be found for four fermion Greens functions which may also include double poles [Becirevic et al., 2004]. Both methods work equally well in practice and we chose the second for subtracting pole contributions from the relevant B_K mixing coefficients Δ_{1k}.

2.4.4. Some remarks on perturbative renormalization

Perturbative calculations in the RI scheme can also be used to estimate the influence of non-perturbative effects on the measured data. The matching of lattice data to continuum perturbation theory can either be achieved by dividing the lattice data by the perturbative running and fitting the remaining curve to some appropriate model, or by fitting to a linear combination of the perturbative running and some other contributions, such as pole terms or $\mathcal{O}((pa)^k)$ cutoff effects. These two approaches differ by higher order effects and we used the first one in our studies (cf. 4.2.2 and 4.3.1).

The *Callan-Symanzik*- or *renormalization group equation* (RGE), describing the scale-dependence of the quark mass, is given by [cf. e.g. Chetyrkin and Retey, 2000][79]

$$\mu^2 \frac{\mathrm{d}}{\mathrm{d}\mu^2} m(\mu^2) = m(\mu^2) \gamma_m(\alpha_s(\mu^2)) = -m \sum_{i \geq 0} \gamma_m^{(i)} \left(\frac{\alpha_s}{\pi}\right)^{i+1} , \tag{2.298}$$

with the strong coupling α_s and perturbatively computable anomalous dimensions $\gamma_m^{(i)}$. The former obeys the differential equation [Chetyrkin and Retey, 2000]

$$\mu^2 \frac{\mathrm{d}}{\mathrm{d}\mu^2} \frac{\alpha_s(\mu^2)}{\pi} = \beta(\alpha_s) = -\sum_{i \geq 0} \beta_i \left(\frac{\alpha_s}{\pi}\right)^{i+2} , \tag{2.299}$$

where the running coefficients β_i can be evaluated perturbatively as well. The beta-function coefficients β_i as well as the quark mass anomalous dimensions γ_m have been computed in QCD up to four loop order by van Ritbergen et al. [1997]; Vermaseren et al. [1997] in the $\overline{\text{MS}}$ and by Chetyrkin and Retey [2000] in the RI scheme. Using an appropriate numerical integrator, one can easily compute the running of the coupling and quark mass in either schemes down to scales $\mu \gg \Lambda_{\text{QCD}}$.
Usually results are quoted in a continuum scheme like $\overline{\text{MS}}$, which involves applying a (finite) scheme conversion C. For the quark mass we have

$$C_m = 1 + \sum_{i > 0} C_m^{(i)} \left(\frac{\alpha_s}{\pi}\right)^i , \tag{2.300}$$

---

[79]See [Peskin and Schroeder, 1995, p. 410f] for a detailed derivation.

where the coefficients $C_m^{(i)}$ were computed perturbatively by Chetyrkin and Retey [2000].

Consider now composite expressions such as local four-fermion operators, where all internal lines are contracted onto a single point. We discussed in (2.246), that physical amplitudes can be expressed as matrix elements of the condensed operator times a renormalization constant and Wilson coefficient. The computation of these renormalization constants is more complicated compared to the renormalization of bilinear operators.
The first complication is the mixing of different dimension six operators under renormalization, leading to coupled renormalization group equations.
The second problem is the manifestation of an inherent ambiguity of the $\overline{\text{MS}}$-scheme, originating from dimensional regularization. This technique reduces the degree of divergence of loop integrals by reducing the number of dimensions from D to $D - 2\epsilon$. It is ambiguous to define whether the ϵ-dimensional part $\hat{\gamma}_5$ of γ_5 should commute or anti-commute with the other γ_μ. In many calculations of renormalization constants for bilinear operators, this ambiguity does not propagate into the final results, but for local four-fermion operators it does. We define $\hat{\gamma}_5$ to anti-commute with all other γ_i's, as γ_5 does in four dimensions. This scheme is called NDR-$\overline{\text{MS}}$, *naively-dimensional-regularized*-$\overline{\text{MS}}$.

Assuming the 5×1 column vector of Wilson coefficients $\mathbf{C}^\pm(\mu^2)$, we can adopt the equation (2.298) to describe the running of these Wilson coefficients

$$\mu^2 \frac{\mathrm{d}}{\mathrm{d}\mu^2} \mathbf{C}^\pm(\mu^2) = \gamma^\pm(\mu)^t \, \mathbf{C}^\pm(\mu^2), \qquad (2.301)$$

where $\gamma^\pm(\mu)$ now is a 5×5 anomalous dimension matrix (ADM). It can be expanded in powers of α_s via

$$\gamma^\pm(\mu) = \frac{\alpha_s}{4\pi} \, \gamma^{(0)\pm} + \frac{\alpha_s^2}{(4\pi)^2} \, \gamma^{(1)\pm} + \mathcal{O}(\alpha_s^3). \qquad (2.302)$$

The coefficient matrices $\gamma^{(i)\pm}$ have been computed perturbatively up to two loop level in [Ciuchini et al., 1998; Buras et al., 2000], where for B_K we are especially interested in γ_{11}^+. All calculations in that reference were done using the NDR-$\overline{\text{MS}}$ scheme. Also the conversion factor for converting between $\overline{\text{MS}}$ and RI scheme is given:

$$\mathbf{C}^{\text{RI}\pm}(\mu^2) = \left(1 - \frac{\alpha_s}{4\pi} \Delta r_{\overline{\text{MS}} \to \text{RI}}^t\right) \mathbf{C}^{\overline{\text{MS}}\pm}(\mu^2) + \mathcal{O}(\alpha_s^2). \qquad (2.303)$$

Note that $\Delta r_{\overline{\text{MS}} \to \text{RI}}^t$ depends on the gauge fixing parameter ξ, because the RI scheme depends on the choice of the gauge. It turns out that the gauge parameter does not cancel in the calculations and hence has to be renormalized. In Landau gauge ($\xi = 0$) however, all terms containing ξ drop out.[80]

---

[80]The starting value $\xi = 0$ is a fixed point of its RGE.

3. Scaling and stability tests

The success of lattice calculations is highly dependent on the used actions and algorithms. A good balance between CPU demand and 'conceptual cleanness' has to be found for obtaining a cost-effective setup. For example, theoretically appealing chiral overlap fermions [Narayanan and Neuberger, 1993a, 1994, 1993b, 1995; Neuberger, 1998a,b] require a huge amount of CPU time. This renders calculations at the physical pion mass and in sufficiently large volumes on present day computers with state-of-the-art algorithms extremely difficult. If chirality is not a critical issue, there are powerful alternatives: as discussed in section 2.3.3, the use of smearing improves the chirality of the Wilson Dirac operator. The computational overhead of smearing is more than compensated by the reduced computational costs of the (R)HMC trajectories: smearing does not change the condition number of the Dirac operator but drastically reduces its fluctuations, keeping the low modes away from zero. The combination of smearing with the advanced algorithms presented in sections 2.3.4 is a highly efficient way to perform lattice calculations as we will see in the following section.[1]

The two actions used in our dynamical calculations are both based on the tree-level improved Lüscher-Weisz gauge action and (also tree-level improved) clover Wilson operator (cf. section 2.3.1). The two approaches we used differ by their smearing recipes. The first action uses 6 step EXP smearing (see section 2.3.3 for details) with smearing parameter $\rho = 0.11$. The second action is 2 step HEX smeared with the parameters $(\alpha_1, \alpha_2, \alpha_3) = (0.95, 0.76, 0.38)$. Calculations in quenched QCD show that the dependence of observables on the smearing is quite mild [Capitani et al., 2006; Durr, 2009]. Some exploratory studies suggest that this persists in the full theory [Kamleh et al., 2004; Hasenfratz et al., 2007; Schaefer et al., 2007; Hoffmann et al., 2007; Moran and Leinweber, 2008], as long as a comparable amount of smearing is used.

In fact, in our studies we have proven this assumption true for our two types of smearing. In order to be able to give a comprehensive overview, we tested our actions with respect to stability, performance and the absence of unphysical phases as well as ergodicity. Testing the scaling behaviour within a simple framework is also very useful in order to determine what can be expected from large scale calculations like those we performed when computing the physical hadron spectrum [Durr et al., 2009; Dürr et al., 2008], light quark masses [Durr et al., 2010] and B_K [Durr et al., 2011a]. Some of the scaling tests are performed in the quenched approximation, where we used the Wilson plaquette action but the same smearing prescriptions as in the corresponding full QCD calculations.

For generating dynamical quark configurations, we used the RHMC with all optimizations discussed in section 2.3.4. In the quenched case, we combined four overrelaxation sweeps with one pseudo heat bath update.

---

[1]In this section, I will review the results from our publications [Durr et al., 2009, 2011b, 2010] as well as the "Supporting Online Material" of [Dürr et al., 2008]. The scaling study of quenched B_K was not published before.

Concerning the stability of our setup, we did not expect any problems. Nevertheless, we tested the 6 EXP action for a possible metastable behaviour and found that these unphysical effects were absent (cf. section 3.1). Since the 2 HEX smearing is approximately equivalent to the 6 EXP one, we are very convinced that it also fulfills all stability criteria. Both actions are ultra-local, as it is also discussed in 3.1. For all tested observables in the range of interest, both actions perform equally well. This is shown by the N_f=3 hadron masses scaling studies in section 3.2. The scaling study for the quenched quark mass has been restricted to the 2 HEX choice, but we found very good agreement with results from the literature (cf. 3.2.2). The same applies to the scaling study for quenched B_K (cf. 3.2.3). I close this section by discussing finite volume effects and the chiral behaviour of our actions. These analyses were carried out on some of the the N_f=2+1 datasets also used in our phenomenological computations. It is recommended to use these data sets, since the size of finite volume effects and the appearance of chiral logs highly depends on the box sizes and pion masses used in the calculations.

3.1. Stability and locality of smeared actions

A general concern about smearing is, that informations contained in a single link can be propagated all around the lattice and especially around the boundaries, if the smearing parameters are too aggressive and a large number of iterations is used. It is especially problematic if the smearing prescription is adjusted to the lattice spacing, since this may introduce a continuum-non-irrelevant coupling range.[2] In contrast to that, Symanzik scaling is fulfilled if the action is local [Symanzik, 1983a,b]. For any fermionic action, there are two different notions of locality:

1) Locality in coordinate space, i.e.

$$\|D(x,y)\| < \text{const.}\, e^{-\lambda|x-y|}, \tag{3.1}$$

with $\lambda = \mathcal{O}(a^{-1})$. This ensures that the Dirac operator D does not couple arbitrary separated quarks in the continuum limit because the extension of the coupling range dies off faster than the lattice spacing goes to zero.
In our case, this requirement is trivially fulfilled because our Dirac operator at most couples nearest neighbour fields and hence $D \sim \delta(x+1-y) + \delta(x-y)$.

2) Locality with respect to gauge fields:

$$\left\|\frac{\delta D(x,y)}{\delta U(z)}\right\| < \text{const.}\, e^{-\lambda|(x+y)/2-z|}, \tag{3.2}$$

where also $\lambda = \mathcal{O}(a^{-1})$.

Also the second requirement is fulfilled for our actions as can be seen from figure 3.1. This figure displays the l.h.s. of (3.2) in the Frobenius norm versus the Euclidian distance $|x-z|$ in lattice units for our 6 EXP.[3] Mathematically, the ultra-locality range of this action is $r/a = 6$

---

[2]For example if the iteration level is increased with β.

[3]It is sufficient to investigate the case $x = y$ because of coordinate space locality.

what can also be learned from the plot. Within this range, the dependence of $D(x,x)$ on the thin link fields U drops off exponentially for $3 \leq |x-z|/a \leq 6$ with a decay constant $\lambda \approx 2.2a^{-1}$. Therefore, our actions even fulfill the locality condition (3.2) within the ultra-locality range. A good agreement between different values for β is also observed.

We have not reproduced this figure for the 2 HEX action, since the ultra-locality range is even smaller in that case. Mathematically, the 2 HEX action has $r/a = 4$ and we also expect (3.2) to be fulfilled within this range. However, since the 2 HEX ultra-locality range is smaller than that of the 6 EXP action, this property will probably be obscured by short range terms. We can summarize that both our actions are ultra-local in coordinate space and with respect to the gauge fields. Furthermore, they fulfill the locality condition (3.2) within the ultra-locality range.

3.1.1. Absence of unphyisical meta-stabilities

In some dynamical Wilson fermion simulations, the occurrence of an unphysical first-order phase transition has been reported [Della Morte et al., 2005a; Aoki et al., 2005]. This has been interpreted as the presence of a lower bound for the quark mass where sensible physical calculations can be performed. It was observed that this phenomenon occurs only on coarse lattices and that gauge action improvement decreases this lower bound on the quark mass. Additionally, $\mathcal{O}(a)$-improved Wilson fermions in combination with improved gauge actions made the problem disappear for all lattice spacings investigated by Aoki et al. [2005]. Jansen et al. [2007] showed that one level of EXP smearing weakens the phenomenon.

Since physical first-order phase transitions can only occur in infinite volume, the appearance of such phase transition in a finite volume signals a failure of the updating algorithm in finding the true minimum of the effective potential. Hence, for finite-volume simulations, it is important to ask whether the update algorithm can thermalize the system for a sensible set of parameters in a manageable number of updating steps. If this is the case, the unphysical phase transitions will be absent.

In order to investigate this issue, we took two $16^3 \times 32$ configurations. One consists of random links and the other one was thermalized in an $N_f=2+1$ simulation at $\beta = 3.3$ with $am_{ud}^{\mathrm{PCAC}} = 0.0066$, corresponding to a pion mass of approximately $240\,\mathrm{MeV}$ and $am_s^{\mathrm{PCAC}} = 0.0677$ which roughly corresponds to the physical strange quark mass. The chosen β is the smallest cutoff we considered in our studies.

Starting from the random configuration, we performed a 'downward' updating sequence by subsequently lowering the pion mass. From $am_{ud}^{\mathrm{PCAC}} \approx 0.0243$, going over 0.0173, 0.0131, 0.0086 and finishing at 0.0066. This corresponds to a range of pion masses $M_\pi \sim 440\,\mathrm{MeV} - 240\,\mathrm{MeV}$. Each simulation at the next (lower) mass point started from the previous (heavier) point by applying 100 trajectories for thermalization and 300 trajectories for measuring the plaquette expectation value $\langle P \rangle$. Analogous we performed an 'upward' sequence, starting from a thermalized configuration at $am_{ud}^{\mathrm{PCAC}} = 0.0066$ and increasing the light quark mass up to $am_{ud}^{\mathrm{PCAC}} \approx 0.0243$. In between we applied measurements at the same masses already used for the downward sequence. Also here, 100 trajectories for thermalizing each mass point and 300 trajectories for measuring the plaquette were generated. If the update algorithm had been inefficient, the 100 thermalization steps would not have been sufficient to fully thermalize the system, leading to a hysteresis in $\langle P \rangle$ versus aM_π. The results for this cycle are shown in figure 3.2, where no signal of a hysteresis can be seen.

In a similar test, we measured the plaquette expectation value in dependence of the HMC time during thermalization from a 'hot' or 'cold' configuration [Durr et al., 2007]. In both cases, the same average plaquette was reached within a reasonable number of update steps. Thus, regardless of the starting configuration, our algorithm evolves the system to the correct equilibrium state in a reasonable number of steps. We are convinced that our 2 HEX action would perform equally well in this study and hence did not repeat it for this action.

3.1.2. Mass-gap, topology and plaquette expectation values

In quenched QCD, the (unsmeared) clover fermion operator may have one or several eigenvalues close to the origin or with a negative real part. This problem even occurs at not very light quark masses, so that inversions on these configurations fail. Such configurations are referred to as 'exceptional'.

In dynamical simulations using an HMC algorithm, such configurations would not appear if infinitesimally small timescales could be used. Trajectories where at least one eigenvalue of the Hermitian Wilson operator $H_W = \gamma_5 D_W$ approaches zero will be repelled by an infinite back-driving force. For finite timescales however, the near-zero modes are only approximately suppressed. This may cause the HMC evolution to fail, so it is natural to monitor the (magnitude of the) smallest eigenvalue within an HMC evolution and check if its distance to zero is sufficiently large during the entire run. In a given ensemble, the distribution of the smallest eigenvalue is approximately Gaussian, hence if its center μ is several σ away from zero the simulation is deemed safe [Del Debbio et al., 2006]. Since we use even-odd preconditioning, the relevant quantity to observe is the smallest eigenvalue of the reduced, γ_5-Hermitian operator

$$D_{W,\mathrm{red}} = \frac{1}{2}\big(D_{oo} - D_{ee}^{-1} D_{eo}\big). \tag{3.3}$$

The D_{ab} can be considered as block-operators, where D_{ee}, D_{oo} only couple even to even and odd to odd sites respectively, and D_{eo} couples odd to even sites. The factor $1/2$ aligns its IR eigenvalues with the low-lying eigenvalues of the full operator. For our 6 EXP action and the smallest pion mass ($M_\pi/M_\rho = 0.60$, cf. section 3.2), the eigenvalue distributions are shown in figure 3.3, where β ranges from 2.8 to 3.76. Even at the coarsest lattice, the peak is several sigma away from the origin. This situation even improves when going to finer lattices since the center of the peak shifts to the right and its width rapidly decreases.

For phenomenological applications, it is important to know how the spectral gap evolves when lowering the light quark mass. Instead of measuring the smallest eigenvalue itself, we measured the closely related quantity n_{CG}^{-1}, the inverse iteration count for the lightest pseudofermion in the action. The results for the 6 EXP action are displayed in figure 3.4 and for our 2 HEX action in figure 3.5. In both cases, we can find a clear gap providing the evidence for the stability of our algorithm. Furthermore, we measured the energy violation ΔH on all ensembles throughout the whole runs and ensured that $\langle \exp(-\Delta H) \rangle$ is compatible with one. Since the acceptance probability of the Metropolis step is given by $P_{\mathrm{acc}} = \min(1, \exp(-\Delta H))$, it is provided that the acceptance rate is sufficiently large ($\gtrsim 90\%$ in all our runs).

The update algorithm has to sample different topological sectors adequately in order for being ergodic. Generically this sampling becomes more difficult when small lattice spacings are used. This means, at fixed physical quark masses, the autocorrelation of the topological
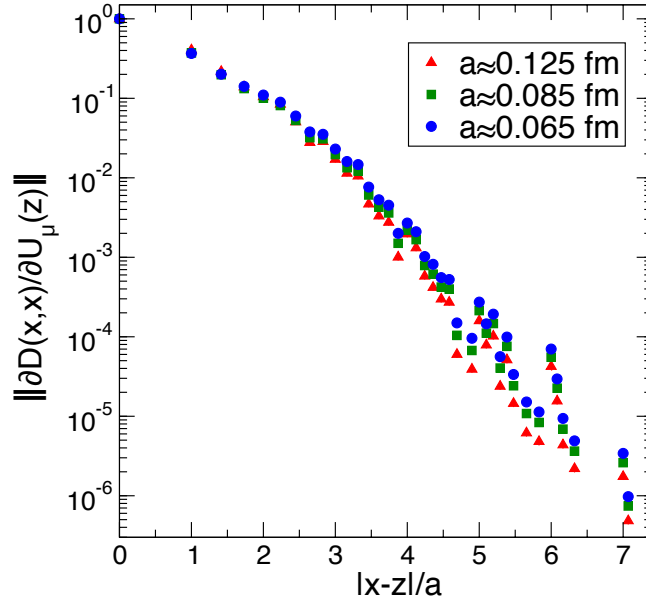
Figure 3.1.: Gauge field dependence of Dirac operator D versus the euclidian distance $|x-z|/a$ in lattice units. The ultra-locality range in lattice units is equal to 6 and we find a large exponential decay with a decay constant of $\lambda \approx 2.2a^{-1}$. Note that it is sufficient to evaluate D on spot x, since it is ultra-local in coordinate space [from Durr et al., 2009].
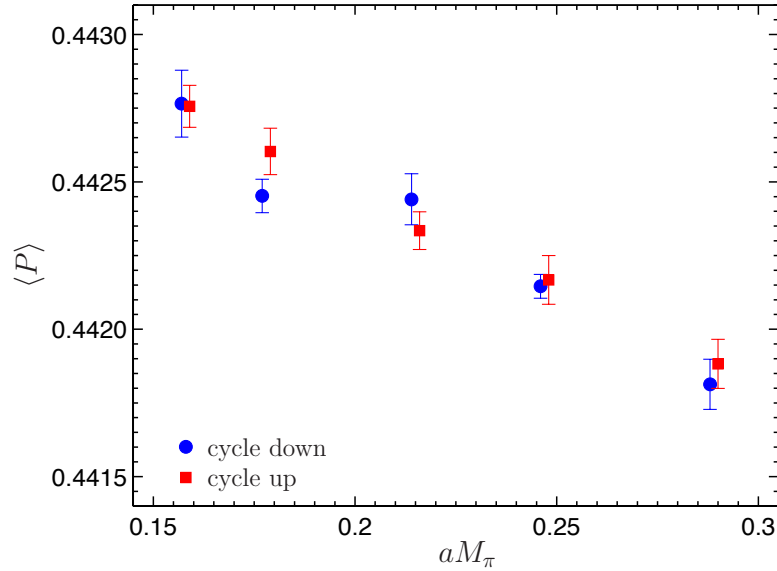
Figure 3.2.: Absence of hysteresis in the plaquette cycle. The data are from an N_f=2+1 run on a $16^3 \times 32$ lattice at $\beta = 3.3$ with fixed strange quark mass $am_s^{\mathrm{PCAC}} = 0.0677$. The light quark masses vary between $am_{ud}^{\mathrm{PCAC}} \approx 0.0243$ and $am_{ud}^{\mathrm{PCAC}} = 0.0066$ in ascending (squares) or descending (circles) order. The second dataset is slightly shifted along the x-axis for better readability [from Durr et al., 2009].

charge increases when the lattice spacing is decreased, signaling a reduced tunneling rate. However, the strength of this reduction is highly algorithm and action dependent.

In our simulations, we measured a reduced tunneling rate for small lattice spacings, but in the range of considered parameters we did not observe any dramatic slowing down of tunneling events and hence no drastically increasing autocorrelation times (cf. figure 3.7 and 3.8). We tested this for both actions using the gluonic definition of the topological charge (cf. section 2.3.2) for different types of smearing. We applied different numbers of HYP smearing steps (20 and 30 levels) to the 2 HEX data and six steps of EXP smearing to the 6 EXP data. For the smearing parameters, we used the conservative parameters $(\alpha_1, \alpha_2, \alpha_3) = (0.75, 0.6, 0.3)$ in the former and $\rho = 0.11$ in the latter case.

Figure 3.7 shows the renormalized topological charge on one of the 6 EXP data sets. The renormalization factor, computed by the minimization of (2.120), is very close to one. The autocorrelation times of the renormalized topological charge are of $\mathcal{O}(10)$ trajectories and we expect the corresponding value for the physically more relevant q_{ren}^2 to be even lower. The quantity q_{ren}^2 is more important, since it is more closely related to the topological susceptibility χ_{top}. Furthermore, we know from experiment that the strong interaction does not violate CP (cf. section 2.2.3). Since q_{ren} and $-q_{\mathrm{ren}}$ are related by a CP transformation, the sign of the charge is irrelevant.

The unrenormalized 2 HEX-topological charges obtained from the different HYP smearing levels (cf. figure 3.8 a) are very close to each other and the corresponding renormalization factors very close to one. Furthermore, the charges are symmetrically distributed around zero as it is expected from theory [Leutwyler and Smilga, 1992] and numerical studies [cf. e.g. Kurth, 2007]. The integrated autocorrelation time of q_{ren}^2 is 29.3(8.1).

In any case, the algorithm does not stay in a fixed topological sector and thus these results provide evidence for a good ergodicity of our algorithm. Figure 3.6 shows the MD history of some representative ensembles in our 6 EXP and 2 HEX production runs. Also here, we find no evidences for possible instabilities.
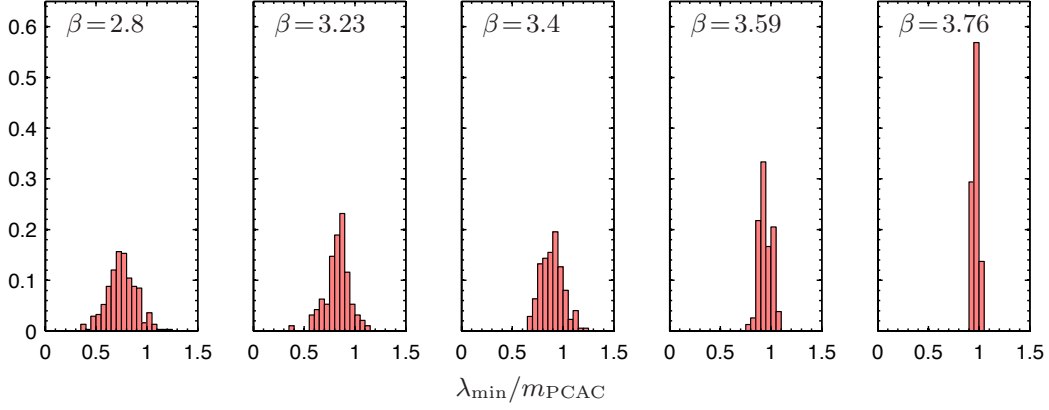
Figure 3.3.: Magnitude of the smallest eigenvalue of the preconditioned Hermitian Dirac operator in units of the PCAC mass. At each β, the lightest run ($M_\pi/M_\rho = 0.60$) is shown [from Durr et al., 2009].
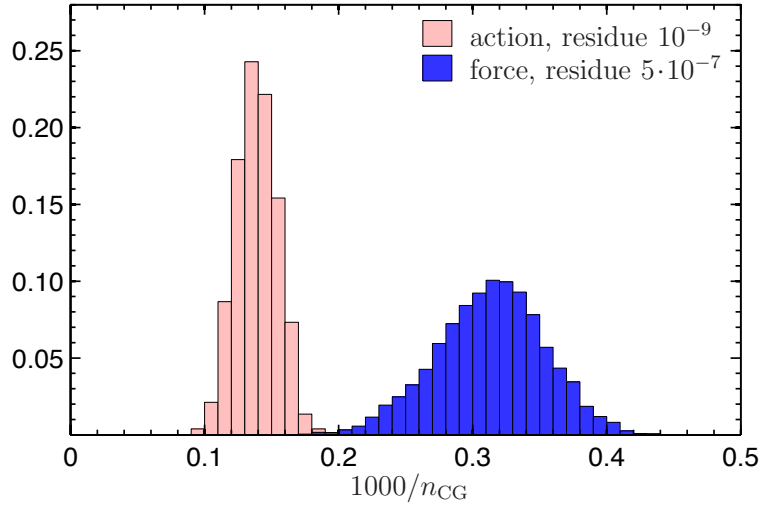
Figure 3.4.: Inverse iteration count of our linear solver at a light M_π for the lightest pseudo-fermion in the action for the 6 EXP action. The results are from an N_f=2+1 run on a $48^3 \times 64$ lattice at $\beta = 3.57$ with $am_{ud}^{\mathrm{PCAC}} = 0.0056$ and $am_s^{\mathrm{PCAC}} = 0.044$, corresponding to $M_\pi \sim 190\,\mathrm{MeV}$ [from Durr et al., 2009].
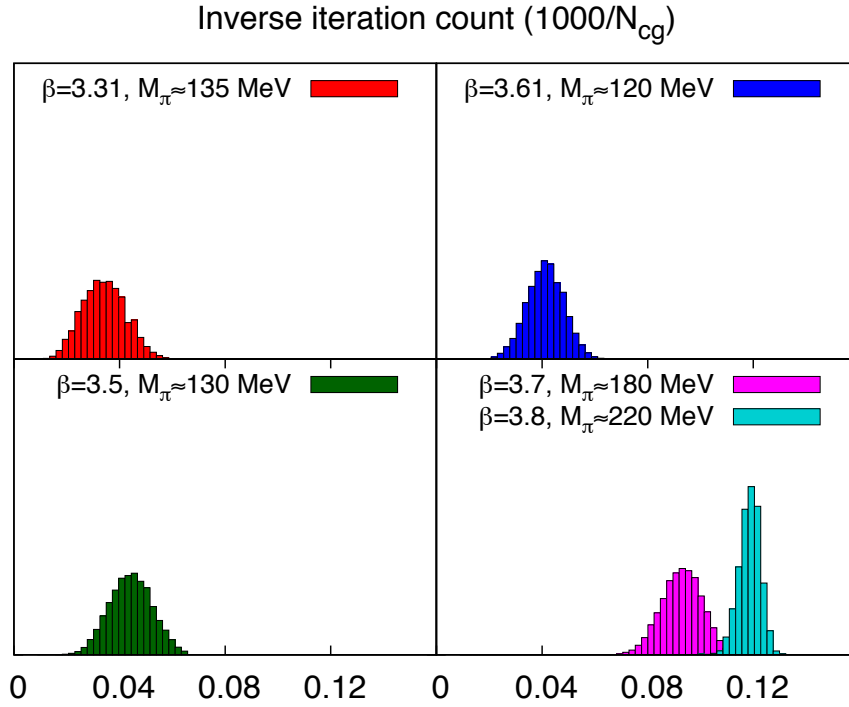
Figure 3.5.: Inverse iteration count for the 2 HEX action at different β and lightest quark mass for the lightest pseudofermion in the ensemble [from Durr et al., 2010].
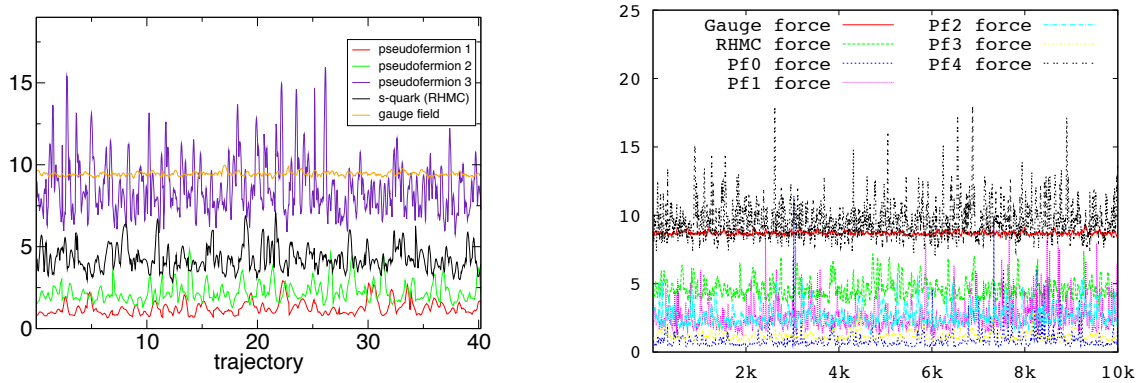
(a) 6 EXP action at the smallest pion mass $M_\pi \sim$ 190 MeV.

(b) 2 HEX action at $\beta = 3.31$ and "physical" pion mass.

Figure 3.6.: History of molecular dynamics forces for the 6 EXP and 2 HEX actions for some 'representative' ensembles. The smoothest curve is the gauge force, and the average contributions from the different pseudofermions to the total force increases with their masses. We can see no signs of instabilities in all our simulations (from the SOM for [Dürr et al., 2008] and [Durr et al., 2010]).
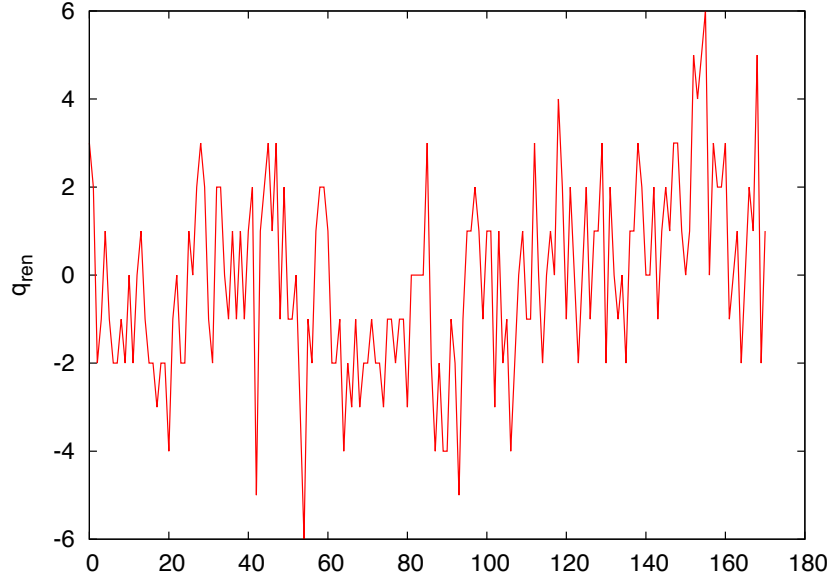
(a) History of the renormalized topological charge.
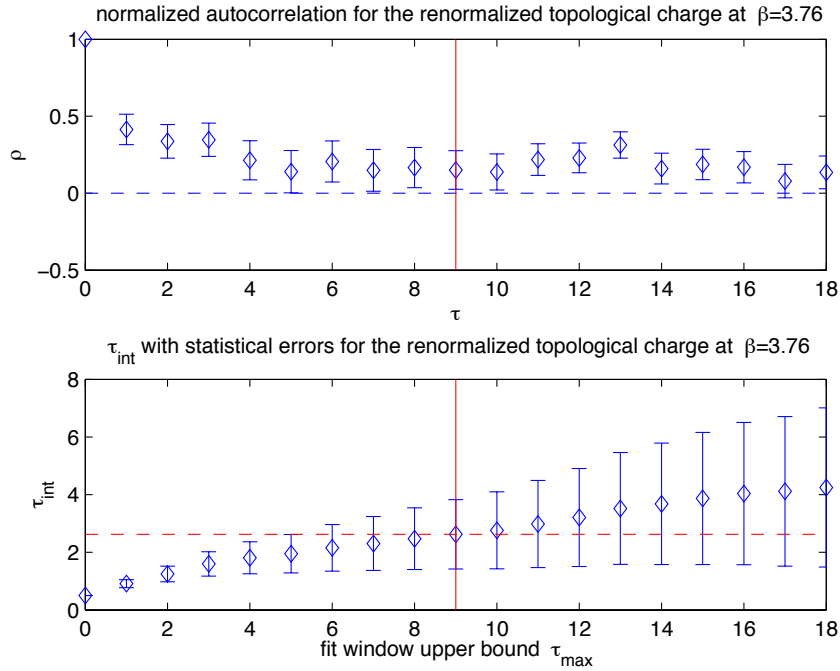
(b) Autocorrelation function ρ (top) and integrated autocorrelation time (bottom) for the renormalized topologcial charge. The dashed red horizontal line in the bottom plot is the integrated autocorrelation time for this ensemble (plots generated using the Γ-Method from [Wolff, 2004] where the accompanying MATLAB code was used).

Figure 3.7.: History of the renormalized topological charge (a) and the corresponding autocorrelation function plot (b) for the 6 EXP action measured on the finest lattice for $N_f{=}3$ ($\beta = 3.75$, $aM_\pi = 0.2019(20)$) ($Z \approx 1.14$). Note that the x-axis is in configuration time and the separation of subsequent configurations are 10 trajectories. This means that the autocorrelation is of $\mathcal{O}(10)$ trajectories .
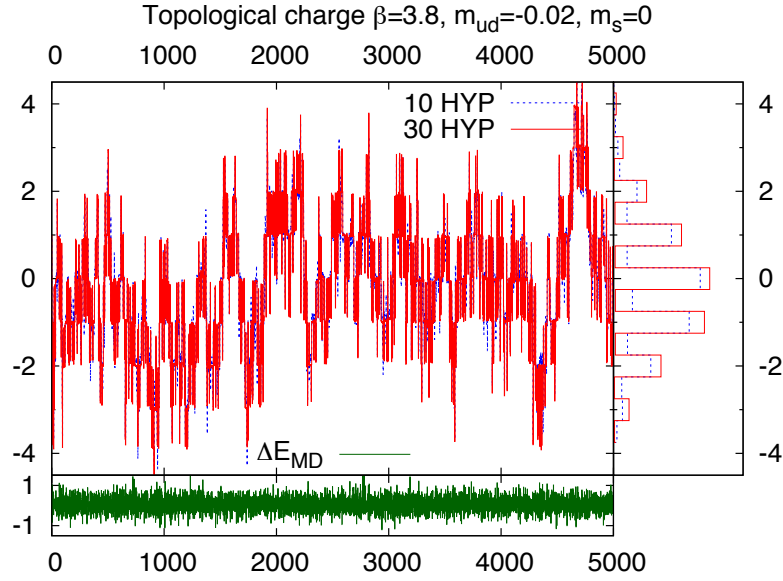
(a) History of unrenormalized topological charge.
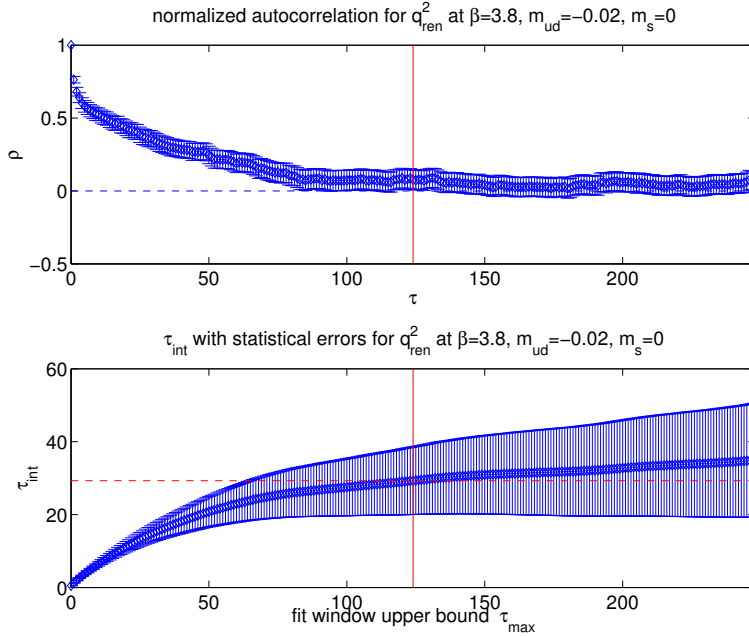
(b) Integrated autocorrelation time.

Figure 3.8.: History of the renormalized topological charge ($Z \approx 1.06$) for the 2 HEX action and two different sets of HYP smearing levels (a, top, blue and red) together with the HMC energy violation history (a, bottom, green). Since the topological tunneling rate is expected to decrease with the lattice spacing and our definition of the topological charge (2.121) is well suited for measurements in small volumes, only the finest lattice with the smallest volume is shown. The algorithm does not stay in a fixed topological sector and the integrated autocorrelation time of q^2_{ren} shown in (b) equals 29.3(8.1) trajectories [from Durr et al., 2010].

3.2. Scaling tests

In the previous section we have seen that our action is ultra-local. When using it in combination with the HMC algorithm, we did not observe any meta-stabilities or problems with ergodicity and stability. Now we can focus on the quality of our scaling, namely the broadness of the scaling window and the size of the scaling corrections for some observables of interest.

3.2.1. Scaling of $N_f{=}3$ hadron masses

We start by discussing the scaling of the $N_f{=}3$ hadron spectrum for both of our actions. Again, we used our optimized HMC combined with the tree-level improved Lüscher-Weisz gauge action and a smeared clover-improved Wilson operator. Two flavours are handled by he HMC, whereas the integration of the third is carried out by our RHMC. This test can therefore be regarded as a field test for phenomenological $N_f{=}2{+}1$ calculations.

We used lattices with at least four lattice spacings and approximately constant physical volumes. The spatial extents of our lattices range from $L/a = 8$ to $L/a = 24$, where we doubled the extent in time direction in order to be able to extract correlators properly. The bare couplings vary between $\beta = 3.23$ and 3.76, where we generated an additional coarse lattice with $\beta = 2.8$ for the 6 EXP action. On the two finest lattices, we performed measurements after every 10 trajectories, whereas on the coarser, this spacing was increased to 20 trajectories. The statistical errors were computed using a moving-block-bootstrap technique (cf. section 2.3.5) with a bin size of 2 and 8 configurations for the coarsest and finest lattices respectively. The number of bootstrap samples is chosen to be 2000, because the calculated bootstrap errors saturate at ≈ 1500 samples. At each beta, we ran fully unquenched simulations at a minimum of four masses, such that the ratio M_π/M_ρ lays in between 0.60 and 0.68. It is preferable to use rather large masses in order to enhance possible discretization effects of order aM.

After fixing to Coulomb gauge, we measured the correlators using multiple Gaussian sources on different time slices. The width of the sources was set to $L/4$ and is thus approximately constant in physical units. The effective masses (cf. 2.3.6) computed from these correlators reached a plateau very quickly so that sensible fitting ranges, where excited states contributions are small, could be easily defined (cf. figure 3.9 for a typical effective mass plot). The hadron masses were extracted by correlated single channel cosh or sinh fits to the correlators. In order to estimate a remaining excited state contribution, we decreased the lower end of the fit window by up to two time slices and repeated the procedure. The difference in the fit results was propagated into the systematic error. For each β, we interpolated $(aM_\pi)^2, aM_\rho, aM_N, aM_\Delta$ linearly in am^{PCAC} to a common quark mass at a determined M_π/M_ρ. This is shown for the 6 EXP action at $\beta = 3.59$ in figure 3.10. The errors of am^{PCAC} are of $\mathcal{O}(10^{-4})$ and therefore barely visible at this scale. The scaling tests for the baryon spectrum were performed at four different values of M_π/M_ρ ranging from 0.60 to 0.68. All of these points can be reached by interpolation so no extrapolation in the quark mass is necessary. Table 3.1 summarizes the values of am^{PCAC}, aM_π, aM_ρ, aM_N and aM_Δ after interpolation to our four M_π/M_ρ ratios. We also list $M_\pi L$ which is roughly constant for fixed M_π/M_ρ. The table also shows that we are deep in the $M_\pi L$ regime even for our lightest masses, so that we could safely neglect finite volume effects. Even if this criterion alone does not guarantee the smallness of finite volume effects, our scaling study would still be meaningful: the fact that
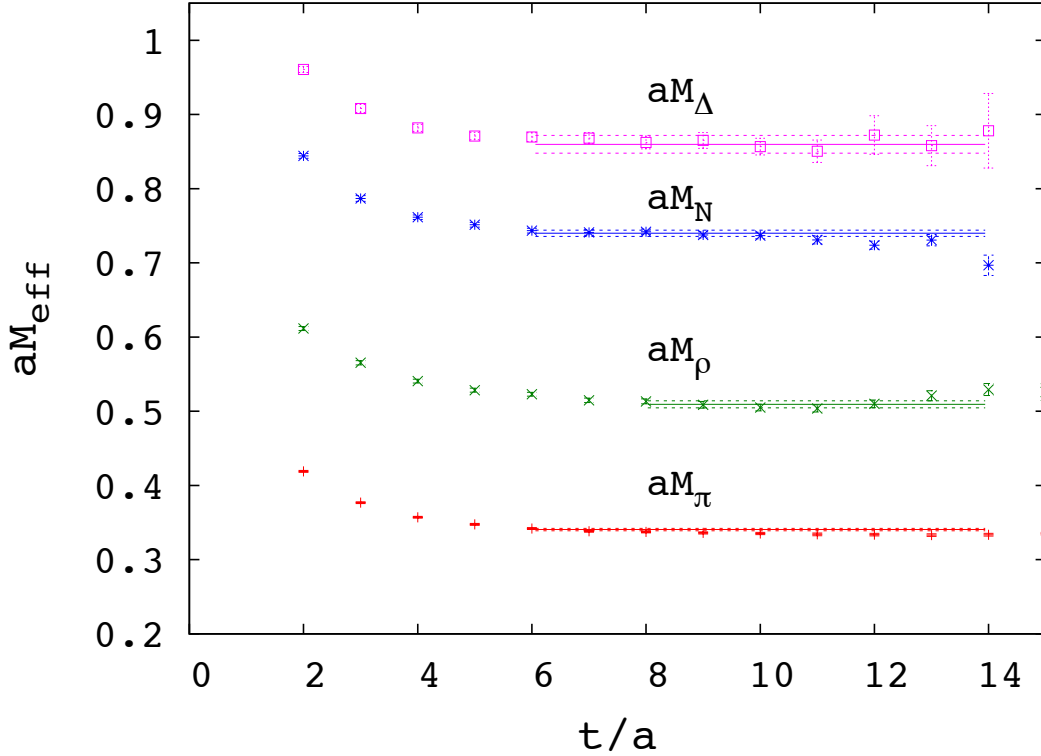
Figure 3.9.: Effective masses of the hadron spectrum on the 6 EXP ensemble with $L/a = 16$, $\beta = 3.59$, $am^{\mathrm{PCAC}} = 0.04608(12)$. The points are obtained by solving equation $C(t-1)/C(t+1) = f(am_{\mathrm{eff}}(t-1-T/2))/f(am_{\mathrm{eff}}(t+1-T/2))$, where $f(x) = \cosh(x)$ (for π and ρ) or $\sinh(x)$ (for N and Δ). The horizontal lines denote the fitted masses along with the error bars. The fit range is indicated by the length of the lines [from Durr et al., 2009].

our boxes have a fixed physical size ensures that possible finite volume effects are of the same size for all data at a given M_π/M_ρ ratio.

All masses are known to better than 2% and this is also true for their ratios due to correlations. Figure 3.11 shows the continuum extrapolations of M_N/M_π and M_Δ/M_π at the ratios $M_\pi/M_\rho = 0.60, 0.64, 0.68$ for both actions assuming $\mathcal{O}(a^2)$ cutoff effects, measured in units of M_ρ^{-2}. The baryon masses are normalized by M_π in order to separate clearly the three lines of constant physics. The horizontal and vertical error bars shown in the plots are all purely statistical and were both incorporated into the fits. The results for the continuum extrapolation are displayed in table 3.2. As expected, all masses agree within errors. The point at $\beta = 2.8$ for the 6 EXP data was not included in the fits but it agrees with the corresponding continuum limits at the 3%-level (cf. figure 3.11).

Although our clover coefficient is close to a non-perturbative determined value, we cannot exclude $\mathcal{O}(\alpha_s a)$ effects even from our precise data, covering a factor of seven in units of a^2. Hence, we chose a fourth ratio $M_\pi/M_\rho = [2(M_K^{\mathrm{phys}})^2 - (M_\pi^{\mathrm{phys}})^2]^{1/2} \approx 0.67$ and identify M_ρ with the mass of the physical ϕ. Therefore we could express our lattice spacing in physical
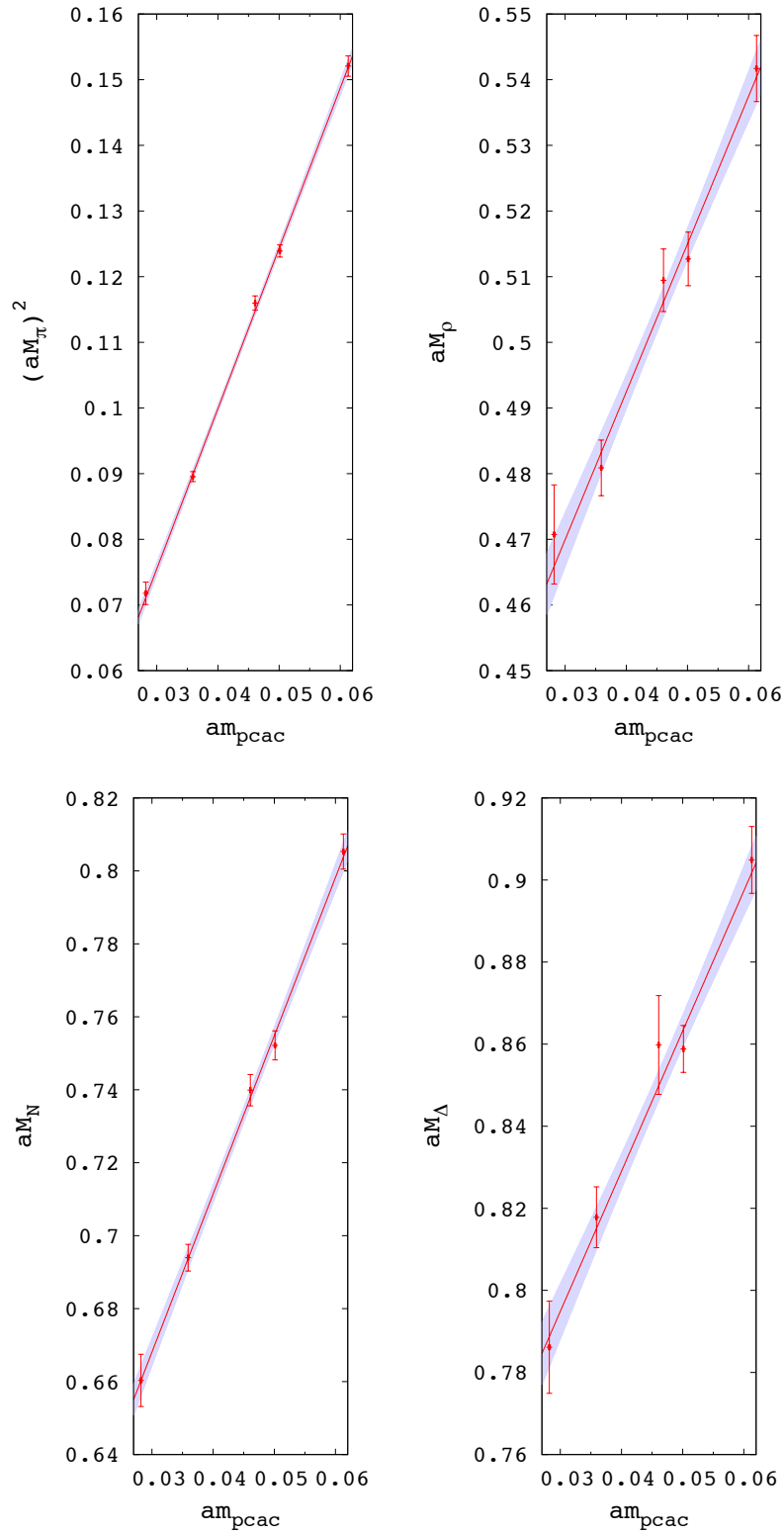
Figure 3.10.: Linear fits of the spectrum in terms of the bare PCAC quark mass. The displayed dataset is from the 6 EXP study at $\beta = 3.59$ with $L/a = 16$. The line indicates the central value of the interpolation and the shaded region is the corresponding 1σ statistical error band [from Durr et al., 2009].

(a) 6 EXP

M_π/M_ρ	L/a	β	am_{PCAC}	LM_π	aM_π	aM_ρ	aM_{N}	aM_Δ
	8	2.80	0.0676(11)	4.55	0.5688(26)	0.9480(44)	1.3605(73)	1.5944(75)
	10	3.23	0.0468(28)	4.44	0.4437(57)	0.7395(95)	1.064(12)	1.248(10)
0.60	12	3.40	0.0456(16)	4.60	0.3830(34)	0.6384(57)	0.9236(74)	1.0823(87)
	16	3.59	0.0324(8)	4.56	0.2852(26)	0.4754(43)	0.6785(44)	0.8006(38)
	24	3.76	0.0229(5)	4.85	0.2019(20)	0.3365(33)	0.4825(34)	0.5708(20)
	8	2.80	0.0839(8)	5.03	0.6292(21)	0.9832(33)	1.4341(43)	1.6581(59)
	10	3.23	0.0607(23)	4.95	0.4950(47)	0.7735(73)	1.127(10)	1.3074(82)
0.64	12	3.40	0.0568(13)	5.12	0.4268(23)	0.6669(35)	0.9711(62)	1.1282(71)
	16	3.59	0.0396(7)	5.03	0.3146(23)	0.4916(36)	0.7099(35)	0.8279(29)
	24	3.76	0.0284(6)	5.41	0.2256(18)	0.3524(28)	0.5081(29)	0.5933(29)
	8	2.80	0.1050(11)	5.60	0.6993(22)	1.0284(32)	1.5286(52)	1.7401(65)
	10	3.23	0.0796(21)	5.57	0.5574(52)	0.8198(76)	1.212(11)	1.389(10)
0.68	12	3.40	0.0718(13)	5.76	0.4798(30)	0.7055(44)	1.0354(47)	1.1903(52)
	16	3.59	0.0488(7)	5.57	0.3483(22)	0.5122(32)	0.7495(30)	0.8624(44)
	24	3.76	0.0359(10)	6.11	0.2546(25)	0.3744(37)	0.5434(38)	0.6242(39)

(b) 2 HEX

M_π/M_ρ	L/a	β	am_{PCAC}	LM_π	aM_π	aM_ρ	aM_{N}	aM_Δ
	10	3.23	0.0487(16)	4.49	0.4485(47)	0.7475(78)	1.0699(76)	1.2749(86)
0.60	12	3.40	0.0445(4)	4.49	0.3743(17)	0.6238(28)	0.8984(27)	1.0602(32)
	16	3.59	0.0318(4)	4.48	0.2798(15)	0.4664(25)	0.6653(29)	0.7824(47)
	24	3.76	0.0225(12)	4.87	0.2028(47)	0.3380(78)	0.4823(71)	0.5667(14)
	10	3.23	0.0627(12)	4.98	0.4976(34)	0.7775(53)	1.1253(53)	1.3201(63)
0.64	12	3.40	0.0559(4)	5.01	0.4173(15)	0.6521(23)	0.9454(22)	1.0995(33)
	16	3.59	0.0399(3)	5.00	0.3123(12)	0.4880(19)	0.7020(28)	0.8167(40)
	24	3.76	0.0282(10)	5.44	0.2267(36)	0.3542(56)	0.5090(56)	0.5932(95)
	10	3.23	0.0811(15)	5.56	0.5556(40)	0.8170(59)	1.1980(68)	1.3794(82)
0.68	12	3.40	0.0714(8)	5.64	0.4696(28)	0.6906(41)	1.0094(47)	1.1529(59)
	16	3.59	0.0510(4)	5.63	0.3519(14)	0.5174(20)	0.7522(30)	0.8637(37)
	24	3.76	0.0362(9)	6.15	0.2561(30)	0.3767(43)	0.5459(45)	0.6299(72)

Table 3.1.: Results of the interpolation of aM_π, aM_ρ, aM_N and aM_Δ, obtained from simulations performed at different bare quark masses and gauge couplings, to the reference points $M_\pi/M_\rho = 0.60, 0.64, 0.68$ for the 6 EXP (a) and 2 HEX (b) scaling runs (table (a) from [Durr et al., 2009]).

	M_π/M_ρ	0.60	0.64	0.68	0.67 $(\alpha_s a)$ [MeV]	0.67 (a^2) [MeV]
6 EXP	M_N	2.369(22)(08)	2.239(14)(04)	2.128(11)(02)	1483(09)(02)	1488(08)(01)
	M_Δ	2.839(34)(28)	2.628(22)(10)	2.434(18)(16)	1710(14)(07)	1713(12)(07)
2 HEX	M_N	2.392(32)(12)	2.245(19)(03)	2.120(10)(04)	1480(09)(02)	1485(08)(02)
	M_Δ	2.779(52)(32)	2.611(31)(11)	2.467(28)(33)	1723(18)(19)	1725(15)(15)

Table 3.2.: Continuum limits for M_N and M_Δ at the different M_π/M_ρ ratios. The first error is statistical and the second one our systematic error. It includes different fit ranges for extracting the masses from correlators. The last two columns show the cotinuum limits of the $\mathcal{O}(\alpha_s a)$ and $\mathcal{O}(a^2)$ extrapolations at $M_\pi/M_\rho = 0.67$ in physical units. All results agree within errors.

units and compute $\alpha_s(\mu)$ for arbitrary scales μ using 4-loop perturbation theory [van Ritbergen et al., 1997] for three active flavours. Using this setup we repeated the analysis, this time assuming $\mathcal{O}(\alpha_s a)$ or $\mathcal{O}(a^2)$ scaling.[4] The plots are shown in figure 3.12 and the corresponding continuum limits can be found in the last two columns of table 3.2. As expected, all continuum limits for the respective masses are compatible within errors. The fit qualities slightly favour $\mathcal{O}(a^2)$ scaling, but for later phenomenological applications we included both scaling assumptions into our final estimates and enhanced our systematic error accordingly. Note that the scaling window extends at least up to $\simeq 0.16$ fm and the scaling corrections, i.e. the deviation of the measured baryon masses on the coarsest lattices from their continuum limit, are at most around 2% for M_Δ and the 2 HEX action.

We have demonstrated in a dedicated scaling test of light baryon masses, including five lattice spacings with a total variation by almost a factor of three, that scaling violations associated with the use of our both actions in full QCD are small for these quantities. For lattice spacings up to 0.16 fm, the discretization errors on the light baryon masses do not exceed 2% for all lattice spacings up to 0.19 fm. A small slope in the continuum extrapolation is very useful for obtaining precise continuum limits. Futhermore, all data below 0.16 fm seem to be inside the scaling window, which is in line with findings of Kamleh et al. [2008] where a different approach to link smearing is taken.
As a final conclusion we can recommend both actions for phenomenological calculation of hadron masses and expect this also to be true for comparable improvements. In part 4.1, I will show physical results for the non-singlet low-lying hadron spectrum of QCD, computed using our 6 EXP approach.

---

[4]In our original paper [Durr et al., 2009], we assumed $\mathcal{O}(a)$ instead of $\mathcal{O}(\alpha_s a)$ scaling. However, the statements on the quality of the scaling we made here also hold for the results of that paper. In our computation of the spectrum [Dürr et al., 2008] we compared $\mathcal{O}(a^2)$ to $\mathcal{O}(a)$ scaling, and the scaling study [Durr et al., 2009] was performed in order to prove that this important computation is reliable and as precise as stated. However, since $\mathcal{O}(\alpha_s a)$ is closer to $\mathcal{O}(a^2)$ scaling than $\mathcal{O}(a)$ to $\mathcal{O}(a^2)$ scaling, the assumptions in [Dürr et al., 2008] may have at worst slightly increased the systematic errors of our final results.

(a) 6 EXP

(b) 2 HEX
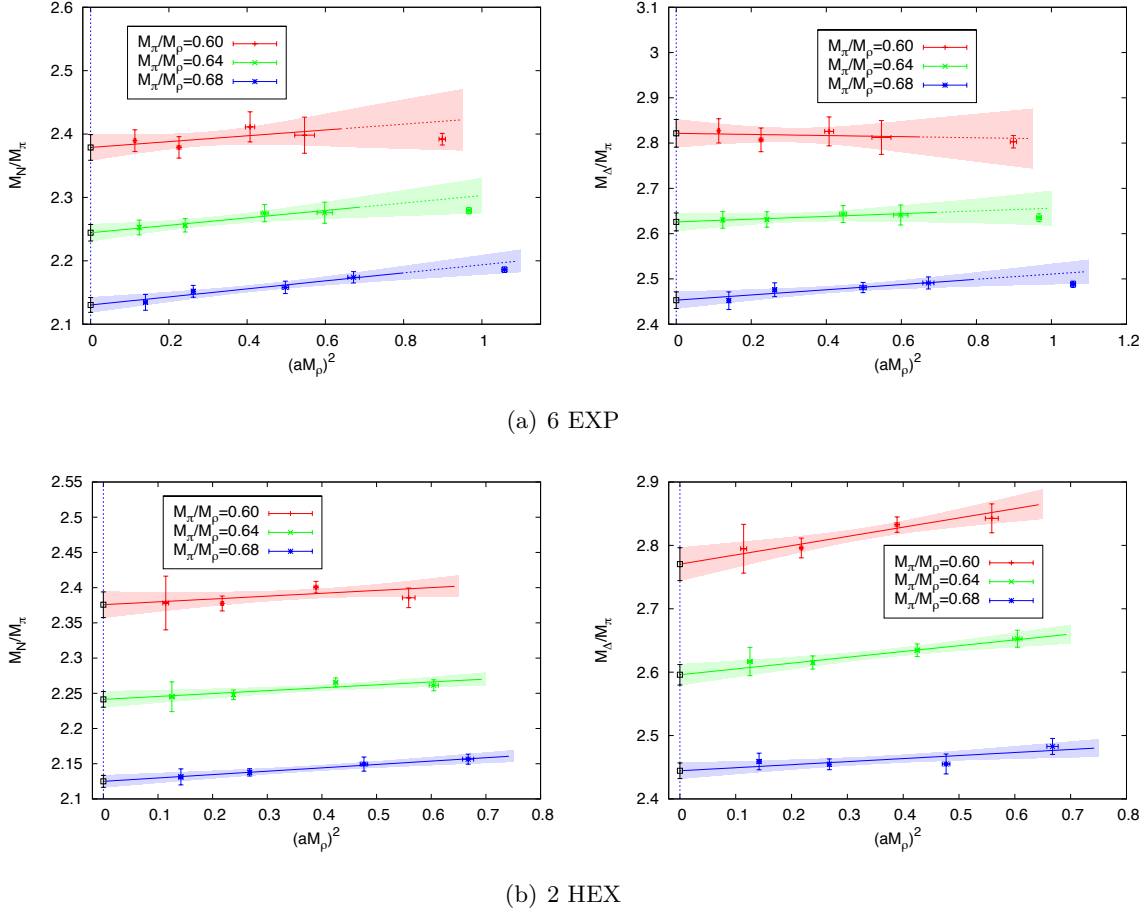
Figure 3.11.: Continuum extrapolation of the spin $1/2$ and $3/2$ baryon masses versus the lattice spacing squared in units of M_ρ^{-2} for both actions. The fits include the data from $\beta = 3.76$ to $\beta = 3.23$, where the curve in (a) is extended to $\beta = 2.8$ for comparison. In case of the 2 HEX action at $\beta = 3.76$ and small quark masses, the error is significantly larger compared to that of the 6 EXP data. Since the statistics is of $\mathcal{O}(1000)$ trajectories in both cases, this indicates that the 2 HEX action is slightly less efficient than the 6 EXP action. In that sense, we approximately doubled the statistics for $\beta = 3.59$ and 3.4, so that their error bars are much smaller than those of the 6 EXP data (plots for 6 EXP action are published in [Durr et al., 2009]).

(a) 6 EXP

(b) 2 HEX
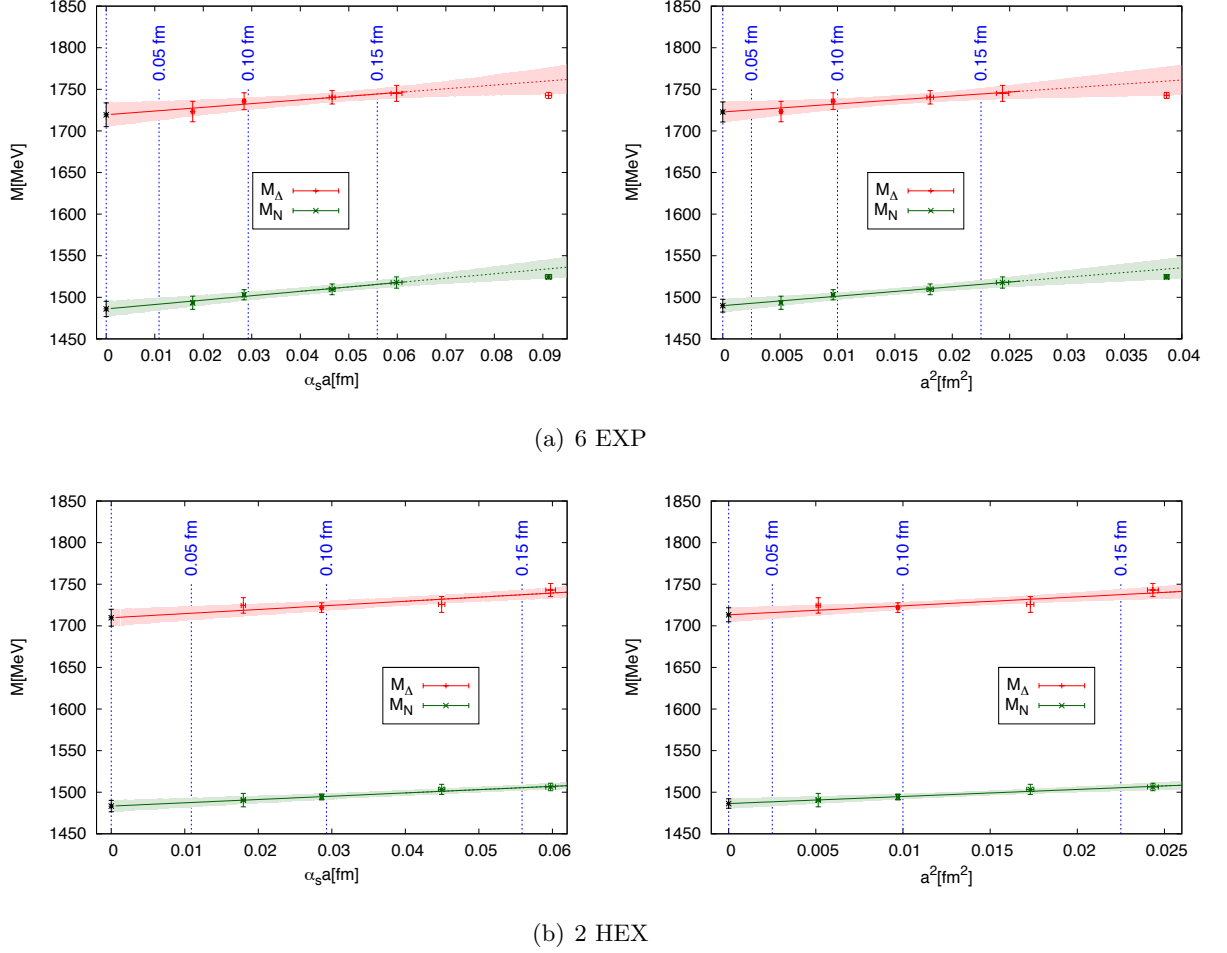
Figure 3.12.: Continuum extrapolation of the spin $1/2$ and $3/2$ baryon masses for both actions assuming $\mathcal{O}(a^2)$ and $\mathcal{O}(\alpha_s a)$ scaling. The strong coupling α_s at the given scales was computed using 4-loop perturbation theory with three active flavours. All continuum limits from the four fits agree within errors as expected. From visual inspection, one cannot exclude one of the scaling assumptions but the fit qualities slightly favour $\mathcal{O}(a^2)$ over $\mathcal{O}(\alpha_s a)$ scaling. Thus, we decided to include both scaling assumptions into our finals estimates and therefore into our systematic error (6 EXP $\mathcal{O}(a^2)$ plot from [Durr et al., 2009] and 2 HEX plots from [Durr et al., 2010]).

3.2.2. Scaling of quenched quark masses

After the successful scaling tests of the hadron masses, we tested the scaling of a different kind of observable. This was the quenched average heavy-light quark mass $m_{ud}+m_s$, which, unlike hadron masses, required renormalization. In this test, we aimed at reproducing the results of Garden et al. [2000] using our setup. This means that we computed the continuum limit of $m_{ud}+m_s$ in the RI and $\overline{\text{MS}}$ scheme for our 2 HEX action within a quenched simulation. We used the pure Wilson plaquette action (2.109) to generate configurations at five different lattice spacings with β ranging from 5.7366 to 6.3. Each time we saved 600 well de-correlated configurations for the analysis (i.e. 200 for determining the renormalization factors Z_S and 400 for computing the bare quark masses am^{VWI}).

The couplings and geometries were chosen to realize a physical box size of $L \simeq 1.84\,\text{fm}$ (see table 3.3) by using our fit to the Necco-Sommer data (cf. appendix B). On each set, at least four quark masses were used to safely interpolate to $M_{\text{P}}\,r_0 = 1.299$, where M_{P} is the pseudoscalar mass and its value in r_0 units has been chosen to match (the isopospin averaged) $M_K^{\text{phys}}\,r_0$ assuming $r_0 = 0.49\,\text{fm}$ [Sommer, 1994a]. The main aspects of this computation were also used for determining m_{ud} and m_s in a full QCD calculation (cf. 4.2). We computed the x-axis intersection of m^{PCAC} versus $m^{(\text{bare})}$ which follows a linear relationship. This intersection point defines m^{crit} and thus, using the input bare masses, we obtained the unrenormalized m^{VWI}.

We determined $Z_S(\mu,a)$ non-perturbatively in the RI scheme (cf. 2.4.2) with the trace-subtraction improvement [Capitani et al., 2001; Becirevic et al., 2000; Martinelli et al., 2001; Maillart and Niedermayer, 2008, also cf. section 2.4.3]. Hence we replaced all propagators S in the RI procedure with their trace-subtracted counterparts $\bar{S} = S - \text{Tr}[S]/4$, removing a contact term of $\mathcal{O}(a)$ from the renormalization factors. To improve translational invariance, we always used four different sources at the hyper-diagonal positions

$$x_0 \in \left\{ (0,0,0,0), \left(\frac{L_x}{4}, \frac{L_y}{4}, \frac{L_z}{4}, \frac{L_t}{4} \right), \left(\frac{L_x}{2}, \frac{L_y}{2}, \frac{L_z}{2}, \frac{L_t}{2} \right), \left(\frac{3L_x}{4}, \frac{3L_y}{4}, \frac{3L_z}{4}, \frac{3L_t}{4} \right) \right\} \quad (3.4)$$

for computing the momentum-space propagators and Greens functions (cf. expression (2.242)). Note that the obtained Z_S is the non-singlet scalar renormalization constant because all quark disconnected contributions vanish in the quenched theory. Before computing the momenta using the bosonic momentum definition

$$p^2 \equiv \sum_{\nu=1}^{4} \hat{p}_\nu^2 = \frac{4}{a^2} \sum_{\nu=1}^{4} \sin^2(ap_\nu/2), \quad (3.5)$$

with $ap_\nu = 2\pi x_\nu / L_\nu$, we applied a hyper-diagonal cylinder cut on the dual lattice [Leinweber et al., 1998]. This procedure significantly improves the data since the renormalization factors obtained from there are not as highly affected by the breaking of $O(4)$ invariance as those at momenta which lie close to one axis. We ended up with values of $Z_S^{\text{RI}}(\mu,a)$ at different momenta pa which survived this cut.

In order to be able to control systematic effects in the determination of RI renormalization constants, we have to consider that:

1. the renormalization scale μ has to be significantly below the cutoff π/a (upper window condition).

2. the renormalization scale μ has to be in the perturbative regime in order to match the non-perturbative data to perturbation theory, i.e. $\mu \gg \Lambda_{\mathrm{QCD}}$ (lower window condition).

3. the chiral limit $m \to 0$ has to be under control.

To solve these problems, we applied the following methods:

Ad 1. We found that for $\mu < \pi/(2a)$, deviations from the continuum Dirac operator's dispersion relation were acceptable (cf. section 2.4.2). The choice $\mu' = 2.1$ fulfilled this strict window condition on our four finest lattices (cf. figure 3.13).

Ad 2. In order to fulfill the second condition, we would have had to set $\mu \geq 3\,\mathrm{GeV}$, because the perturbative expectation describes our data for these scales (cf. figure 3.14). However, we were not able to choose these large scales because this would have violated condition 1 on the coarser lattices. To circumvent this restriction, we used the ratio-extrapolation method described in section 2.4.3.
According to formula (2.290), we set $\mu = 3.5\,\mathrm{GeV}$ (and $\mu' = 2.1\,\mathrm{GeV}$ as mentioned above). For this μ, the strict window condition was fulfilled for the three finest lattice spacings. By performing a linear fit of $R_S(\mu, \mu', a)$, only including these lattices and assuming $\mathcal{O}(\alpha_s a)$ or $\mathcal{O}(a^2)$ scaling, we computed the non-perturbative continuum running $R_S(3.5\,\mathrm{GeV}, 2.1\,\mathrm{GeV})$ (cf. figure 3.16). This extrapolation is well controlled, since the slope of the fit is very mild (as expected from visual inspection of 3.13). We used the extrapolated running to compute $Z_S(3.5\,\mathrm{GeV}, a)$ on all lattice spacings.

Ad 3. We performed a linear extrapolation to the chiral limit in $(M_{\mathrm{P}}\, r_0)^2$ for all scales μ. This point-by-point extrapolation gives reliable results because the slope in these extrapolations is extremely flat (cf. figure 3.15).

Finally we computed the renormalized quark mass $m^{\mathrm{VWI}} r_0(\mu)$ at $\mu = 3.5\,\mathrm{GeV}$ in the RI scheme via (2.202). We converted this value to the $\overline{\mathrm{MS}}$ scheme at $2\,\mathrm{GeV}$ for illustrative reasons using 4-loop perturbation theory [van Ritbergen et al., 1997; Vermaseren et al., 1997; Chetyrkin and Retey, 2000].[5] The result was identified with the heavy-light quark mass average $(m_s + m_{ud})\, r_0$ and extrapolated into the continuum limit by again applying both of our scaling assumptions (cf. figure 3.17). Using our method for propagating statistical and systematic errors from section 2.3.5, we obtained the combined result in the continuum limit

$$(m_s + m_{ud})^{\overline{\mathrm{MS}}} r_0(2\,\mathrm{GeV}) = 0.2609(39)(28), \qquad (3.6)$$

where the first error is statistical and the second one is systematic. We computed the statistical error by repeating the analysis on 2000 bootstrap samples. For obtaining the systematic error, we used three different fit ranges for extracting the masses from the correlators, two different scaling assumptions for the continuum limit and three scales $\mu = 3, 3.5$ and $4\,\mathrm{GeV}$ at which we matched the non-perturbative results to perturbation theory. The dominant source of systematic uncertainty is the continuum extrapolation, contributing by about 1% to the total systematic error.

---

[5]In order to determine a starting value for the quenched strong coupling α_s, we used $\Lambda_{QCD} = 242.43\,\mathrm{MeV}$ which was converted from results of Capitani et al. [1999] by consistently assuming $r_0 = 0.49\,\mathrm{fm}$.

Our result (3.6) is in perfect agreement with the continuum value $(m_s + m_{ud})r_0 = 0.261(9)$ quoted by the ALPHA collaboration [Garden et al., 2000]. It is consistent within less than 1σ with the result $0.274(18)$ given by JLQCD [Aoki et al., 1999] and, within less than 2σ, with the value $0.312(28)$ obtained in a quenched overlap computation [Durr and Hoelbling, 2005]. There is some tension with the result $0.293(6)$ by CP-PACS [Aoki et al., 2003a] but this result does not include any systematic error estimation for the perturbative renormalization involved in their computations.

Assuming $r_0 = 0.49\,\mathrm{fm}$ and $m_s/m_{ud} \approx 27.5$ as suggested by the results from section 4.2, our result (3.6) can be used to compute the quenched strange quark mass

$$m_s^{\overline{\mathrm{MS}}}(2\,\mathrm{GeV}) = 101.4(1.5)(1.1). \tag{3.7}$$

This value does not include any error related to the use of perturbation theory as well as the inherent quenched scale setting ambiguity.

The scaling window of the continuum extrapolation extends up to $a \approx 0.15\,\mathrm{fm}$ where we observe mild scaling corrections below 8%. The coarsest data point at $\beta = 5.7366$ therefore lies outside the scaling window. The qualities of fit slightly favour $\mathcal{O}(a^2)$ over $\mathcal{O}(\alpha_s a)$ scaling and the fact that the coarsest data point is closer to the fit curve for the former assumption may emphasize this preference.

Our conclusion is that the 2 HEX action is well suited for computing light quark masses in lattice simulations.

β	$L^3 \times T$	$(m_s + m_{ud})r_0$
5.7366	$12^3 \times 24$	0.3070(50)
5.8726	$16^3 \times 32$	0.2801(50)
5.9956	$20^3 \times 40$	0.2758(52)
6.1068	$24^3 \times 48$	0.2654(42)
6.3000	$32^3 \times 64$	0.2685(29)

Table 3.3.: Simulation parameters and measured quenched quark masses in the $\overline{\mathrm{MS}}$ scheme at 2 GeV [from Durr et al., 2010].
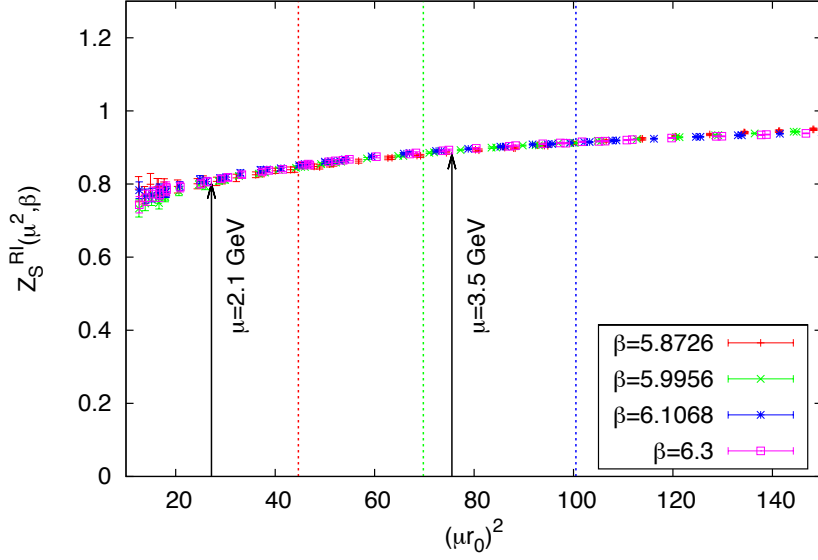
Figure 3.13.: Multiplicatively matched Z_S. The colored dashed vertical bars denote the cutoff $p = \pi/(2a)$ for the three coarsest lattice spacings. For $\beta = 6.3$, $(\mu r_0)^2 \approx 179$ is off the scale. We see very nice agreement of the data for the different lattice spacings and hence expect that discretization effects are small. Note that a slight (a^2-dependent) linear slope was fitted out in this matching (cf. also figure 3.14). This plot is taken from [Kurth et al., 2010].
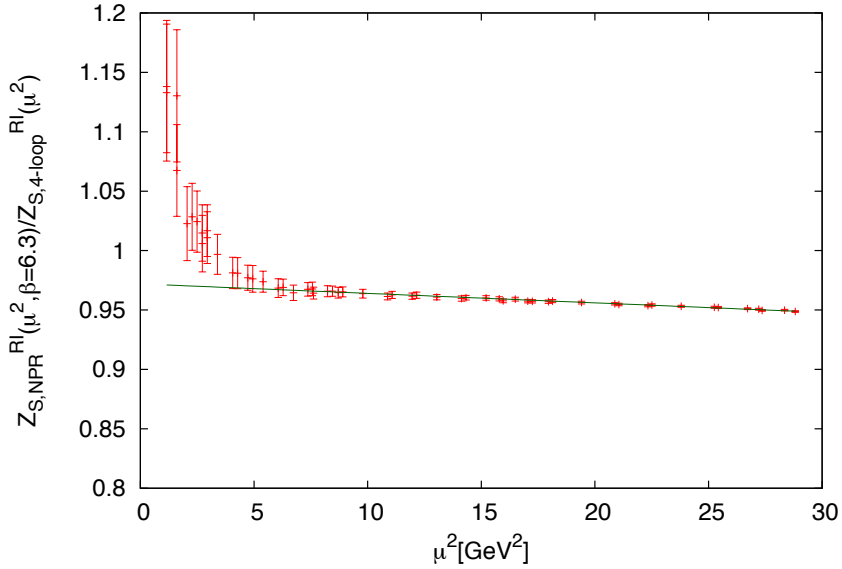
Figure 3.14.: Scalar renormalization factors $Z_S^{\mathrm{RI}}(\mu)$ on the finest lattice ($\beta = 6.3$) divided by the perturbative four-loop running [Chetyrkin and Retey, 2000]. The remaining linear slope is a cutoff effect proportional to $(pa)^2$ and of $\mathcal{O}(10^{-4})$. Thus it gives a small contribution to the systematic error.
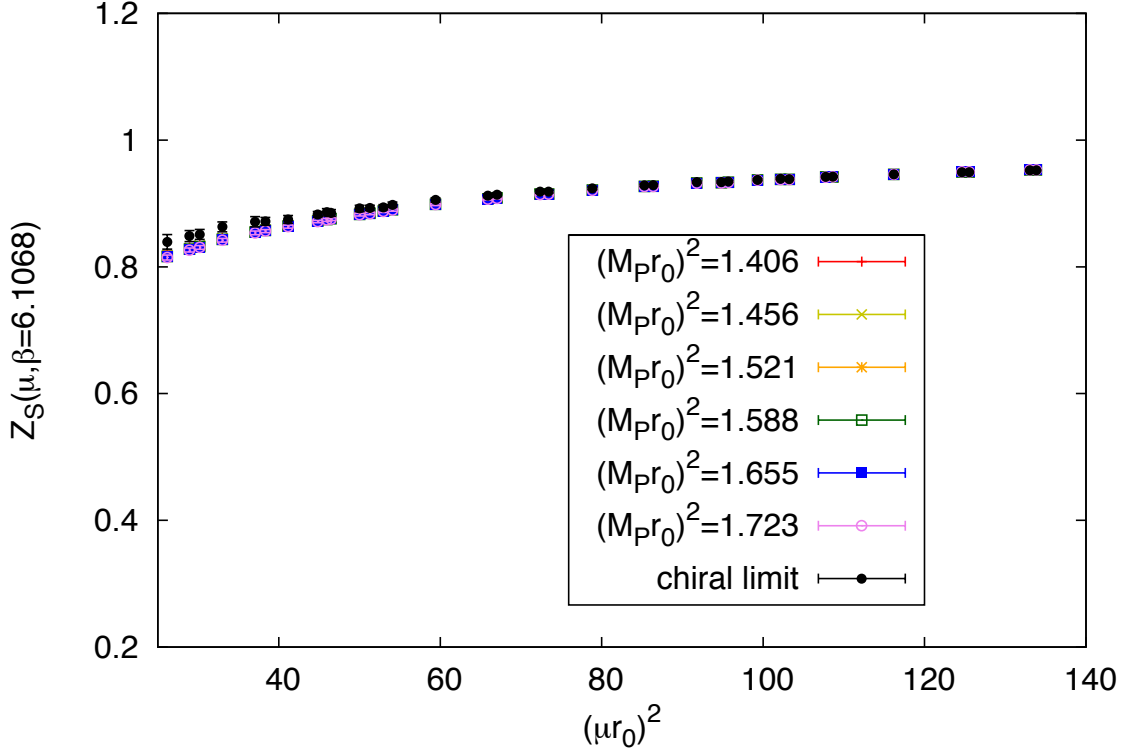
Figure 3.15.: Chiral extrapolation of Z_S at $\beta = 6.1068$. The different symbols collapse because the chiral extrapolation is extremely flat in the region of interest and the statistical error bars on the data points for $(\mu r_0)^2 > 60$ are smaller than the symbols.
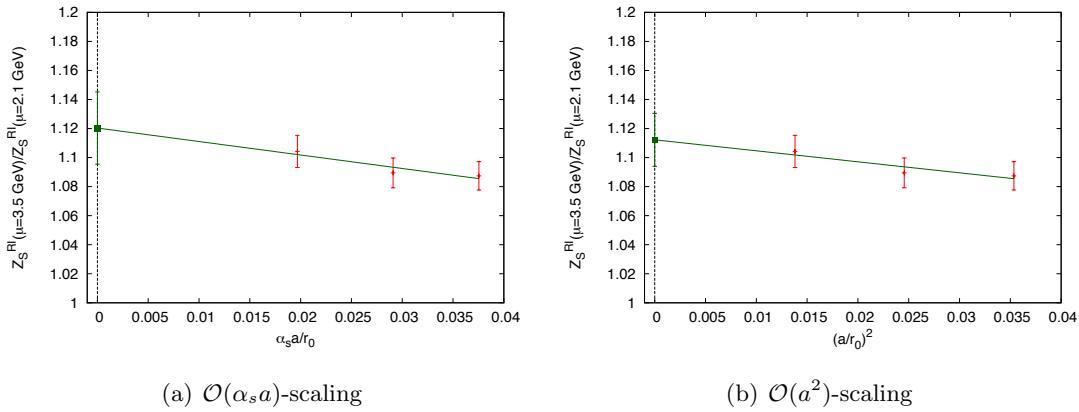
(a) $\mathcal{O}(\alpha_s a)$-scaling

(b) $\mathcal{O}(a^2)$-scaling

Figure 3.16.: Continuum extrapolation of (2.290) for Z_S on the three finest lattices, assuming $\mathcal{O}(\alpha_s a)$ (a) or $\mathcal{O}(a^2)$ scaling (b). The extrapolation is fairly flat as already expected from figure 3.13 [cf. Kurth et al., 2010].
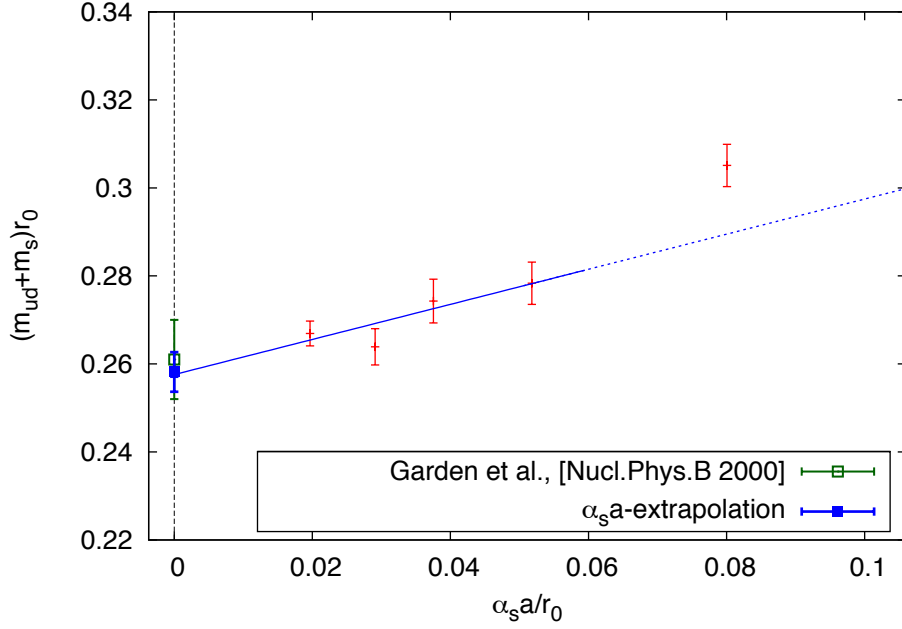
(a) $\mathcal{O}(\alpha_s a)$-scaling
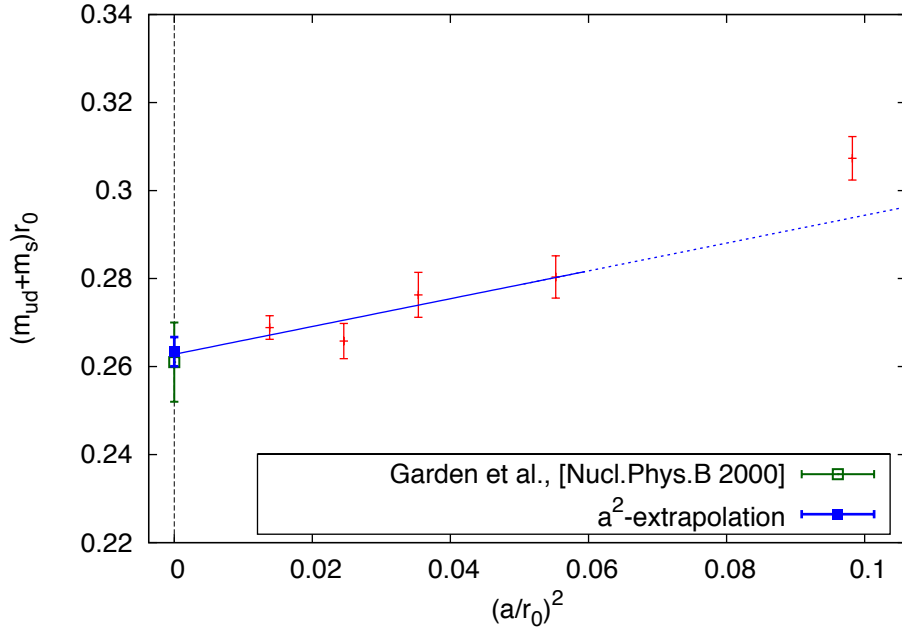
(b) $\mathcal{O}(a^2)$-scaling

Figure 3.17.: Continuum extrapolation of quenched $(m_s + m_{ud})^{\mathrm{RI}}$ at $2\,\mathrm{GeV}$ in units of r_0 [from Durr et al., 2010; Kurth et al., 2010].

3.2.3. Scaling of quenched kaon bag parameter B_K

The calculation of the kaon bag parameter B_K is complicated by the mixing of $O^{\Delta S=2} = O_1$ with same-dimension operators $O_2, \ldots O_5$ under renormalization (cf. section 2.4.2). Since the latter are chirally enhanced with respect to O_1 [cf. e.g. Aoki et al., 2006], the extraction of the mixing coefficients Δ_{1k} is a delicate task. Thus, before going to predict B_K using a full N_f=2+1 calculation, it is useful to study this quantity in the quenched approximation. In this testbed, all data analysis methods can be developed and optimized before being applied to the dynamical case.

This computation was performed on some of the configurations used for calculating the quenched quark mass (cf. section 3.2.2). The coarsest lattice spacing at $\beta = 5.7366$ was not used, because the low momentum cutoff did not allow for a safe extraction of the mixing coefficients. However, all configurations for the remaining four lattice spacings between $\beta = 5.8726$ and $\beta = 6.3$ could be used in this study. Analogously, from the 600 well decorrelated configurations per beta, we used 200 for extracting renormalization and mixing coefficients and the remaining 400 for computing the bare matrix elements. The large constant physical volume with $L \simeq 1.84\,\mathrm{fm}$ and $m_{ud} = m_s$, leading to large pseudoscalar masses M_P, guarantee that possible finite volume effects to B_K are very small according to Becirevic and Villadoro [2004]. However, we still correct for these effects using their corresponding formulas. Furthermore, we used at least four quark masses per lattice spacing allowing for safe chiral extrapolations of the renormalization factors as well as interpolation of the renormalized B_K to the physical kaon mass. The scale setting procedure is the same as in section 3.2.2.

Non-perturbative renormalization

Analogous to section 3.2.2, we used the non-perturbative RI scheme to compute the axial-current renormalization factor Z_A, necessary to renormalize the denominator in (2.102). The additional renormalization factors for the four fermion operator O_1 was also obtained non-perturbatively (cf. section 2.4.2). Before extracting the Greens functions, the trace-subtraction (cf. section 2.4.3) was applied to the propagators in order to remove an $O(a)$ contact term. We also used four point sources located on the lattice hyper-diagonal in order to improve translational invariance. Furthermore, we applied hyper-diagonal cylinder cuts in order to minimize $O(4)$ breaking effects.

For partially canceling systematic effects in the multiplicative renormalization constant $Z_{B_K} = Z_{11}^+/Z_A^2$, with Z_{11}^+ being defined in (2.253), we compute

$$Z_{B_K}^{\mathrm{RI}} = \left(\frac{Z_{11}^+}{Z_q^2}\right)^{\mathrm{RI}} \cdot \left(\frac{Z_q^2}{Z_A^2}\right)^{\mathrm{RI}} \tag{3.8}$$

directly from the RI data. Thus, there is no need to calculate Z_q separately as was done in section 3.2.2. However, we have checked that the results from both procedures are in good agreement. To improve the matching of the non-perturbative data to continuum perturbation theory, we apply the ratio-extrapolation method (cf. section 2.4.3). In this case, we considered

the ratio

$$R_{B_K}^{\mathrm{RI}}(3.5\,\mathrm{GeV}, \mu, a) = \frac{Z_{B_K}^{\mathrm{RI}}(3.5\,\mathrm{GeV}, a)}{Z_{B_K}^{\mathrm{RI}}(\mu, a)}, \tag{3.9}$$

for $2.3\,\mathrm{GeV} \leq \mu \leq 3.5\,\mathrm{GeV}$. The continuum extrapolation of this ratio involved the three finest lattice spacings and was performed assuming $O(\alpha_s a)$ or $O(a^2)$ scaling. The resulting non-perturbative continuum running $R_{B_K}^{\mathrm{RI}}(3.5\,\mathrm{GeV}, \mu)$ was divided by the two-loop perturbative expectation in order to test the agreement of our non-perturbative data with perturbation theory. Figure 3.18 shows that the deviation from two-loop continuum perturbation theory [cf. Ciuchini et al., 1998; Buras et al., 2000] is smaller than 0.5% for $2.7\,\mathrm{GeV} \leq \mu \leq 3.5\,\mathrm{GeV}$. In order to estimate the systematic effects coming from the remaining uncertainties, we read off $Z_{B_K}^{\mathrm{RI}}$ at the three different scales $\mu \in \{2.8, 3.0, 3.4\}$ and transformed them to the higher scale $\mu = 3.5\,\mathrm{GeV}$ using our non-perturbative continuum running. All three possibilities were propagated into the systematic error.

The relevant mixing coefficients Δ_{1k} were computed by solving the system of linear equations
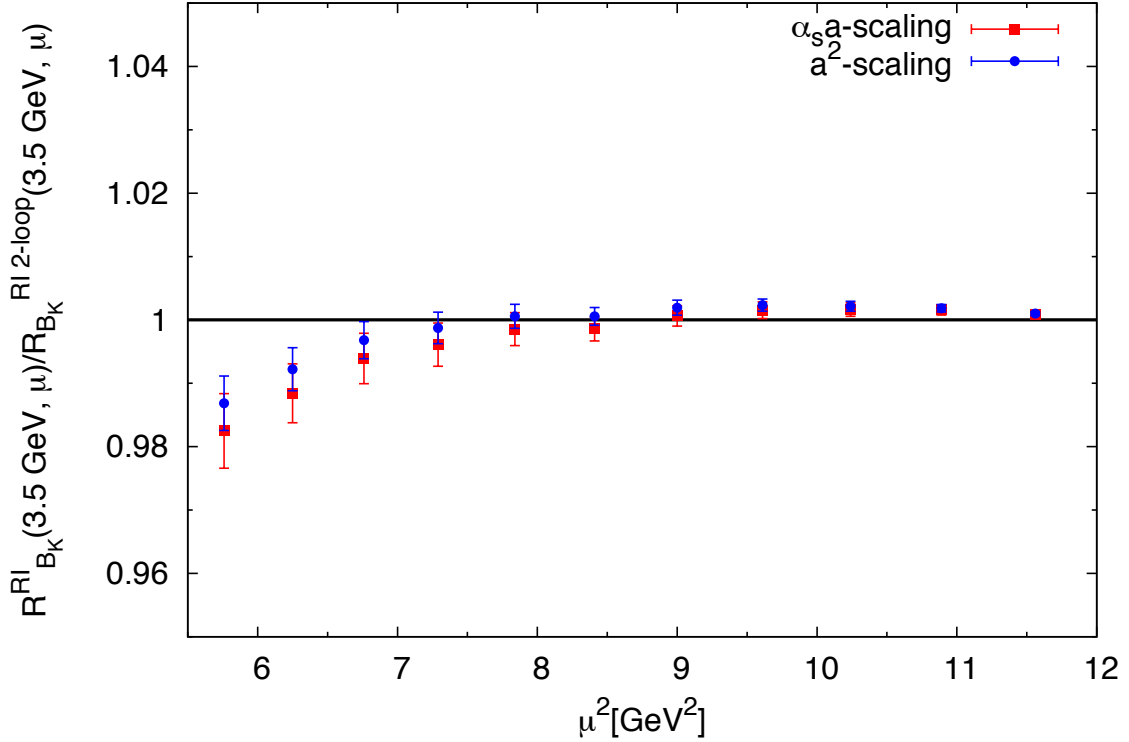
Figure 3.18.: Non-perturbative running obtained by extrapolating (3.9) into the continuum using the three finest lattice spacings, assuming $\mathcal{O}(\alpha_s a)$ (squares) or $\mathcal{O}(a^2)$ (circles) scaling. The data are divided by the two-loop perturbative running from Ciuchini et al. [1998]; Buras et al. [2000], also normalized at $\mu = 3.5\,\mathrm{GeV}$. We observe that both runnings agree within a reasonable range of scales between $2.7\,\mathrm{GeV}$ and $3.5\,\mathrm{GeV}$ to better than 0.5%.

(2.276). Note that the extracted mixing coefficients still have a mass dependence which has to be removed. Furthermore, their infrared behaviour is distorted by an $\mathcal{O}(p^{-2})$ term, probably a Goldstone boson contribution attributed to virtual pion exchanges. Thus we apply the

subtraction (cf. section 2.4.3)

$$\Delta_{1k}^{\text{sub}}(a, m_1, m_2) = \frac{m_1\,\Delta_{1k}(a, m_1) - m_2\,\Delta_{1k}(a, m_2)}{m_1 - m_2} \qquad (3.10)$$

which removes this leading term. The remaining momentum dependence comes from discretization terms of $\mathcal{O}((pa)^2)$ and double Goldstone terms of $\mathcal{O}(p^{-4})$. We applied combined fits to remove these terms and the remaining mass dependence. To estimate systematic uncertainties coming from this procedure, we used different fit ranges and different fit models including either only a $(pa)^2$ discretization term or an additional double Goldstone boson pole-term proportional to p^{-4}. Figure 3.19 shows the pole subtracted mixing coefficients Δ_{1k}^{sub} for $\beta = 5.9956$ with removed quark mass dependence and fitted by functions linear in $(ap)^2$. The mass dependence was found to be very small in all cases and could be removed by the combined fit in a stable manner.

Matrix elements

We computed the traces in the numerator shown diagrammatically in figure 2.7 in section 2.3.8 for all five operators $O_1, \ldots, O_5$. We used different random sources at $t = 0$ and $t = T/2$, where T is the temporal extent of the lattice. In order to suppress statistical fluctuations, we used the same random sources for computing the matrix elements in the numerator. The operator was inserted at $t = \tau$ where τ was varied over the whole temporal extent. Since the r.h.s. of expression (2.224) is independent of τ for sufficiently large separations $0 \ll \tau \ll T/2$ we observed a plateau between this temporal points. Note that the signal propagates through the boundaries due to the boundary conditions. Therefore, we observed a similar plateau for $T/2 \ll \tau \ll T$. Thus we improved the statistics by symmetrizing the plateaus with respect to $T/2$. The remaining averaged plateau was fitted by a constant using three different fit ranges in order to estimate possible contributions coming from excited states. Figure 3.20 shows the fits to the plateau of $Q_1(\tau)$ for $\beta = 5.9956$ and lightest quark mass along with their 1σ error bands. We observe good agreement within errors since the plateau is well pronounced. Combining the mixing coefficients with the bare matrix elements allows for decomposing the renormalized B_K into the different contributions from the individual Q_i. Figure 3.21 shows this decomposition for the relatively coarse lattice at $\beta = 5.9956$ and $M_{\text{P}} \sim 480\,\text{MeV}$. We observed that chiral symmetry breaking effects are very small, because $98.7(1.1)\%$ of the contributions to B_K come from Q_1.

Combined analysis

After obtaining the renormalized B_K, we performed a combined continuum extrapolation and interpolation to the physical isospin-averaged kaon mass $M_K^{\text{phys}} = 494.2\,\text{MeV}$. Since our data straddle the physical point, we used a Taylor ansatz for describing the quark mass and scale dependence. The generic form is given by

$$B_K^{\text{RI}}\big(3.5\,\text{GeV}, M_{\text{P}}^2, a\big) = B_K^{\text{RI}}\big(3.5\,\text{GeV}\big) \cdot \big(1 + a_1 M_{\text{P}}^2 + a_2 M_{\text{P}}^4\big) + d(a), \qquad (3.11)$$

(a) $\Delta_{12}^{\mathrm{sub}}$

(b) $\Delta_{13}^{\mathrm{sub}}$

(c) $\Delta_{14}^{\mathrm{sub}}$

(d) $\Delta_{15}^{\mathrm{sub}}$
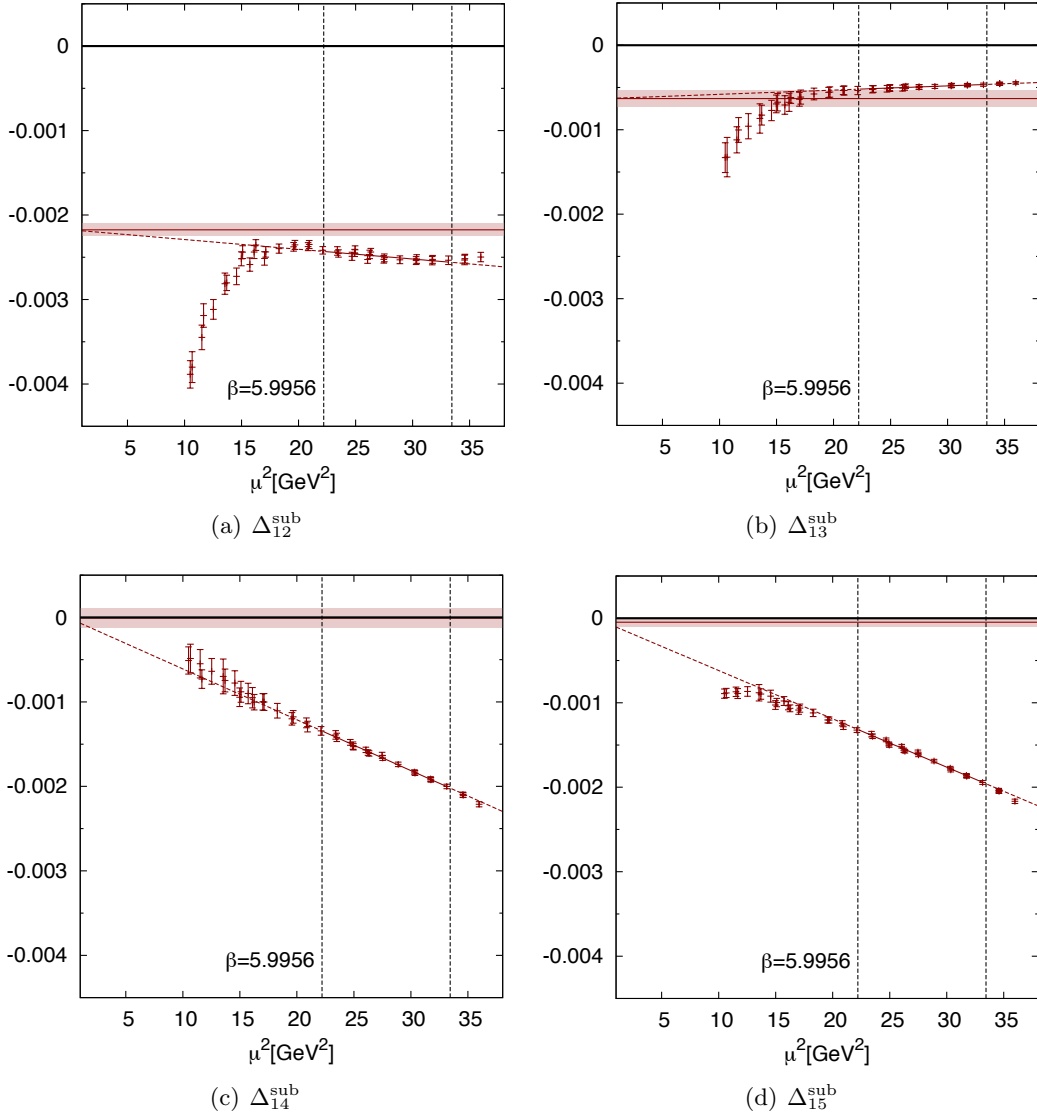
Figure 3.19.: Quenched pole subtracted mixing coefficients $\Delta_{1k}^{\mathrm{sub}}$ at $\beta = 5.9956$ plotted versus the momentum scale μ^2. The remaining small mass dependence was removed by a combined fit to the subtracted data. We observe that the momentum dependence is well described by a $(pa)^2$ term in the fitting regions denoted by the dashed vertical lines. To estimate systematic uncertainties induced by the choice of the fit window or fitting function, we used different fit ranges and fitting functions including an additional p^{-4} pole term. All these possibilities were propagated into the systematic error.

where $d(a)$ is proportional to either a^2 or $\alpha_s a$ and α_s was computed by using 4-loop perturbation theory (cf. section 3.2.2). In order to estimate systematic effects attributed to the choice of the fitting function, we used different models with a_1 free and $a_2 = 0$ or both parameters free. This also estimates higher order effects in M_{P}. We do not include terms compatible with zero in our fits. A sample fit linear in M_{P}^2 is displayed in figure 3.22. The chiral behaviour
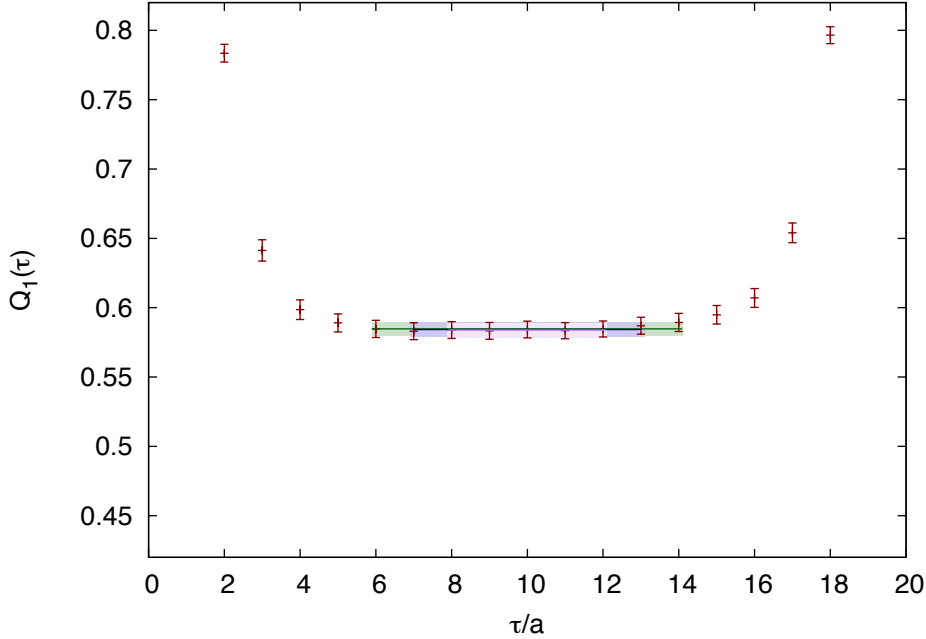
Figure 3.20.: Constant fits to quenched plateau for Q_1 at $\beta = 5.9956$ and $M_{\mathrm{P}} \sim 480\,\mathrm{MeV}$. Different colors represent different fit ranges along with their 1σ error bands. Note that we observe nice agreement between the extracted plateau values. However, we propagated the small deviations into the final systematic error by repeating the analysis for all different fit ranges.

is relatively mild and thus the interpolation in the quark mass well under control. The same is true for the continuum extrapolation as shown in figure 3.23 since the scaling corrections are on the 4% level.   To estimate the final overall error we used the procedure described in section 2.3.5. Thus, we performed the analysis on 2000 moving block bootstrap samples with atomic block size since the samples are well de-correlated. To obtain the systematic errors, we repeated the whole analysis for

- 2 different fit ranges for extracting the masses from the correlators as well as 3 different fit ranges for extracting the bare matrix elements

- 2 different scalings proportional to either $\alpha_s a$ or a^2 in the continuum extrapolation of the running as well as renormalized B_K

- 3 different scales for extracting the renormalized matrix elements and converting them to our reference scale $3.5\,\mathrm{GeV}$ using our non-perturbative continuum running

- 3 different pseudoscalar mass cuts

- 2 different fit functions and 3 different fit ranges for extracting the mixing coefficients

- 2 different functional forms in the final combined fit.

This yielded in total 2592 different analyses and hence as many values for B_K along with their qualities of fit. The weighted median of the corresponding distribution is our final value and the central 68% probability the systematic error. The final value for our quenched B_K,
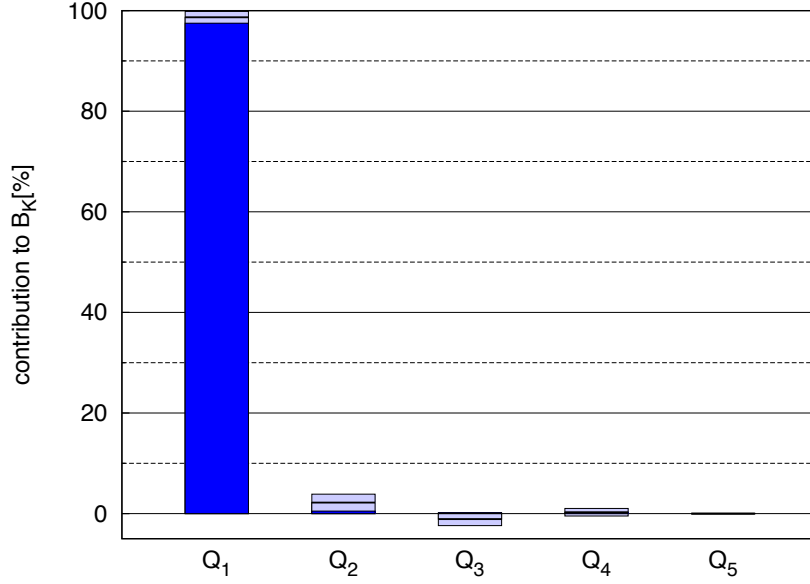
Figure 3.21.: Contributions to the renormalized B_K from the individual Q_i for $\beta = 5.9956$ and lightest mass ($M_{\mathrm{P}} \sim 480\,\mathrm{MeV}$). The blue bars denote the total contribution of the corresponding matrix element Q_i to the renormalized B_K and the lighter regions their overall uncertainty. If chiral symmetry is unbroken, operator Q_1 contributes solely to B_K. Here, chiral symmetry is broken but the contribution from Q_1 is already 98.7(1.1)%. Therefore, chiral symmetry breaking effects are very small and thus well under control.

quoted in different schemes (RI, RGI, $\overline{\mathrm{MS}}$-NDR) is

$$B_K^{\mathrm{RI}}(3.5\,\mathrm{GeV}) = 0.5428(50)(158) \tag{3.12}$$

$$\hat{B}_K = 0.7809(72)(227) \tag{3.13}$$

$$B_K^{\overline{\mathrm{MS}}-NDR}(2\,\mathrm{GeV}) = 0.5671(52)(165), \tag{3.14}$$

where the first error is statistical and the second systematic. The value for $B_K^{\mathrm{RI}}(3.5\,\mathrm{GeV})$ is our main, fully non-perturbative result and the conversion to other schemes was performed using results from 2-loop perturbation theory [Ciuchini et al., 1998; Buras et al., 2000]. We neglected the systematic error induced by the truncation of the perturbative series, since the dominant uncertainty comes from the quenched scale setting ambiguity. Because we do not attempt to compare our quenched result to full QCD, we also omitted estimating an error for this. A breakup of the overall systematic error into different sources of uncertainties is displayed in table 3.4. It exhibits the dominant source of systematic uncertainty, viz. the subtraction of mixing operators. This error collects all uncertainties attributed to the choice of different ranges and functions for fitting the non-perturbative mixing coefficients. It is large due to the fact that the dominant subtracted mixing coefficient $\Delta_{12}^{\mathrm{ren}}$ could equally well be fitted with a term linear in $(ap)^2$ as well as an additional term proportional to p^{-4} (cf. figure 3.19 (a)), resulting in a large spread of the extracted mixing coefficient (cf. figure 3.21). The large quark mass interpolation uncertainty tells us that the interpolation is strongly affected by terms of higher order in M_{P}^2. If our data would cover a broader range in M_{P}^2, this error
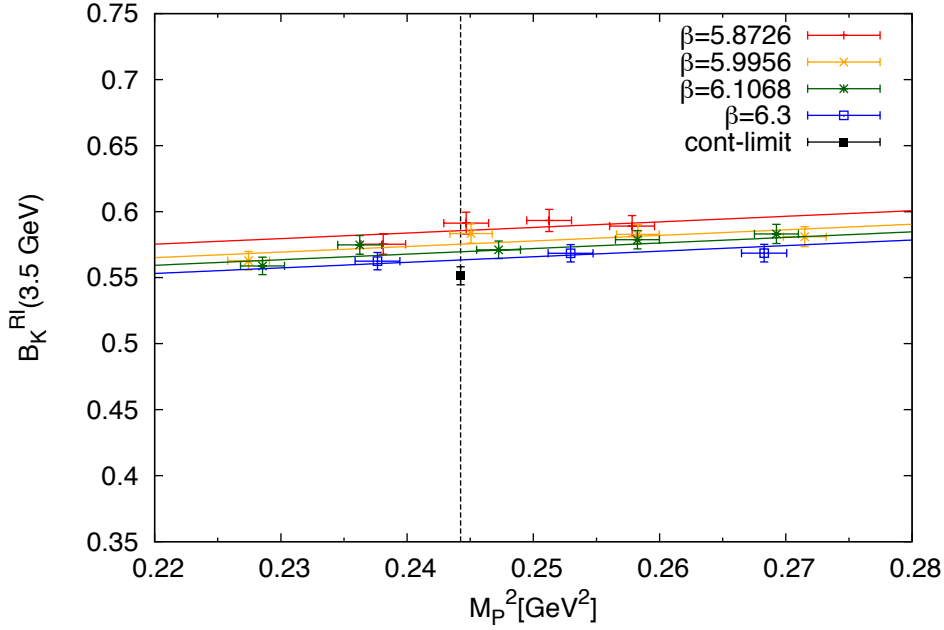
Figure 3.22.: Combined continuum extrapolation and interpolation to the physical quark mass of quenched B_K for one of our 2592 fits which assumes a linear dependence of B_K on M_P^2. The black square denotes the resulting $B_K^{\mathrm{RI}}(3.5\,\mathrm{GeV})$ and the dashed vertical line the physical kaon mass. The quark mass interpolation is well under control since we observe a mild chiral behaviour.
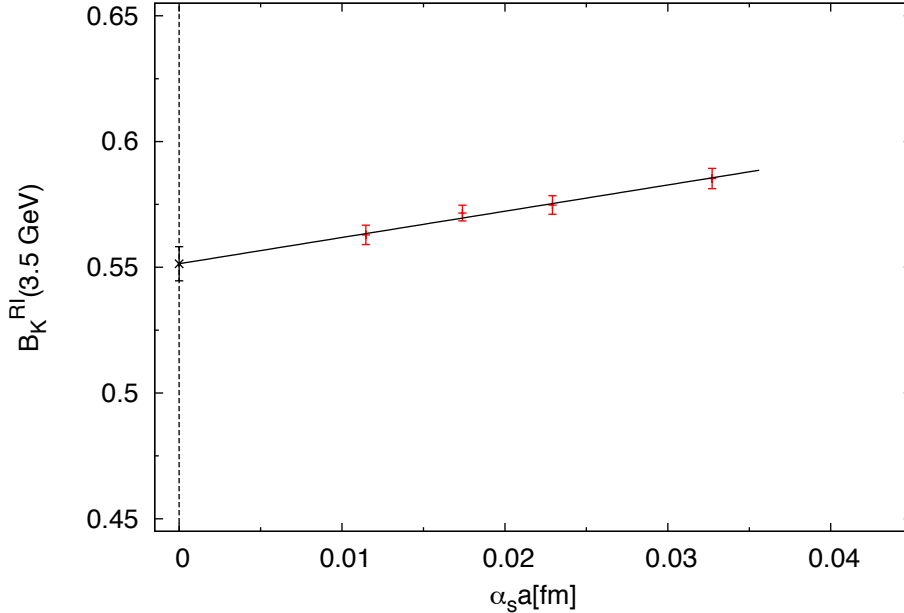
Figure 3.23.: Continuum limit of quenched $B_K^{\mathrm{RI}}(3.5\,\mathrm{GeV})$ obtained from the combined fit in figure 3.22. The scaling corrections, i.e. the relative deviation of B_K from the coarsest to the finest lattice, are around 4%.

would reduce since one of our two chiral forms would be preferred and the corresponding qualitites-of-fit enhanced. The further systematic uncertainties are subdominant and shall not be discussed in detail.

Our final result in the RGI framework is compared to different quenched results from other lattice groups in figure 3.24, showing good agreement and reasonable error bars. Thus, our lattice setup and analysis approach is expected to be well suited for computing B_K in N_f=2+1 flavour QCD.

total	mixing	M_{P}^2 interpolation	continuum limit	excited states	NPT matching
0.0158	0.0105	0.0095	0.0039	0.0013	0.0013

Table 3.4.: Individual contributions to total systematic error from different sources of uncertainty. The approximately equally dominant contributions come from subtracting the operator mixing as well as the interpolation in the quark mass. Analogous to our previous quenched scaling study (cf. section 3.2.2), the uncertainty attributed to different scaling assumptions is at the percent level. As expected from figures 3.18 (concerning non-perturbative matching scale uncertainties) and 3.20 (concerning excited states uncertainties), the last two contributions to the systematic error are subdominant. The quadratic sum of all contributions does not reproduce the overall systematic error due to correlations.
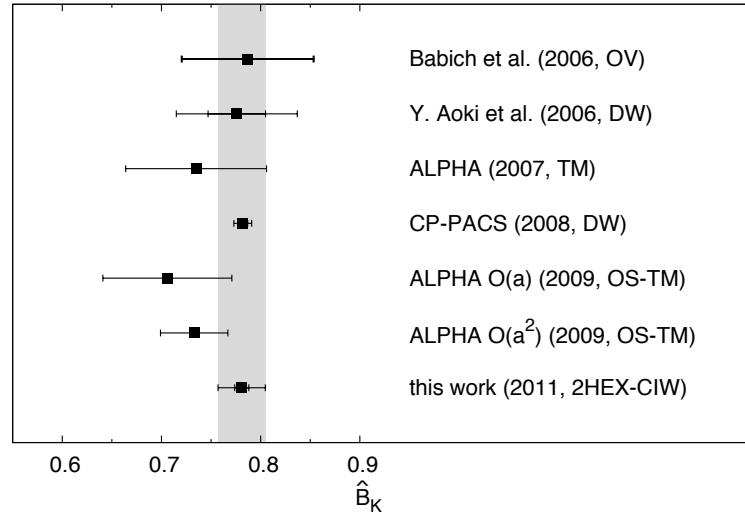
Figure 3.24.: Results for quenched $\hat{B}_K$ from the last 5 years. The grey band is drawn in order to help comparing our result (bottom) to those of other groups (top to 6th). The agreement is good and the error bars are reasonable, giving confidence that our method of analysis is well suited for predicting B_K in dynamical QCD. The references are (from top to 4th): Babich et al. [2006], Aoki et al. [2006], Dimopoulos et al. [2007], Nakamura et al. [2008] and Dimopoulos et al. [2009] (5th and 6th).

3.2.4. Finite volume effects

In general, finite volume effects can be described by the frameworks briefly sketched in section 2.3.5. Here, we will have a closer look at finite volume corrections of type I, i.e. corrections to stable states coming from squeezing the surrounding pion cloud. The results for our finite volume runs are displayed in figures 3.25 and 3.26 for the 2 HEX and 6 EXP data respectively. In both cases, we observe good agreement with the analytical expectations from χPT [Colangelo et al., 2005, 2006]. We could also establish a global fit to all our data in various volumes if we adjusted the free coefficient in (2.168). We found that the deviation of this fit from the χPT prediction became large below $M_\pi L < 3$, which is mainly due to the fact that χPT becomes questionable in boxes around that value.

It is important to stress that only data points fulfilling either $M_\pi L \geq 4$ or $L \sim 6$ fm entered the final analyses for determining the spectrum, the light quark masses and B_K. Nevertheless, the remaining points were corrected for their small finite volume effects by using the appropriate relations from Colangelo et al. [2005, 2006]; Becirevic and Villadoro [2004].
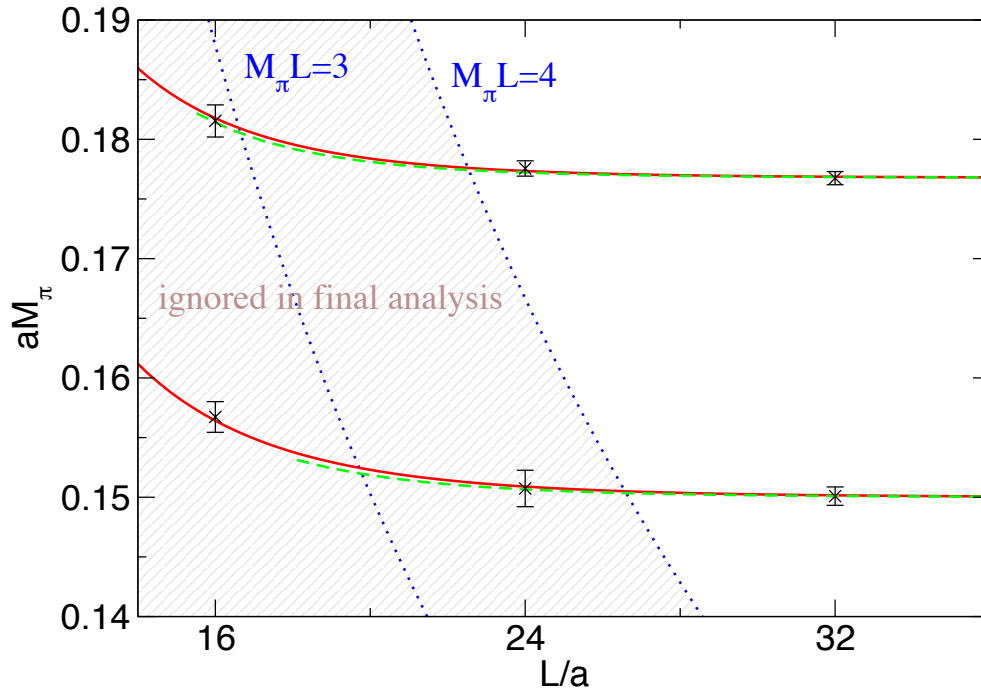
Figure 3.25.: Dedicated finite volume analysis for 2 HEX action at $\beta = 3.31$ with $M_\pi \simeq 250$ MeV (lower) and $M_\pi \simeq 300$ MeV (upper). The dashed green curves represent the χPT fits by Colangelo et al. [2005] and the solid red curves our fits. The dotted blue lines indicate the boundaries $M_\pi L = 3$ and $M_\pi L = 4$ (taken from [Durr et al., 2010]).
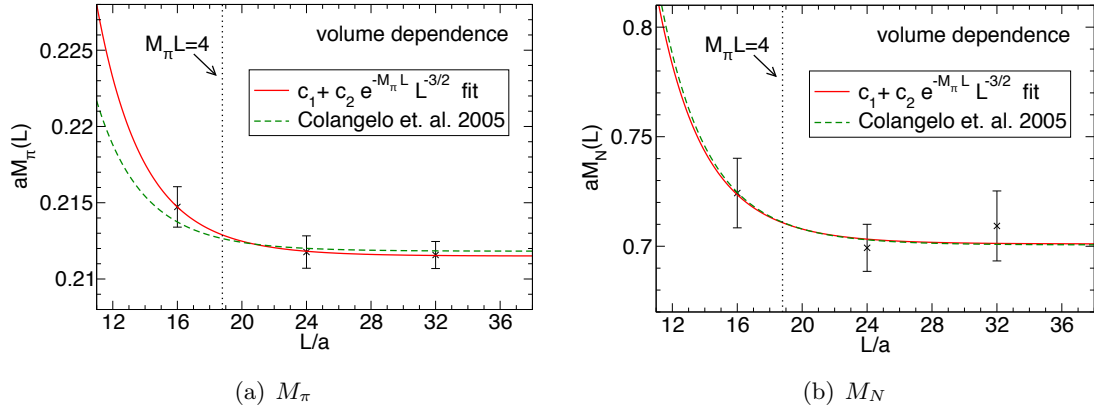
Figure 3.26.: Volume dependence of the π (a) and N (b) masses for one simulation point at $a \approx 0.125$ fm and $M_\pi \simeq 320$ MeV. The solid red curves represent our fits and the dashed green ones the analytical expectation from Colangelo et al. [2005, 2006] (taken from the SOM for [Dürr et al., 2008]).

3.2.5. Chiral behaviour

To illustrate the quality of our results obtained at physical or heavier values of the average up-down quark mass $m_{ud} = (m_u + m_d)/2$, we investigated whether the pion mass and decay constants can be described by χPT. The prediction from SU(2) χPT at NLO are given by [Gasser and Leutwyler, 1984]

$$M_\pi^2 = M^2 \left[1 + \frac{x}{2} \ln \left(\frac{M^2}{\Lambda_3^2} \right) \right] \tag{3.15}$$

$$F_\pi = F \left[1 - x \ln \left(\frac{M^2}{\Lambda_4^2} \right) \right], \tag{3.16}$$

with $x = M^2/(4\pi F^2)$ and $M^2 = 2Bm_{ud}$. The NNLO expressions for these quantities have been worked out by Colangelo et al. [2001]. Note, that in contrast to SU(3) χPT, the mass of the strange quark in the above expressions is not treated as light. The LEC's Λ_k thus carry information on these high energy degrees of freedom.

Figure 3.27 shows the quantities $M_\pi^2/m_{ud}^{\mathrm{PCAC}}$ and F_π plotted versus m_{ud}^{PCAC} at an intermediate lattice spacing ($\beta = 3.5$) for our 2 HEX dataset. The pion mass reaches down to $M_\pi \simeq 135$ MeV (for more details, cf. section 4.2). For $M_\pi < 400$ MeV, our results could be jointly fitted with the formulae (3.15), (3.16), with acceptable $\chi^2/$dof and reasonable values for the LEC's. However, a precise determination of these low energy constants is beyond the scope of the present work. Note that we did not produce the equivalent figure 3.27 for our 6 EXP action, because our average pion mass is much larger there. The 2 HEX data set is our first data set containing pion masses down to its physical value. Hence, the chiral behaviour is much more pronounced here than in our older 6 EXP data set.

(a) $(aM_\pi)^2$ (b) aF_π
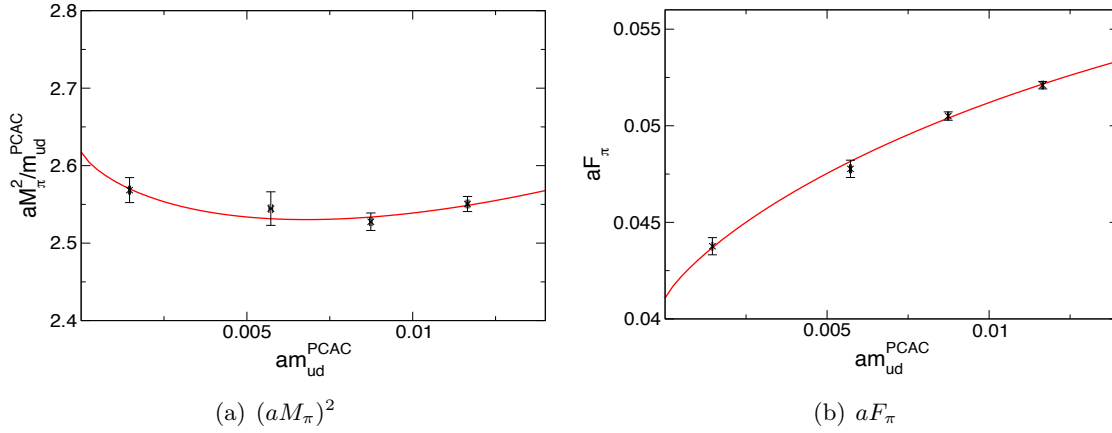
Figure 3.27.: Chiral behaviour of $(aM_\pi)^2/m_{ud}$ (a) and unrenormalized aF_π (b) for our four lightest ensembles at $\beta = 3.5$ for the 2 HEX data. The bare strange quark mass was kept fixed at $am_s = -0.006$, which is very close to m_s^{phys}. A joint fit to (3.15) and (3.16) yields reasonable values for the LEC's Λ_3 and Λ_4. The error bars are statistical [from Durr et al., 2010].

3.3. Summary and conclusions

The tests show that both our actions

- are ultra-local by construction and even fulfill the locality condition within the ultra-locality range.

- do not show any unphysical meta-stabilities in our simulations.

- possess a well pronounced mass gap, hence simulations at physical quark masses are possible (and feasible).

- show good topological tunneling with a symmetric distribution around zero for the topological charge at least up to $a \approx 0.5\,\text{fm}$. The physically relevant autocorrelation times of q_{ren}^2 are of $\mathcal{O}(10)$ trajectories so that we do not expect major difficulties in a sufficient sampling of different topological sectors.

- possess large scaling windows up to $a \approx 0.16\,\text{fm}$ and down to $0.5\,\text{fm}$ when hadron masses are considered. The scaling corrections are small and do not exceed the 3%-level.

Furthermore, in case of the quenched strange quark mass, we can state that the 2 HEX action has a large scaling window up to $a \approx 0.15\,\text{fm}$ and fairly mild scaling corrections below 8%. The situation for the quenched kaon bag parameter B_K is a bit different, since a reliable extraction of the mixing coefficients fails on the coarsest lattice. Thus, the scaling window extends only up to $a \approx 0.12\,\text{fm}$, but nevertheless still allows to perform a safe continuum limit. The scaling corrections from the coarse lattice included in the analysis to the finest lattice are on the 4% level and thus well under control.

The finite volume corrections are very small in the $M_\pi L > 4$ region and remaining effects can be subtracted in a controlled manner.

In 2 HEX simulations with dynamical quarks we observed a quark mass dependence of M_π^2 and F_π which is fully compatible with SU(2) χPT expectations.

Additionally, smeared fermions are computationally relatively cheap and, compared to other dynamically improved actions, easy to implement. In principle, no expensive parameter tuning is required or at least can be reduced to a minimum.

Thus we can recommend the 6 EXP and 2 HEX action for the use in phenomenological applications. Both actions are comparably efficient so that either choice may only depend on personal taste or computational resources. The 2 HEX action has a better ultra-locality range than the 6 EXP formulation, but, on the other hand, is computationally more demanding: its smearing prescription either requires to keep several copies of the lattice in the RAM which may heavily drain the machines' memory resources, or a significant fraction of performance is lost if the smearing is applied time-slice by time-slice. Therefore, 6 EXP smearing can be the better choice when simulations are performed on devices with limited memory, such as graphics cards.

4. Physical quantities from 2+1 dynamical flavours

The successful scaling studies and stability tests presented in the last chapter paved the way for precise computations of important physical observables from first principles.

A large leap forward in this context is our reproduction of a relevant part of the physical particle spectrum by lattice QCD. We were able to prove that QCD is a correct theory for describing the low-lying hadron masses up to percent-level precision. This result is presented and discussed in section 4.1.[1]

Unlike hadron masses, physical quark masses are hard to measure in experiment because they form bound hadronic states.[2] Our results on the hadron spectrum have proven the common assumption that the mass of a hadron and therefore of our world is mainly attributed to the binding energy and not to the mass of its constituents. Still it was unsatisfactory to not know these important standard model parameters precisely. Reliably and precisely computed light quark masses can be used as input parameters for perturbative calculations, which in turn can then improve the predictions of perturbative cross sections. With more precise input parameters and reduced error bars, it might be possible to discover deviations from standard model expectations in upcoming LHC experiments. Furthermore, the specific values for the quark masses are important to understand the stability of matter, since a reversed hierarchy between m_u and m_d would imply a proton decay.

In section 4.2, I present the precision computation of the three light quark masses u, d and s with full control over all errors.[3]

A third extremely interesting and important application of lattice QCD is the computation of hadronic corrections to weak matrix elements sensitive to CP violation. CP violation is a key ingredient for the explanation of baryon-asymmetry which developed during the baryogenesis in the early universe [Sacharow, 1968]. The computed matrix elements can be combined with electroweak perturbative calculations and then compared to fits involving experimental quark flavour mixing data. This allows estimating possible BSM contributions to standard model mixing amplitudes.

In the final section of this part 4.3, I present our precise lattice prediction of the kaon bag parameter B_K, which can be related to the electroweak indirect CP violation parameter ϵ.[4]

---

[1]Published in Dürr et al. [2008] and the corresponding SOM.
[2]This does not apply to the heavy top quark since it decays before it can form a bound state.
[3]Published in Durr et al. [2011b, 2010].
[4]See part 2.2.6 for details on ϵ. A publication about our computation of B_K is in preparation [Durr et al., 2011a].

4.1. Hadron spectrum

More than 99% of the mass of the visible universe is made up of protons and neutrons, and both particles are much heavier than the sum of their constituents. If the standard model is correct in this aspect, it should explain that large difference.
Over the past 20 years, many collaborations performed lattice calculations and published results on this topic. The spectrum computed in quenched QCD agreed with the experimental results for typical hadron masses up to 10% [Aoki et al., 2000]. The systematic uncertainties of quenching compared to $N_f=2$ flavour simulations have been observed to be beyond that level of precision [Aoki et al., 2000, 2003a]. The agreement of lattice QCD with experiment significantly improved when light sea quark effects were included [Davies et al., 2004]. Owing to the continuous progress since then, lattice QCD calculations can now be performed with light sea quarks at physical values [Aoki et al., 2009][5]. Additional calculations including these sea quark effects have appeared in the literature [Bernard et al., 2001a; Aubin et al., 2004a; Ukita et al., 2007; Gockeler et al., 2007; Antonio et al., 2007; Walker-Loud et al., 2009; Del Debbio et al., 2007; Alexandrou et al., 2008; Noaki et al., 2007].
However, all these calculations are not ab initio, because all of them neglected one or more important ingredients.
These ingredients are:

- The inclusion of dynamical effects of sea quark masses with an exact algorithm and the use of an action whose universality class is QCD.

- A complete determination of the light ground-state masses of flavour non-singlet mesons, octet and decuplet baryons is necessary. Three of these have to be used to fix m_{ud}, m_s and the overall scale.

- Many results in the literature work with small volumes ($M_\pi L < 4$) so that finite volume corrections are significant. Resonances require a special treatment, their finite volume corrections are much more involved (cf. 2.3.5).

- Some results lack controlled extrapolations to the physical quark masses m_{ud} and m_s. Whereas the interpolation in the comparatively heavy strange quark mass m_s is straightforward, a chiral extrapolation to the physical value of m_{ud} is much more complicated. In order to perform a controlled extrapolation in this quantity, computationally expensive calculations at pion masses around $200\,\text{MeV}$ or less are needed.

- A controlled extrapolation to the continuum, requiring at least three different lattice spacings in order to guarantee that the scaling region of the action is reached.

We present our results on the ab initio calculation of the non-singlet low lying hadron spectrum including all five of these ingredients with full control over all possible statistical and systematic errors.

---

[5] When this computation in 2007/2008 was performed, the volumes were still quite small.

4.1.1. Details of the simulations

We used the same setup as in our 6 EXP hadron masses scaling study (cf. chapter 3), i.e. a tree-level improved clover Wilson operator together with the tree-level improved Lüscher-Weisz gauge action. For the EXP smearing we used again $\rho = 0.11$ and 6 iteration levels.

We worked on spatial volumes as large as $L^3 \simeq (4\,\text{fm})^3$ and temporal extents up to $T \sim 2L \approx 8\,\text{fm}$ and ensured that $M_\pi L > 4$ on all our lattices. Besides significantly reducing finite volume corrections (cf. 2.3.5), this choice also reduced statistical fluctuations. The reason for this is that the spatial summation in correlators needed to project the correlation function to zero momentum is proportional to L^3, and the time-extent available to extract the effective masses is again proportional to L. Hence, for a given pion mass M_π, the increase of statistics is proportional to the ratio of volumes, e.g. 1300 trajectories at $M_\pi L = 4$ roughly correspond to 4000 trajectories at $M_\pi L = 3$.

Autocorrelation analysis

The autocorrelation times of the plaquette and that of the conjugate gradient iteration count are less than approximately ten trajectories. Therefore we performed our measurements on every tenth trajectory. The integrated autocorrelation time of the physically relevant q_{ren}^2 is at worst three times larger than this value, so that we do not observe significant long range correlations (cf. 3.1.2).

We computed the spectrum by using Gaussian smeared sources and sinks of constant physical radii $r \approx 0.32\,\text{fm}$ on eight time slices. These kind of sources are less affected by excited state contaminations than point sources and sinks (cf. figure 4.1). We varied the bootstrap blocking size in order to check for remaining autocorrelation effects in quantities where the autocorrelation function cannot be measured directly, e.g. in case of hadron masses. All results from these tests were in good agreement and thus we conclude that our data show no further correlations.

Finite volume effects and extraction of the masses

The treatment of finite volume effects of type I was already discussed in 3.2.4. Also, corrections of type II could be mostly treated as described in 2.3.5. However, out of the $14 \cdot 12 = 168$ mass determinations (14 sets of lattice spacings, see table 4.1 for details) there were two cases for which the mass M_X of the resonant state was larger than that of the lowest scattering state. These exceptions were the ρ and Δ for the lightest pion mass point at $a \approx 0.085\,\text{fm}$. For these two cases, the energy of the lowest lying state was already dominated by the contribution from the neighboring two particle state. More precisely, the energy of the scattering state depended only very weakly on the mass of the resonant state M_X, which therefore could not be extracted reliably without imposing precise information on the decay width Γ_X. Since we want to avoid using more experimental input than necessary, these points were neglected in the determination of M_ρ and M_Δ. Thus, and only for the Δ and ρ channels, these two points were excluded from the analysis.

Completely analogous to the proceeding in section 3.2.1, we extracted the hadron masses by applying correlated cosh or sinh fits to the correlators. Figure 4.2 shows the effective mass

(a) π channel   (b) N channel
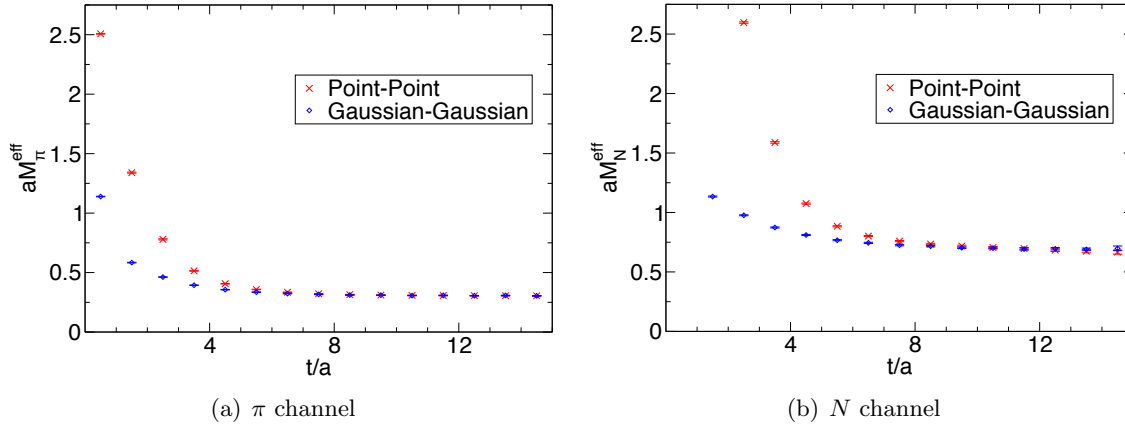
Figure 4.1.: Effective masses for different kinds of sources. Whereas point sources have ef-
              fectively zero extent, our Gaussian sources have radii $r \approx 0.32\,\text{fm}$ and clearly a
              better overlap to hadronic ground states. This translates into larger and cleaner
              plateaus (from SOM for [Dürr et al., 2008]).

plateaus for our lightest ensemble at $M_\pi \approx 190\,\text{MeV}$ and $a \approx 0.085\,\text{fm}$.

4.1.2. Approaching the physical mass point and the continuum limit

In order to be able to estimate the systematic errors induced by setting the scale as well as
extrapolating the masses to the physical point and the continuum, we applied several different
methods for each of these steps. We considered two different methods of setting the scale and
for each of these we followed two different strategies to extrapolate to the physical mass point.
Additionally, we applied three different cuts on the maximum pion mass. We also used two
different valid parametrizations for the continuum extrapolation to estimate the dependence
of our results on the choice of the specific fit model. Furthermore, we set the scale by using
either the Ω or the Ξ baryon. The very precisely known pion and kaon masses were always
'sacrificed' for setting the light and strange quark masses and thus could not be 'predicted'
by this calculation.
The two methods of setting the scale were namely the

- *ratio method*: this method is motivated by the fact that lattice QCD measurements
  are always dimensionless combinations of observables, e.g. mass ratios. The advantage
  of using mass ratios is that possible cutoff effects cancel. Also statistical uncertainties
  might be suppressed due to correlations. To sketch this method for the Ξ scale setting:
  consider the ratios $r_X = M_X/M_\Xi$ and parametrize them by using $r_\pi = M_\pi/M_\Xi$ and
  $r_K = M_K/M_\Xi$. The continuum extrapolated surface parametrized by $r_X(r_\pi, r_K)$ is an
  unambiguous prediction for a particle of type X (some points on these surface were
  already determined by Durr et al. [2009] (see also section 3.2.1). For illustrational
  purposes it is suitable to plot one-dimensional slices of this surface. The one-dimensional
  parametrizations for the nucleon and omega mass in figure 4.4 were obtained by setting
  the combination $2r_K^2 - r_\pi^2$ to its physical value of 0.27 and moving the data points
  accordingly using the fit formula.

β	am_{ud}	am_s	$L^3 \cdot T$	#traj.
	-0.0960	-0.057	$16^3 \cdot 32$	10000
	-0.1100	-0.057	$16^3 \cdot 32$	1450
3.3	-0.1200	-0.057	$16^3 \cdot 64$	4500
	-0.1233	-0.057	$16^3 \cdot 64 \,/\, 24^3 \cdot 64 \,/\, 32^3 \cdot 64$	5000 / 2000 / 1300
	-0.1265	-0.057	$24^3 \cdot 64$	10000
	-0.0318	$0.0 \,/\, -0.010$	$24^3 \cdot 64$	1650 / 1650
	-0.0380	$0.0 \,/\, -0.010$	$24^3 \cdot 64$	1350 / 1550
3.57	-0.0440	$0.0 \,/\, -0.007$	$32^3 \cdot 64$	1000 / 1000
	-0.0483	$0.0 \,/\, -0.007$	$48^3 \cdot 64$	500 / 1000
	-0.0070	0.0	$32^3 \cdot 96$	1100
	-0.0130	0.0	$32^3 \cdot 32$	1450
3.7	-0.0200	0.0	$32^3 \cdot 96$	2050
	-0.0220	0.0	$32^3 \cdot 96$	1350
	-0.0250	0.0	$40^3 \cdot 96$	1450

Table 4.1.: Bare masses, lattice sizes and statistics. The table depicts the 14 simulation points, ordered by the light quark masses. Due to the additive renormalization constant, the bare masses can be negative. All these points were included into a combined chiral and continuum extrapolation. Additionally, a dedicated finite volume study has been performed for one choice of masses on the coarsest lattice. The points at $\beta = 3.57$ have been repeated for a different strange quark mass (from SOM for [Dürr et al., 2008]).
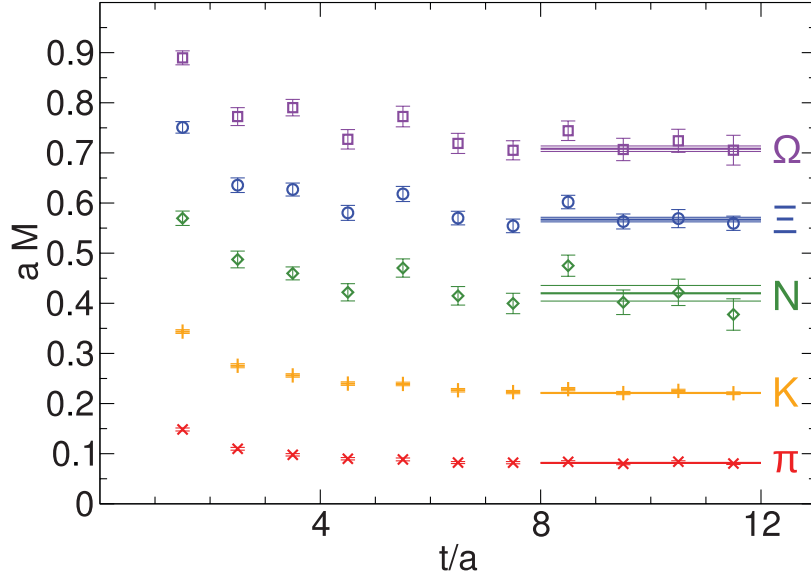
Figure 4.2.: Effective masses at $M_\pi \sim 190\,\text{MeV}$ and $a \approx 0.085\,\text{fm}$ and physical strange quark mass, for the π, K, N, Ξ and Ω channel. The horizontal lines are the masses obtained by correlated cosh or sinh fits to the correlators. Their length denote the fit size in lattice units [from Dürr et al., 2008].

In direction of the strange quark mass, a linear interpolation in r_K^2 is sufficient because our chosen m_s is already tuned very close to its physical value. On the other hand, some channels showed a curvature in the r_π^2 dependence. Therefore, a series expansion around a chosen pion mass point was needed. The singular choice $r_\pi = 0$ corresponds to chiral perturbation theory. Another possibility is to use a non-singular expansion point, e.g. a point lying inside the range of measured r_π. We applied both methods and will refer to them as *chiral fit* or *Taylor fit* respectively. Besides the typical pseudo-Goldstone boson terms proportional to M_π^2, χPT predicts terms proportional to M_π^3 [Langacker and Pagels, 1974] for masses of particles which are no pseudo-Goldstone bosons. This is provided by our chiral fit strategy. As a generic expansion around a reference point $(r_{\pi,\mathrm{ref}}, r_{K,\mathrm{ref}})$, we applied the ansatz

$$r_X(r_\pi, r_K) = r_{X,\mathrm{ref}} + \alpha_X \left(r_\pi^2 - r_{\pi,\mathrm{ref}}^2 \right) + \beta_X \left(r_K^2 - r_{K,\mathrm{ref}}^2 \right) + \mathcal{O}(r_\pi^3, r_K^3). \qquad (4.1)$$

In case of the chiral fits, the higher orders were chosen proportional to r_π^3 and the reference point $(r_{\pi^2,\mathrm{ref}}, r_{K,\mathrm{ref}}^2) = (0, \bar{r}_K^2)$, where $\bar{r}_K^2$ is the midpoint between our values of r_K^2, which straddle the physical value.[6]

For the Taylor fit we chose the reference point $(r_{\pi,\mathrm{ref}}^2, r_{K,\mathrm{ref}}^2) = (\hat{r}_\pi^2, \bar{r}_K^2)$, with $\bar{r}_K^2$ as defined before and $\hat{r}_\pi^2$ is the midpoint between the physical pion point and the largest simulated r_π^2 considered in the fit. Note that in this case, all our data and reference points are well inside the radius of convergence which is defined by the nearest singular points at $r_\pi^2 = 0$ and $r_K^2 = 0$. It shows that higher order contributions proportional to r_π^4 were sufficient for the Taylor fit.

The combined extrapolation to the physical mass point was performed by applying both strategies, where the deviation propagated into our systematic error. The range of applicability of these extrapolations is not known a priori, and the higher order contributions were compatible with zero for the vector mesons for all different pion mass cuts. Nevertheless, these terms have been included in the analysis. On the baryonic sector, the higher order contributions became significant and the difference between the results obtained by these different types of fits allowed us to estimate yet higher order terms which were not included into our fits. In order to improve this estimate further, we applied three different cuts to the pion masses. In the first cut, we included all 14 simulation points, in the second cut we neglected all points with pion masses above $r_\pi = 0.38$ which removed two points from the fit. The third cut was even more strict because we neglected all points with pion masses above $r_\pi = 0.31$, which removed three additional points from the fit. Again, the different results for the extrapolations using these three different fits contributed to our systematic error.

To summarize the *ratio method* as a practitioners guide: use the input data ratios r_X, r_π and r_K to determine $r_X(r_{\pi,\mathrm{ref}}^2, r_{K,\mathrm{ref}}^2)$, α_X and β_X and then r_X at the physical point using an extra/interpolation. This is done by applying two different fit formulae (chiral and Taylor) and using three different pion mass cuts for each of them.

- *mass independent scale setting*: this method is much more conventional compared to the ratio method discussed above. The input mass M_Ξ (or M_Ω) is first extrapolated to the physical point, given by the experimental values of M_π/M_Ξ and M_K/M_Ξ. This

---

[6]This means we used SU(2) χPT, where the strange quark is treated as heavy. For SU(3) χPT we would have had to choose $(r_{\pi,\mathrm{ref}}^2, r_{K,\mathrm{ref}}^2) = (0,0)$.

value can then be identified with the physical value of M_Ξ and thus one obtains a scale for the specific lattice spacing. This procedure can be repeated on all lattice spacings and our chiral and Taylor extrapolations can be performed as in the ratio method before, this time using the quantities M_π, M_K and M_Ξ in physical units instead of the ratios. We applied the same pion mass cuts as in the ratio method which translates into $M_\pi = 560\,\mathrm{MeV}$ and $M_\pi = 450\,\mathrm{MeV}$ for the two more strict cuts. Again, all different fits contributed to our systematic error.

As discussed in section 3.2.1 and [Durr et al., 2009], typical hadron masses deviate from their continuum values by less than approximately 1% for lattice spacings up to $a \approx 0.125\,\mathrm{fm}$. Furthermore, we showed in [Durr et al., 2009] that cutoff effects are linear in a^2 for $0.065\,\mathrm{fm} \leq a \leq 0.125\,\mathrm{fm}$ and even above. Hence we allowed the quantities $r_X(r_\pi, r_K)$ and $M_X(M_\pi, M_K)$ to acquire a linear dependence in a^2. In order to estimate the effect of possible higher order contributions in a, we also performed an extrapolation linear in the lattice spacing and propagate the difference into our systematic error.
Both the continuum and chiral extrapolations were carried out simultaneously in a combined correlated fit.

4.1.3. Analysis of statistical and systematic errors

Beside the systematic uncertainties we accounted for in the discussion above, we also included several other possible systematic contributions in our results. In order to estimate the possible contributions of excited states in fitting the correlation functions, we used 18 different time intervals. These intervals vary from large time values where we can definitely exclude significant excited state contributions, down to small time values where excited states contributions are not visible in the effective mass plateau but might influence the fit. We ended up having two methods of normalizing the hadron masses, two strategies to extrapolate to the physical pion mass, three pion mass cuts, two different continuum extrapolations as well as eighteen time intervals for the fits of the two point functions. This resulted in $2 \cdot 2 \cdot 3 \cdot 2 \cdot 18 = 432$ different values for each single hadron mass. Each of them coming with a weight proportional to its goodness-of-fit. Therefore, from the 432 different fits for each hadron we obtained a histogram whose entries are weighted according to their fit quality. Our result for the hadron mass is then given by the median and the error by the central 68% probability. The corresponding histogram for the nucleon mass is shown in figure 4.3, where the arrow denotes its median. The statistical errors have been estimated by repeating the whole analysis on 2000 MB bootstrap samples with a block size of 1.[7] Hence, we obtained 2000 distributions for each hadron and thus 2000 medians. The central 68% of the distribution of the bootstrapped medians is our statistical error. The two different types of errors have been summed up quadratically, where we expect this to be the most fair and reliable estimator. The individual contributions to our final systematic errors are given in table 4.2.
Note, that taking the quadratic sum of errors to obtain an overall error is only allowed for statistically independent Gaussian distributions, which is not the case for our systematic error. However, the correlation is very small and would even decrease our final overall error if completely taken into account. Thus, our final error is slightly overestimated, as can be seen

---

[7]Due to the decorrelation of our measurements, larger values for the block size did not affect the results significantly.

by the perfect agreement of all our values with experiment. From naive statistics, we would
expect that approximately 2/5 of our data points are off the experimental prediction, hence
~ 3 measurements out of 10.

Before proceeding to the presentation of our results, I discuss a last source of possible system-
atic uncertainties: in lattice QCD applications, the electromagnetic interactions are neglected
and isospin is an exact symmetry. However, electromagnetic and mass isospin breaking ef-
fects typically contribute to a small fraction of 1% to masses of light vector mesons and
baryons [Gasser and Leutwyler, 1982]. Furthermore, the electromagnetic contribution to the
mass splitting between members of the same isospin multiplet is also well below the 1%-level
[Gasser and Leutwyler, 1982]. We accounted for these effects by isospin averaging the exper-
imental masses to which we compare our results. This removed the leading isospin breaking
terms, ending up with higher order corrections of only a small fraction of 1%. For the pion
and kaon masses we used the isospin averaging as well as Dashen's theorem [Dashen and
Weinstein, 1969] in order to determine the leading electromagnetic effects. Higher order cor-
rections to this theorem are expected to be below the 3 per mil level [Aubin et al., 2004c] so
that it is safe to neglect them in our calculation.

4.1.4. Results and discussion

Our final result for the non-singlet low-lying hadron spectrum is compared to the experimental
values in figure 4.5 and table 4.3. We observe a perfect agreement with the experimental data
and thus our studies strongly suggest that QCD is the correct theory of strong interaction
at hadronic energy scales. The computation of the hadron spectrum was one of the most
important steps in understanding where 99% of the visible matter comes from. Furthermore,
it shows that lattice computations will be one of the most important tools to proof the non-
perturbative regimes of the standard model and especially QCD. In this context, I present
our results on the light quark masses in the next section 4.2.
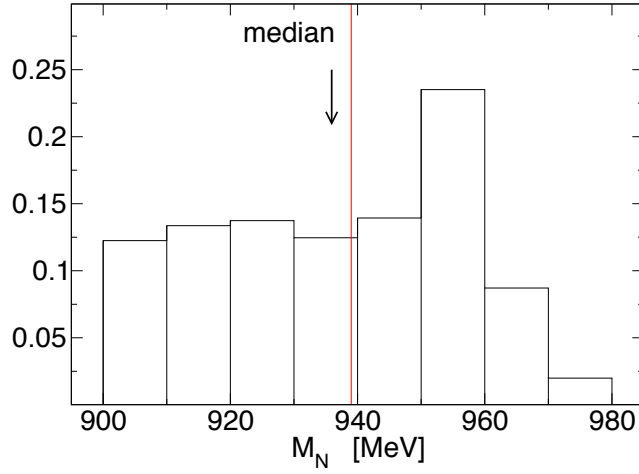
Figure 4.3.: Distribution of nucleon masses obtained from our different fits. The arrow depicts the computed median whereas the experimental value for the nucleon mass is indicated by the vertical line (from SOM for [Dürr et al., 2008]).

channel	continuum extrapolation	chiral fits/normalization	excited states	finite volume
ρ	0.20	0.55	0.45	0.20
K^*	0.40	0.30	0.65	0.20
N	0.15	0.90	0.25	0.05
Λ	0.55	0.60	0.40	0.10
Σ	0.15	0.85	0.25	0.05
Ξ	0.60	0.40	0.60	0.10
Δ	0.35	0.65	0.95	0.05
Σ^*	0.20	0.65	0.75	0.10
Ξ^*	0.35	0.75	0.75	0.30
Ω	0.45	0.55	0.60	0.05

Table 4.2.: Error budget as fractions from total systematic error. All results represent averages from the Ξ an Ω scale setting sets. The columns correspond to uncertainties related to two different continuum extrapolations ($\mathcal{O}(a)$ or $\mathcal{O}(a^2)$) (column 2), two different fit ansaetze (chiral and Taylor) for extrapolating to the physical mass point as well as three different pion mass cuts (column 3), then 18 different fit intervals for the extraction of the masses from the correlators (column 4) and finally the finite volume corrections (column 5). The quadratic sum of all errors does not combine exactly to 1 because of correlations and non-Gaussian nature of the underlying distributions. The finite volume corrections of the decouplet resonances increase with increasing strange content because the total systematic error decreases so that the absolute finite volume corrections are of the same level. The black horizontal line separates the vector mesons from the baryon and the octet from the decuplet sector (from SOM for [Dürr et al., 2008]).
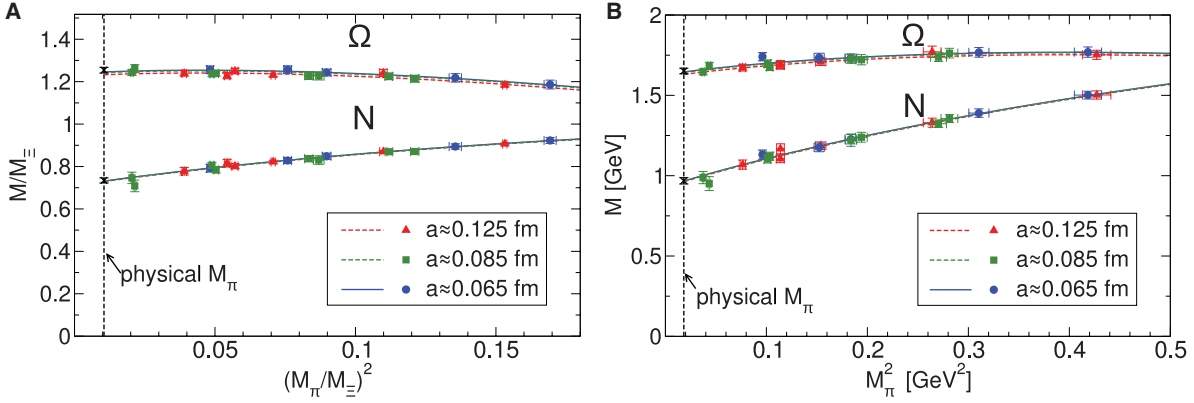
Figure 4.4.: Pion mass dependence of the nucleon N and Ω for all three values of the lattice spacing. Figure (A) depicts the extrapolation in the ratio method, figure (B) the extrapolation using the mass independent scale setting where the scale is set by M_Ξ at the physical point. The red triangles and dashed curves correspond to $a \approx 0.125$ fm, the green squares and dashed curves to $a \approx 0.085$ fm and the blue circles and solid curves to $a \approx 0.065$ fm. The points and curves were obtained by projecting the corresponding two dimensional surfaces along the $2M_K^2 - M_\pi^2$ direction onto its physical value. The black vertical lines represent the physical pion mass and the black circles on top of these lines the combined continuum and chiral extrapolations. The lattice spacing dependence of our results is barely statistically significant, despite the factor of around 3.7 separating the points on the finest and coarsest lattices. The χ^2/dof of these fits for both channels are 7.10/14 (N) and 9.46/14 (Ω) for (A) as well as 9.33/14 (N) and 10.6/14 (Ω) respectively for (B) [from Dürr et al., 2008].

X	Experimental values[Yao et al., 2006]	M_X (Ξ set)	M_X (Ω set)
ρ	0.775	0.775(29)(13)	0.778(30)(33)
K^*	0.894	0.906(14)(04)	0.907(15)(8)
N	0.939	0.936(25)(22)	0.953(29)(19)
Λ	1.116	1.114(15)(05)	1.103(23)(10)
Σ	1.191	1.169(18)(15)	1.157(25)(15)
Ξ	1.318	1.318	1.317(16)(13)
Δ	1.232	1.248(97)(61)	1.234(82)(81)
Σ^*	1.385	1.427(46)(35)	1.404(38)(27)
Ξ^*	1.533	1.565(26)(15)	1.561(15)(15)
Ω	1.672	1.676(20)(15)	1.672

Table 4.3.: Spectrum results in GeV. The first error quoted is statistical and the second error systematic. Note that the experimental masses have been isospin averaged. This average is at most within 3.5 MeV of the masses of all its members. Octet masses are more accurate than the decuplet masses and the precision also increases with the strange content. As a consequence, the Δ mass is the least precise result. Again, the black horizontal lines separate the vector meson from the baryon and the octet from the decuplet sector (from SOM for [Dürr et al., 2008]).
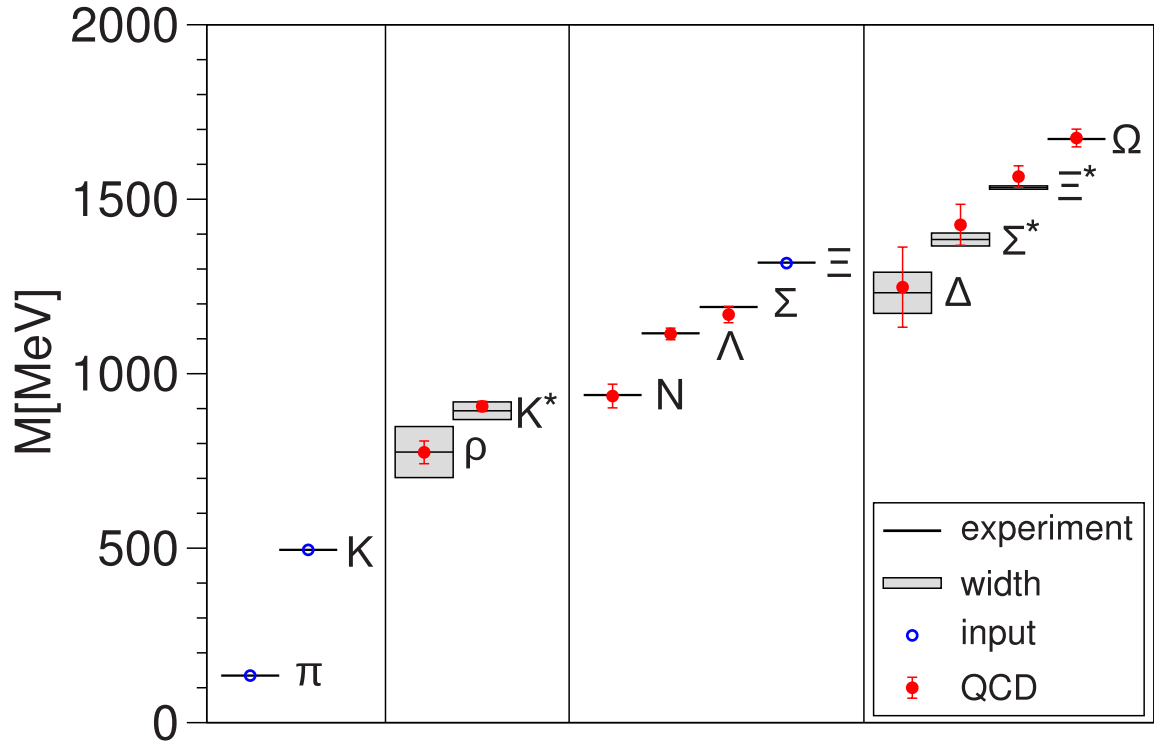
Figure 4.5.: Light hadron spectrum of QCD for the Ξ scale setting set. The horizontal bars and shaded bands denote the experimental values along with their decay widths for strongly decaying particles. Our results are indicated by the red circles and the combined statistical and systematic errors by the corresponding error bars. The blue circles represent the input quantities necessary to fix the quark masses (M_π, M_K) and the scale (M_Ξ). The plot for the Ω scale setting is completely analogous. We see a very good agreement of the computed quantities with experimental measurements, hence strongly indicating that QCD is the correct theory for describing strong interactions also at perturbatively inaccessible low energies [from Dürr et al., 2008].

4.2. Quark masses

In 2.1 we discussed that the standard model of particle physics has many free parameters, e.g. the coupling strengths, quark and lepton masses, mixing angles or gauge boson masses, the higgs mass etc. Obviously, ordinary matter[8] can be described by six fundamental parameters: three couplings for the strong, electromagnetic and gravitational interaction, as well as three masses, i.e. the mass of the electron m_e and the light quark masses m_u, m_d. Through virtual corrections, the strange quark mass m_s also contributes to the nucleon mass. Since the masses of heavier quarks mostly exceed the total energy of the hadronic state, their contribution to the nucleon mass is negligible. Whereas the three couplings and the electron mass are known to an accuracy of better than a few per mil, the light and strange quark masses are only poorly known. The Particle Data Group quotes them with conservative errors of around 25% [Nakamura et al., 2010]. The reason for this large uncertainty is attributed to the fact that (light) quark masses are inaccessible by direct measurements. The strong interaction confines quarks into hadrons in such a way that a single quark cannot be isolated. Furthermore, the strength of interaction is such that the masses of hadrons are not simple sums of their constituent masses but highly affected by complicated non-perturbative strong dynamics (cf. part 4.1). This confinement or *infrared slavery* is the counterpart of the theory's asymptotic freedom at high energies.

Lattice QCD is known for several decades now, but a large amount of computational and algorithmic development was necessary to reach a level where quark masses can be extracted reliably with a high precision. In case of the hadron spectrum, many computations have been performed in the quenched approximation [cf. Garden et al., 2000, for the most precise result on m_s]. Besides introducing an uncontrolled uncertainty by neglecting the fermion determinant, quenched QCD calculations also cannot reach the region of physical up- and down-quark masses due to the occurrence of exceptional configurations.[9] Although the inclusion of sea quark effects [Eicker et al., 1997; Ali Khan et al., 2002; Aoki et al., 2003b; Gockeler et al., 2006; Della Morte et al., 2005b] was an important step, physical quark masses still have been out of reach due to algorithmic reasons. The first major breakthrough came with the MILC collaboration [Aubin et al., 2004b] which used a N_f=2+1 staggered dynamical fermion formulation with larger volumes and smaller quark masses. More recent calculations give results with root-mean-squared of the pion taste partners down to 258 MeV and use even finer lattices [Bazavov et al., 2010, 2009]. On a subset of the MILC configurations, HPQCD made an attempt to indirectly obtain the light quark masses by measuring the m_c/m_s ratio [McNeile et al., 2010]. However, the aggressive error estimates on their input quantities and the use of a non-unitary staggered fermion formalism does not fulfill the requirements of a fully controlled ab initio determination. Recently, also ETMC [Blossier et al., 2010] and RBQCD [Aoki et al., 2011] have presented results with significantly larger error bars.

The improvement of algorithms [Hasenbusch, 2001; Luscher, 2005], the use of theoretically sound Wilson and domain wall fermions for ab initio calculations [Dürr et al., 2008; Allton et al., 2008] as well as reaching physically small m_{ud} for the first time (albeit in small volumes and at a single lattice spacing [Aoki et al., 2009]), marked the second breakthrough in determining the light quark masses. If we again apply the criteria for a complete ab initio

---

[8]By which we mean visible matter which does not decay weakly.

[9]This occurs when some eigenvalues of the valence Dirac operator get close to zero. In full QCD, such configurations are suppressed by a large back-driving force within the molecular dynamics evolution.

determination with full control over all errors from part 4.1, many of the above mentioned results will fail. In case of quark masses, we have to add two important criteria to those mentioned in that section:

- Non-perturbative treatment in all steps. Only this treatment allows to remove the uncertainties coming from the truncation of the perturbative series completely from the determination. Of course, the use of perturbation theory together with a fair estimation of these truncation errors is also justified but this usually enlarges the overall systematic error.

- Careful choice of input parameters. The quark masses and scale should be set with experimentally well measured observables whose error bars are undisputed. Furthermore, these observables should not contain any hidden assumptions such as empirical models. Our studies fulfill this requirement by using the experimentally well known quantities M_π, M_K and M_Ω, as done before in 4.1. Taking derived quantities like r_1 and m_c instead can be problematic. The error bar on m_c used by McNeile et al. [2010] is 13 times smaller than the established PDG value [Nakamura et al., 2010]. Similarly, due to the difficulty in determining r_1 (and its related value r_0) and quantifying its systematic uncertainty, its continuum limit is disputed.

We determined the light and strange quark masses m_u, m_d and m_s with a precision of below 2% within an ab initio lattice calculation. The pion masses we used range down to their physical values (and even below) and the box sizes reach up to 6 fm. We used five lattice spacings for the continuum extrapolation and the renormalization is performed completely non-perturbatively. These precise results could be obtained by using improved methods which circumvent some inherent difficulties in the procedures we used. Namely these are the *ratio-difference-method* for calculating the quark masses (cf. 2.3.7), the *ratio-extrapolation-method* to circumvent the RI window problem and the trace subtraction to remove a specific $\mathcal{O}(a)$ artifact (cf. 2.4.3) as well as our advanced data analysis technique to propagate all statistical and systematic errors reliably into the final result (cf. section 2.3.5 and [Dürr et al., 2008]). The second extremely important ingredient are our data points computed directly at physical pion masses or even below. Since the necessary extrapolations in m_{ud} become interpolations, the related systematic uncertainties are drastically reduced.

4.2.1. Simulation details and scale setting

We first determined the renormalized averaged light quark masses $m_{ud} = (m_u + m_d)/2$ and strange quark mass m_s at the physical point in the continuum. The results on m_{ud} and m_s/m_{ud} were then combined using dispersive information based on $\eta \to 3\pi$ decays to obtain m_u and m_d separately. For determining the bare quark masses we used our 2 HEX smeared tree-level improved clover Wilson action with 2+1 dynamical flavours (cf. 3). The strange quark mass m_s was held fixed to its approximate physical value and the pion masses we used range down to $M_\pi = 120$ MeV. We simulated at five different lattice spacings ranging from $a \approx 0.116$ fm down to 0.054 fm and box sizes as large as $L^3 \simeq (6 \text{ fm})^3$. Furthermore, we ensured that $M_\pi L \geq 4$ and/or $L \geq 5$ fm for all points included in the final analysis. To determine the renormalization factors, we generated configurations using the same action with three degenerate dynamical flavours and ensured that $M_\pi L \sim 4$ for the smallest pion masses

used in the computations. Tables 4.4 and 4.5 display an overview of all simulation parameters. Note that the quoted pion masses correspond to one possible choice of the correlation functions fitting range and the errors are purely statistical.

We set the scale by using the experimental isospin averaged and electromagnetic corrected values of M_π, M_K and M_Ω. This was done by using the framework as given by FLAG [Colangelo et al., 2010b], which is essentially the refined version of an analysis presented by MILC [Aubin et al., 2004c]. The bottom line of these analyses are that one should use the input masses $M_\pi = 134.8(3)\,\text{MeV}$ and $M_K = 494.2(5)\,\text{MeV}$ which agree with the experimentally measured neutral pion mass M_{π^0} and averaged kaon mass $\overline{M}_K = [(M_{K^+}^2 + M_{K^0}^2)/2]^{1/2}$ respectively. The physical point can be found by comparing the measured ratios M_π/M_Ω and M_K/M_Ω to their corresponding experimental values and the lattice spacing by computing $a\,M_\Omega/M_\Omega^{\text{phys}}$ using $M_\Omega^{\text{phys}} = 1.672\,\text{GeV}$ [Nakamura et al., 2010]. As discussed in part 4.1, one can also use M_Ξ to set the scale. We have also seen that correlation functions of decuplet members are noisier than those of octet members. On the other hand, increasing strange content means decreasing statistical fluctuations. In [Dürr et al., 2008], where pion masses down to $190\,\text{MeV}$ were used, these effects balanced each other rendering M_Ω and M_Ξ equally good choices. This time, our pion masses are as low as $120\,\text{MeV}$ and hence these competing effects prefer the use of M_Ω which does not contain light valence quarks. Within this context, we used the conventional mass-independent-scale-setting (cf. section 4.1.1).

The masses in our ensembles straddle the physical values of M_π^2 and $M_{s\bar{s}}^2 \equiv 2M_K^2 - M_\pi^2$. Therefore it suffices to use a parametrization of aM_Ω as a function of $(aM_\pi)^2$ and $(aM_{s\bar{s}})^2$ which describes the entire data set. The Taylor ansatz

$$aM_\Omega = c_0 + c_1(aM_\pi)^2 + c_2(aM_{s\bar{s}})^2 + c_3(aM_{s\bar{s}})^2 \tag{4.2}$$

perfectly describes our data.

The integrated autocorrelation times for the plaquette and the inverse iteration count of the conjugate gradient in the HMC Metropolis step are of $\mathcal{O}(10)$ trajectories. Depending on these measurements, we took every fifth to tenth configuration for our final analysis. Results on the autocorrelation of the topological charge, which, as a global quantity, usually shows the largest autocorrelation times, were already presented in section 3.1.2. We showed that the integrated autocorrelation time of the physically relevant q_{ren}^2 is of $\mathcal{O}(10)$ configurations so that we did not observe any further correlations in our data. We also checked for remaining thermalization effects by dropping the first 20-100 configurations but found no significant changes in our results. In order to reduce the relative weight of excited states in hadronic correlators, we used Gaussian sources and sinks with radii $r \approx 0.32\,\text{fm}$.

Additional checks concerning finite volume corrections, chiral behaviour, algorithmic stability and scaling behaviour were already presented in chapter 3. We corrected for possible finite volume effects which were always below the 0.5% level and even smaller at the physical point. A landscape plot demonstrating the quality of our data concerning pion masses and volumes is shown in figure 4.6.
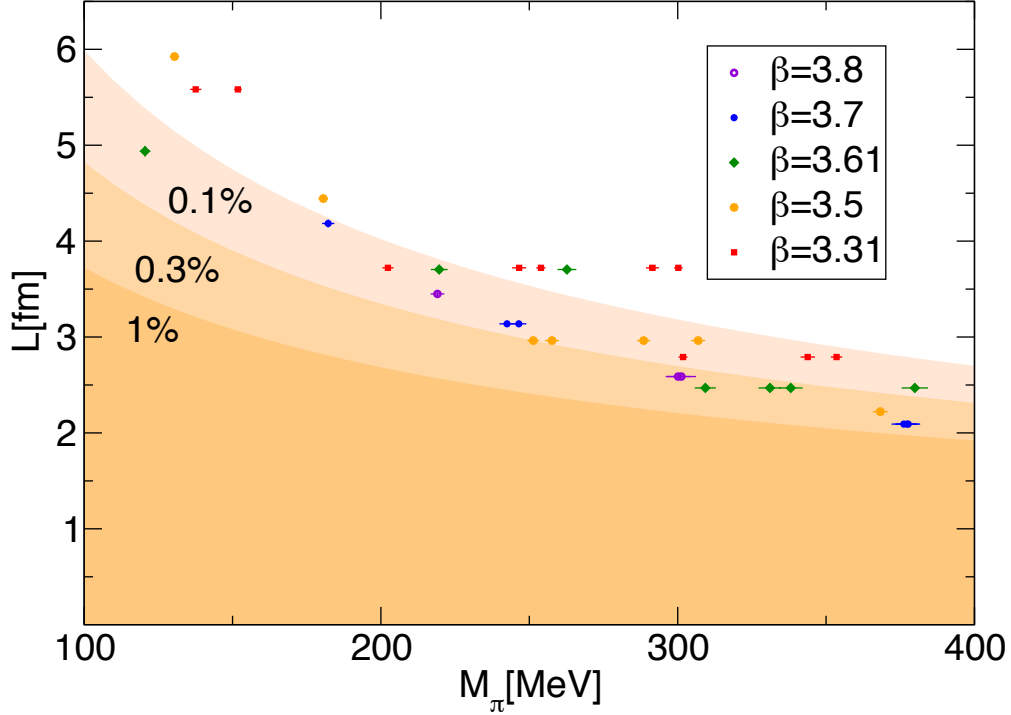
Figure 4.6.: Landscape plot of all our N_f=2+1 ensembles. The percentage labels of the
different shaded regions denote the lower boundaries for the expected relative
finite volume corrections on M_π as given by Colangelo et al. [2005]. In all our
runs these corrections are smaller than 0.5% where we still correct for these tiny
effects [from Durr et al., 2010].

3.31	$16^3 \times 32$	3.5	$24^3 \times 48$	3.61	$24^3 \times 48$	3.7	$32^3 \times 64$	3.8	$32^3 \times 64$
-0.04	4780	-0.006	2560	-0.0045	4620	-0.0060	1010	0.000	505
-0.06	3320	-0.010	3140	-0.0085	3680	-0.0085	1050	-0.004	635
-0.07	2420	-0.012	2580	-0.0100	4140	-0.0110	1020	-0.008	500
-0.08	2500	-0.020	2700	-0.0200	3140	-0.0140	1290	-0.012	1030
		-0.035	1090	-0.0250	1230	-0.0160	1020	-0.014	1000

Table 4.4.: Bare masses, volumes and number of trajectories of our dedicated N_f=3 simula-
tions for RI renormalization. The β-values are the same as in our phenomenological
runs, cf. table 4.5. Note that RI renormalization factors are in general statistically
very precise, so only $\mathcal{O}(1000)$ trajectories are sufficient [from Durr et al., 2010].

β	am_{ud}^{bare}	am_s^{bare}	volume	# traj.	aM_π	$M_\pi L$
	-0.07000	-0.0400	$16^3 \times 32$	1650	0.3530(12)	5.61
	-0.09000	-0.0400	$24^3 \times 48$	1600	0.2083(08)	5.00
	-0.09300	-0.0400	$24^3 \times 48$	4350	0.1775(06)	4.30
	-0.09300	-0.0400	$32^3 \times 48$	2500	0.1771(05)	5.65
	-0.09530	-0.0400	$32^3 \times 48$	1225	0.1500(13)	4.81
3.31	-0.09756	-0.0400	$32^3 \times 48$	2600	0.1202(11)	4.00
	-0.09900	-0.0400	$48^3 \times 48$	1700	0.0887(06)	4.26
	-0.09933	-0.0400	$48^3 \times 48$	1240	0.0804(13)	3.94
	-0.09000	-0.0440	$24^3 \times 64$	1065	0.2024(10)	4.86
	-0.09300	-0.0440	$32^3 \times 64$	1030	0.1717(08)	5.50
	-0.09530	-0.0440	$32^3 \times 64$	1300	0.1457(09)	4.66
	-0.04800	-0.0023	$32^3 \times 64$	1500	0.1354(06)	4.33
	-0.02500	-0.0060	$16^3 \times 32$	12000	0.2898(07)	4.62
	-0.03100	-0.0060	$24^3 \times 48$	3000	0.2535(05)	6.07
	-0.03600	-0.0060	$24^3 \times 48$	1800	0.2250(08)	5.41
	-0.04100	-0.0060	$24^3 \times 48$	4000	0.1921(05)	4.61
3.5	-0.04370	-0.0060	$24^3 \times 48$	3900	0.1725(04)	4.13
	-0.04900	-0.0060	$32^3 \times 64$	1100	0.1212(08)	3.90
	-0.05294	-0.0060	$64^3 \times 64$	1100	0.0613(06)	3.92
	-0.04100	-0.0120	$24^3 \times 64$	1020	0.1884(08)	4.52
	-0.04630	-0.0120	$32^3 \times 64$	1065	0.1445(06)	4.62
	-0.04900	-0.0120	$32^3 \times 64$	1000	0.1174(06)	3.76
	-0.05150	-0.0120	$48^3 \times 64$	1200	0.0835(07)	4.01
	-0.02000	0.0045	$32^3 \times 48$	2100	0.1993(3)	6.36
	-0.02800	0.0045	$32^3 \times 48$	3910	0.1488(4)	4.75
	-0.03000	0.0045	$32^3 \times 48$	2000	0.1322(4)	4.24
	-0.03121	0.0045	$32^3 \times 48$	2200	0.1211(2)	3.87
3.61	-0.03300	0.0045	$48^3 \times 48$	2100	0.1026(4)	4.93
	-0.03440	0.0045	$48^3 \times 48$	1100	0.0864(4)	4.15
	-0.03650	-0.0030	$64^3 \times 72$	1004	0.0468(5)	3.00
	-0.02000	-0.0042	$32^3 \times 48$	1750	0.1969(4)	6.30
	-0.03000	-0.0042	$32^3 \times 48$	1450	0.1297(5)	4.17
	-0.00500	0.0500	$32^3 \times 64$	1000	0.2227(04)	7.13
	-0.01500	0.0500	$32^3 \times 64$	1170	0.1711(03)	5.48
	-0.02080	0.0010	$32^3 \times 64$	1150	0.1251(04)	4.00
	-0.01500	0.0000	$32^3 \times 64$	1115	0.1644(04)	5.26
3.7	-0.02080	0.0000	$32^3 \times 64$	1030	0.1245(06)	3.98
	-0.02540	0.0000	$48^3 \times 64$	1420	0.0821(03)	3.94
	-0.02700	0.0000	$64^3 \times 64$	1045	0.0603(03)	3.86
	-0.02080	-0.0050	$32^3 \times 64$	1405	0.1249(04)	4.00
	-0.02540	-0.0050	$48^3 \times 64$	1320	0.0806(03)	3.87
	-0.01400	0.0300	$32^3 \times 64$	1325	0.1242(5)	3.97
	-0.01900	0.0300	$48^3 \times 64$	1045	0.0830(4)	3.99
3.8	-0.00900	0.0000	$32^3 \times 64$	2280	0.1523(4)	4.87
	-0.01400	0.0000	$32^3 \times 64$	1055	0.1249(5)	4.00
	-0.01900	0.0000	$48^3 \times 64$	1080	0.0836(4)	4.01
	-0.02100	0.0000	$64^3 \times 144$	1200	0.0598(2)	3.83

Table 4.5.: Overview of our N_f=2+1 simulations. The scales at β = 3.31, 3.5, 3.61, 3.7, 3.8 correspond to a = 0.1163(4), 0.0926(6), 0.0771(8), 0.0652(6), 0.0539(5) fm, respectively. The smallest pion mass per coupling is M_π = 136(2), 131(2), 120(2), 182(2), 219(2)MeV [from Durr et al., 2010].

4.2.2. Non-perturbative renormalization of quark masses

Quark masses are input parameters of the Lagrangian and thus they have to be tuned in order to reproduce the experimental low-energy spectrum of hadron masses. This immediately determines the quark masses in the (action specific) lattice cutoff scheme. For comparing the results with different lattice computations or some continuum scheme like $\overline{\text{MS}}$ or RGI, one has to convert them from the original cutoff-scheme to a scheme where the renormalization scale μ is not tied to the lattice spacing a.

We calculated the bare quark masses using our ratio-difference method (2.213) and (2.204) for full QCD. This method avoids complications coming from quark-line-disconnected contributions [Gockeler et al., 2006; Bhattacharya et al., 2006; Rakow, 2005] and renders the computation of the additive mass renormalization as well as the pseudoscalar renormalization constant Z_P unnecessary (cf. section 2.3.7 for details).

Determination of the scalar renormalization factor

The scalar renormalization factor was computed non-perturbatively in the RI scheme on our $N_f{=}3$ ensembles by applying all refinements already used in 3.2.2. This means that we applied the trace- subtraction to remove $\mathcal{O}(a)$ contact terms from the propagators (cf. section 2.4.3) and used four point sources sitting on the lattice hyper-diagonal in order to improve translational invariance. Again we applied hyper-diagonal cylinder cuts to suppress artifacts attributed to SO(4) breaking. We used the VWI to determine Z_V and thus Z_q^{RI} (cf. section 2.4.1). Figure 4.7 shows an example of the precise plateaus from which we determined the vector renormalization factor Z_V.
After obtaining Z_S for different lattice spacings and masses, we had to perform a controlled chiral extrapolation and to deal with the strict window problem.
The latter could be circumvented by our ratio-extrapolation method described in section 2.4.3 and used before in 3.2.2. In close analogy to the quenched analysis, we chose $\mu = 4\,\text{GeV}$ and $\mu' = 2.1\,\text{GeV}$ according to formula (2.290). The strict window condition for μ was met on the three finest and that for μ' on all lattices. Additionally, the scale $\mu = 4\,\text{GeV}$ was well inside the perturbative regime (cf. figure 4.9), allowing for later conversions to continuum perturbation theory. The continuum extrapolation of $R_S(\mu, \mu', a)$ was performed linearly assuming $O(\alpha_s a)$ or $O(a^2)$ scaling. The obtained continuum running $R_S(\mu, \mu')$ was multiplied by $Z_S(\mu', a)$ in order to obtain $Z_S(\mu, a)$ on all lattices. Figure 4.8 shows the multiplicatively matched Z_S before the above procedure was applied. The running is very universal in the considered range $2.1\,\text{GeV} \le \mu \le 4\,\text{GeV}$ and discretization effects are smaller than the statistical uncertainty. This implies that the continuum extrapolation of $R_S(\mu, \mu', a)$ is essentially flat and thus well controlled.
Although a complete non-perturbative determination of the quark masses is perfectly valid, it is useful to convert the measurements into a continuum scheme like $\overline{\text{MS}}$ or RGI for comparison. The matching factors performing this change of schemes have been computed perturbatively up to 4-loop order by Chetyrkin and Retey [2000]. The matching should be performed in a region where the agreement of the data with perturbation theory is good. Additionally, as also suggested by figure 4.10, the perturbative higher-order corrections and the deviation from one of the perturbative scheme conversion constant is smaller for larger scales μ [Chetyrkin

and Retey, 2000]. At our matching scale $\mu = 4\,\mathrm{GeV}$, the uncertainty related to this is at the 0.5% level and therefore subdominant. We converted to the $\overline{\mathrm{MS}}$ and RGI schemes using 4-loop running [Chetyrkin and Retey, 2000; Garden et al., 2000], where the matching function of Garden et al. [2000] was adjusted to the $N_f{=}3$ case.

As discussed in section 2.4.2, the RI scheme is a massless renormalization scheme but all $N_f{=}3$ simulations use finite quark masses in the approximate range $m_s^{\mathrm{phys}}/3 < m < m_s^{\mathrm{phys}}$. At some point, a chiral extrapolation is necessary. In order to have full control over the systematic effects coming, we used two different methods to extrapolate the data into the chiral limit.

1. We first extrapolated all Z_S for each β linearly in the quark mass into the chiral limit. Then we applied the procedure described above to immediately obtain $m^{\mathrm{RI}}(4\,\mathrm{GeV})$. This is exactly what we also did in the quenched scaling study (c.f. section 3.2.2 and [Kurth et al., 2010; Durr et al., 2010]).

2. We interchanged the order of limits. We first interpolated our Z_S values for each β to a reference quark mass $m^{\mathrm{ref}} = 70\,\mathrm{MeV}$. This value was chosen because it could safely be reached by interpolation on all lattice spacings. The resulting Z_S factors are no RI renormalization constants but defined in an intermediate scheme with reference mass m^{ref}. In that scheme, we determined the renormalized light and strange quark masses at the renormalization scales $\mu = 1.3$ and $2.1\,\mathrm{GeV}$ and extrapolated into the continuum. This yielded $m^{\mathrm{RI-m}}(\mu)$, where RI-m denotes a RI related massive renormalization scheme. Using the ratio extrapolation at $\mu' = 4\,\mathrm{GeV}$ and $\mu'' = 1.3$ as well as $\mu'' = 2.1\,\mathrm{GeV}$ along with the massive $Z_S^{\mathrm{RI-m}}$, we obtained the continuum matching factor transforming $m^{\mathrm{RI-m}}(\mu)$ into $m^{\mathrm{RI-m}}(4\,\mathrm{GeV})$ for both μ''. This means that

$$m^{\mathrm{RI-m}}(4\,\mathrm{GeV}) = m^{\mathrm{RI-m}}(\mu)\frac{Z_S^{\mathrm{RI-m}}(\mu)}{Z_S^{\mathrm{RI-m}}(4\,\mathrm{GeV})}. \qquad (4.3)$$

We then multiplied the l.h.s. with $Z_S^{\mathrm{RI-m}}(4\,\mathrm{GeV})/Z_S^{\mathrm{RI}}(4\,\mathrm{GeV})$ [10] to obtain $m^{\mathrm{RI}}(4\,\mathrm{GeV})$. This result was compared to the one we obtained from method 1.

Scheme and scale	m_s	m_{ud}	m_u	m_d
RI(4GeV)	96.4(1.1)(1.5)	3.503(48)(49)	2.17(04)(10)	4.84(07)(12)
RGI	127.3(1.5)(1.9)	4.624(63)(64)	2.86(05)(13)	6.39(09)(15)
$\overline{\mathrm{MS}}$(2GeV)	95.5(1.1)(1.5)	3.469(47)(48)	2.15(03)(10)	4.79(07)(12)

Table 4.6.: Renormalized quark masses in the RI/MOM scheme at $\mu = 4\,\mathrm{GeV}$, and after conversion to RGI and the $\overline{\mathrm{MS}}$ scheme at $\mu = 2\,\mathrm{GeV}$. The fully non-perturbative RI values in the first row are our main results. The first two columns emerge directly from our lattice calculation, the last two additionally incorporate dispersive information on Q. The precision of m_s and m_{ud} is below the 2% level, for m_u and m_d it is about 5% and 3%, respectively. The ratio $m_s/m_{ud} = 27.53(20)(08)$ is independent of the scheme and accurate to better than 1% [Durr et al., 2010].

---

[10]This ratio was obtained by extrapolating the corresponding a-dependent ratio into the continuum. The existence of this limit is discussed in section 2.4.3.
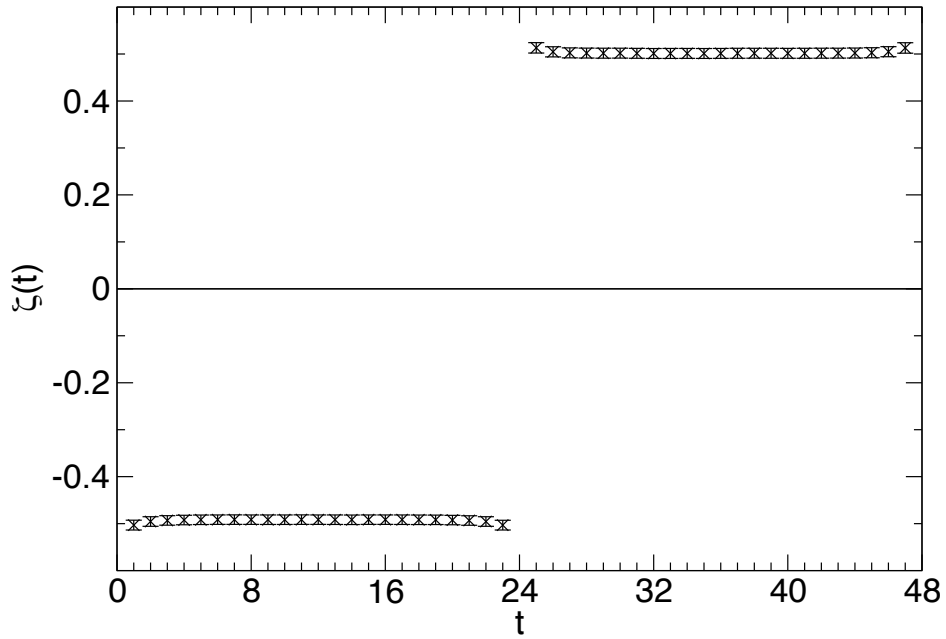
Figure 4.7.: The ratio $\zeta(t)$ as defined in 2.232 for the N_f=3 ensemble at $\beta = 3.61$ and $am = -0.0045$. The plateau is well pronounced and the errors are very small [from Durr et al., 2010].
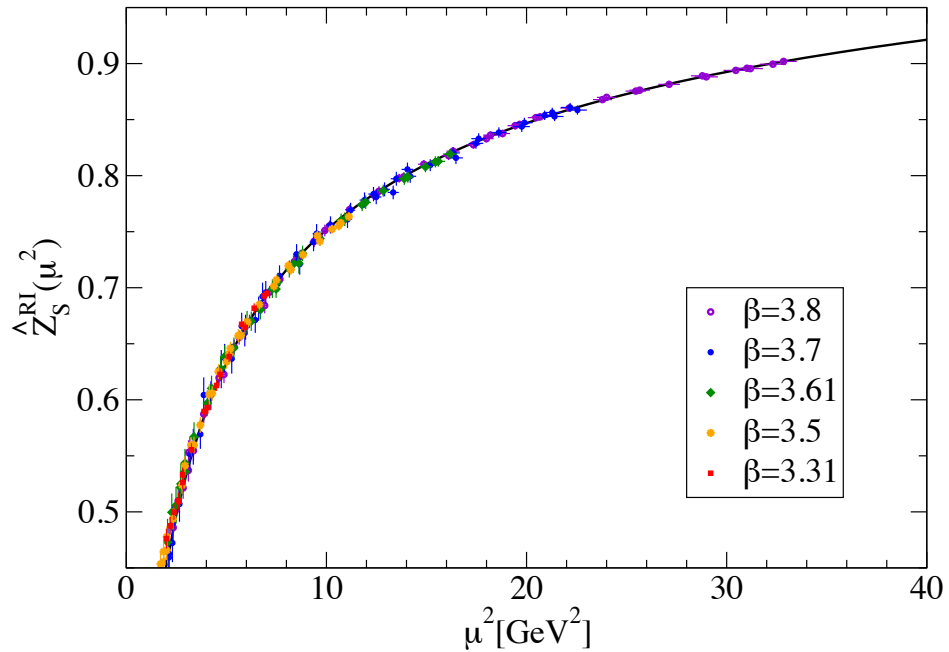
Figure 4.8.: Multiplicatively matched renormalization factors $Z_S^{\mathrm{RI}}(\mu, a)$ as function of the bosonic momentum squared. For each beta, only $a\mu \leq \pi/2$ are included. The solid line represents a Padé ansatz where the 1-loop anomalous dimension is built in as a contraint [from Durr et al., 2010].
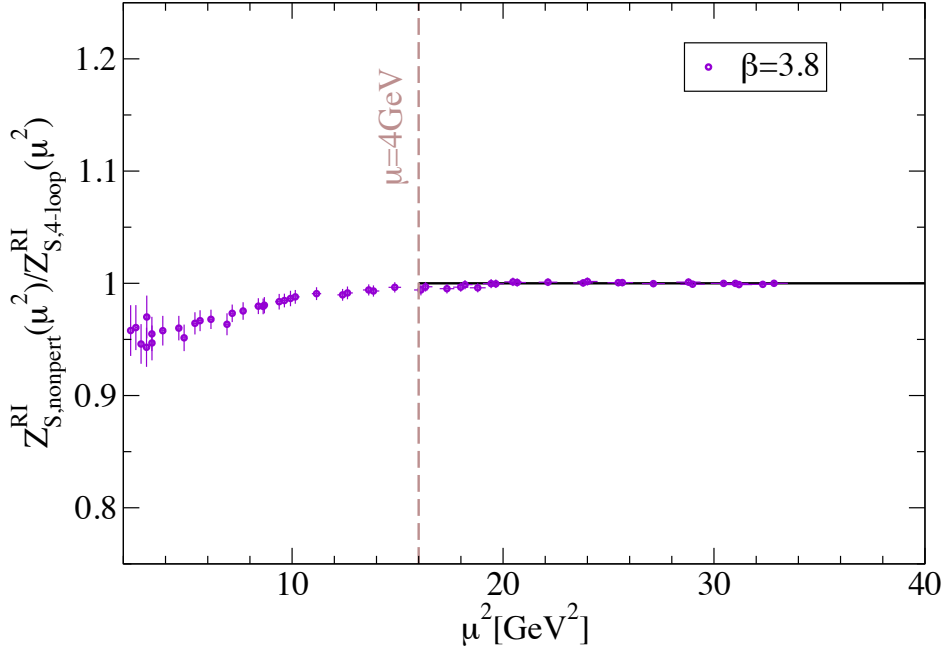
Figure 4.9.: Non-perturbative Z_S for $\beta = 3.8$ divided by the perturbative 4-loop running. The plateau shows that the data agree with perturbation theory for $\mu \geq 4\,\text{GeV}$ [from Durr et al., 2010].

(a) RI-scheme

(b) $\overline{\text{MS}}$-scheme
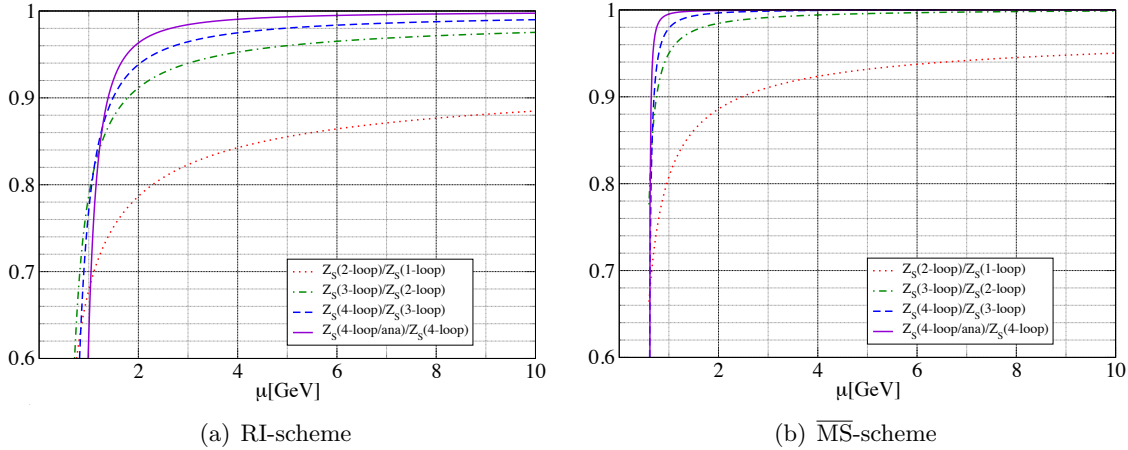
Figure 4.10.: Ratio of perturbatively evaluated Z_S^{RI} (a) and $Z_S^{\overline{\text{MS}}}$ (b) at different loop orders. The renormalization group equations have been integrated numerically using 1-loop through 4-loop anomalous dimensions. To estimate higher loop contributions, we employ the analytic expression at 4-loop level [Chetyrkin and Retey, 2000], which differs from the numerically integrated one by 5-loop effects. This ratio is denoted by "4-loop/ana" [from Durr et al., 2010].

We can summarize that all continuum extrapolations are extremely flat and the masses obtained using both methods described above differ by around 1%. This implies that all limiting procedures are fully controlled. As in the quenched studies, all continuum extrapolations were performed assuming $\mathcal{O}(\alpha_s a)$ or $\mathcal{O}(a^2)$ scaling, where the differences propagated into our systematic error using our standard assessment of systematic errors. The $\mathcal{O}(\alpha_s a)$ continuum extrapolation for m_{ud}, m_s and the universal ratio m_s/m_{ud} are shown in figure 4.11. The final results for m_{ud}, m_s as well as m_u and m_d at different renormalization scales and schemes are shown in table 4.6. The splitting of m_{ud} into separate values for m_u and m_d is discussed below.

4.2.3. Removing the degeneracy from m_{ud}

Before the resources for phenomenological lattice computations were available, the most reliable source of information on light quark masses were current algebra and its descendant χPT. Due to the fact that its low energy constants cannot be predicted by χPT itself but have to be computed by matching the effective field theory to QCD, χPT can only predict quark mass ratios where these LEC's cancel. Accordingly, we can compare our results on m_s/m_{ud} to the one predicted by SU(3)-χPT in order to learn something about its convergence pattern. Furthermore, we can combine our values of m_{ud} and m_s with the best available information on another ratio Q to obtain a result for the individual quark masses m_u, m_d.

Comparing our measured m_s/m_{ud} to χPT predictions

We start with the tree-level χPT relations for the meson masses

$$M_\pi^2 = B_0(m_u + m_d) \tag{4.4}$$
$$M_{K^\pm}^2 = B_0(m_u + m_s) \tag{4.5}$$
$$M_{K^0}^2 = B_0(m_d + m_s) \tag{4.6}$$
$$M_\eta^2 = B_0(m_u + m_d + 4m_s)/3, \tag{4.7}$$

where no electromagnetic corrections are included.[11] Putting in the experimental masses on the l.h.s., one obtains three predictions. The first is the famous Gell-Mann-Okubo mass relation

$$3M_\eta^2 + M_\pi^2 \simeq 2M_{K^\pm}^2 + 2M_{K^0}^2, \tag{4.8}$$

which evaluates to $0.919\,\mathrm{GeV}^2 \simeq 0.938\,\mathrm{GeV}^2$. This amounts to a 7% accuracy. On the other hand

$$\left(M_{K^\pm}^2 + M_{K^0}^2\right)/M_\pi^2 = (m_s + m_{ud})/m_{ud} \tag{4.9}$$
$$M_\eta^2/M_\pi^2 = (2m_s + m_{ud})/(3m_{ud}) \tag{4.10}$$

yield $m_s/m_{ud} \simeq 25.1$ and $m_s/m_{ud} \simeq 23.4$ respectively. Again, this spread suggests a precision of a few percent. Since the η undergoes significant mixing with the η', formula (4.9) should

---

[11]Masses of particles without superscripts denote isospin averages over the corresponding physical ones, i.e. $M_\pi^2 = (M_{\pi^0}^2 + M_{\pi^\pm}^2)/2$, $M_K^2 = (M_{K^0}^2 + M_{K^+}^2)/2$
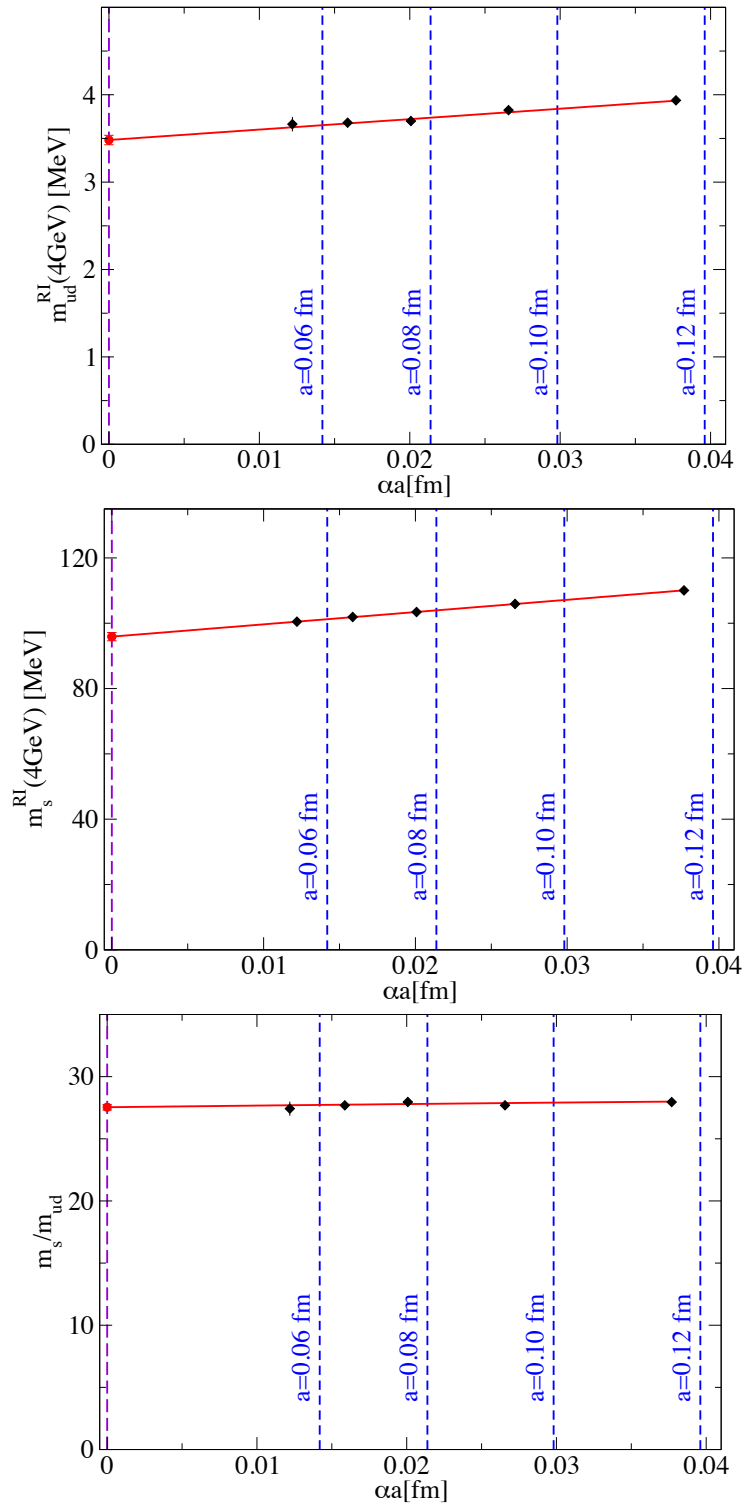
Figure 4.11.: Continuum extrapolation of m_{ud} (top), m_s (middle) and m_s/m_{ud} (bottom) versus $\alpha_s a$. The fits represent one of our 288 analyses with a good fit quality [from Durr et al., 2011b].

be preferred over (4.10). Omitting all equations including M_η^2 yields the estimates

$$\frac{m_u}{m_d} = \frac{M_{K^\pm}^2 - M_{K^0}^2 + M_\pi^2}{M_{K^0}^2 - M_{K^\pm}^2 + M_\pi^2} \simeq 0.66 \qquad (4.11)$$

$$\frac{m_s}{m_d} = \frac{M_{K^\pm}^2 + M_{K^0}^2 - M_\pi^2}{M_{K^0}^2 - M_{K^\pm}^2 + M_\pi^2} \simeq 20.8, \qquad (4.12)$$

which again do not include electromagnetic effects. These can be accounted for by extending the chiral framework to include photon interactions. In that case, the relative leading order contributions in α_{QED} in the 3-flavour chiral limit are the same for the pion and kaon mass, i.e.

$$\left[M_{\pi^\pm}^2 - M_{\pi^0}^2 \right]_{\text{QED}} = \left[M_{K^\pm}^2 - M_{K^0}^2 \right]_{\text{QED}}, \qquad (4.13)$$

also known as the Dashen's theorem [Dashen and Weinstein, 1969]. The QED corrections are the largest contributions to the mass splitting of $\pi^\pm$ and π^0, since isospin breaking effects are proportional to $(m_u - m_d)^2$ and therefore tiny [Leutwyler, 1996].[12] This allows to compute the leading order improved relations [Weinberg, 1977; Leutwyler, 1996]

$$\frac{m_u}{m_d} = \frac{M_{K^\pm}^2 - M_{K^0}^2 + 2M_{\pi^0}^2 - M_{\pi^\pm}^2}{M_{K^0}^2 - M_{K^\pm}^2 + M_{\pi^\pm}^2} \simeq 0.56 \qquad (4.14)$$

$$\frac{m_s}{m_d} = \frac{M_{K^\pm}^2 + M_{K^0}^2 - M_{\pi^\pm}^2}{M_{K^0}^2 - M_{K^\pm}^2 + M_{\pi^\pm}^2} \simeq 20.2, \qquad (4.15)$$

where we used the most recent PDG input from Nakamura et al. [2010] in order to obtain the estimates on the r.h.s.. From this we obtain

$$\frac{m_s}{m_{ud}} = \frac{2}{\frac{m_d}{m_s} + \frac{m_u}{m_d}\frac{m_d}{m_s}} \simeq 25.9. \qquad (4.16)$$

Comparing this to our result of $m_s/m_{ud} = 27.53(20)(08)$ (see caption of table 4.6), we find that higher order χPT contributions are on the 6% level and hence the relatively simple estimate (4.16) is surprisingly precise.

Leutwyler's ellipse

As shown before, χPT is well suited to address quark mass ratios. However, in the previous sections we mostly dealt with leading order contributions which do not include chiral logs coming from loop diagrams in the perturbative expansion. Fortunately, there are some combinations of χPT predictions allowing to form ratios from leading order quantities in which the NLO contributions cancel. Consider for example the expressions [Gasser and Leutwyler,

---

[12]Note that this does not apply to the mass splitting of $K^\pm$ and K^0. In that case, isospin breaking is the dominant effect [Leutwyler, 1996].

1985; Leutwyler, 1996]

$$\frac{M_K^2}{M_\pi^2} = \frac{m_{ud} + m_s}{m_u + m_d}\left(1 + \Delta + \mathcal{O}(m^2)\right) \qquad (4.17)$$

$$\frac{M_{K^0}^2 - M_{K^+}^2}{M_K^2 - M_\pi^2} = \frac{m_d - m_u}{m_s - m_{ud}}\left(1 + \Delta + \mathcal{O}(m^2)\right), \qquad (4.18)$$

where Δ is the same in both cases and is of the form

$$\Delta = \frac{8(M_K^2 - M_\pi^2)}{F_\pi^2}(2L_8 - L_5) + \chi\text{logs}. \qquad (4.19)$$

The factors L_8 and L_5 are LEC's from the $\mathcal{O}(p^4)$ χPT Lagrangian, necessary to cancel divergences from one-loop diagrams. The remaining effects are denoted by the term χlogs, because these are essentially logarithmic terms in the particle masses. The quantity F_π^2 is the pion decay constant. By taking the ratio of (4.17) and (4.18), these NLO contributions cancel and we end up with the (from χPT's perspective) robust double ratio [Leutwyler, 1996]

$$Q^2 \equiv \frac{m_s^2 - m_{ud}^2}{m_d^2 - m_u^2}. \qquad (4.20)$$

When neglecting the numerically tiny term m_{ud}^2/m_s^2 one can rewrite this expression into the equation for an ellipse

$$\left(\frac{m_u}{m_d}\right)^2 + \frac{1}{Q^2}\left(\frac{m_s}{m_d}\right)^2 = 1. \qquad (4.21)$$

Relying on Dashen's theorem or refinements thereof [Colangelo et al., 2010b], one can in principle attempt to determine the value of Q from the masses of the charged and neutral kaon and pion. Since we are aiming at computing the isospin splitting from first principles, it is necessary to use a determination of Q which does not include additional assumptions. It turns out that the most suitable method for calculating Q is to use results from dispersion theory on the $\eta \rightarrow 3\pi$ decay rate. Dispersion theory mainly relies on the axioms of quantum field theory and is therefore conceptually as ab initio as lattice QCD itself. The decay $\eta \rightarrow 3\pi$ is especially sensitive to isospin breaking [Leutwyler, 1996] and not much affected by electromagnetic effects [Ditsche et al., 2009]. The value for Q coming out of these calculations [Kambor et al., 1996; Anisovich and Leutwyler, 1996; Colangelo et al., 2009] is therefore the optimal choice for determining the isospin splitting. Note, that due to presently incomplete or unprecise available data, some additional input beside the axioms of quantum field theory is required [see e.g. Colangelo et al., 2009]. To account for such provisional effects, Leutwyler assigned his estimate $Q = 22.3(8)$ [Leutwyler, 2009] a much larger error bar than claimed in the publications his result is based on.

We regard this result to be the most accurate available, if one is not willing to resort to model assumptions. To extend our lattice determinations by the computation of m_u and m_d, we rewrite equation (4.20) and (4.21) to

$$\frac{1}{Q^2} = 4\left(\frac{m_{ud}}{m_s}\right)^2 \frac{m_d - m_u}{m_d + m_u}. \qquad (4.22)$$

Using the value for Q quoted above together with our measurement

$$\frac{m_s}{m_{ud}} = 27.53(20)(08) \tag{4.23}$$

yields for the light quark mass asymmetry parameter

$$\frac{m_d - m_u}{m_d + m_u} = 0.381(05)(27), \tag{4.24}$$

where the error on Q is considered as a systematic error. This asymmetry parameter is equivalent to $m_u/m_d = 0.448(06)(29)$. Combining (4.24) with our result $m_{ud}^{\text{RI}}(4\,\text{GeV}) = 3.503(48)(49)\,\text{MeV}$ we obtain

$$m_u^{\text{RI}}(4\,\text{GeV}) = 2.17(04)(10)\,\text{MeV}, \quad m_d^{\text{RI}}(4\,\text{GeV}) = 4.84(07)(12)\,\text{MeV}. \tag{4.25}$$

All our results on the quark masses are summarized in table 4.6 and quoted in Durr et al. [2011b, 2010].

In this part we determined m_u and m_d based on our lattice results m_{ud} and m_s/m_{ud} together with the dispersive input Q. Given that our simulation points bridge the physical values of m_{ud} and m_s, the chiral framework is no longer needed in the first two quantities and thus χPT is only used in some subdominant contributions to Q, which is mainly determined by dispersion theory.

Physics implication, robustness and outlook

An important conclusion from the previous section is that our result (4.24) excludes a vanishing up-quark mass by about 22 standard deviations. This is a consequence of the dispersively determined Q being entirely inconsistent with 13.8 which is necessary to enforce $m_u = 0$ using our results on m_{ud} and m_s/m_{ud}. Note that the latter quantity has been determined to sub-percent precision in our calculations. Our precise results together with the dispersive calculation of Q, which excludes large corrections to Dashen's theorem, rule out the simplest proposed solution to the *strong CP problem* (for a brief discussion cf. section 2.2.3). This corroborates the previous findings of Leutwyler [1996]. Note that the way in which we have used phenomenological information is designed to ensure that the so-called *Kaplan-Manohar ambiguity* is circumvented in our derivation of m_u and m_d. This ambiguity expresses the fact that the quark condensate and certain low-energy constants can be redefined, resulting in a shift on m_s/m_d and m_u/m_d along Leutwyler's ellipse [Kaplan and Manohar, 1986]. However, these transformations do not change the aspect-ratio of the ellipse which is encoded in Q.[13] Let us point out that there is conceptually no big difference between using M_π, M_K, M_Ω and Q. Although the former three quantities can be directly accessed in experiment and Q is a derived quantity, it nevertheless is obtained from well settled dispersion theory calculations with some small contributions from chiral perturbation theory. Note that also the input masses had to be corrected using theoretical assumptions concerning isospin averaging and removing electromagnetic effects. Of course, there is still room for improvement because our directly measured m_{ud} has 2% precision and the split quantities m_u and m_d are only known to 5%

---

[13]The value for Q is only affected through NNLO contributions proportional to $m_d - m_u$. These corrections are numerically on the per mil level and therefore irrelevant for the present discussion as well as in the near future.

and 3% accuracy. The major contribution to this error comes from systematic uncertainties in Q. Improvements on this parameter may be possible [Anisovich and Leutwyler, 1996], but reaching accuracies below the percent level most probably requires a different approach. One of these approaches might be the use of N_f=1+1+1 lattice QCD joined with the abelian gauge group U(1) to account for electromagnetic effects. Together with the precisely known experimental values for M_{K^+} and M_{K^0} as input parameters, such approaches will probably lead to determinations of m_u and m_d with superior precision.

4.2.4. Treatment of statistical and systematic errors

I will finally describe the different contributions which went into the errors of our final results quoted in table 4.6. The main procedure was to establish a correlated global fit to all 47 simulation points of table 4.5, where the continuum limit and the extra-/interpolation to the physical point was performed simultaneously. We repeated the entire analysis for different interpolation formulae, mass cuts, discretization terms, fit ranges and renormalization procedures.

The chiral extra-/interpolation is often done using SU(2) or SU(3) χPT [Gasser and Leutwyler, 1984, 1985], where the expansion points of the perturbative series in terms of squared pion and kaon masses are at $(0, M_{K,\mathrm{phys}}^2)$ or $(0, 0)$ respectively. The corresponding formulae for a quantity vanishing in the chiral limit contain terms proportional to M_π^2 as well as chiral logs proportional to $M_\pi^4 \ln(M_\pi^2/\Lambda^2)$ with know pre-factors and the chiral symmetry breaking scale Λ. In practice, the knowledge on the pre factors is of limited use because they contain parameters which are not known in the specific simulation or distorted by large error bars. Using phenomenological input for these parameters is not the best choice when considering a full ab initio calculation. Furthermore, even advanced fitting algorithms cannot safely distinguish between M_π^4 ad $M_\pi^4 \ln(M_\pi^2/\Lambda^2)$ terms if the masses are not sufficiently large so that the log becomes visible. However, the applicability of χPT itself is in question in this region. The most optimal choice for chiral extrapolations is choosing an expansion point within the range covered by the data set. Together with a suitable Taylor ansatz, good results can be obtained [Dürr et al., 2008].
We used both fitting methods in order to be able to estimate higher order systematic effects. We started by solving the SU(2) χPT mass formula (3.15) for m_{ud} in two different ways

$$m_{ud} = \frac{M_\pi^2}{2B} \left(1 - \frac{1}{2} \frac{M_\pi^2}{(4\pi F_\pi)^2} \ln\left(\frac{M_\pi^2}{\Lambda_3^2}\right) \right) (1 + c_s \Delta) \tag{4.26}$$

$$m_{ud} = \frac{M_\pi^2}{2B} \left/ \left(1 + \frac{1}{2} \frac{M_\pi^2}{(4\pi F_\pi)^2} \ln\left(\frac{M_\pi^2}{\Lambda_3^2}\right) \right) (1 + c_s \Delta) \right. , \tag{4.27}$$

which differ by NNLO effects. Here we introduced the hadronic quantity

$$\Delta = 2M_K^2 - M_\pi^2 - [2M_K^2 - M_\pi^2]^{\mathrm{phys}}, \tag{4.28}$$

so that the latter term is essentially a linear fit in m_s centered at its physical value. It accounted for small deviations of our input strange quark masses from their physical values

[Dürr et al., 2008]. Alternatively we used Taylor expansions for m_{ud} and m_s

$$m_{ud} \;=\; c_1 + c_2 M_\pi^2 + c_3 M_\pi^4 + c_4 \Delta \qquad\qquad (4.29)$$
$$m_s \;=\; c_5 + c_6 M_\pi^2 + c_7 \Delta + c_8 \Delta^2. \qquad\qquad (4.30)$$

Augmenting these fit formulas with terms proportional to Δ^2 and M_Π^4 respectively yielded coefficients consistent with zero for these terms.

In total we used three different ansaetze for performing the chiral extra-/interpolation. We enhanced them by applying the two different mass cuts $M_\pi < 348, 380\,\text{MeV}$ in order to test for the significance of our fit models to higher order contributions in M_π^2. We also applied the pion mass cuts $M_\pi < 380, 480\,\text{MeV}$ to the M_Ω extrapolation (cf. formula (4.2)) necessary for setting the scale. Thus we used in total four different pion mass cuts.

To reduce contributions from excited states in the correlation functions, we used Gaussian sources with radii $r \approx 0.32\,\text{fm}$ as already done in Dürr et al. [2008]. We tested for excited state contributions by applying correlated single- and double-channel fits to the correlators. We found complete agreement of the data with single-channel fits around $t_{\min} \approx 0.7\,\text{fm}$ for the meson channels and $t_{\min} \approx 0.8\,\text{fm}$ for the Ω correlation functions. This amounts to $at_{\min} = \{6, 8, 9, 11, 13\}$ for $\beta = \{3.31, 3.5, 3.61, 3.7, 3.8\}$ and to 20% larger $at_{\min}$ for baryons. Again, we repeated the whole analysis using the more conservative fit ranges starting at $at_{\min} = \{7, 9, 11, 13, 15\}$. The upper end of the interval was chosen to be at $at_{\max} = 2.7\,at_{\min}$ or $T/2 - 1$ for lattice extends shorter than $5.4\,at_{\min}$. It is important to approximately keep the size of the fit window independent of $at_{\min}$ so that all fits for a single beta but different $at_{\min}$ have the same number of degrees of freedom. Otherwise we would have lost sensitivity to possible excited states contributions: in fitting ranges with smaller $at_{\min}$, these effects would have been (partly) compensated by a larger number of degrees of freedom and hence the χ^2/ndf's would not have been comparable. On the other hand, this comparability is an important requirement in our error analysis method since all results are weighted by their corresponding goodness-of-fit and are thus compared by those.

To summarize, we used two different ranges for fitting the correlators in order to ensure that possible effects coming from excited states are under control.

As already discussed in part 3, our action has formally $\mathcal{O}(\alpha_s a)$ cutoff effects. Since the application of smearing suppresses this term, it is possible that our leading discretization errors are of $\mathcal{O}(a^2)$. The cutoff dependence of different observables can be different, thus we assumed $\mathcal{O}(\alpha_s a)$ or $\mathcal{O}(a^2)$ scaling in the continuum extrapolation of the quark masses as well as in the ratios of renormalization factors (cf. section 4.2.2). This added four possibilities to the final analysis.

In order to assess the statistical errors we used the moving block bootstrap with 2000 bootstrap samples and a block size ranging from 1 to 10, where two atomic blocks were separated by 10 HMC trajectories (cf. the autocorrelation analysis in 4.2.1).

Altogether we ended up with three ansaetze for the quark mass interpolation, four pion mass cuts, two different intervals for fitting the correlators, four fit models for the continuum extrapolation and three ways of performing the RI renormalization. This yielded a total of 288 analyses, where our final result and error estimates were computed analogous to the procedure described in 4.1.

Table 4.7 shows the different contributions to the systematic error. It exhibits the cutoff effects as the dominant source of systematic uncertainty in our results.

cen. val.	σ_{stat}	σ_{syst}	plateau	scale set	fit form	mass cut	renorm.	cont.
3.503	0.048	0.049	0.330	0.034	0.030	0.157	0.080	0.926
96.43	1.13	1.47	0.207	0.005	0.031	0.085	0.085	0.970
27.531	0.196	0.083	0.513	0.200	0.023	0.320	—	0.771

Table 4.7.: Disentangled contributions to the systematic uncertainty of m_{ud}^{phys}, m_s^{phys} and $m_s^{\text{phys}}/m_{ud}^{\text{phys}}$ (from top to bottom). Entries in columns 1-3 are in MeV and refer to the RI scheme at $\mu = 4\,\text{GeV}$. Columns 4-10 indicate the relative share of the systematic error given in column 3 (the squares of these numbers add up to 1). The headers of these columns refer to the plateau range in the primary observables, the overall scale setting, the interpolation ansatz to tune to the physical mass point, the cut in the pion mass, the details of the renormalization procedure (read-off scale, chiral extrapolation), and the continuum extrapolation [Durr et al., 2010].

4.2.5. Summary

We determined the average light and strange quark masses m_{ud} and m_s with 2% accuracy in an N_f=2+1 lattice calculation using non-perturbative renormalization for the quark masses. Our data cover five lattice spacings in the range $0.054-0.116\,\text{fm}$, pion masses down to $120\,\text{MeV}$ and volumes up to $6\,\text{fm}$. This allowed for performing safe interpolations in the quark masses, an extrapolation into the continuum and an infinite volume limit.

We exploited the different renormalization pattern of VWI and AWI quark masses to circumvent difficulties in RI renormalization using dynamical Wilson-type quarks and imposing $\mathcal{O}(a)$ improvement. We bypassed the RI window problem with the continuum extrapolation method for ratios of renormalization constants. Our main results for m_{ud} and m_s are in the RI scheme at $4\,\text{GeV}$ obtained fully non-perturbatively. To allow for comparison with the literature, we converted our results perturbatively into the $\overline{\text{MS}}$ and RGI schemes (cf. table 4.6). In this step the use of perturbation theory is unavoidable but figure 4.9 shows that our data is inside the perturbative region for $\mu \geq 4\,\text{GeV}$.

A direct lattice determination of m_u and m_d is beyond the scope of this calculation and not feasible at this time. The reason for this is that much computing time has to be spent in order to tune the quark masses to their physical values. As soon as machine power increases and algorithmic developments improve, a N_f=1+1+1 setup, probably also including electromagnetic effects, might become feasible and a direct high precision measurement of m_u, m_d and m_s possible. Nevertheless, using the dispersive input Q we were able to compute the up- and down-quark masses with an accuracy of 5% and 3% respectively.

The values from table 4.6 can be compared to N_f=2+1 quark mass calculations from literature. According to the most recent lattice averages performed by FLAG [Colangelo et al., 2010b],[14] our results are in very good agreement.

We conclude that our results provide precise and reliable input for upcoming phenomenological calculations in which light quark mass values are required.

---

[14]note, that these did not yet include our results, so that a comparison is allowed

4.3. Kaon bag parameter B_K

The most important and final project of this thesis is the prediction of the kaon bag parameter B_K, which can be related to CP violation in the standard model (cf. section 2.2.6). Compared to our calculations presented in the previous sections, this computation additionally involved the complicated subtraction of operator mixing (cf. section 2.4.2), since our fermion discretization breaks chiral symmetry explicitly.

In the following, I can often refer to 4.2, since a lot of the basic work was already done in that section. This especially applies to the generated ensembles, from which we could use a large fraction for this calculation. We had to neglect the largest lattice spacing of $a \approx 0.115\,\mathrm{fm}$ since it did not provide a sufficiently large momentum cutoff for extracting the relevant renormalization factors. However, four different lattice spacings between $0.054\,\mathrm{fm} \lesssim a \lesssim 0.093\,\mathrm{fm}$ still remained, allowing for a safe continuum extrapolation. Furthermore, we added a few more quark masses to some of the existing lattice spacings. Our N_f=2+1 data straddle the physical pion mass and thus allowed for a safe interpolation in the averaged up- and down-quark mass m_{ud}. We discussed the smallness of finite volume effects of the pion mass on all our ensembles in section 4.2.1, illustrated by the plot shown in figure 4.6. We produced the same plot for the estimated finite volume corrections to B_K (cf. figure 4.12) by using the appropriate formulas of Becirevic and Villadoro [2004]. Note, that these formulas are dependent on M_π^2 and M_K^2. Thus, and only for illustrative purposes, we flattened out the latter dependence by keeping the difference $2M_K^2 - M_\pi^2$ fixed to its physical value. Since this difference is proportional to the strange quark mass and our data are close to m_s^{phys}, we consider this being a good approximation. We observe that our estimated finite volume corrections to B_K are below 0.3% and thus well under control. However, we still correct for this small effect in the final fit using the same formulas. In order to set the scale, we used the results from section 4.2.

4.3.1. Non-perturbative renormalization

This is the most important part of the calculation. As described in section 2.4.2, the mixing coefficients have to be extracted reliably since the matrix elements of $Q_2, \ldots, Q_5$ are chirally enhanced with respect to Q_1. In our analysis we closely followed the procedures already used for the determination of quenched B_K in section 3.2.3.

We computed the dynamics matrix D as described in section 2.4.2 for at least five quark masses per β. From that matrix we computed the mixing coefficients Δ_{1k} by solving the linear system of equations (2.276) and then computed the (massive) un-mixed Z_{11}^+ using the full set of equations (2.275).[15] Furthermore, we improved the signal by canceling statistical and systematic effects in the ratio $Z_{B_K} = Z_{11}^+/Z_A^2$, which can be directly obtained from non-perturbative RI data without having to compute Z_q in an intermediate step. However, we checked that a separate computation of Z_{11}^+ and Z_A using the Z_q determined in section 4.2 yielded compatible results.

---

[15]Formally, the un-mixing is defined in a massless scheme where no additional chiral symmetry breaking induced by non-vanishing quark masses occurs. In order to test whether our proceeding is valid, we swapped the different steps. This means that we first extrapolated into the chiral limit and then performed the un-mixing. Since our non-perturbative renormalization data depend only very lightly on the quark mass, we found no significant deviations between these two procedures. Therefore, the use of either one is perfectly valid on our level of precision.
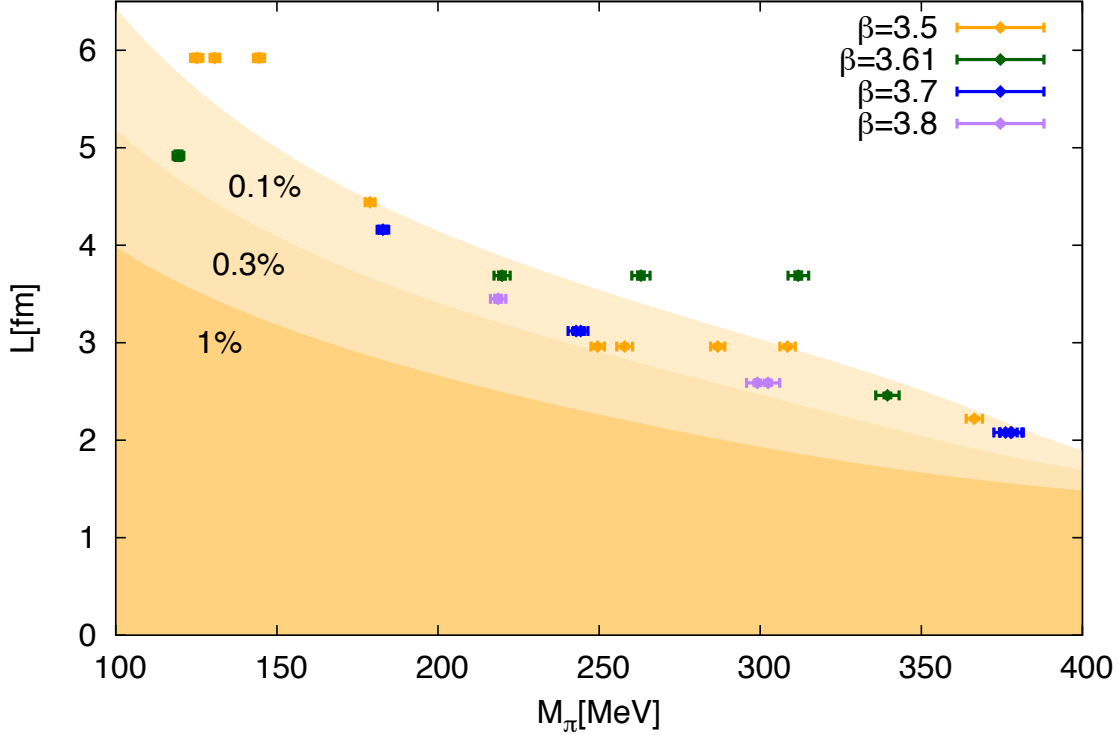
Figure 4.12.: Estimated finite volume effects on B_K using the 1-loop χPT finite volume formulas of Becirevic and Villadoro [2004] with flattened M_K^2 direction by setting $2M_K^2 - M_\pi^2$ to its physical value. Our data points are colored according to the lattice cutoff and the shaded bands denote the estimated finite volume corrections to B_K at different %-levels as indicated by the labels 1%, 0.3% and 0.1%. The strong deviation from the exponential-like behaviour for large pion masses is due to cancellations in the finite volume formulas: when M_π reaches the SU(3) symmetric point, contributions coming from π, K and η-loops almost cancel each other. Due to this, our estimated finite volume effects are below the 0.3% level and thus well under control.

In order to improve the matching to 2-loop continuum perturbation theory, we applied the ratio extrapolation (see section 2.4.3), i.e. we computed the continuum limit of

$$R_{B_K}(3.5\,\text{GeV}, \mu, a) = \frac{Z_{B_K}(3.5\,\text{GeV}, a)}{Z_{B_K}(\mu, a)} \tag{4.31}$$

in the RI scheme, by applying a linear fit including data from the three smallest lattice spacings. Again, we assumed either $\mathcal{O}(\alpha_s a)$ or $\mathcal{O}(a^2)$ scaling and propagated the difference into our systematic error. The non-perturbative continuum running $R_{B_K}(3.5\,\text{GeV}, \mu)$ obtained by this procedure can be compared to the expected continuum running computed in 2-loop perturbation theory [Ciuchini et al., 1998; Buras et al., 2000]. Figure 4.13 shows the ratio of this two quantities and we observe that both runnings agree to better than 1% for scales between $1.8\,\text{GeV} \leq \mu \leq 3.5\,\text{GeV}$ under both scaling assumptions. We read off $Z_{B_K}(\mu, a)$ at three different scales $\mu \in \{2.8, 3.0, 3.4\}$ and obtained $Z_{B_K}(3.5\,\text{GeV}, a)$ by com-
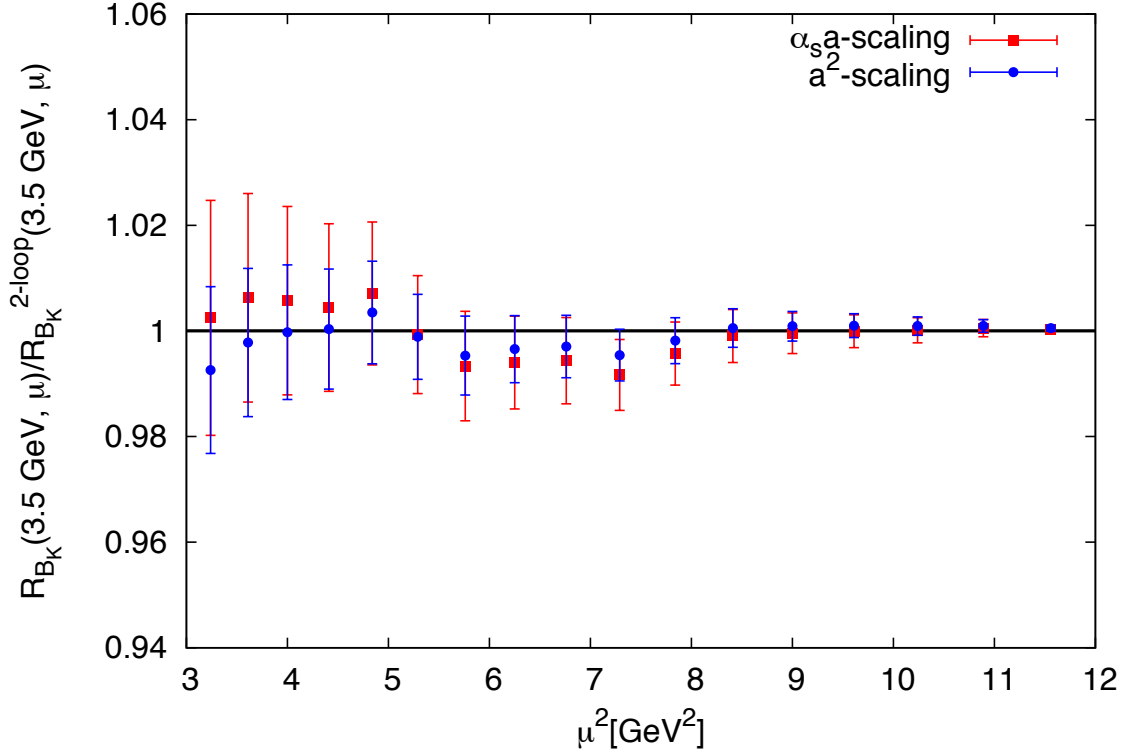
Figure 4.13.: Non-perturbative running of Z_{B_K} in the RI scheme normalized at 3.5GeV, obtained by extrapolating (4.31) into the continuum, assuming $\mathcal{O}(\alpha_s a)$ (squares) or $\mathcal{O}(a^2)$ (circles) scaling. It was divided by the perturbative 2-loop expectation from [Ciuchini et al., 1998; Buras et al., 2000], which was normalized at the same scale. We observe good agreement of the two runnings for $1.8\,\text{GeV} \leq \mu \leq 3.5\,\text{GeV}$.

puting $R_{B_K}(3.5\,\text{GeV}, \mu) \cdot Z_{B_K}(\mu, a)$. The different choices of μ propagated into our systematic error.

The relevant mixing coefficients Δ_{1k} are affected by non-perturbative poles, most probably attributed to the exchange of virtual pions with zero-momentum [Aoki et al., 2008; Sturm et al., 2009]. We subtracted these terms by computing the difference (3.10) for different quark masses m_i. As in the quenched case, the remaining major contributions to the subtracted mixing coefficients come from discretization errors proportional to $(ap)^2$ as well as p^{-4}-poles. The mass dependence is rather small and thus subdominant. We removed all these effects by applying suitable combined fits as shown in figure 4.14. In order to estimate the systematic contributions attributed to the specific choice of the fitting function as well as the fit window, we used 4 different fit windows and 2 fit models which either included only an $(ap)^2$ term or an additional p^{-4} term. All different choices were propagated into the systematic error. We found that all mixing coefficients except for Δ_{14} and Δ_{15} were compatible with zero within errors. The significant mixing coefficients were nevertheless small and vanished slowly with the lattice spacing (cf. figure 4.14).
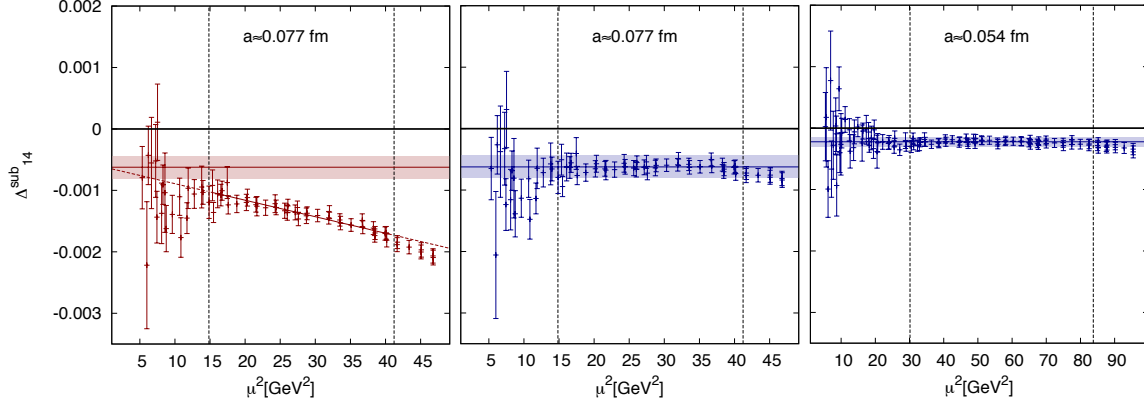
Figure 4.14.: Subtracted mixing coefficient $\Delta^{\mathrm{sub}}_{14}$ for $a \approx 0.077$ fm prior to removing discretiza-
tion effects proportional to $(ap)^2$ (left panel). The mass dependence was removed
by the fit and the red horizontal line denotes the extracted mixing coefficient
along with its 1σ error band. The next panel shows the same data with the dis-
cretization term removed. The right panel shows the same data for $a \approx 0.054$ fm.
We observe that the extracted mixing coefficient is very small and vanishes slowly
for $a \to 0$.

4.3.2. Matrix elements

Analogous to our proceeding in part 3.2.3, we computed the matrix elements $Q_1, \ldots, Q_5$ by
evaluating the r.h.s. of expression (2.224). Therefore, we used random sources at $t = 0$ and
$t = T/2$, where T is the temporal extent of the lattice, and varied the operator insertion time-
slice τ. Note, that we needed only four inversions per random source pair: one for each quark
mass and random source. As in 3.2.3, we improved our statistics by symmetrizing our data
with respect to $T/2$ and applied constant fits to the corresponding plateaus (see figure 4.15
for an example). We used 3 different fit ranges in order to estimate possible contributions
coming from excited states. All choices were propagated into our final systematic error.
By combining the mixing coefficients with the obtained Q_i, we were able to decompose the
renormalized B_K into the contributions from the individual Q_i. This decomposition is shown
in figure 4.16 for $a \approx 0.077$ fm and $M_\pi \sim 120$ MeV. The matrix element Q_1 would contribute
to B_K alone, if chiral symmetry were unbroken. In our case, this contribution is 98.1(1.2)%
for the data point shown in 4.16, indicating that our action has good chiral properties.

4.3.3. Final analysis

We performed a combined continuum extrapolation and interpolation in the quark masses
using different fit functions which can be combined in the single generic form

$$B_K^{\mathrm{RI}}(3.5 \,\mathrm{GeV}, x, y, a) = B_K^{\mathrm{RI}}(3.5 \,\mathrm{GeV}) \cdot f(x, y) + d(a), \qquad (4.32)$$
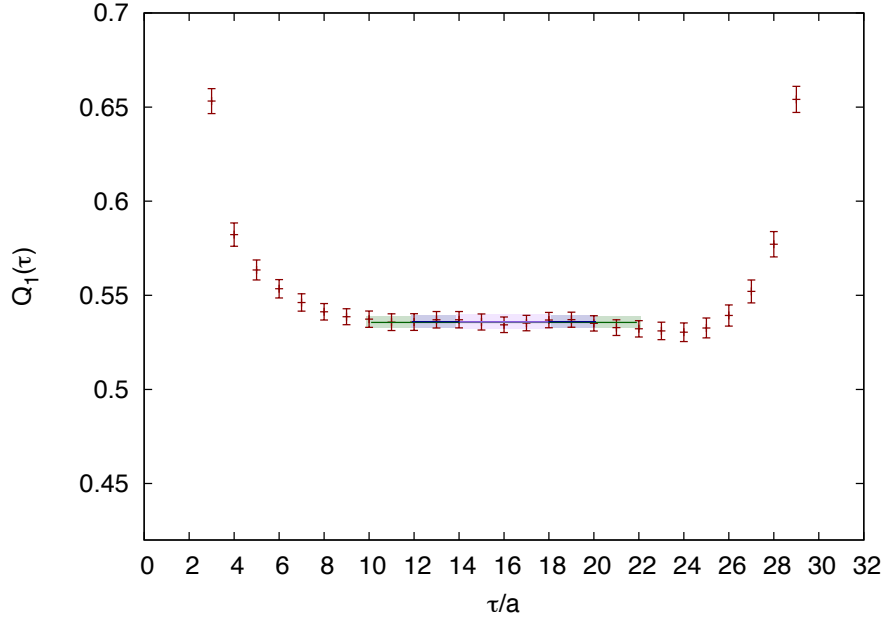
Figure 4.15.: Plateau for Q_1 at $a \approx 0.065\,\mathrm{fm}$, with $M_\pi \sim 245\,\mathrm{MeV}$ and time extent $T/a = 64$. The data are symmetrized with respect to $t = T/2$. The different solid lines represent constant fits for different fitting ranges and the shaded regions the statistical error. All fits to the different ranges agree very well within the errors.
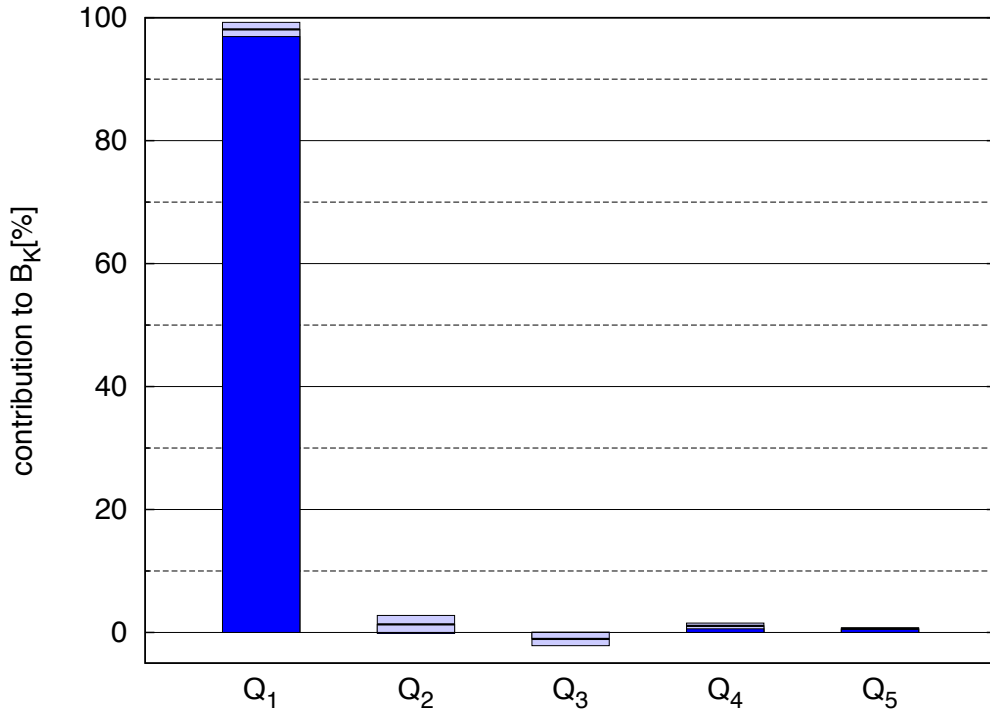
Figure 4.16.: Decomposition of contributions to renormalized B_K from the individual Q_i at $a \approx 0.077\,\mathrm{fm}$ and $M_\pi \sim 120\,\mathrm{MeV}$. The fact that Q_1 contributes to $98.1(1.2)\%$ testifies that our action has good chiral properties.

where $f(x, y)$ with $x = M_\pi^2$ and $y = 2M_K^2 - M_\pi^2$ is a functional form describing quark mass dependence. The generic form of f is

$$f(x, y) = \left[1 + a_{10}x + a_{20}x^2 + a_{01}y + a_{11}xy - \frac{a_\chi x}{32\pi^2 f_0^2} \ln\left(\frac{x}{\mu}\right) \right]. \qquad (4.33)$$

We used different Taylor fits with always a_χ kept fixed to zero and a_{10}, a_{01} left free as well as either a_{11} or a_{20} free or set to zero. This estimates higher order effects in the quark masses. We also applied two different SU(2)-χPT inspired fits with $a_\chi = 1, a_{10} = a_{20} = 0$ and f_0, μ, a_{01} free as well as a_{11} either left free or kept fixed to zero. Since B_K is automatically tree-level on-shell improved, we chose the lattice spacing dependence $d(a)$ to be proportional to either $\alpha_s a$ or a^2 as done in the analyses before. We do not include terms compatible with zero in our fits. The physical input pion and kaon masses were corrected for isospin and electromagnetic effects. One of our Taylor fits with $\alpha_s a$ scale dependence is shown in figure 4.17. All different fitting functions used in the analysis yielded comparable qualities of fit when they were applied to the same data set.
We also tried SU(2)-χPT fits of the form

$$B_K^{\mathrm{RI}}(3.5\,\mathrm{GeV}, x, y, a) = B_K^{\mathrm{RI}}(3.5\,\mathrm{GeV}) \cdot \left[1 + b_1 y - \frac{1}{32\pi^2 f_\pi^2} \ln\left(\frac{x}{\mu^2}\right) \right] + d(a), \qquad (4.34)$$

with fixed $f_\pi = 93\,\mathrm{MeV}$ and leaving b_1, μ as free parameters. Our data were also perfectly consistent with these fits and thus to χPT predictions. However, we did not include them into the final analysis in order to avoid redundancies. To illustrate the quality of our data, the continuum limit of figure 4.17 is shown explicitly in figure 4.18. Note that the continuum scaling is very flat.   The statistical error was computed on 2000 moving block bootstrap samples with sufficiently large block size. To estimate the systematic error we repeated the analysis using

- 2 different fit ranges to extract pion and kaon masses from the correlators

- 3 different fit ranges for extracting the bare matrix elements Q_i

- 4 different fit windows and 2 fit functions for obtaining the mixing terms

- 3 different scales for extracting the renormalized matrix elements

- $\alpha_s a$ or a^2 scaling for the final fit and in the continuum extrapolation of the running

- 2 different pion mass cuts, i.e. only considering $M_\pi < 340\,\mathrm{MeV}$ or $M_\pi < 380\,\mathrm{MeV}$

- 5 different fit functions for performing the final fit.

This yields 5760 different analysis and each analysis gives an estimate for $B_K^{\mathrm{RI}}(3.5\,\mathrm{GeV})$ and a corresponding quality of fit. The median of this distribution gave our central value and the central 68% the systematic error. We obtain for our final result

$$B_K^{\mathrm{RI}}(3.5\,\mathrm{GeV}) = 0.5308(56)(23), \qquad (4.35)$$

where the first error is statistical and the second one systematic. The dominant contribution to the systematic error arises from subtracting the mixing terms (0.0021) followed by excited states uncertainties (0.0007) as well as the quark mass interpolation and extrapolating into the continuum (both 0.0006).
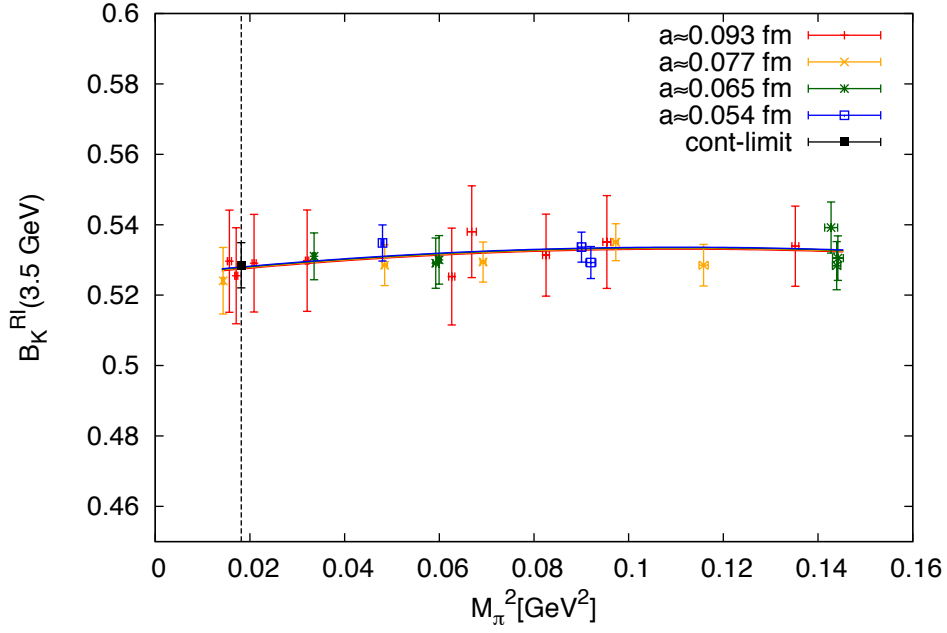
(a) interpolation in m_{ud}
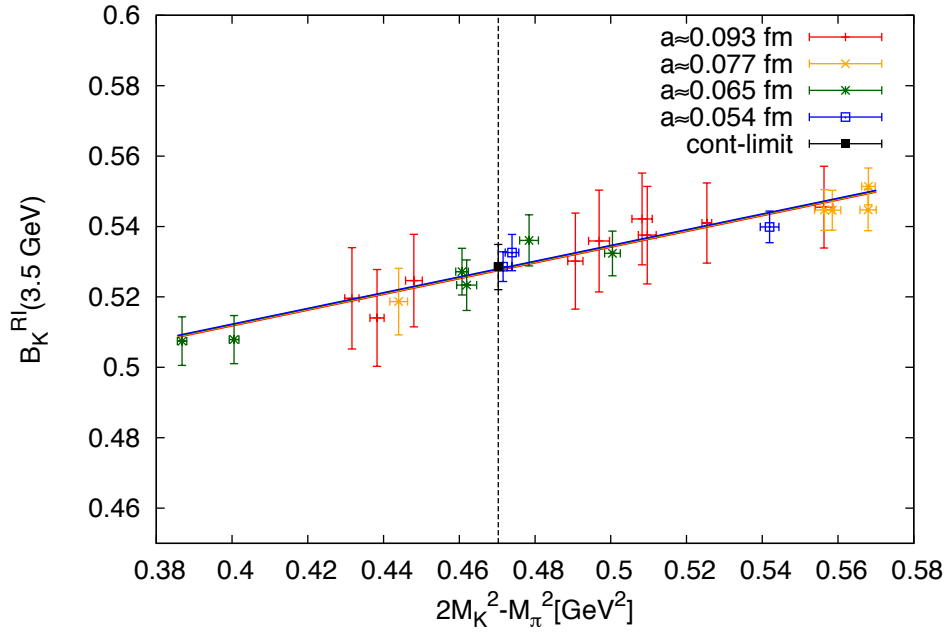
(b) interpolation in m_s

Figure 4.17.: Combined continuum extrapolation and interpolation to physical quark masses of B_K using a Taylor ansatz with $a_{11} = 0$ and a_{20} left free. The physical quark masses are denoted by the dashed vertical line and the black square represents the result for $B_K^{\mathrm{RI}}(3.5\,\mathrm{GeV})$. The interpolation in m_{ud} is relatively mild, whereas the data show a substantially stronger dependence on m_s. Nevertheless, the quark mass interpolation is fully under control in both cases. The continuum extrapolation is essentially flat, as can be also seen from figure 4.18.
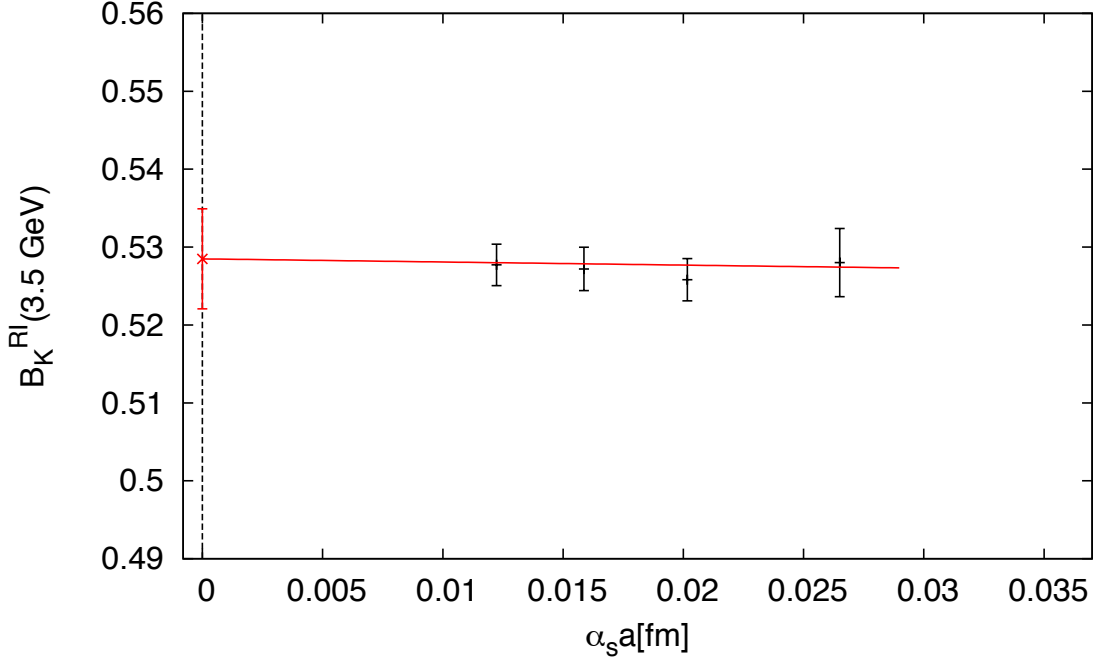
Figure 4.18.: Continuum extrapolation of B_K obtained from the fit displayed in 4.17.

Note that result (4.35) is fully non-perturbative, but the conversion to other schemes such as $\overline{\text{MS}}$-NDR or the RGI framework involves the use of perturbation theory. Thus, it is necessary to estimate the uncertainty attributed to the truncation of the perturbative series. Figure 4.19 shows the relative difference between numerical 1-loop and 2-loop as well as numerical and analytical 2-loop running, using the anomalous dimensions of [Ciuchini et al., 1998; Buras et al., 2000]. The β-function was always evaluated to 4-loop order using the coefficients from [van Ritbergen et al., 1997]. At the relevant scale $\mu = 3.5\,\text{GeV}$, the 2-loop to 1-loop corrections are around 2% and the analytical 2-loop to numerical 2-loop corrections around 0.5%. The full conversion factor from the RI scheme to $\overline{\text{MS}}$-NDR at the same scale is around 1.6%. Since higher order corrections are typically much smaller [Buchalla et al., 1996], we added the rather conservative truncation error of 1% to our converted results. These read in RGI and $\overline{\text{MS}}$-NDR respectively:

$$\hat{B}_K = 0.7727(81)(34)(77), \tag{4.36}$$

$$B_K^{\overline{\text{MS}}-\text{NDR}}(2\,\text{GeV}) = 0.5644(59)(25)(56). \tag{4.37}$$

Figure 4.20 shows the recent standard model expectation as well as results from other lattice groups. Our result is in good agreement with global standard model fits to flavour mixing data obtained by CKMfitter [ICHEP 10 update to Charles et al., 2005]. We are also consistent with expectations obtained by UTfit [Bona et al., 2006] by either including all decays ($\hat{B}_{K,\text{all}} = 0.94(17)$) or neglecting the semileptonic channels ($\hat{B}_{K,\text{no-sl}} = 0.88(13)$) in the fits. Concerning recent results from literature, we also observe reasonable agreement.
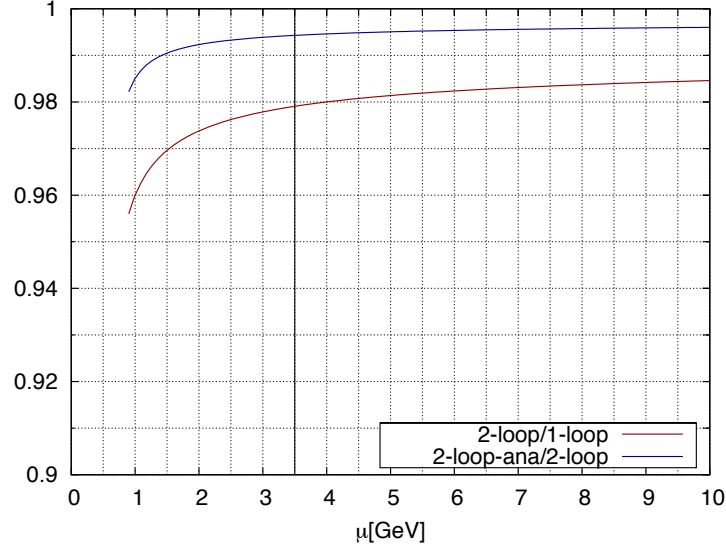
Figure 4.19.: Convergence of the perturbative series for Z_{B_K} up to 2-loop obtained by using the anomalous dimensions from [Ciuchini et al., 1998; Buras et al., 2000] and always the 4-loop β-function with coefficients from [van Ritbergen et al., 1997]. The red curve denotes the numerically integrated 2-loop running divided by the 1-loop running and normalized at infinity. The blue curve shows the same for the analytical 2-loop running divided by the 2-loop running obtained numerically. Although only results up to NNLO are available, the perturbative series shows good convergence. At $\mu = 3.5\,\mathrm{GeV}$ (black vertical bar), the uncertainties due to the truncation of the perturbative series are expected not to exceed 1%.
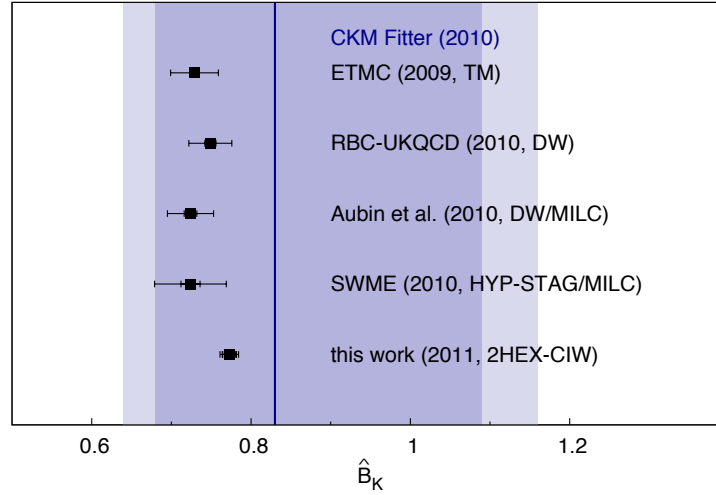
Figure 4.20.: Comparison of our result with the value for B_K obtained by CKMfitter [ICHEP 10 update to Charles et al., 2005, vertical line]. The dark and light bands correspond to CKMfitter's 1σ and 2σ confidence intervals respectively. The results from different N_f=2 [Constantinou et al., 2011, 1st] and N_f=2+1 (Aubin et al., 2010, Aoki et al., 2010, Bae et al., 2010, 2nd to 4th) lattice computations are also shown..

4.3.4. Summary and Discussion

We determined the kaon bag parameter B_K in dynamical N_f=2+1 flavour simulations in RI scheme at $3.5\,\text{GeV}$ with around 1.2% precision and converted it into continuum schemes such as $\overline{\text{MS}}$ or RGI, conservatively assuming a perturbative uncertainty of 1%. Our result agrees with standard model expectations and with results from other lattice groups.

In section 2.2.6 and appendix D, we related B_K to the indirect CP violation parameter ϵ, also denoted by ϵ_K in modern flavour physics literature [cf. e.g. Nakamura et al., 2010]. Since ϵ_K constrains the apex of the UT triangle in global standard model fits to flavour mixing data, it is worth to comment on the impact of our result for these kind of fits.

The large error bar assigned to the fitted B_K by CKMfitter indicates, that ϵ_K is rather insensitive to B_K. The errors quoted by UTfit are smaller[16], but also well above 10% and therefore stating a similar insensitivity. The explanation for this is, that ϵ_K is currently dominated by other sources of uncertainties. Consider for example the CKM matrix element $|V_{cb}|$: since $\epsilon_K \propto |V_{cb}|^4$, it is very sensitive to uncertainties in $|V_{cb}|$. Exclusive determinations of $|V_{cb}|$ from semi-leptonic B decays and inclusive determinations are only marginally consistent, inducing a $\sim 2.5\%$ overall error of that matrix element [cf. e.g. Lunghi and Soni, 2011a].[17] Therefore, the error of ϵ_K is currently dominated by the uncertainty of $|V_{cb}|$ [Laiho et al., 2010].

An additional systematic error is introduced by neglecting long-distance corrections in the B_K calculation. These stem from from virtual charm exchanges in box diagrams $(a), (b)$ or gauge boson exchanges in penguins $(c), (d)$ in figure 2.2. Recent perturbative calculations using experimental inputs suggest that long-distance corrections to ϵ_K are at the -5% level [Buras et al., 2010].

I finally conclude, that we do not find evidence for new fundamental contributions to indirect CP violation in $K{\to}\pi\pi$ decays [Durr et al., 2011a]. This supports the reasoning of Lunghi and Soni [2011a,b], who expect significant new physics contributions to B-meson decays and mixings instead.

---

[16]Their Bayesian approach considers the standard model being a collection of individual theories, allowing for independently distributed input and output parameters. This disrespects the standard model framework as being a unified theory with strong correlations between different observables and parameters, possibly leading to an under-estimation of the total error.

[17]Note, that V_{ub} can be used instead, but the discrepancy between values obtained from semi-leptonic and inclusive decays is even larger for this CKM matrix element [Lunghi and Soni, 2011a,b].

5. Summary and Outlook

After 40 years of lattice QCD, we are at a stage where we can test the strong dynamics of the standard model up to a high precision. We showed that the experimentally observed low-lying hadron spectrum of QCD could be recovered from first principles. This calculation received much attention in the past few years and was "considered to be a 'milestone' [Wilczek, 2008] 'in a 30-year effort of theoretical and computational physics' [Kronfeld, 2008]" [Krieg, 2008, p. 74].

Furthermore, we predicted the light quark masses m_u, m_d, m_s with uncertainties of at most 5%, providing reliable input for upcoming phenomenological predictions. Additionally, this calculation allowed us to exclude the $m_u = 0$ solution to the strong CP-problem by about 22 standard deviations.

Finally, we were able to compute the kaon bag parameter B_K with an uncertainty below 2%. Also here, we found no significant deviation from standard model expectations. This is in-line with the assumptions of Lunghi and Soni [2011a,b], who expect that new CP-violating physics is largely contributing to B-meson processes.

In that sense, I can conclude, that the work presented in this thesis is a large leap forward in testing standard model predictions from first principles using lattice QCD.

Although our computations have already been very precise and extensive, it is always possible to think of improvements and extensions. In case of the hadron spectrum, we only included the low-lying non-singlet particles so far. Adding excited states requires the implementation and application of new techniques suitable for extracting these excited states properly. State of the art methods to mention here are variational approaches [Michael, 1985; Luscher and Wolff, 1990; Blossier et al., 2009]. The idea is to consider cross-correlators of operators having the same quantum numbers but which couple to different energy states. Using a generalized eigenvalue approach, the energy levels of the excited states can be extracted, given that the base of operators was chosen wisely.

Extracting the ground state of singlet particles is also very complicated, because their correlation functions involve the computation of disconnected diagrams. Compared to standard (diluted) random source approaches, the distillation method [Peardon et al., 2009; Morningstar et al., 2010] is able to reduce statistical fluctuations in such computations significantly. The method is based on the fact that Jacobian (Laplacian) smearing suppresses the higher eigenmodes of the lattice Laplace operator. Distillation goes a step further and only projects out the lowest eigenvalues and eigenvectors, used to build distillation projectors which can be inserted into Greens functions. Depending on the number of computed eigenvectors, the inversion of the Dirac operator significantly simplifies since the dimension of the subspace is much smaller than the lattice volume. Thus, a forward lattice Dirac operator inversion becomes feasible. The distillation method can also improve the overlap of operators to a certain state [Bulava et al., 2010] and thus also improves the signal in the variational approaches discussed before.

Additionally, one can compute the hadron spectrum in N_f=2+1+1 simulations, i.e. including a dynamical charm quark. However, since the charm quark is heavy compared to the mesons and octet-baryons and approximately of the same mass as the decuplet-baryons, its influence on the ground state energies is expected to be small. Nevertheless, it would be interesting to investigate the size of dynamical charm effects which might be significant for excited states. On the far end, the inclusion of isospin breaking and electromagnetic effects would lead to interesting insights into the degeneracy of the nucleon masses and thus the stability of matter.

The quark mass study can also be extended to N_f=2+1+1 calculations, allowing for measuring the charm quark mass. Even more interesting is the inclusion of isospin breaking and electromagnetic effects in order to determine the individual m_u and m_d in a direct lattice calculation, since this would remove the large uncertainties coming from the use of dispersion theory completely. Isospin breaking can be incorporated by using 3 degenerate flavours in our RHMC. The most time-consuming part would be to tune the quark masses to their physical values. An extension of the method described in [Horsley, 2011] may help performing this task. The inclusion of (quenched) electromagnetic effects is also investigated in recent lattice calculations [Duncan et al., 1996; Blum et al., 2007; Portelli et al., 2010].

The study of the kaon bag parameter only involved the first term of the OPE. We neglected long-range contributions induced by virtual charm quark exchanges in the box diagrams (a) and (b) of figure 2.2. The penguin diagram (c) is suppressed by powers of $m_K^2/m_c^2 \sim \mathcal{O}(15\%)$ with respect to these active charm contributions, naively suggesting a $\mathcal{O}(2\%)$ contribution to B_K. Using large N_c expansion of the corresponding dimension-8 effective operator, Cata and Peris [2003] argue that the true contributions are even smaller. However, these contributions should be considered in future lattice computations. Using χPT, Buras et al. [2010] estimated, that long-distance corrections in kaon mixing contribute by about -4%. Nevertheless, a lattice calculation with full control over all errors would be preferable.[1]
In order to obtain tightened error bounds on ϵ_K, a precise determination of $|V_{cb}|$ (or $|V_{ub}|$ respectively) is inevitable. As soon as these improved bounds on ϵ_K are established, it would be interesting to compute BSM contributions to B_K arising from operators $O_2, \ldots Q_5$ in table 2.2. Among other things, this introduces a coupling of right handed particles to flavour changing currents. By considering the corresponding coupling constants as free parameters, one can obtain bounds on these couplings by comparing the computed ϵ_K with the experimental expectation.

Finally, the RI/MOM scheme might be replaced by the symmetric RI/SMOM scheme [Sturm et al., 2009] in future studies. This new scheme helps suppressing infrared divergencies in RI renormalization constants. However, still a lot of effort has to go into the investigation of unitarity violations and finite volume effects, associated with the commonly used twisted boundary conditions [Arthur and Boyle, 2011].

---

[1] See [Christ, 2010; Sachrajda, 2010] for recent developments.

Acknowledgements

A. Notation

- Euclidian gamma matrices and combinations ($\mu, \nu = 1, \ldots, 4$):

$$\{\gamma_\mu, \gamma_\nu\} = 2\delta_{\mu\nu}, \tag{A.1}$$

$$\gamma_5 = \gamma_1\gamma_2\gamma_3\gamma_4, \tag{A.2}$$

$$\gamma_{R/L} = \frac{1}{2}(1 \pm \gamma_5), \tag{A.3}$$

$$\sigma_{\mu\nu} = \frac{1}{2}[\gamma_\mu, \gamma_\nu], \tag{A.4}$$

$$\tilde{\sigma}_{\mu\nu} = \frac{1}{2}\varepsilon_{\mu\nu\alpha\beta}\sigma_{\alpha\beta} \equiv \gamma_5\sigma_{\mu\nu}, \tag{A.5}$$

- Some notation from RI renormalization procedure. In case of bilinears:

$$V_\mu \equiv \gamma_\mu, \tag{A.6}$$

$$A_\mu \equiv \gamma_\mu\gamma_5, \tag{A.7}$$

$$S \equiv \mathbf{1}, \tag{A.8}$$

$$P \equiv \gamma_5, \tag{A.9}$$

$$T_{\mu\nu} \equiv \sigma_{\mu\nu}. \tag{A.10}$$

The projectors belonging to these Dirac factors are are very simple: in the two point function case, it is $P_\Gamma = \Gamma^\dagger$.

The four-fermion operators are denoted as follows:

$$SS = \mathbf{1} \otimes \mathbf{1}, \tag{A.11}$$

$$PP = \gamma_5 \otimes \gamma_5,, \tag{A.12}$$

$$SP = \mathbf{1} \otimes \gamma_5, \tag{A.13}$$

$$PS = \gamma_5 \otimes \mathbf{1}, \tag{A.14}$$

$$VV = \sum_{\mu=1}^{4} V_\mu \otimes V_\mu, \tag{A.15}$$

$$AA = \sum_{\mu=1}^{4} A_\mu \otimes A_\mu, \tag{A.16}$$

$$VA = \sum_{\mu=1}^{4} V_\mu \otimes A_\mu, \tag{A.17}$$

$$AV = \sum_{\mu=1}^{4} A_\mu \otimes V_\mu, \tag{A.18}$$

$$TT = \sum_{\mu=1}^{4} \sum_{\nu=\mu+1}^{4} \sigma_{\mu\nu} \otimes \sigma_{\mu\nu}, \tag{A.19}$$

$$T\tilde{T} = \sum_{\mu=1}^{4} \sum_{\nu=\mu+1}^{4} \sigma_{\mu\nu} \otimes \tilde{\sigma}_{\mu\nu}. \tag{A.20}$$

Other four fermion operators can be built upon these by taking linear combinations. Note that in case of the tensor operator, the summation runs only over the six independent Lorentz indices.

The projectors to the operators $O_i^\pm, \mathcal{O}_i^\pm$ are, also because of the mixing, slightly more involved and have been worked out by Donini et al. [1999]. The projectors to the parity conserving operators $O_i^\pm$ are (N_c is the number of colours):

$$P_1^\pm \equiv +\frac{1}{64N_c(N_c \pm 1)}(P_{VV} + P_{AA}), \tag{A.21}$$

$$P_2^\pm \equiv +\frac{1}{64(N_c^2 - 1)}(P_{VV} - P_{AA}) \pm \frac{1}{32N_c(N_c^2 - 1)}(P_{SS} - P_{PP}), \tag{A.22}$$

$$P_3^\pm \equiv \pm\frac{1}{32N_c(N_c^2 - 1)}(P_{VV} - P_{AA}) + \frac{1}{16(N_c^2 - 1)}(P_{SS} - P_{PP}), \tag{A.23}$$

$$P_4^\pm \equiv +\frac{(2N_c \pm 1)}{32N_c(N_c^2 - 1)}(P_{SS} + P_{PP}) \mp \frac{1}{32N_c(N_c^2 - 1)}P_{TT}, \tag{A.24}$$

$$P_5^\pm \equiv \mp\frac{1}{32N_c(N_c^2 - 1)}(P_{SS} + P_{PP}) + \frac{(2N_c \mp 1)}{96N_c(N_c^2 - 1)}P_{TT}. \tag{A.25}$$

The projectors to the parity violating operators $\mathcal{O}_i^\pm$ are:

$$\mathcal{P}_1^\pm \equiv -\frac{1}{64N_c(N_c \pm 1)}(P_{VA} + P_{AV}), \tag{A.26}$$

$$\mathcal{P}_2^\pm \equiv -\frac{1}{64(N_c^2 - 1)}(P_{VA} + P_{AV}) \mp \frac{1}{32N_c(N_c^2 - 1)}(P_{SP} - P_{PS}), \tag{A.27}$$

$$\mathcal{P}_3^\pm \equiv \mp\frac{1}{32N_c(N_c^2 - 1)}(P_{VA} - P_{AV}) - \frac{1}{16(N_c^2 - 1)}(P_{SP} - P_{PS}), \tag{A.28}$$

$$\mathcal{P}_4^\pm \equiv +\frac{(2N_c \pm 1)}{32N_c(N_c^2 - 1)}(P_{SP} + P_{PS}) \mp \frac{1}{32N_c(N_c^2 - 1)}P_{T\tilde{T}}, \tag{A.29}$$

$$\mathcal{P}_5^\pm \equiv \mp\frac{1}{32N_c(N_c^2 - 1)}(P_{SP} + P_{PS}) \mp \frac{(2N_c \mp 1)}{96N_c(N_c^2 - 1)}P_{T\tilde{T}}. \tag{A.30}$$

The projectors P_{XY} with $X, Y \in \{A, P, S, V, Q, T, \tilde{T}\}$ are given by the appropriate expressions (A.11-A.20).

B. The Sommer parameter r_0

The Wilson loops defined in (2.108) have an important physical implication; they are related to the so-called *static quark potential*. For showing this, consider only Wilson loops which have a spatial and a time extend for now. Let us denote the spatial extend by R and the temporal one by T.[1] Using the gauge freedom, we can apply temporal gauge fixing so that all links in time direction are equal to one (consider a lattice with infinite time extend for simplicity). Then, the trace in (2.108) reduces to a trace over two lines of spatial links:

$$
\begin{aligned}
W_C(R,T) &= \left\langle \mathrm{Tr}\left[\left(\prod_{k=0}^{R} U_i(x+\hat{i}k)\right) \left(\prod_{k=R}^{0} U_{-i}(x+\hat{i}(k+1)+\hat{0}T)\right)\right]\right\rangle \\
&= \left\langle \mathrm{Tr}\left[P(x,R,0)P^\dagger(x,R,T)\right]\right\rangle,
\end{aligned}
\tag{B.1}
$$

where we introduced the shorthand notation

$$
P(x,R,T) = \prod_{k=0}^{R} U_i(x+\hat{i}k+\hat{0}T).
\tag{B.2}
$$

Inserting in the r.h.s of (B.1) a complete set of states $|k\rangle$ yields

$$
\begin{aligned}
W_C(R,T) &= \sum_k \langle 0|P(x,R,0)|k\rangle\langle k|P^\dagger(x,R,T)|0\rangle \\
&= \sum_k |\langle 0|P(x,R,0)|k\rangle|^2\, e^{-T(E_k(R)-E_0(R))},
\end{aligned}
\tag{B.3}
$$

where we additionally define

$$
E_1(R) - E_0(R) = V(R),
\tag{B.4}
$$

so that we obtain the famous *area-law*

$$
W_C(R,T) \overset{T\to\infty}{\sim} e^{-T\, V(R)}.
\tag{B.5}
$$

In order to show why $V(R)$ can indeed be seen as the potential between two static, and thus infinitely heavy, quarks, we would need to introduce the hopping parameter expansion [cf. e.g. Gattringer and Lang, 2010, p. 114ff]. This would lead too far for this appendix so that I will only sketch the main points in the line of argumentation.

The propagation of quarks is described by the inverse Dirac operator D^{-1}. In case of heavy quarks, it can be expanded in powers of $1/m$ or, more precisely, in powers of the hopping parameter κ. The term multiplied by κ is called hopping term H, since it contains the nearest-neighbour interactions of D. Terms such as $(\kappa H)^n$, appearing in the power series of D^{-1},

---

[1] For non-planar loops, the spatial extend R is usually calculated by using the euclidian norm.

162

connect quarks and anti-quarks which are separated by n sites in a gauge invariant way, i.e. through appropriate products of gauge links.

In the limit $\kappa \to 0$, the shortest connection between a quark and an anti-quark gives the dominant contribution to this power series, since all other possible paths are multiplied with additional powers of κ. This shortest connection is exactly the Wilson loop and, according to this argumentation, the static quark potential will receive significant contributions from hopping terms of higher order in κ at small distances R. This is where the approximation of the static quark potential by Wilson loops breaks down.

Let us now have a closer look at $V(R)$. In QED, one would expect a coulomb term such as B/R for a small coupling g, but we also know that the gluons interact with each other forming a flux tube between a pair of a quark and an anti-quark. The energy of this tube is expected to grow linearly with the distance. Thus we can make the ansatz

$$V(R) = A + \frac{B}{R} + \sigma R, \tag{B.6}$$

where A is an arbitrary normalization for the potential. It turns out that this ansatz fits lattice data very well. It is even possible to assume the validity of a bosonic string model which predicts all of the three parameters and also fits lattice data very well [Necco and Sommer, 2002]. The potential $V(R)$ can be used to set the scale a, by using the Sommer radius r_0 [Sommer, 1994a]. It is defined by the equation

$$r_0^2 \left. \frac{\mathrm{d}}{\mathrm{d}R} V(R) \right|_{R=r_0} = 1.65, \tag{B.7}$$

which corresponds to a physical value of $r_0 \approx 0.49\,\mathrm{fm}$ [Sommer, 1994a]. The dimensionless ratio r_0/a can be acquired from lattice data by combining the parametric form (B.6) with the definition of r_0 (B.7) to obtain

$$-B + \sigma r_0^2 = 1.65 \tag{B.8}$$

and finally in lattice units

$$\frac{r_0}{a} = \sqrt{\frac{1.65 + B}{\sigma\, a^2}}, \tag{B.9}$$

where B and σa^2 can be directly measured on the lattice. The most precise data measuring r_0 for the Wilson action in the quenched approximation come from Necco and Sommer [2002]. In our work, we do not apply the polynomial fit to r_0/a suggested there, but we use the Padé model

$$\ln(r_0/a) = \frac{4\pi^2}{33}\beta\frac{1 + d_1/\beta + d_2/\beta^2}{1 + d_3/\beta + d_4/\beta^2} \tag{B.10}$$

instead. This we have already done in Dürr et al. [2007] and is described in more detail by Kurth [2007, p. 97f]. This ansatz converges in the weak coupling limit $\beta \to \infty$ to the right perturbative value. The ansatz (B.10) fitted to the data of Necco and Sommer [2002] gives $d1 = 8.2384$, $d2 = 15.310$, $d3 = -2.7395$ and $d4 = -11.526$ as well as $\chi^2/\mathrm{ndf} = 0.91$. In [Kurth, 2007, p. 98], the fit is shown in figure E.1. We used our parametrization as well as $r_0 = 0.49\,\mathrm{fm}$ for setting the scale in the quenched scaling analyses (cf. sections 3.2.2 and 3.2.3).

C. Gauge fixing

As discussed in 2.2, gauge invariance is a central principle of QCD. The lattice formulation preserves this property and physical observables have to be gauge invariant. For showing this, consider a gauge variant observable $O[U] \neq O[U']$, with $U'_\mu(x) = G(x)U_\mu(x)G(x+\hat{\mu})^\dagger \equiv GU'\tilde{G}$ and $G(x), U_\mu(x) \in \mathrm{SU}(3)$, $\forall\, \mu, x$. We can write

$$\langle O \rangle = \frac{1}{Z} \int \mathrm{D}U\, e^{-S[U]} O[U] \tag{C.1}$$

$$= \frac{1}{Z} \int \mathrm{D}(GU\tilde{G})\, e^{-S[GU\tilde{G}]} O[GU\tilde{G}] \tag{C.2}$$

$$= \frac{1}{Z} \int \mathrm{D}U\, e^{-S[U]} O[U'], \tag{C.3}$$

where we used the gauge invariance of the action and the invariance properties of the Haar measure. The gauge transformation G can be chosen arbitrarily so that we are allowed to integrate over it

$$\langle O \rangle = \int \mathrm{D}G\, \langle O[GU\tilde{G}] \rangle. \tag{C.4}$$

Any (Yang-Mills) gauge variant functional O can be written as an open chain of multiplied links $C(x, x')$, where x and x' with $x' \neq x$ (cf. C.1) are the starting end ending points of the linkchain respectively. We can integrate over all gauge transformations G at the endpoint x without changing the expectation value of $C(x, x')$:

$$\langle C(x, x') \rangle = \int \mathrm{d}G(x)\, \langle G(x)\, C(x, x')\, G^\dagger(x') \rangle = \int \mathrm{d}G(x)\, G(x) \langle C(x, x')\, G^\dagger(x') \rangle = 0. \tag{C.5}$$

Thus, the expectation value of any gauge variant quantity is equal to zero.

One could ask why we need gauge fixing at all, if physical observables are gauge invariant? First, it can simplify specific computations. In the calculation of Wilson loops for example, it is suitable to use the temporal gauge $U_4(x_4, \mathbf{x}){=}\mathbf{1}\,\forall\, x_4 < T{-}1$, since it drastically reduces the number of necessary link multiplications. Second, gauge fixing is necessary when gauge variant quantities such as renormalization coefficients are computed. Also gauge variant improvements require gauge fixing, e.g. the use of Gaussian smeared sources in spectroscopy. The most popular gauges (and the ones we used in this work) are the *Coulomb* and the *Landau gauge*. In the continuum, the gauge fixing condition for both of them can be stated as

$$\sum_{\mu=1}^{n} \partial_\mu A^\mu(x) = 0, \tag{C.6}$$

where $n = 4$ or $n = 3$ for Landau or Coulomb gauge respectively. The former gauge imposes a condition on the fields in all directions and therefore is sometimes called a *complete gauge*.
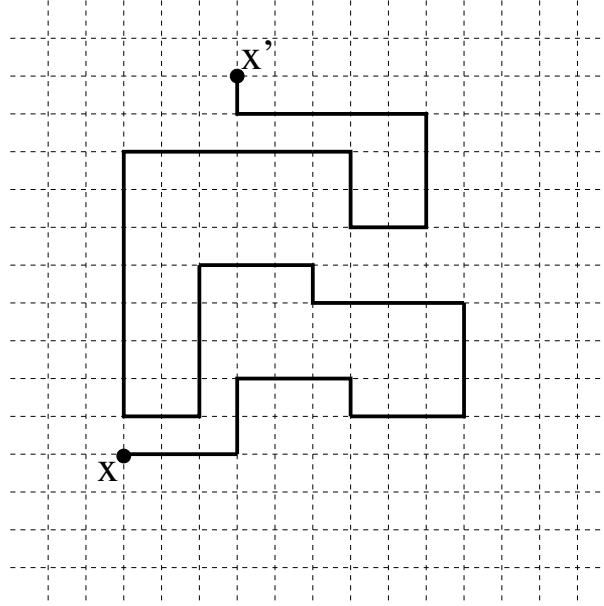
Figure C.1.: Chain of links $C(x, x')$ with open ends $(x' \neq x)$ in two dimensions.

We now convert (C.6) to a formula for the link variables U. The condition (C.6) is equivalent to the problem of finding an extremal value of the functional [Gattringer and Lang, 2010, p. 52]

$$W[A] = \sum_{\mu=1}^{n} \int \mathrm{d}^4x \ \mathrm{Tr}[A_\mu(x) \, A^\mu(x)]. \tag{C.7}$$

Hence in the extremum, $W[A]$ should be invariant under infinitesimal gauge transformations (cf. formula (2.5))

$$A_\mu(x) \to A_\mu(x) + \varepsilon \left(i[\alpha(x), A_\mu(x)] - \partial_\mu \alpha(x) \right). \tag{C.8}$$

Applying (C.8) to (C.7) yields after some lines of algebra

$$W[A] \to W[A] - 2\varepsilon \sum_{\mu=1}^{n} \int \mathrm{d}^4x \ \mathrm{Tr}[A^\mu(x) \, \partial_\mu \alpha(x)]$$

$$= W[A] + 2\varepsilon \sum_{\mu=1}^{n} \int \mathrm{d}^4x \ \mathrm{Tr}[\partial_\mu A^\mu(x) \, \alpha(x)], \tag{C.9}$$

where we performed an integration by parts and assumed that $\alpha(x)$ vanishes at the boundaries. Since the second term of (C.9) has to vanish for any $\alpha(x) \in \mathrm{SU}(3)$, we recover (C.6). The continuum QCD expression (C.7) has a simple lattice counterpart [cf. Gattringer and Lang, 2010, p. 52]:

$$W_{\mathrm{lat}} = -a^2 \sum_{\mu=1}^{n} \sum_{x} \mathrm{Tr}\left(U_\mu(x) + U_\mu^\dagger(x) \right). \tag{C.10}$$

Note that for $U_\mu(x) = \exp(iaA_\mu(x))$ and small cutoff a, we indeed recover (C.7). Therefore, in order to fix the gauge to Landau or Coulomb gauge, one has to find a gauge transformation

G which is an extremum of

$$F[G] = -a^2 \sum_{\mu=1}^{n} \sum_{x} \mathrm{Tr}\left(G(x)\, U_\mu(x)\, G^\dagger(x + \hat{\mu}) + G(x + \hat{\mu})\, U_\mu^\dagger(x)\, G^\dagger(x) \right). \tag{C.11}$$

To tackle this optimization problem, different minimization techniques and corresponding improvements such as overrelaxation are used [cf. Giusti et al., 2001, and references therein]. Note, that F has in general multiple stationary points which are referred to as *Gribov copies* and discussed in detail in the review [Giusti et al., 2001] and references therein.

D. Remarks on diagrammatic $K^0 - \bar{K}^0$ mixing

We discussed the weak contributions to neutral kaon mixing in section 2.2.6 and argued that the process is dominated by diagrams (a) and (b) depicted in figure 2.2. Since these diagrams are related by Fierz symmetry, we consider only diagram (a) for now.

Using electroweak Feynman rules and setting all external momenta to zero, we can write the corresponding amplitude as follows [cf. e.g. Lellouch, 2011, p. 26]

$$-i\mathcal{M} = \frac{g_2^4}{4} \int \frac{\mathrm{d}^4 k}{(2\pi)^4} i D_{\mu\nu}^W(k) \, i D_{\rho\sigma}^W(k) \, (\bar{d}_L \gamma^\mu S(k) \gamma^\sigma s_L)(\bar{d}_L \gamma^\nu S(k) \gamma^\rho s_L), \qquad (\text{D.1})$$

where g_2 is the electroweak non-diagonal SU(2) coupling,

$$q_L = \gamma_L q, \quad \bar{q}_L = \bar{q}\gamma_R \qquad (\text{D.2})$$

are left-handed projected spinors and

$$D_{\mu\nu}^W(k) = \frac{-g_{\mu\nu} + k_\mu k_\nu / M_W^2}{k^2 - M_W^2} \qquad (\text{D.3})$$

is the W-boson propagator in unitary gauge, allowing us to disregard box diagrams with internal Higgs lines. Furthermore we defined

$$\lambda_q \equiv V_{qd}^* V_{qs} \qquad (\text{D.4})$$

and

$$S(k) = \sum_{q=u,c,t} \lambda_q \frac{1}{\not{k} - m_q}. \qquad (\text{D.5})$$

CKM matrix unitarity implies $\sum_q \lambda_q = 0$ and thus

$$S(k) = \sum_{q=c,t} \lambda_q \left(\frac{1}{\not{k} - m_q} - \frac{1}{\not{k} - m_u} \right) \approx \sum_{q=c,t} \lambda_q \frac{k^2 m_q + \not{k} \, m_q^2}{k^2(k^2 - m_q^2)}, \qquad (\text{D.6})$$

where we used $m_u \approx 0$ in the last step. Note that the GIM mechanism is in action here: if all up-type quark masses were degenerate, $S(k)$ would be identical to zero and thus no neutral kaon mixing would occur.

Next we contract the W-boson propagator with the γ-matrix indices, obtaining the expression

$$-i\mathcal{M} = \frac{g_2^4}{4} \int \frac{\mathrm{d}^4 k}{(2\pi)^4} \frac{-1}{(k^2 - M_W^2)^2} \sum_{\substack{q_1,q_2=c,t \\ i,j,k,l}} \lambda_{q_1} \lambda_{q_2} \bar{d}_i s_j \bar{d}_k s_l \, T_{q_1 q_2; ijkl}, \qquad (\text{D.7})$$

where

$$T_{q_1 q_2; ijkl} \equiv \Big[(\gamma_\mu \gamma_L S_{q_1} \gamma_\sigma \gamma_L)_{ij} (\gamma^\mu \gamma_L S_{q_2} \gamma^\sigma \gamma_L)_{kl} + \frac{1}{M_W^4} (\slashed{k} \gamma_L S_{q_1} \slashed{k} \gamma_L)_{ij} (\slashed{k} \gamma_L S_{q_2} \slashed{k} \gamma_L)_{kl}$$

$$- \frac{1}{M_W^2} \Big((\gamma_\mu \gamma_L S_{q_1} \slashed{k} \gamma_L)_{ij} (\gamma^\mu \gamma_L S_{q_2} \slashed{k} \gamma_L)_{kl} + (\slashed{k} \gamma_L S_{q_1} \gamma_\sigma \gamma_L)_{ij} (\slashed{k} \gamma_L S_{q_2} \gamma^\sigma \gamma_L)_{kl} \Big) \Big], \tag{D.8}$$

and

$$S_{q_i} = \frac{k^2 m_{q_i} + \slashed{k}\, m_{q_i}^2}{k^2 (k^2 - m_{q_i}^2)}. \tag{D.9}$$

In order to simplify (D.8), we use the generalized Fierz transformation [Nishi, 2005]

$$\Gamma_{ij}^A \Gamma_{kl}^B = \frac{1}{4} \sum_{C,D} \mathrm{Tr}[\Gamma^A \, \Gamma_C \, \Gamma^B \, \Gamma_D] \, \Gamma_{il}^D \Gamma_{jk}^C \tag{D.10}$$

in the 16 component chiral basis

$$\Gamma^X \in \{ \gamma_R, \gamma_L, \gamma_R \gamma^\mu, \gamma_L \gamma^\mu, \sigma^{\mu\nu} \}, \quad \Gamma_X \in \{ \gamma_R, \gamma_L, \gamma_L \gamma_\mu, \gamma_R \gamma_\mu, \sigma^{\mu\nu}/2 \}. \tag{D.11}$$

In our case, the traces we have to evaluate are of the type

$$\mathrm{Tr}\big[\gamma_\mu \gamma_L S_{q_1} \gamma_\sigma \gamma_L \Gamma_C \gamma_\nu \gamma_L S_{q_2} \gamma_\rho \gamma_L \Gamma_D \big]. \tag{D.12}$$

Irrespective of whether the part of S_{q_i} proportional to $\mathbf{1}$ or $\slashed{k}$ is picked, all traces except those for $\Gamma_C, \Gamma_D = \gamma_L \gamma_\mu$ cancel, because otherwise factors $\gamma_L \gamma_R$ would meet inside the trace. This means, that the tensor product is proportional to $(\bar{d}_L \gamma_\mu s_L)(\bar{d}_L \gamma^\mu s_L)$. Performing the traces and using the dimensional regularization identity $k_\mu k_\nu = g_{\mu\nu} k^2/4$, the sum in (D.7) reduces to

$$\sum_{q_1, q_2 = c,t} \lambda_{q_1} \lambda_{q_2} \frac{-4\, m_{q_1}^2 m_{q_2}^2}{k^2 (k^2 - m_{q_1}^2)(k^2 - m_{q_2}^2)} \left(1 - \frac{k^2}{4M_W^2} \right)^2 \times (\bar{d}_L \gamma_\mu s_L)(\bar{d}_L \gamma^\mu s_L) \tag{D.13}$$

Using the Fermi coupling $G_F = g_2^2/(4\sqrt{2} M_W^2)$, the final result for $\mathcal{M}$ can be written as [compare Lellouch, 2011, p. 27]

$$\mathcal{M} = \frac{G_F^2 M_W^2}{2\pi^2} \big(\lambda_t^2 S_{tt} + \lambda_c^2 S_{cc} + 2\lambda_c \lambda_t S_{ct} \big) \times (\bar{d}_L \gamma_\mu s_L)(\bar{d}_L \gamma^\mu s_L), \tag{D.14}$$

with

$$S_{q_1 q_2} = \frac{4i}{\pi^2 M_W^2} \int \mathrm{d}^4 k \, \frac{m_{q_1}^2 m_{q_2}^2}{k^2 (k^2 - m_{q_1}^2)(k^2 - m_{q_2}^2)} \frac{\left(1 - \frac{k^2}{4M_W^2} \right)^2}{\left(1 - \frac{k^2}{M_W^2} \right)^2}. \tag{D.15}$$

Interpreting the external quark fields as operators and contracting them with external $K^0, \bar{K}^0$ states, one can obtain the off-diagonal mass matrix element M_{12}.[1] The values for λ_q as well

---

[1] Modulus a symmetry factor of $1/2$, which arises in order to compensate for double-counting when contracting the four-fermion operator $(\bar{d}_L \gamma_\mu s_L)(\bar{d}_L \gamma^\mu s_L)$ with external kaon states.

as the quark masses m_q suggest that $\mathrm{Re}M_{12}$ is dominated by the cc term [Lellouch, 2011, p. 27]:

$$\frac{G_F^2 M_W^2}{4\pi^2}\, S_{cc} = \frac{iG_F^2}{\pi^4} \int \mathrm{d}^4 k \frac{m_c^4}{k^2(k^2 - m_c^2)^2} + \mathcal{O}(M_W^{-6}). \tag{D.16}$$

Clearly, this integral is dominated by momenta between 0 and m_c, i.e. long-range contributions rendering a reliable lattice computation of ΔM_K difficult.

The situation is different if the indirect CP violation parameter ϵ is considered [Lellouch, 2011, p. 28f]. It is sensitive to the interference of different $K \to \pi\pi$ processes like the ones displayed in figure D.1. The CKM matrix element appearing in diagram (a) is λ_u, whereas

(a)   (b)
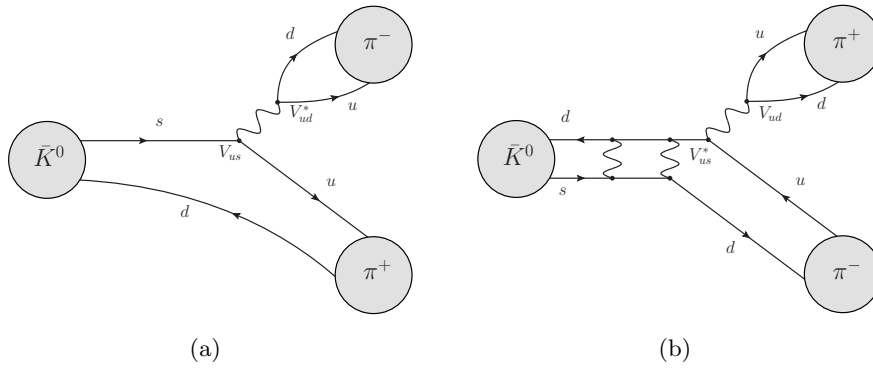
Figure D.1.: Diagrams describing electroweak $K \to \pi\pi$ decays. Indirect CP violation is attributed to the interference of these two diagrams, giving rise to a non-vanishing relative phase ϵ.

diagram (b) depends on λ_u^* and M_{12} coming from the box diagram we discussed above. This means, that the relative phase between these two weak decays is given by[2]

$$\epsilon \sim \frac{\mathrm{Im}[(\lambda_u^*)^2 M_{12}]}{\mathrm{Re}[(\lambda_u^*)^2 M_{12}]}. \tag{D.17}$$

The denominator can be estimated by current experiments measuring ΔM_K. Concerning the numerator, note that

$$(\lambda_u^*)^2 M_{12} = \frac{G_F^2 M_W^2}{4\pi^2} \big((\lambda_u^* \lambda_t)^2 S_{tt} + (\lambda_u^* \lambda_c)^2 S_{cc} + 2(\lambda_u^* \lambda_c)(\lambda_u^* \lambda_t) S_{ct} \big) \times \langle K^0 | O^{\Delta S = 2} | \bar{K}^0 \rangle, \tag{D.18}$$

with $O^{\Delta S = 2} = (\bar{d}s)_{V-A}(\bar{d}s)_{V-A}$. The quantities $\lambda_u^* \lambda_q$ are rephasing invariants with the property $\mathrm{Im}[\lambda_u^* \lambda_c] = -\mathrm{Im}[\lambda_u^* \lambda_t] = J$. This gives

$$\mathrm{Im}\left[(\lambda_u^*)^2 M_{12}\right] = \frac{G_F^2 M_W^2}{2\pi^2} J \left(\mathrm{Re}(\lambda_u^* \lambda_t)(S_{tt} - S_{ct}) - \mathrm{Re}(\lambda_u^* \lambda_c)(S_{cc} - S_{ct}) \right) \times \langle K^0 | O^{\Delta S = 2} | \bar{K}^0 \rangle. \tag{D.19}$$

---

[2]We neglect the contribution $\xi = \mathrm{Im}A_0 / \mathrm{Re}A_0$ [Lellouch, 2011, p. 28]. However, this and other long-distance contributions induce a $\mathcal{O}(5\%)$ correction to ϵ [Buras and Guadagnoli, 2008; Buras et al., 2010] and have to be considered in further studies.

To see that the remaining integrals are dominated by momenta between m_c and m_t, consider the integrand of $S_{tt} - S_{ct}$:[3]

$$\frac{m_t^4}{k^2(k^2 - m_t^2)^2} - \frac{m_t^2 m_c^2}{k^2(k^2 - m_t^2)(k^2 - m_c^2)} = \frac{m_t^4(k^2 - m_c^2) - (k^2 - m_t^2)m_t^2 m_c^2}{k^2(k^2 - m_c^2)(k^2 - m_t^2)^2} = \frac{m_t^2(m_t^2 - m_c^2)}{(k^2 - m_c^2)(k^2 - m_t^2)^2}.$$

Thus, ϵ can be reliably computed using the above relations augmented by a non-perturbative computation of $\langle K^0 | O^{\Delta S=2} | \bar{K}^0 \rangle$.

---

[3]We dropped the W-boson propagator dependence for brevity.

E. Calculations and proofs for lattice techniques

Many aspects of the following calculations presented here have been published in Durr et al. [2010], in references therein, or are textbook standard.

E.1. Chain rule for Lie-derivatives

Within the HMC, we need to compute the contribution $\delta S_F / \delta U$ to the total force (cf. section 2.3.4). In case of smeared links, S_F depends only indirectly on the thin links U, viz. via the smeared links V. In order to handle these nested dependencies, we need to derive a chain rule for Lie-derivatives. As a prerequisite, we need to be able to compute derivatives $\partial_\omega M^{-1}$ of invertible matrices M. Consider:

$$0 = \partial_\omega(MM^{-1}) = (\partial_\omega M)M^{-1} + M\,\partial_\omega M^{-1}. \tag{E.1}$$

Solving for $\partial_\omega M^{-1}$ gives:

$$\partial_\omega M^{-1} = -M^{-1}(\partial_\omega M)M^{-1}. \tag{E.2}$$

Consider now a complex-valued function f on the group space SU(3): $f(U) \in \mathbb{C}$, $\forall U \in \mathrm{SU}(3)$. The Lie-derivative of f is given by (compare expression (2.151) from section 2.3.4)

$$\delta_{U_i} f(U) = \frac{\partial f(U)}{\partial \omega^i} = \partial_\omega f\left(e^{i\omega t_i}U\right)\big|_{\omega=0} = \lim_{\omega\to 0} \frac{f\left(e^{i\omega t_i}U\right) - f\left(U\right)}{\omega}, \tag{E.3}$$

with normalized generators $t_i \in \mathfrak{su}(3)$ satisfying $\mathrm{Tr}(t_i\, t_j) = \delta_{ij}$ [1] as well as

$$\frac{\delta f}{\delta U} = \sum_i t_i\, \delta_{U_i} f. \tag{E.4}$$

The use of normalized generators does not change the reasoning of section 2.3.4, but simplifies the following calculations.
Expression (E.3) can be rewritten as

$$\delta_{U_i} f = \mathrm{Tr}\left(t_i\, U\, \frac{\partial f}{\partial U^T}\right), \tag{E.5}$$

---

[1] This can be achieved by rescaling all Gell-Mann matrices with $\sqrt{2}$.

where the partial derivative of f with respect to U (or its transpose) is meant to be the derivative with respect to the matrix elements itself, e.g.

$$\frac{\partial U_{cd}}{\partial U_{ab}} = \delta_{ca}\,\delta_{bd}. \tag{E.6}$$

Using $U^\dagger = U^{-1}$ and (E.2), we find for the derivative of $U^\dagger$ with respect to U:

$$\frac{\partial U_{cd}^\dagger}{\partial U_{ab}} = -U_{ca}^\dagger U_{bd}^\dagger. \tag{E.7}$$

If the function f is real-valued, we can write

$$\frac{\delta f}{\delta U} = \sum_i t_i\,\delta_{U_i} f = \sum_i t_i\,\mathrm{Tr}\left(t_i\, U\,\frac{\partial f}{\partial U^T}\right) = \mathrm{P_{TA}}\left\{U\,\frac{\partial f}{\partial U^T}\right\}, \tag{E.8}$$

where $\mathrm{P_{TA}}$ was defined in (2.125). For proving the last step, we have to show that for any given 3×3 matrix M, the projection operator can be recast as

$$\mathrm{P_{TA}}\{M\} = \sum_k t_k\,\mathrm{Re}\,\mathrm{Tr}(t_k\,M). \tag{E.9}$$

This can be easily seen by rewriting the matrix M as follows:[2]

$$M = \sum_k t_k\,(m_k + i n_k) + \mathbf{1}(c + ib), \tag{E.10}$$

with

$$m_k = \mathrm{Re}\,\mathrm{Tr}(t_k\,M); \quad n_k = \mathrm{Im}\,\mathrm{Tr}(t_k\,M); \quad c = \mathrm{Re}\,\mathrm{Tr}(M); \quad b = \mathrm{Im}\,\mathrm{Tr}(M), \tag{E.11}$$

wgere all parameters m_k, n_k, c, b have to be real. We find

$$M - M^\dagger = 2\sum_k t_k\,m_k + 2ib; \quad \mathrm{Tr}(M - M^\dagger) = \mathrm{Tr}(2ib) = 6ib. \tag{E.12}$$

And thus

$$\frac{1}{2}[M - M^\dagger] - \frac{1}{6}\mathrm{Tr}[M - M^\dagger] = \sum_k t_k\,m_k = \sum_k t_k\,\mathrm{Re}\,\mathrm{Tr}(t_k\,M). \tag{E.13}$$

Note that this projection also satisfies

$$\mathrm{Re}\,\mathrm{Tr}\left(\mathrm{P_{TA}}\{M\}\,N\right) = \mathrm{Re}\,\mathrm{Tr}\left(\mathrm{P_{TA}}\{N\}\,M\right). \tag{E.14}$$

For our force calculation, we additionally need the derivative of the smeared link V with respect to the thin link U, hence the derivative of an SU(3)-valued function V. Using the

---

[2]This decomposition is complete: note that any 3×3 complex matrix can be described by 18 independent real-valued parameters. Here we have 8 m_k and 8 n_k and c, b.

generators t_k, a small change of U can be written as (compare (E.3))

$$U \to U' = \exp\left(\sum_{k=1}^{8} \omega_k\, t_k\right) U, \tag{E.15}$$

and accordingly a small change of V as

$$V \to V' = \exp\left(\sum_{k=1}^{8} \eta_k\, t_k\right) V, \tag{E.16}$$

with some real coefficients ω_k, η_k. Since V depends on U, the η_i are real-valued functions of the ω_k, where $\eta_i(0) = 0$, $\forall\, i$. This implies that

$$
\begin{aligned}
\frac{\partial V'}{\partial \omega^k} &= \frac{\partial}{\partial \omega^k}\left[\exp\left(\sum_{i=1}^{8} \eta_i\, t_i\right) V\right] \\
&= \frac{\partial(\sum_{i=1}^{8} \eta_i\, t_i)}{\partial \omega^k} V + \mathcal{O}(\eta_i^2) \\
&= \left(\sum_{i=1}^{8} \frac{\partial \eta_i}{\partial \omega^k} t_i\right) V + \mathcal{O}(\eta_i^2),
\end{aligned}
\tag{E.17}
$$

and hence in the $\omega_k \to 0$ limit

$$\delta_{U_k} V = \sum_{i=1}^{8} \frac{\partial \eta_i}{\partial \omega^k}\, t_i\, V. \tag{E.18}$$

Using the usual chain rule

$$\frac{\partial f}{\partial \omega^k} = \sum_{i=1}^{8} \frac{\partial f}{\partial \eta^i} \frac{\partial \eta_i}{\partial \omega^k}, \tag{E.19}$$

we find in the limit:

$$\delta_{U_k} f = \sum_{i=1}^{8} (\delta_{V_i} f)\, \frac{\partial \eta_i}{\partial \omega^k}. \tag{E.20}$$

As a last ingredient, we have to rewrite equation (E.18)

$$\frac{\partial \eta_i}{\partial \omega^k} = \mathrm{Tr}\left(t_i\, (\delta_{U_k} V)\, V^\dagger\right). \tag{E.21}$$

Hence we obtain for the chain rule for *Lie-derivatives of* SU(3)-*valued functions*:

$$\delta_{U_k} f = \mathrm{Tr}\left(\frac{\delta f}{\delta V}\, (\delta_{U_k} V)\, V^\dagger\right). \tag{E.22}$$

This can be formally stated as

$$\frac{\delta f}{\delta U} = \frac{\delta f}{\delta V} \star \frac{\delta V}{\delta U}. \tag{E.23}$$

E.2. Analyticity of HEX smearing

Using the results of the last part, we can complete the proof for the analytic dependence of our HEX smeared action on the thin link fields U.[3] I will discuss the special case of one step HEX smearing, where the generalization to multiple steps of HEX smearing can be carried out in the same manner but it is much more involved.
We need to compute the derivative of the (real-valued) action S_F:

$$\frac{\delta S_F}{\delta U} = \frac{\delta S_F}{\delta V} \star \frac{\delta V}{\delta U}, \tag{E.24}$$

where the first factor $\delta S_F/\delta V$ of the star product is more or less trivial: just treat the smeared fields V as the fundamental degrees of freedom and do the calculation. On the other hand, the second factor is more involved. Consider[4]

$$\delta_{U_k} S_F = \Sigma_{ab}\big(\delta_{U_k} V_{ba}\big) = \Sigma_{ab}\ \mathrm{Tr}\left(t_k\, U\, \frac{\partial V_{ba}}{\partial U^T}\right), \tag{E.25}$$

where the sum over a, b is implied and

$$\Sigma \equiv V^\dagger \frac{\delta S_F}{\delta V}, \tag{E.26}$$

which is easy to compute. Since S_F is real-valued, we can write

$$\frac{\delta S_F}{\delta U} = \mathrm{P_{TA}}\left\{U\Sigma_{ab}\frac{\partial V_{ba}}{\partial U^T}\right\}. \tag{E.27}$$

The last HEX substep is given by $V = \exp(A)U$ with $A = \mathrm{P_{TA}}\{\Gamma^{(3)}U^\dagger\}$ (cf. 2.126), therefore[5]

$$\frac{\delta S_F}{\delta U} = \mathrm{P_{TA}}\left\{U\Sigma_{ab}\frac{\partial V_{ba}}{\partial U^T}\right\} = \mathrm{P_{TA}}\{U\Sigma\exp(A)\} + \mathrm{P_{TA}}\left\{U\Sigma_{ab}\frac{\partial\exp(A)_{bc}}{\partial U^T}U_{ca}\right\}. \tag{E.28}$$

The Cayley-Hamilton theorem and some algebra yields [Morningstar and Peardon, 2004]

$$\mathrm{d}\exp(A) = \mathrm{Tr}(A\,\mathrm{d}A)B_1 + \mathrm{Tr}(A^2\,\mathrm{d}A)B_2 + f_1\,\mathrm{d}A + f_2\{A,\mathrm{d}A\}, \tag{E.29}$$

where B_1, B_2 are second-order polynomicals in A and f_1, f_2 complex constants which depend on the trace and determinant of A. Using this identity and some cyclic permutations of the

---

[3]The same proof for EXP-smeared links was worked out by Morningstar and Peardon [2004]
[4]I use the notation introduced in section 2.3.3 throughout this calculation.
[5]The first term on the r.h.s can easily be computed when rewriting the expression

$$\mathrm{P_{TA}}\left\{U\Sigma_{ab}\exp(A)\frac{\partial U_{ab}}{\partial U^T}\right\} = \sum_k t_k\,\mathrm{Re}\sum_{i,j,k,l,a,b}(t_k)_{ij}U_{jk}\Sigma_{ab}\exp(A)_{bl}\frac{\partial U_{la}}{\partial U_{ki}}$$

with the definition of the projector from (2.125).

traces we obtain for the second term of the r.h.s. of (E.28):

$$\mathrm{P_{TA}}\left\{U\Sigma_{ab}\frac{\partial\exp(A)_{bc}}{\partial U^T}U_{ca}\right\}$$

$$= \mathrm{P_{TA}}\left\{U\frac{\partial A_{ab}}{\partial U^T}\left[\mathrm{Tr}(U\Sigma B_1)A + \mathrm{Tr}(U\Sigma B_2)A^2 + f_1 U\Sigma + f_2\{U\Sigma, A\}\right]_{ba}\right\}, \qquad (E.30)$$

where $A = \mathrm{P_{TA}}\{\Gamma^{(3)}U^\dagger\}$. Since this projector is linear, we can drag any derivative inside so that it acts onto its argument. Furthermore, we can use identity (E.14) to obtain

$$\mathrm{P_{TA}}\left\{U\frac{\partial\mathrm{P_{TA}}\{M\}_{ab}}{\partial U^T}N_{ba}\right\} = \mathrm{P_{TA}}\left\{U\frac{\partial M_{ab}}{\partial U^T}\mathrm{P_{TA}}\{N\}_{ba}\right\}, \qquad (E.31)$$

and hence we can shuffle the projector in $A = \mathrm{P_{TA}}\{\Gamma^{(3)}U^\dagger\}$ to the square brackets in (E.30). Note that

$$U\frac{\partial(\Gamma^{(3)}U^\dagger)_{ab}}{\partial U^T}\mathrm{P_{TA}}\{\dots\}_{ba} = U\frac{\partial\Gamma^{(3)}_{ab}}{\partial U^T}(U^\dagger\,\mathrm{P_{TA}}\{\dots\})_{ba} - \mathrm{P_{TA}}\{\dots\}\,\Gamma^{(3)}U^\dagger. \qquad (E.32)$$

Now we define

$$Z \equiv U^\dagger\,\mathrm{P_{TA}}\{\mathrm{Tr}(U\Sigma B_1)A + \mathrm{Tr}(U\Sigma B_2)A^2 + f_1 U\Sigma + f_2\{U\Sigma, A\}\} \qquad (E.33)$$

in order to obtain a more condensed notation. Combining everything yields the compact expression

$$\mathrm{P_{TA}}\left\{U\Sigma_{ab}\frac{\partial V_{ba}}{\partial U^T}\right\} = \mathrm{P_{TA}}\left\{U(\Sigma V - Z\Gamma^{(3)})U^\dagger + U\frac{\partial\Gamma^{(3)}_{ab}}{\partial U^T}Z_{ba}\right\}. \qquad (E.34)$$

Now, remember that the U dependence of $\Gamma^{(3)}$ comes only from $V^{(2)}$. Thus, we can write $(Z^{(3)} = Z)$

$$\mathrm{P_{TA}}\left\{U\Sigma_{ab}\frac{\partial V_{ba}}{\partial U^T}\right\} = \mathrm{P_{TA}}\left\{U(\Sigma V - Z^{(3)}\Gamma^{(3)})U^\dagger\right\} + \mathrm{P_{TA}}\left\{U\Sigma^{(2)}_{ab}\frac{\partial V^{(2)}_{ba}}{\partial U^T}\right\}, \qquad (E.35)$$

where we defined

$$\Sigma^{(2)}_{ab} = \frac{\partial\Gamma^{(3)}_{cd}}{\partial V^{(2)}_{ba}}Z^{(3)}_{dc}. \qquad (E.36)$$

We end up with the U dependence of S_F for one step HEX smearing

$$\frac{\delta S_F}{\delta U} = \sum_{i=3,2,1}\mathrm{P_{TA}}\left\{U(\Sigma^{(i)}V^{(i)} - Z^{(i)}\Gamma^{(i)})U^\dagger\right\} + \mathrm{P_{TA}}\{U\Sigma^{(0)}\}, \qquad (E.37)$$

with $V^{(3)} = V$ and the recursive definition of $\Sigma^{(i)}$

$$\Sigma^{(i)}_{ab} = \frac{\partial\Gamma^{(i+1)}_{cd}}{\partial V^{(i)}_{ba}}Z^{(i+1)}_{dc}, \forall\, i = 0, 1, 2. \qquad (E.38)$$

The remaining staple derivative can be computed in a straightforward manner. The only difficulty arises from keeping track of all Lorentz indices, which have been dropped for brevity in this calculation.

This calculation has been published in [Durr et al., 2010] and extends the calculations by Morningstar and Peardon [2004]; Hasenfratz et al. [2007]. Some more analytical as well as numerical treatments for the dynamically smeared FLiC fermions can be found in [Kamleh et al., 2004].

E.3. Random sources

In order to calculate quark-line diagrams, it is useful to replace the point-propagator contractions by random-source-propagator contractions. This is done by using U(1) random-wall sources

$$|\chi(\mathbf{x}, T)\rangle_{\alpha,c} = e^{i2\pi\, r(\mathbf{x},c)}/N, \tag{E.39}$$

where $r(\mathbf{x}, c) \in [0; 1[$ is a random number different for any color c and location $\mathbf{x}$ and N is an appropriate normalization. Note that these sources are diagonal in spin α in order not to destroy the spin structure of the propagator. Additionally, the following identity is fulfilled for an infinite number of random sources

$$\sum_{\chi,\xi} c_1,\alpha_1 \langle \chi(\mathbf{x}, T)|\xi(\mathbf{y}, T)\rangle_{\alpha_2, c_2} = \delta_{\mathbf{xy}}\, \delta_{c_1 c_2}\, \delta_{\alpha_1 \alpha_2}\, \delta_{\chi\xi}, \tag{E.40}$$

so that $\sum_{\chi} |\chi\rangle\langle\chi|$ will be close to the identity matrix for many different random sources χ. Consider now the pseudoscalar correlator $\langle \bar{P}(t)P(0)\rangle$ with $P(t) = \sum_{\mathbf{x}} \bar{\psi}(\mathbf{x}, t)\gamma_5\psi(\mathbf{x}, t)$. In terms of quark propagators, this expression can be written as

$$\langle \bar{P}(t)P(0)\rangle = \sum_{\mathbf{x},\mathbf{y}} \mathrm{Tr}\left[\gamma_5 S\big((\mathbf{x}, t) \leftarrow (\mathbf{y}, 0)\big)\gamma_5 S\big((\mathbf{y}, 0) \leftarrow (\mathbf{x}, t)\big)\right], \tag{E.41}$$

where $S((\mathbf{x}, t) \leftarrow (\mathbf{y}, 0))$ is the quark propagator from $(\mathbf{y}, 0)$ to $(\mathbf{x}, t)$. Expression (E.41) can be rewritten in terms of random sources as follows:[6]

$$\sum_{\mathbf{x},\mathbf{y}} \mathrm{Tr}\left[\gamma_5 S\big((\mathbf{x}, t) \leftarrow (\mathbf{y}, 0)\big)\gamma_5 S\big((\mathbf{y}, 0) \leftarrow (\mathbf{x}, t)\big)\right] \approx \sum_{\chi,\xi} \langle\xi(t)|\gamma_5 D^{-1}|\chi(0)\rangle\langle\chi(0)|\gamma_5 D^{-1}|\xi(t)\rangle$$

$$= \sum_{\chi,\xi} |\langle\xi(t)|\gamma_5 D^{-1}|\chi(0)\rangle|^2. \tag{E.42}$$

Since different measurements on a single configuration are correlated, it is often more efficient to increase the number of configurations than the number of random sources per configuration. The identity condition still holds for the ensemble average.

---

[6]As a matter of convenience we are dropping all color and spinor indices.

List of Figures

List of Tables

Bibliography

S. L. Adler.
  Axial vector vertex in spinor electrodynamics.
  Phys. Rev., 177:2426–2438, 1969.
  doi: 10.1103/PhysRev.177.2426.

S. L. Adler and W. A. Bardeen.
  Absence of higher order corrections in the anomalous axial vector divergence equation.
  Phys. Rev., 182:1517–1536, 1969.
  doi: 10.1103/PhysRev.182.1517.

M. Albanese, F. Costantini, G. Fiorentini, F. Flore, M. P. Lombardo, R. Tripiccione, P. Bacilieri,
  L. Fonti, P. Giacomelli, E. Remiddi, M. Bernaschi, N. Cabibbo, E. Marinari, G. Parisi, G. Salina,
  S. Cabasino, F. Marzano, P. Paolucci, S. Petrarca, F. Rapuano, P. Marchesini, and R. Rusack.
  Glueball Masses and String Tension in Lattice QCD.
  Phys. Lett., B192:163–169, 1987.
  doi: 10.1016/0370-2693(87)91160-9.

C. Alexandrou et al.
  Light baryon masses with dynamical twisted mass fermions.
  Phys. Rev., D78:014509, 2008.
  doi: 10.1103/PhysRevD.78.014509.

A. Ali Khan et al.
  Light Hadron Spectroscopy with Two Flavors of Dynamical Quarks on the Lattice.
  Phys. Rev., D65:054505, 2002.

A. Ali Khan et al.
  Accelerating the hybrid Monte Carlo algorithm.
  Phys. Lett., B564:235–240, 2003.
  doi: 10.1016/S0370-2693(03)00703-2.

A. Ali Khan et al.
  The nucleon mass in $N(f) = 2$ lattice QCD: Finite size effects from chiral perturbation theory.
  Nucl. Phys., B689:175–194, 2004.

B. Alles, M. D'Elia, A. Di Giacomo, and R. Kirchner.
  A critical comparison of different definitions of topological charge on the lattice.
  Phys. Rev., D58:114506, 1998.
  doi: 10.1103/PhysRevD.58.114506.

C. Allton et al.
  Physical Results from 2+1 Flavor Domain Wall QCD and SU(2) Chiral Perturbation Theory.
  Phys.Rev., D78:114509, 2008.
  doi: 10.1103/PhysRevD.78.114509.

I. S. Altarev et al.

A NEW UPPER LIMIT ON THE ELECTRIC DIPOLE MOMENT OF THE NEUTRON.
Phys. Lett., B102:13, 1981.
doi: 10.1016/0370-2693(81)90202-1.

A. V. Anisovich and H. Leutwyler.
Dispersive analysis of the decay $\eta \rightarrow 3\pi$.
Phys. Lett., B375:335–342, 1996.
doi: 10.1016/0370-2693(96)00192-X.

D. Antonio et al.
First results from 2+1 Flavor Domain Wall QCD: Mass Spectrum, Topology Change and Chiral Symmetry with L(s) = 8.
Phys.Rev., D75:114501, 2007.
doi: 10.1103/PhysRevD.75.114501.

S. Aoki et al.
Non-perturbative determination of quark masses in quenched lattice QCD with the Kogut-Susskind fermion action.
Phys. Rev. Lett., 82:4392–4395, 1999.
doi: 10.1103/PhysRevLett.82.4392.

S. Aoki et al.
Quenched Light Hadron Spectrum.
Phys. Rev. Lett., 84:238–241, 2000.
doi: 10.1103/PhysRevLett.84.238.

S. Aoki et al.
Light Hadron Spectrum and Quark Masses from Quenched Lattice QCD.
Phys. Rev., D67:034503, 2003a.
doi: 10.1103/PhysRevD.67.034503.

S. Aoki et al.
Light hadron spectroscopy with two flavors of O(a) improved dynamical quarks.
Phys.Rev., D68:054502, 2003b.
doi: 10.1103/PhysRevD.68.054502.

S. Aoki et al.
Bulk first-order phase transition in three-flavor lattice QCD with O(a)-improved Wilson fermion action at zero temperature.
Phys. Rev., D72:054510, 2005.
doi: 10.1103/PhysRevD.72.054510.

S. Aoki et al.
2+1 Flavor Lattice QCD toward the Physical Point.
Phys. Rev., D79:034503, 2009.
doi: 10.1103/PhysRevD.79.034503.

Y. Aoki et al.
The kaon B-parameter from quenched domain-wall QCD.
Phys. Rev., D73:094507, 2006.
doi: 10.1103/PhysRevD.73.094507.

Y. Aoki et al.
Non-perturbative renormalization of quark bilinear operators and B_K using domain wall fermions.
Phys. Rev., D78:054510, 2008.
doi: 10.1103/PhysRevD.78.054510.

Y. Aoki et al.
Continuum Limit of B_K from 2+1 Flavor Domain Wall QCD.
2010.

Y. Aoki et al.
Continuum Limit Physics from 2+1 Flavor Domain Wall QCD.
Phys.Rev., D83:074508, 2011.
doi: 10.1103/PhysRevD.83.074508.

R. Arthur and P. A. Boyle.
Step Scaling with off-shell renormalisation.
Phys. Rev., D83:114511, 2011.
doi: 10.1103/PhysRevD.83.114511.

C. Aubin, C. Bernard, C. E. DeTar, S. A. Gottlieb, E. Gregory, et al.
Light hadrons with improved staggered quarks: Approaching the continuum limit.
Phys.Rev., D70:094505, 2004a.
doi: 10.1103/PhysRevD.70.094505.

C. Aubin, J. Laiho, and R. S. Van de Water.
The neutral kaon mixing parameter B_K from unquenched mixed-action lattice QCD.
Phys. Rev., D81:014507, 2010.
doi: 10.1103/PhysRevD.81.014507.

C. Aubin et al.
First determination of the strange and light quark masses from full lattice QCD.
Phys.Rev., D70:031504, 2004b.
doi: 10.1103/PhysRevD.70.031504.

C. Aubin et al.
Light pseudoscalar decay constants, quark masses, and low energy constants from three-flavor lattice QCD.
Phys. Rev., D70:114501, 2004c.
doi: 10.1103/PhysRevD.70.114501.

R. Babich et al.
K0 anti-K0 mixing beyond the standard model and CP- violating electroweak penguins in quenched QCD with exact chiral symmetry.
Phys. Rev., D74:073009, 2006.
doi: 10.1103/PhysRevD.74.073009.

T. Bae et al.
B_K using HYP-smeared staggered fermions in $N_f = 2 + 1$ unquenched QCD.
Phys. Rev., D82:114509, 2010.
doi: 10.1103/PhysRevD.82.114509.

C. A. Baker et al.
An improved experimental limit on the electric dipole moment of the neutron.
Phys. Rev. Lett., 97:131801, 2006.
doi: 10.1103/PhysRevLett.97.131801.

T. Bakeyev et al.
Non-perturbative renormalisation and improvement of the local vector current for quenched and unquenched Wilson fermions.
Phys. Lett., B580:197–208, 2004.
doi: 10.1016/j.physletb.2003.11.050.

W. A. Bardeen.
   Anomalous Ward identities in spinor field theories.
   Phys. Rev., 184:1848–1857, 1969.
   doi: 10.1103/PhysRev.184.1848.

A. Bazavov et al.
   Results from the MILC collaboration's SU(3) chiral perturbation theory analysis.
   PoS, LAT2009:079, 2009.

A. Bazavov et al.
   Full nonperturbative QCD simulations with 2+1 flavors of improved staggered quarks.
   Rev. Mod. Phys., 82:1349–1417, 2010.
   doi: 10.1103/RevModPhys.82.1349.

D. Becirevic and G. Villadoro.
   Impact of the finite volume effects on the chiral behavior of f(K) and B(K).
   Phys. Rev., D69:054010, 2004.
   doi: 10.1103/PhysRevD.69.054010.

D. Becirevic, V. Gimenez, V. Lubicz, and G. Martinelli.
   Light quark masses from lattice quark propagators at large momenta.
   Phys. Rev., D61:114507, 2000.
   doi: 10.1103/PhysRevD.61.114507.

D. Becirevic et al.
   Renormalization constants of quark operators for the non- perturbatively improved Wilson action.
   JHEP, 08:022, 2004.
   doi: 10.1088/1126-6708/2004/08/022.

J. S. Bell and R. Jackiw.
   A PCAC puzzle: pi0 → gamma gamma in the sigma model.
   Nuovo Cim., A60:47–61, 1969.
   doi: 10.1007/BF02823296.

C. W. Bernard and T. A. DeGrand.
   Perturbation theory for fat-link fermion actions.
   Nucl. Phys. Proc. Suppl., 83:845–847, 2000.

C. W. Bernard, T. Burch, K. Orginos, D. Toussaint, T. A. DeGrand, et al.
   The QCD spectrum with three quark flavors.
   Phys.Rev., D64:054506, 2001a.
   doi: 10.1103/PhysRevD.64.054506.

C. W. Bernard et al.
   f(B) for various actions: Approaching the continuum limit with dynamical fermions.
   Nucl. Phys. Proc. Suppl., 94:346–349, 2001b.
   doi: 10.1016/S0920-5632(01)00923-9.

T. Bhattacharya, R. Gupta, W. Lee, S. R. Sharpe, and J. M. S. Wu.
   Improved bilinears in lattice QCD with non-degenerate quarks.
   Phys. Rev., D73:034504, 2006.
   doi: 10.1103/PhysRevD.73.034504.

B. Blossier, M. Della Morte, G. von Hippel, T. Mendes, and R. Sommer.
   On the generalized eigenvalue method for energies and matrix elements in lattice field theory.
   JHEP, 04:094, 2009.
   doi: 10.1088/1126-6708/2009/04/094.

B. Blossier et al.
Average up/down, strange and charm quark masses with Nf=2 twisted mass lattice QCD.
Phys.Rev., D82:114513, 2010.
doi: 10.1103/PhysRevD.82.114513.

T. Blum, T. Doi, M. Hayakawa, T. Izubuchi, and N. Yamada.
Determination of light quark masses from the electromagnetic splitting of pseudoscalar meson masses
computed with two flavors of domain wall fermions.
Phys. Rev., D76:114508, 2007.
doi: 10.1103/PhysRevD.76.114508.

M. Bochicchio, L. Maiani, G. Martinelli, G. C. Rossi, and M. Testa.
Chiral Symmetry on the Lattice with Wilson Fermions.
Nucl. Phys., B262:331, 1985.
doi: 10.1016/0550-3213(85)90290-1.

M. Bona et al.
The unitarity triangle fit in the standard model and hadronic parameters from lattice QCD: A
reappraisal after the measurements of Delta(m(s)) and BR(B → tau nu/tau).
JHEP, 10:081, 2006.
doi: 10.1088/1126-6708/2006/10/081.

G. Buchalla, A. J. Buras, and M. E. Lautenbacher.
Weak decays beyond leading logarithms.
Rev. Mod. Phys., 68:1125–1144, 1996.
doi: 10.1103/RevModPhys.68.1125.

J. Bulava et al.
Nucleon, Δ and Ω excited states in $N_f = 2 + 1$ lattice QCD.
Phys. Rev., D82:014507, 2010.
doi: 10.1103/PhysRevD.82.014507.

A. J. Buras.
Weak Hamiltonian, CP violation and rare decays.
1998.

A. J. Buras and D. Guadagnoli.
Correlations among new CP violating effects in Δ F = 2 observables.
Phys.Rev., D78:033005, 2008.
doi: 10.1103/PhysRevD.78.033005.

A. J. Buras, M. Misiak, and J. Urban.
Two-loop QCD anomalous dimensions of flavour-changing four-quark operators within and beyond
the standard model.
Nucl. Phys., B586:397–426, 2000.
doi: 10.1016/S0550-3213(00)00437-5.

A. J. Buras, D. Guadagnoli, and G. Isidori.
On ϵ_K beyond lowest order in the Operator Product Expansion.
Phys. Lett., B688:309–313, 2010.
doi: 10.1016/j.physletb.2010.04.017.

N. Cabibbo and E. Marinari.
A New Method for Updating SU(N) Matrices in Computer Simulations of Gauge Theories.
Phys. Lett., B119:387–390, 1982.
doi: 10.1016/0370-2693(82)90696-7.

C. G. Callan, Jr. and J. A. Harvey.
  Anomalies and Fermion Zero Modes on Strings and Domain Walls.
  Nucl. Phys., B250:427, 1985.
  doi: 10.1016/0550-3213(85)90489-4.

S. Capitani.
  Lattice perturbation theory.
  Phys.Rept., 382:113–302, 2003.
  doi: 10.1016/S0370-1573(03)00211-4.

S. Capitani, M. Luscher, R. Sommer, and H. Wittig.
  Nonperturbative quark mass renormalization in quenched lattice QCD.
  Nucl.Phys., B544:669–698, 1999.
  doi: 10.1016/S0550-3213(98)00857-8.

S. Capitani, S. Dürr, and C. Hölbling.
  Rationale for UV-filtered clover fermions.
  JHEP, 11:028, 2006.

S. Capitani et al.
  Renormalisation and off-shell improvement in lattice perturbation theory.
  Nucl. Phys., B593:183–228, 2001.
  doi: 10.1016/S0550-3213(00)00590-3.

O. Cata and S. Peris.
  Long-distance dimension-eight operators in B(K).
  JHEP, 03:060, 2003.

J. Charles et al.
  CP violation and the CKM matrix: Assessing the impact of the asymmetric B factories.
  Eur. Phys. J., C41:1–131, 2005.
  doi: 10.1140/epjc/s2005-02169-1.
  URL `http://ckmfitter.in2p3.fr`.

T.-P. Cheng and L.-F. Li.
  Gauge theory of elementary particle physics.
  Oxford Science Publications, 10th edition, 2004.

K. G. Chetyrkin and A. Retey.
  Renormalization and running of quark mass and field in the regularization invariant and MS-bar schemes at three and four loops.
  Nucl. Phys., B583:3–34, 2000.
  doi: 10.1016/S0550-3213(00)00331-X.

N. H. Christ.
  Computing the long-distance contribution to second order weak amplitudes.
  PoS, LATTICE2010:300, 2010.

M. Ciuchini et al.
  Next-to-leading order QCD corrections to Delta(F) = 2 effective Hamiltonians.
  Nucl. Phys., B523:501–525, 1998.
  doi: 10.1016/S0550-3213(98)00161-8.

M. Ciuchini et al.
  2000 CKM triangle analysis: A Critical review with updated experimental inputs and theoretical parameters.

JHEP, 07:013, 2001.
URL http://www.utfit.org/.

M. A. Clark and A. D. Kennedy.
Accelerating Dynamical Fermion Computations using the Rational Hybrid Monte Carlo (RHMC)
Algorithm with Multiple Pseudofermion Fields.
Phys. Rev. Lett., 98:051601, 2007.
doi: 10.1103/PhysRevLett.98.051601.

M. A. Clark, B. Joo, and A. D. Kennedy.
Comparing the R algorithm and RHMC for staggered fermions.
Nucl. Phys. Proc. Suppl., 119:1015–1017, 2003.
doi: 10.1016/S0920-5632(03)01748-1.

G. Colangelo, J. Gasser, and H. Leutwyler.
pi pi scattering.
Nucl. Phys., B603:125–179, 2001.
doi: 10.1016/S0550-3213(01)00147-X.

G. Colangelo, S. Durr, and C. Haefeli.
Finite volume effects for meson masses and decay constants.
Nucl. Phys., B721:136–174, 2005.
doi: 10.1016/j.nuclphysb.2005.05.015.

G. Colangelo, A. Fuhrer, and C. Haefeli.
The pion and proton mass in finite volume.
Nucl. Phys. Proc. Suppl., 153:41–48, 2006.
doi: 10.1016/j.nuclphysbps.2006.01.004.

G. Colangelo, S. Lanz, and E. Passemar.
A New Dispersive Analysis of $\eta \to 3\pi$.
PoS, CD09:047, 2009.

G. Colangelo, A. Fuhrer, and S. Lanz.
Finite volume effects for nucleon and heavy meson masses.
Phys. Rev., D82:034506, 2010a.
doi: 10.1103/PhysRevD.82.034506.

G. Colangelo et al.
Review of lattice results concerning low energy particle physics.
2010b.

S. Coleman.
Aspects of Symmetry: Selected Erice Lectures.
Cambridge University Press, 1988.
ISBN 0521318270.

M. Constantinou et al.
Non-perturbative renormalization of quark bilinear operators with Nf=2 (tmQCD) Wilson fermions
and the tree- level improved gauge action.
JHEP, 08:068, 2010.
doi: 10.1007/JHEP08(2010)068.

M. Constantinou et al.
BK-parameter from Nf = 2 twisted mass lattice QCD.
Phys. Rev., D83:014505, 2011.
doi: 10.1103/PhysRevD.83.014505.

M. Creutz, L. Jacobs, and C. Rebbi.
  Monte Carlo Computations in Lattice Gauge Theories.
  Phys. Rept., 95:201, 1983.
  doi: 10.1016/0370-1573(83)90016-9.

N. Cundy, M. Teper, and U. Wenger.
  Topology and chiral symmetry breaking in SU(N(c)) gauge theories.
  Phys. Rev., D66:094505, 2002.
  doi: 10.1103/PhysRevD.66.094505.

R. F. Dashen and M. Weinstein.
  Soft pions, chiral symmetry, and phenomenological lagrangians.
  Phys. Rev., 183:1261–1291, 1969.
  doi: 10.1103/PhysRev.183.1261.

C. T. H. Davies et al.
  High-precision lattice QCD confronts experiment.
  Phys. Rev. Lett., 92:022001, 2004.
  doi: 10.1103/PhysRevLett.92.022001.

T. A. DeGrand, A. Hasenfratz, and T. G. Kovacs.
  Optimizing the chiral properties of lattice fermion actions.
  1998.

T. A. DeGrand, A. Hasenfratz, and T. G. Kovacs.
  Instantons and exceptional configurations with the clover action.
  Nucl. Phys., B547:259–280, 1999.
  doi: 10.1016/S0550-3213(99)00126-1.

L. Del Debbio and C. Pica.
  Topological susceptibility from the overlap.
  JHEP, 02:003, 2004.

L. Del Debbio, L. Giusti, M. Luscher, R. Petronzio, and N. Tantalo.
  Stability of lattice QCD simulations and the thermodynamic limit.
  JHEP, 02:011, 2006.
  doi: 10.1088/1126-6708/2006/02/011.

L. Del Debbio, L. Giusti, M. Luscher, R. Petronzio, and N. Tantalo.
  QCD with light Wilson quarks on fine lattices (I): First experiences and physics results.
  JHEP, 0702:056, 2007.
  doi: 10.1088/1126-6708/2007/02/056.

M. Della Morte, R. Hoffmann, F. Knechtli, and U. Wolff.
  Impact of large cutoff-effects on algorithms for improved Wilson fermions.
  Comput. Phys. Commun., 165:49–58, 2005a.
  doi: 10.1016/j.cpc.2004.09.009.

M. Della Morte et al.
  Non-perturbative quark mass renormalization in two-flavor QCD.
  Nucl. Phys., B729:117–134, 2005b.
  doi: 10.1016/j.nuclphysb.2005.09.028.

C. DeTar and T. DeGrand.
  Lattice Methods For Quantum Chromodynamics.
  World Scientific Publishing, 1st edition, 2006.

P. Dimopoulos, H. Simma, and A. Vladikas.
Quenched B_K-parameter from Osterwalder-Seiler tmQCD quarks and mass-splitting discretization
effects.
JHEP, 07:007, 2009.
doi: 10.1088/1126-6708/2009/07/007.

P. Dimopoulos et al.
Flavour symmetry restoration and kaon weak matrix elements in quenched twisted mass QCD.
Nucl. Phys., B776:258–285, 2007.
doi: 10.1016/j.nuclphysb.2007.03.051.

P. A. M. Dirac.
The Lagrangian in quantum mechanics.
Phys. Z. Sowjetunion, 3:64–72, 1933.

C. Ditsche, B. Kubis, and U.-G. Meissner.
Electromagnetic corrections in eta $\rightarrow$ 3 pi decays.
Eur. Phys. J., C60:83–105, 2009.
doi: 10.1140/epjc/s10052-009-0863-z.

A. Donini, V. Gimenez, G. Martinelli, M. Talevi, and A. Vladikas.
Non-perturbative renormalization of lattice four-fermion operators without power subtractions.
Eur. Phys. J., C10:121–142, 1999.
doi: 10.1007/s100529900097.

J. F. Donoghue, E. Golowich, and B. R. Holstein.
Dynamics of the standard model, volume 1.
Cambridge monographs on particle physics, nuclear physics and cosmology, 2nd edition, 1992.

S. Duane, A. D. Kennedy, B. J. Pendleton, and D. Roweth.
Hybrid Monte Carlo.
Phys. Rev. B, 195:216–222, 1987.

A. Duncan, E. Eichten, and H. Thacker.
Electromagnetic Splittings and Light Quark Masses in Lattice QCD.
Phys. Rev. Lett., 76:3894–3897, 1996.
doi: 10.1103/PhysRevLett.76.3894.

S. Durr.
Logarithmic link smearing for full QCD.
Comput. Phys. Commun., 180:1338–1357, 2009.
doi: 10.1016/j.cpc.2009.02.013.

S. Durr and C. Hoelbling.
Continuum physics with quenched overlap fermions.
Phys. Rev., D72:071501, 2005.
doi: 10.1103/PhysRevD.72.071501.

S. Dürr, Z. Fodor, C. Hölbling, and T. Kurth.
Precision study of the SU(3) topological susceptibility in the continuum.
JHEP, 04:055, 2007.

S. Durr et al.
Mixed action simulations: approaching physical quark masses.
PoS, LAT2007:113, 2007.

S. Dürr et al.
  Ab-Initio Determination of Light Hadron Masses.
  Science, 322:1224–1227, 2008.
  doi: 10.1126/science.1163233.

S. Durr et al.
  Scaling study of dynamical smeared-link clover fermions.
  Phys. Rev., D79:014501, 2009.
  doi: 10.1103/PhysRevD.79.014501.

S. Durr et al.
  Lattice QCD at the physical point: Simulation and analysis details.
  2010.

S. Durr et al.
  Precision computation of the kaon bag parameter.
  2011a.

S. Durr et al.
  Lattice QCD at the physical point: light quark masses.
  Phys. Lett., B701:265–268, 2011b.
  doi: 10.1016/j.physletb.2011.05.053.

N. Eicker et al.
  Light Quark Masses with Dynamical Wilson Fermions.
  Phys. Lett., B407:290–296, 1997.
  doi: 10.1016/S0370-2693(97)00718-1.

R. P. Feynman.
  Space-time approach to nonrelativistic quantum mechanics.
  Rev. Mod. Phys., 20:367–387, 1948.
  doi: 10.1103/RevModPhys.20.367.

R. P. Feynman and A. Hibbs.
  Quantum Mechanics and Path Integrals.
  Nueva York, EUA : McGraw-Hill, 1965.

J. Frison et al.
  Rho decay width from the lattice.
  PoS, LATTICE2010:139, 2010.

H. Fritzsch, M. Gell-Mann, and H. Leutwyler.
  Advantages of the Color Octet Gluon Picture.
  Phys. Lett., B47:365–368, 1973.
  doi: 10.1016/0370-2693(73)90625-4.

S. A. Frolov and A. A. Slavnov.
  An Invariant regularization of the Standard Model.
  Phys. Lett., B309:344–350, 1993.
  doi: 10.1016/0370-2693(93)90943-C.

A. Frommer, B. Nockel, S. Gusken, T. Lippert, and K. Schilling.
  Many masses on one stroke: Economic computation of quark propagators.
  Int. J. Mod. Phys., C6:627–638, 1995.
  doi: 10.1142/S0129183195000538.

M. K. Gaillard and B. W. Lee.
   Rare Decay Modes of the K-Mesons in Gauge Theories.
   Phys. Rev., D10:897, 1974.
   doi: 10.1103/PhysRevD.10.897.

J. Garden, J. Heitger, R. Sommer, and H. Wittig.
   Precision computation of the strange quark's mass in quenched QCD.
   Nucl. Phys., B571:237–256, 2000.
   doi: 10.1016/S0550-3213(99)00714-2.

J. Gasser and H. Leutwyler.
   Quark Masses.
   Phys. Rept., 87:77–169, 1982.
   doi: 10.1016/0370-1573(82)90035-7.

J. Gasser and H. Leutwyler.
   Chiral Perturbation Theory to One Loop.
   Ann. Phys., 158:142, 1984.
   doi: 10.1016/0003-4916(84)90242-2.

J. Gasser and H. Leutwyler.
   Chiral Perturbation Theory: Expansions in the Mass of the Strange Quark.
   Nucl. Phys. B, 250:465, 1985.
   doi: 10.1016/0550-3213(85)90492-4.

C. Gattringer and C. B. Lang.
   Quantum Chromodynamics on the Lattice.
   Springer, 1st edition, 2010.

P. H. Ginsparg and K. G. Wilson.
   A remnant of chiral symmetry on the lattice.
   Phys. Rev., D25:2649, 1982.
   doi: 10.1103/PhysRevD.25.2649.

L. Giusti and A. Vladikas.
   RI/MOM renormalization window and Goldstone pole contamination.
   Phys. Lett., B488:303–312, 2000.
   doi: 10.1016/S0370-2693(00)00837-6.

L. Giusti, M. L. Paciello, C. Parrinello, S. Petrarca, and B. Taglienti.
   Problems on lattice gauge fixing.
   Int. J. Mod. Phys., A16:3487–3534, 2001.
   doi: 10.1142/S0217751X01004281.

S. L. Glashow, J. Iliopoulos, and L. Maiani.
   Weak Interactions with Lepton-Hadron Symmetry.
   Phys. Rev., D2:1285–1292, 1970.
   doi: 10.1103/PhysRevD.2.1285.

M. Gockeler et al.
   Nonperturbative renormalisation of composite operators in lattice QCD.
   Nucl. Phys., B544:699–733, 1999.
   doi: 10.1016/S0550-3213(99)00036-X.

M. Gockeler et al.
   Determination of light and strange quark masses from full lattice QCD.
   Phys. Lett., B639:307–311, 2006.
   doi: 10.1016/j.physletb.2006.06.036.

M. Gockeler et al.
   Probing the chiral limit with clover fermions. II. The Baryon sector.
   PoS, LAT2007:129, 2007.

D. J. Gross and F. Wilczek.
   Ultraviolet behavior of non-abelian gauge theories.
   Phys. Rev. Lett., 30(26):1343–1346, Jun 1973.
   doi: 10.1103/PhysRevLett.30.1343.

R. Gupta.
   Introduction to lattice QCD.
   1997.

M. Hasenbusch.
   Speeding up the Hybrid-Monte-Carlo algorithm for dynamical fermions.
   Phys. Lett., B519:177–182, 2001.
   doi: 10.1016/S0370-2693(01)01102-9.

A. Hasenfratz and F. Knechtli.
   Flavor symmetry and the static potential with hypercubic blocking.
   Phys. Rev., D64:034504, 2001.
   doi: 10.1103/PhysRevD.64.034504.

A. Hasenfratz, R. Hoffmann, and S. Schaefer.
   Hypercubic Smeared Links for Dynamical Fermions.
   JHEP, 05:029, 2007.

S. Hauswirth.
   Light hadron spectroscopy in quenched lattice QCD with chiral fixed-point fermions.
   2002.

G. Heatlie, G. Martinelli, C. Pittori, G. C. Rossi, and C. T. Sachrajda.
   The improvement of hadronic matrix elements in lattice QCD.
   Nucl. Phys., B352:266–288, 1991.
   doi: 10.1016/0550-3213(91)90137-M.

A. Hocker, H. Lacker, S. Laplace, and F. Le Diberder.
   A New approach to a global fit of the CKM matrix.
   Eur. Phys. J., C21:225–259, 2001.
   doi: 10.1007/s100520100729.
   URL http://www.slac.stanford.edu/xorg/ckmfitter/ckm_intro.html.

R. Hoffmann, A. Hasenfratz, and S. Schaefer.
   Non-perturbative improvement of nHYP smeared Wilson fermions.
   PoS, LAT2007:104, 2007.

R. Horsley.
   Lattice QCD with dynamical quarks.
   J. Phys. Conf. Ser., 287:012014, 2011.
   doi: 10.1088/1742-6596/287/1/012014.

R. Horsley, H. Perlt, P. E. L. Rakow, G. Schierholz, and A. Schiller.
Perturbative determination of c_{SW} for plaquette and Symanzik gauge action and stout link clover fermions.
Phys. Rev., D78:054504, 2008.
doi: 10.1103/PhysRevD.78.054504.

T. Inami and C. S. Lim.
Effects of Superheavy Quarks and Leptons in Low-Energy Weak Processes k(L) → mu anti-mu, K+ → pi+ Neutrino anti-neutrino and K0 ↔ anti-K0.
Prog. Theor. Phys., 65:297, 1981.
doi: 10.1143/PTP.65.297.

N. Ishii, S. Aoki, and T. Hatsuda.
The nuclear force from lattice QCD.
Phys. Rev. Lett., 99:022001, 2007.
doi: 10.1103/PhysRevLett.99.022001.

K. Jansen, A. Shindler, C. Urbach, and U. Wenger.
HMC algorithm with multiple time scale integration and mass preconditioning.
PoS, LAT2005:118, 2006.

K. Jansen et al.
Stout Smearing for Twisted Mass Fermions.
PoS, LAT2007:036, 2007.

C. Jarlskog.
Commutator of the Quark Mass Matrices in the Standard Electroweak Model and a Measure of Maximal CP Violation.
Phys. Rev. Lett., 55:1039, 1985.
doi: 10.1103/PhysRevLett.55.1039.

C. Jung.
Status of dynamical ensemble generation.
PoS, LAT2009:002, 2009.

J. Kambor, C. Wiesendanger, and D. Wyler.
Final State Interactions and Khuri-Treiman Equations in $\eta \to 3\pi$ decays.
Nucl. Phys., B465:215–266, 1996.
doi: 10.1016/0550-3213(95)00676-1.

W. Kamleh, D. B. Leinweber, and A. G. Williams.
Hybrid Monte Carlo with fat link fermion actions.
Phys. Rev., D70:014502, 2004.
doi: 10.1103/PhysRevD.70.014502.

W. Kamleh, B. Lasscock, D. B. Leinweber, and A. G. Williams.
Scaling analysis of FLIC fermion actions.
Phys. Rev., D77:014507, 2008.
doi: 10.1103/PhysRevD.77.014507.

D. B. Kaplan.
A Method for simulating chiral fermions on the lattice.
Phys. Lett., B288:342–347, 1992.
doi: 10.1016/0370-2693(92)91112-M.

D. B. Kaplan and A. V. Manohar.
Current Mass Ratios of the Light Quarks.
Phys. Rev. Lett., 56:2004, 1986.
doi: 10.1103/PhysRevLett.56.2004.

A. A. Khan et al.
Axial coupling constant of the nucleon for two flavours of dynamical quarks in finite and infinite volume.
Phys. Rev., D74:094508, 2006.
doi: 10.1103/PhysRevD.74.094508.

M. Kobayashi and T. Maskawa.
CP Violation in the Renormalizable Theory of Weak Interaction.
Prog. Theor. Phys., 49:652–657, 1973.
doi: 10.1143/PTP.49.652.

S. Krieg.
Towards the Confirmation of QCD on the Lattice: Improved Actions and Algorithms.
PhD thesis, JSC, 2008.

A. S. Kronfeld.
The weight of the world is quantum chromodynamics.
Science, 322:1198–1199, 2008.
doi: 10.1126/science.1166844.

T. Kurth.
Numerical Studies of Topology.
Master's thesis, Bergische Universität Wuppertal, April 2007.

T. Kurth et al.
Scaling study for 2 HEX smeared fermions: hadron and quark masses.
PoS, LATTICE2010:232, 2010.

J. Laiho, E. Lunghi, and R. S. Van de Water.
Lattice QCD inputs to the CKM unitarity triangle analysis.
Phys. Rev., D81:034503, 2010.
doi: 10.1103/PhysRevD.81.034503.

P. Langacker and H. Pagels.
Applications of Chiral Perturbation Theory: Mass Formulas and the Decay eta $\to$ 3 pi.
Phys. Rev., D10:2904, 1974.

D. B. Leinweber, T. Draper, and R. M. Woloshyn.
Decuplet baryon structure from lattice QCD.
Phys. Rev., D46:3067–3085, 1992.
doi: 10.1103/PhysRevD.46.3067.

D. B. Leinweber, J. I. Skullerud, A. G. Williams, and C. Parrinello.
Gluon propagator in the infrared region.
Phys. Rev., D58:031501, 1998.
doi: 10.1103/PhysRevD.58.031501.

L. Lellouch.
Flavor physics and lattice quantum chromodynamics.
2011.

H. Leutwyler.
   The ratios of the light quark masses.
   Phys. Lett., B378:313–318, 1996.
   doi: 10.1016/0370-2693(96)00386-3.

H. Leutwyler.
   Light quark masses.
   PoS, CD09:005, 2009.

H. Leutwyler and A. V. Smilga.
   Spectrum of Dirac operator and role of winding number in QCD.
   Phys. Rev., D46:5607–5632, 1992.
   doi: 10.1103/PhysRevD.46.5607.

E. Lunghi and A. Soni.
   Possible evidence for the breakdown of the CKM-paradigm of CP-violation.
   Phys. Lett., B697:323–328, 2011a.
   doi: 10.1016/j.physletb.2011.02.016.

E. Lunghi and A. Soni.
   Demise of CKM and its aftermath.
   2011b.

M. Luscher.
   Volume Dependence of the Energy Spectrum in Massive Quantum Field Theories. 1. Stable Particle
   States.
   Commun. Math. Phys., 104:177, 1986a.
   doi: 10.1007/BF01211589.

M. Luscher.
   Volume Dependence of the Energy Spectrum in Massive Quantum Field Theories. 2. Scattering
   States.
   Commun. Math. Phys., 105:153–188, 1986b.
   doi: 10.1007/BF01211097.

M. Luscher.
   Two particle states on a torus and their relation to the scattering matrix.
   Nucl. Phys., B354:531–578, 1991a.
   doi: 10.1016/0550-3213(91)90366-6.

M. Luscher.
   Signatures of unstable particles in finite volume.
   Nucl. Phys., B364:237–254, 1991b.
   doi: 10.1016/0550-3213(91)90584-K.

M. Luscher.
   Schwarz-preconditioned HMC algorithm for two-flavour lattice QCD.
   Comput. Phys. Commun., 165:199–220, 2005.
   doi: 10.1016/j.cpc.2004.10.004.

M. Luscher.
   Trivializing maps, the Wilson flow and the HMC algorithm.
   Commun.Math.Phys., 293:899–919, 2010a.
   doi: 10.1007/s00220-009-0953-7.

M. Luscher.
Properties and uses of the Wilson flow in lattice QCD.
JHEP, 1008:071, 2010b.
doi: 10.1007/JHEP08(2010)071.

M. Luscher.
Topology, the Wilson flow and the HMC algorithm.
PoS, LATTICE2010:015, 2010c.

M. Luscher and P. Weisz.
Computation of the Action for On-Shell Improved Lattice Gauge Theories at Weak Coupling.
Phys. Lett., B158:250, 1985.
doi: 10.1016/0370-2693(85)90966-9.

M. Luscher and U. Wolff.
How to calculate the elastic scattering matrix in two-dimensional quantum field theories by numerical simulation.
Nucl. Phys., B339:222–252, 1990.
doi: 10.1016/0550-3213(90)90540-T.

V. Maillart and F. Niedermayer.
A specific lattice artefact in non-perturbative renormalization of operators.
2008.

G. Martinelli, C. T. Sachrajda, and A. Vladikas.
A Study of 'improvement' in lattice QCD.
Nucl. Phys., B358:212–230, 1991.
doi: 10.1016/0550-3213(91)90538-9.

G. Martinelli, C. T. Sachrajda, G. Salina, and A. Vladikas.
An Exploratory study of meson spectroscopy and matrix elements with an improved fermion action at Beta = 6.0.
Nucl. Phys., B378:591–615, 1992.
doi: 10.1016/0550-3213(92)90609-F.

G. Martinelli, C. Pittori, C. T. Sachrajda, M. Testa, and A. Vladikas.
A General method for nonperturbative renormalization of lattice operators.
Nucl. Phys., B445:81–108, 1995.
doi: 10.1016/0550-3213(95)00126-D.

G. Martinelli et al.
Non-perturbative improvement of lattice QCD at large momenta.
Nucl. Phys., B611:311–337, 2001.
doi: 10.1016/S0550-3213(01)00342-X.

C. McNeile, C. Davies, E. Follana, K. Hornbostel, and G. Lepage.
High-Precision c and b Masses, and QCD Coupling from Current-Current Correlators in Lattice and Continuum QCD.
Phys.Rev., D82:034512, 2010.
doi: 10.1103/PhysRevD.82.034512.

C. Michael.
Adjoint Sources in Lattice Gauge Theory.
Nucl. Phys., B259:58, 1985.
doi: 10.1016/0550-3213(85)90297-4.

S. Mignani and R. Rosa.
The moving block bootstrap to assess the accuracy of statistical estimates in ising model simulations.
Computer Physics Communications, 92(2-3):203 – 213, 1995.
ISSN 0010-4655.
doi: DOI:10.1016/0010-4655(95)00114-7.

I. Montvay and G. Münster.
Quantum fields on a lattice.
Cambridge monographs on mathematical physics, 2nd edition, 1994.
Cambridge, UK: Univ. Pr. (1994) 491 p. (Cambridge monographs on mathematical physics).

P. J. Moran and D. B. Leinweber.
Over-Improved Stout-Link Smearing.
Phys. Rev., D77:094501, 2008.
doi: 10.1103/PhysRevD.77.094501.

C. Morningstar and M. J. Peardon.
Analytic smearing of SU(3) link variables in lattice QCD.
Phys. Rev., D69:054501, 2004.
doi: 10.1103/PhysRevD.69.054501.

C. Morningstar et al.
The excited hadron spectrum in lattice QCD using a new variance reduction method.
PoS, ICHEP2010:369, 2010.

K. Nakamura et al.
Review of particle physics.
J. Phys., G37:075021, 2010.
doi: 10.1088/0954-3899/37/7A/075021.

Y. Nakamura, S. Aoki, Y. Taniguchi, and T. Yoshie.
Precise determination of B_K and right quark masses in quenched domain-wall QCD.
Phys. Rev., D78:034502, 2008.
doi: 10.1103/PhysRevD.78.034502.

R. Narayanan and H. Neuberger.
Infinitely many regulator fields for chiral fermions.
Phys. Lett., B302:62–69, 1993a.
doi: 10.1016/0370-2693(93)90636-V.

R. Narayanan and H. Neuberger.
Chiral fermions on the lattice.
Phys. Rev. Lett., 71:3251–3254, 1993b.
doi: 10.1103/PhysRevLett.71.3251.

R. Narayanan and H. Neuberger.
Chiral determinant as an overlap of two vacua.
Nucl. Phys., B412:574–606, 1994.
doi: 10.1016/0550-3213(94)90393-X.

R. Narayanan and H. Neuberger.
A Construction of lattice chiral gauge theories.
Nucl. Phys., B443:305–385, 1995.
doi: 10.1016/0550-3213(95)00111-5.

R. Narayanan and H. Neuberger.
Infinite N phase transitions in continuum Wilson loop operators.
JHEP, 03:064, 2006.
doi: 10.1088/1126-6708/2006/03/064.

S. Necco and R. Sommer.
The N(f) = 0 heavy quark potential from short to intermediate distances.
Nucl. Phys., B622:328–346, 2002.
doi: 10.1016/S0550-3213(01)00582-X.

H. Neuberger.
Exactly massless quarks on the lattice.
Phys. Lett., B417:141–144, 1998a.
doi: 10.1016/S0370-2693(97)01368-3.

H. Neuberger.
More about exactly massless quarks on the lattice.
Phys. Lett., B427:353–355, 1998b.
doi: 10.1016/S0370-2693(98)00355-4.

M. Niedermaier and M. Reuter.
The Asymptotic Safety Scenario in Quantum Gravity.
Living Reviews in Relativity, 9(5), 2006.
URL http://www.livingreviews.org/lrr-2006-5.

H. B. Nielsen and M. Ninomiya.
Absence of Neutrinos on a Lattice. 1. Proof by Homotopy Theory.
Nucl. Phys., B185:20, 1981a.
doi: 10.1016/0550-3213(81)90361-8.

H. B. Nielsen and M. Ninomiya.
No Go Theorem for Regularizing Chiral Fermions.
Phys. Lett., B105:219, 1981b.
doi: 10.1016/0370-2693(81)91026-1.

H. B. Nielsen and M. Ninomiya.
Absence of Neutrinos on a Lattice. 2. Intuitive Topological Proof.
Nucl. Phys., B193:173, 1981c.
doi: 10.1016/0550-3213(81)90524-1.

C. C. Nishi.
Simple derivation of general Fierz-like identities.
Am. J. Phys., 73:1160–1163, 2005.
doi: 10.1119/1.2074087.

J. Noaki et al.
Light meson spectrum with N(f) = 2 dynamical overlap fermions.
PoS, LAT2007:126, 2007.

M. Peardon et al.
A novel quark-field creation operator construction for hadronic physics in lattice QCD.
Phys. Rev., D80:054506, 2009.
doi: 10.1103/PhysRevD.80.054506.

M. E. Peskin and D. V. Schroeder.
An Introduction to Quantum Field Theory.
The Advanced Book Program, Westview Press, 1st edition, 1995.

R. Petronzio and E. Vicari.
An Overrelaxed Monte Carlo algorithm for SU(3) lattice gauge theories.
Phys. Lett., B248:159–162, 1990.
doi: 10.1016/0370-2693(90)90032-2.

A. Portelli et al.
Electromagnetic corrections to light hadron masses.
PoS, LATTICE2010:121, 2010.

W. H. Press, S. A. Teukolsky, W. T. Vetterling, and B. P. Flannery.
Numerical Recipes.
Cambridge University Press, 3rd edition, 2007.

P. E. L. Rakow.
Progress towards finding quark masses and the QCD scale Lambda from the lattice.
Nucl. Phys. Proc. Suppl., 140:34–47, 2005.
doi: 10.1016/j.nuclphysbps.2004.11.360.

N. F. Ramsey.
Dipole moments and spin rotations of the neutron.
Physics Reports, 43(10):409 – 421, 1978.
ISSN 0370-1573.
doi: DOI:10.1016/0370-1573(78)90179-5.

A. Sacharow.
Symmetry of the universe. (in german).
Ideen d. Exakt. Wiss., 11:15–27, 1968.

C. Sachrajda.
Phenomenology from the Lattice.
PoS, LATTICE2010:018, 2010.

S. Schaefer, A. Hasenfratz, and R. Hoffmann.
Dynamical simulations with HYP-link Wilson fermions.
PoS, LAT2007:132, 2007.

S. Scherer.
Introduction to chiral perturbation theory.
Adv. Nucl. Phys., 27:277, 2003.

J. C. Sexton and D. H. Weingarten.
Hamiltonian evolution for the hybrid Monte Carlo algorithm.
Nucl. Phys., B380:665–678, 1992.
doi: 10.1016/0550-3213(92)90263-B.

Y. Shamir.
Chiral fermions from lattice boundaries.
Nucl. Phys., B406:90–106, 1993.
doi: 10.1016/0550-3213(93)90162-I.

S. R. Sharpe.
Quenched chiral logarithms.
Phys. Rev., D46:3146–3168, 1992.
doi: 10.1103/PhysRevD.46.3146.

S. R. Sharpe.
Applications of chiral perturbation theory to lattice QCD.
2006.

B. Sheikholeslami and R. Wohlert.
Improved Continuum Limit Lattice Action for QCD with Wilson Fermions.
Nucl. Phys., B259:572, 1985.
doi: 10.1016/0550-3213(85)90002-1.

R. Sommer.
A New way to set the energy scale in lattice gauge theories and its applications to the static force
and alpha-s in SU(2) Yang-Mills theory.
Nucl. Phys., B411:839–854, 1994a.
doi: 10.1016/0550-3213(94)90473-1.

R. Sommer.
A New way to set the energy scale in lattice gauge theories and its applications to the static force
and alpha-s in SU(2) Yang-Mills theory.
Nucl. Phys., B411:839–854, 1994b.
doi: 10.1016/0550-3213(94)90473-1.

M. Stephenson, C. E. Detar, T. A. DeGrand, and A. Hasenfratz.
Scaling and eigenmode tests of the improved fat clover action.
Phys. Rev., D63:034501, 2001.
doi: 10.1103/PhysRevD.63.034501.

C. Sturm et al.
Renormalization of quark bilinear operators in a momentum- subtraction scheme with a nonexceptional subtraction point.
Phys. Rev., D80:014501, 2009.
doi: 10.1103/PhysRevD.80.014501.

K. Symanzik.
Continuum Limit and Improved Action in Lattice Theories. 1. Principles and phi**4 Theory.
Nucl. Phys., B226:187, 1983a.
doi: 10.1016/0550-3213(83)90468-6.

K. Symanzik.
Continuum Limit and Improved Action in Lattice Theories. 2. O(N) Nonlinear Sigma Model in
Perturbation Theory.
Nucl. Phys., B226:205, 1983b.
doi: 10.1016/0550-3213(83)90469-8.

G. 't Hooft and M. J. G. Veltman.
One loop divergencies in the theory of gravitation.
Annales Poincare Phys. Theor., A20:69–94, 1974.

T. Takaishi and P. de Forcrand.
Testing and tuning new symplectic integrators for hybrid Monte Carlo algorithm in lattice QCD.
Phys. Rev., E73:036706, 2006.
doi: 10.1103/PhysRevE.73.036706.

G. 'tHooft and M. Veltman.
Regularization and renormalization of gauge fields.
Nuclear Physics B, 44(1):189–213, 1972.
doi: DOI:10.1016/0550-3213(72)90279-9.

N. Ukita et al.
  Light hadron spectrum with 2+1 flavor dynamical O(a)-improved Wilson quarks.
  PoS, LAT2007:138, 2007.

C. Urbach, K. Jansen, A. Shindler, and U. Wenger.
  HMC algorithm with multiple time scale integration and mass preconditioning.
  Comput. Phys. Commun., 174:87–98, 2006a.
  doi: 10.1016/j.cpc.2005.08.006.

C. Urbach, K. Jansen, A. Shindler, and U. Wenger.
  HMC algorithm with multiple time scale integration and mass preconditioning.
  Comput. Phys. Commun., 174:87–98, 2006b.
  doi: 10.1016/j.cpc.2005.08.006.

T. van Ritbergen, J. Vermaseren, and S. Larin.
  The Four loop beta function in quantum chromodynamics.
  Phys.Lett., B400:379–384, 1997.
  doi: 10.1016/S0370-2693(97)00370-5.

J. Vermaseren, S. Larin, and T. van Ritbergen.
  The four loop quark mass anomalous dimension and the invariant quark mass.
  Phys.Lett., B405:327–333, 1997.
  doi: 10.1016/S0370-2693(97)00660-6.

A. Walker-Loud et al.
  Light hadron spectroscopy using domain wall valence quarks on an Asqtad sea.
  Phys. Rev., D79:054502, 2009.
  doi: 10.1103/PhysRevD.79.054502.

S. Weinberg.
  Non-Abelian Gauge Theories of the Strong Interactions.
  Phys. Rev. Lett., 31(7):494–497, Aug 1973.
  doi: 10.1103/PhysRevLett.31.494.

S. Weinberg.
  The Problem of Mass.
  Trans.New York Acad.Sci., 38:185–201, 1977.

S. Weinberg.
  Effective Gauge Theories.
  Phys. Lett., B91:51, 1980.
  doi: 10.1016/0370-2693(80)90660-7.

S. Weinberg.
  The Quantum Theory of Fields: Foundations, volume 1.
  Cambridge University Press, 6th edition, 1995.

S. Weinberg.
  The Quantum Theory of Fields: Modern Applications, volume 2.
  Cambridge University Press, 4th edition, 1996.

F. Wilczek.
  Particle physics: Mass by numbers.
  Nature, 456:449–450, 2008.
  doi: 10.1038/456449a.

Bibliography

K. G. Wilson.
   Confinement of Quarks.
   Phys.Rev., D10:2445–2459, 1974.
   doi: 10.1103/PhysRevD.10.2445.

K. G. Wilson.
   The origins of lattice gauge theory.
   Nucl. Phys. Proc. Suppl., 140:3–19, 2005.
   doi: 10.1016/j.nuclphysbps.2004.11.271.

K. G. Wilson and J. B. Kogut.
   The Renormalization group and the epsilon expansion.
   Phys. Rept., 12:75–200, 1974.
   doi: 10.1016/0370-1573(74)90023-4.

U. Wolff.
   Monte Carlo errors with less errors.
   Comput. Phys. Commun., 156:143–153, 2004.
   doi: 10.1016/S0010-4655(03)00467-3.

W. M. Yao et al.
   Review of particle physics.
   J. Phys., G33:1–1232, 2006.
   doi: 10.1088/0954-3899/33/1/001.

J. M. Zanotti et al.
   Hadron Masses From Novel Fat-Link Fermion Actions.
   Phys. Rev., D65:074507, 2002.
   doi: 10.1103/PhysRevD.65.074507.

Selbständigkeitserklärung

Hiermit versichere ich, diese Arbeit selbständig verfasst, nur die angegebenen Hilfsmittel benutzt und alle wörtlich oder inhaltlich übernommenen Stellen als solche gekennzeichnet zu haben.

_____	_____
Name	Ort, Datum